Scale-up of gas fermentations - Modelling tools for risk minimisation

A thesis accepted by the Faculty of
Energy-, Process- and Bio-Engineering of the University of Stuttgart
in partial fulfilment of the requirements for the degree of
Doctor of Engineering (Dr.-Ing.)

by

Flora Siebler

born in Remchingen

Supervisor:	Prof. Dr.-Ing. Ralf Takors
Co-Examiner:	Prof. Dr.-Ing. Michael Schlüter
Date of Defence:	March 6, 2020

Institute of Biochemical Engineering
University of Stuttgart

2020

To Erik

"You cannot hope to build a better world without improving the individuals. To that end, each of us must work for his or her own improvement and, at the same time, share a general responsibility for all humanity, our particular duty being to aid those to whom we think we can be most useful."

Marie Curie

Declaration of Authorship

I, Flora SIEBLER, declare that this thesis titled, "Scale-up of gas fermentations - Modelling tools for risk minimisation" and the work presented in it are my own. I confirm that:

- This work was done wholly or mainly while in candidature for a research degree at this University.
- Where any part of this thesis has previously been submitted for a degree or any other qualification at this University or any other institution, this has been clearly stated.
- Where I have consulted the published work of others, this is always clearly attributed.
- Where I have quoted from the work of others, the source is always given. With the exception of such quotations, this thesis is entirely my own work.
- I have acknowledged all main sources of help.
- Where the thesis is based on work done by myself jointly with others, I have made clear exactly what was done by others and what I have contributed myself.

Signed:

Date:

UNIVERSITY OF STUTTGART

Abstract

Faculty IV: Energy-, Process- and Bio-Engineering
Institute of Biochemical Engineering

Doctor of Engineering (Dr.-Ing.)

Scale-up of gas fermentations - Modelling tools for risk minimisation

by Flora SIEBLER

The reduction of greenhouse gas emissions is a global endeavour supported by society, politics and industry. In recent years, circular economy, reducing the exploitation of fossil energy sources, have increased the demand for new solutions when producing commodities and fine chemicals. Caboxydotrophic fermentations with acetogenic bacteria are potential processes in order to reach these goals. They convert gaseous substrates such as CO, and CO_2/H_2 mixtures. However, gases as sole substrate are rather challenging, not only in small lab-scales but especially in large-scale. Transferring an efficient fermentation process from experimental to industrial scales often results in unpredictable performance losses.

This study presents an *in silico* concept minimising possible risks in gas fermentations up-scaling. First, the economical feasibility of various fermentation methods is investigated. Then, two computational tools are presented using *Clostridium ljungdahlii* as model organism and synthesis gas as substrate in a 125 m^3 bubble column reactor. While conceptual design approaches can search through parameter spaces of putative operational windows in very short time, computational fluid dynamics (CFD) approaches provide valuable insight in bacterial behaviour when confronted with stress conditions such as substrate gradients. The latter is currently limited by the available computing power making the interaction of both modelling approaches essential but also a valuable trade-off.

The one-dimensional spatial and temporal discretised approach (1D) shows that proper consideration of gas holdup is key when predict biological performance. An optimum reactor operation mode is identified and further investigated in a high resolution CFD study. Besides precise flow pattern, mixing and circulation times are calculated. Statistical lifeline analysis reveal

possible short- and long-term responses of the organism as well as maximum retention times in limitation zones. In addition, intrinsic bias of 1D models can be adapted and compensated by the results of the CFD simulation.

The combination of economical investigation with modelling tools show high potential for successful scale-up of gas fermentations. With this concept feasibility, reactor design, operation mode and general risk minimisation can be analysed and specified.

Zusammenfassung

Ein globales Anliegen der Gesellschaft, der Politik und der Industrie ist die Reduktion der Treibhausgasfreisetzung. Im selben Zug verlangt die Kreislaufwirtschaft, welche die Ausbeutung von fossilen Rohstoffen reduziert, in den letzten Jahren nach neuen Lösungen zur Herstellung von Grundstoffen und Feinchemikalien. Carboxydotrophe Fermentationen mit acetogenen Bakterien sind potentielle Prozesse, um dieses Ziel zu erreichen. Dabei werden gasförmige Substrate wie CO und CO_2/H_2 verstoffwechselt. Gase als reine Substratquelle stellen jedoch eine Herausforderung nicht nur in kleinen Laborumgebungen sondern speziell in großen Anlagen dar. Das Transferieren eines effizienten Fermentierungsprozesses von Labor zum Industriemaßstab führt häufig zu unvorhergesehenen Leistungsverlusten.

In dieser Studie wird ein *in silico* Konzept vorgestellt, das mögliche Risiken beim Hochskalieren von Gasfermentationen reduziert. Zuerst wird die ökonomische Umsetzbarkeit von verschiedenen Fermentierungsmethoden untersucht. Anschließend werden zwei rechnergestützte Hilfsmittel präsentiert, wobei *Clostridium ljungdahlii* als Modellorganismus und Synthesegas als Substrat in einem 125 m^3 Blasensäulenreaktor fungiert. Während konzeptionelle Planungsansätze in kurzer Zeit durch Parametervariatonen von vermeintliche Betriebsfenstern suchen können, bieten Methoden der numerischen Strömungsmechanik (engl. CFD) wertvolle Einblicke in das Verhalten von Bakterien unter Stressbedingungen wie zum Beispiel Substratgradienten. Letztere Methode ist derzeit vor allem durch die vorhandene Rechenleistung limitiert, welches die Wechselwirkung beider Modelle essentiell macht, gleichzeitig aber auch ein nützlicher Kompromiss ist.

Die eindimensionale, räumlich und zeitlich diskretisierte Methode (1D) zeigt, dass eine angemessene Betrachtung des Gasrückhalts eine zentrale Rolle bei der Vorhersage der biologischen Leistungsfähigkeit spielt. Ein optimaler Betriebsmodus des Reaktors wurde identifiziert und anschließend in einer hochauflösenden CFD Berechnung weiter untersucht. Neben präzisen Strömungsmustern wurden auch Misch- und Zirkulationszeiten berechnet. Statistische Analysen von Lebenslinien deckten sowohl Kurz- und Langzeitreaktionen der Organismen sowie maximale Aufenthaltszeiten in Grenzbereichen auf. Zusätzlich konnten innenwohnende Fehler des 1D Modells durch Lösungen der CFD Berechnung angepasst und kompensiert werden.

Die Kombination aus ökonomischen Untersuchungen in Verbindung mit Modellierungshilfsmitteln weist ein hohes Potential zur erfolgreichen Hochskalierung von Gasfermentationen auf. Mit diesem Konzept können

Umsetzbarkeit, Reaktordesign, Betriebsmodus und generelle Risikominimierung analysiert und spezifiziert werden.

Acknowledgements

First and foremost, I want to thank **Prof. Dr.-Ing. Ralf Takors** for giving me the opportunity to contribute to this motivating gas fermentation project at the Institute of Biochemical Engineering of the University of Stuttgart. His valuable feedback and suggestions throughout the last years have helped me to improve my work as well as my journal publications. Further, I want to thank both, **Prof. Dr.-Ing. Michael Schlüter** and **Prof. Dr.-Ing. Eckart Laurien**, for being the audit committee of this thesis. I also want to express my gratitude to **Prof. Dr.-Ing. Joachim Groß**, **Prof. Ph.D. Carsten Mehring** and **Prof. Dr.-Ing. Ulrich Nieken** for their suggestions during the circulation procedure.

Second, I want to thank **Dr. Alexey Lapin** for his unlimited support in physical and mathematical questions, patience and valuable supervision. Together with **Johannes Wutz**, they taught me all about fluid mechanics and infected me with their fascination of this research field. It was a pleasure working with you.

I am very grateful to have had the possibility to work in an inspiring and supporting team over the last years. Many thanks go to: my fighting partners (metaphorically and literally), modelling group and friends **Maike Kuschel** and **Julia Zieringer**; **Robert Nitschel** for his office therapy, the additional Ossi-Power and primarily his friendship - *P. putida* rules!; my project colleagues and friends **Maria Hermann** and **Sebastian Grenz**; **Max Becker** for his outstanding cake, our great vacations together and his friendship; **Adrian Eilingsfeld** for his graphical talent, technical assistance and interesting discussions; **Richard Schäfer** for his patience and limitless IT support; **Alexander Nieß** for setting up my work environment and recommendations for additional exams; **Martin Siemann-Herzberg** for all the insights into students supervision and university politics he has given me; **Andreas Freund**, **Alexander Dietrich** and **Salaheddine Laghrami** for their technical aid and useful hobbies; **Mira Lenfers-Lücker** and **Attila Teleki** for all the nice coffee and lunch breaks, interesting discussions and above all their friendship. Last but not least, I want to thank the whole **IBVT team** - you made this adventure enjoyable.

The opportunity to supervise six student papers showed me how gratifying and fun tutoring is. I was fortunate to work with **Sarah Müller**, **Paul Harsch** and **Ruphay Fintrup** who were great students. Special thanks go to **Nathanael Heimann** and **Marc Buschlüter**, who accompanied me for a long and pleasant time.

Since the beginning of my PhD thesis, I joined the mentoring program FeelScience of the University of Stuttgart where I met my mentor **Dr. Sommer** and the PhD students of my **E-Team**. I would like to thank you all for the mental support, advice and motivation you gave me along the way.

Without the financial support of the **Federal Ministry of Education and Research** the synthesis gas fermentation project would not have been possible. Therefore, I would like to thank the government and decision makers for funding this important research. At this point, I want to express my gratitude to all project partners of the **University of Ulm** and **Technical University of Munich**. Thank you for your cooperation, all the productive discussions and meetings.

Last but not least, I want to thank my family and friends for their unconditional support and confidence in my abilities. I am also grateful for the friendship of **Oliver Wedell**, **Veronika Sagmeister**, **Rebekka Kienle** and **Marcos Manuel Sánches**. Thank you, for all the nice evenings together and distractions during this journey. I want to thank **Marco Jovanovic** for his motivation and the fun we hand during numeric lessons. Special thanks go to **Martin Paul** and **Leonie Weimann** for their joyful and sometimes spicy lunch breaks, their honesty and above all their friendship. **Julia** and **Lars Lischke**, thank you for all the support, motivation and comfort you gave me during my whole time at the university. You are very dear to me. I thank **Johanna Klees**, **Phillip Ortwein**, **Johannes Hummel**, **Andreas Ulmer**, **Michael Kirchner**, **Ina Dutzi-Kirchner**, **Sabine Nemitz** for being my friends, their support, the fun vacations and the never-ending game nights. I would also like to thank my cousin **Felix Fränkle** for his welcome distractions and sportive activities. I am grateful for the unwavering support of **Patrick Seiler**, who is always there for me and has shown me that family is not defined by blood. Without the loving environment, trust and support of my parents, **Carola** and **Hansjörg Siebler**, I would never have gotten that far. I am very lucky to have you. I also want to thank my sisters **Tosca Siebler** and **Laura Rothweiler** and my brother-in-law **Etienne Rothweiler**, who are always there for me and whom I love very much. I am more than grateful to have **Erik Siebler** by my side, who is not only a loving and understanding partner but also my best friend. Last but not least, I thank **Sami Rothweiler**, **Linnea Lischke** and **Eli Rothweiler** for reminding me why I took part in this project in the first place and for showing me that life consist of much more than work.

Thank you all.

Contents

List of Figures

List of Tables

List of Abbreviations

1D	**1**-**D**imensional approach
ALR	**A**ir**L**ift **R**eactor
ATP	**A**denosine **T**ri**P**hosphate
BC	**B**oundary **C**ondition
BCR	**B**ubble **C**olumn **R**eactor
BDF	**B**ackward **D**ifferentiation **F**ormula
BSD	**B**ubbles **S**ize **D**istribution
CDW	**C**ell **D**ry **W**eight
CFD	**C**omputational **F**luid **D**ynamics
CODH	**C**arbon mono**O**xide **D**e**H**ydrogenase
DNS	**D**irect **N**umerical **S**imulations
DPM	**D**iscrete **P**hase **M**odel
DRW	**D**iscrete **R**andom **W**alk
EU ETS	**E**uropean **U**nion **E**missions **T**rading **S**ystem
FBA	**F**lux **B**alance **A**nalysis
FTS	**F**ischer–**T**ropsch **S**ynthesis
HPLC	**H**igh **P**erformance **L**iquid **C**hromatography
LES	**L**arge **E**ddy **S**imulations
MBR	**M**embrane **B**io**R**eactor
MBBR	**M**oving **B**ed **B**iofilm **R**eactor
MFA	**M**etabolic **F**lux **A**nalysis
MS	**M**ass **S**pectrometry
NAD	**N**icotinamide **A**denine **D**inucleotide
NADP	**N**icotinamide **A**denine **D**inucleotide **P**hosphate
NSE	**N**avier-**S**tokes **E**quation
ODE	**O**rdinary **D**ifferential **E**quation
PBM	**P**opulation **B**alance **M**odel
PDE	**P**artial **D**ifferential **E**quation
RA	**R**eseach **A**nswer
RANS	**R**eynolds-**A**veraged **N**avier-**S**tokes Equation
RNF	**R**hodobacter **N**itrogen **F**ixation

RNG	**R**e-**N**ormalization **G**roup
RQ	**R**eseach **Q**uestion
STR	**S**irred **T**ank **R**eactor
TBR	**T**rickled **B**ed **R**eactor
TC	**T**aylor-**C**Couette
THF	**T**etra**H**ydro**F**olate
UNFCCC	**U**nited **F**ramework **C**onvention on **C**limate **C**hange
VOF	**V**olume **O**f **F**luid

List of Symbols

Nomenclature

a	interfacial area concentration of gas phase	m^{-1}
A	general effective mass transfer area	m^2
A_O	surface of the organism	m^2
A_R	cross sectional area of the reactor	m^2
C	reactor specific constant	$-$
c	concentration	$\mathrm{mol\,m}^{-3}$
c^*	equilibrium concentration of gas in liquid phase	$\mathrm{mol\,m}^{-3}$
$C_\mathrm{fix}(\mathrm{SS})$	total steady state carbon fixation	%
c_T	specific thermal capacity	$\mathrm{J\,kg}^{-1}\,\mathrm{K}^{-1}$
D	dilution rate	h^{-1}
d_B	bubble diameter	m
$\mathcal{D}_\mathrm{L}$	liquid phase dispersion coefficient	$\mathrm{m}^2\,\mathrm{h}^{-1}$
$\mathcal{D}_m$	mass diffusivity in water of gas m	$\mathrm{m}^2\,\mathrm{s}^{-1}$
d_O	diameter of the organism	m
D_R	diameter of the reactor	m
Eo	Eötvös number	$-$
g	gravitational acceleration	$9.81\,\mathrm{m\,s}^{-1}$
H_m^cp	Henry coefficient of gas m	$\mathrm{mol\,L}^{-1}\,\mathrm{atm}^{-1}$
H_R	height of the reactor	m
k	turbulent kinetic energy	$\mathrm{m}^2\,\mathrm{s}^{-2}$ $(\mathrm{J\,kg}^{-1})$
K_CO	Monod constant	$\mathrm{mmol\,g}_\mathrm{CDW}^{-1}$
K_I	CO inhibition constant	$\mathrm{mmol\,g}_\mathrm{CDW}^{-1}$
k_L	mass transfer coefficient	$\mathrm{m\,s}^{-1}$
$K_{\mathrm{Y_{P,X}}}$	half-maximum yield	$\mathrm{mmol\,g}_\mathrm{CDW}^{-1}\,\mathrm{h}^{-1}$
M	molecular weight	$\mathrm{kg\,mol}^{-1}$
Mo	Morton number	$-$

m_s	maintenance demand	$g_{gluc}\, g_{CDW}^{-1}$
n_G	bubble number density	m^{-3}
N_s	total cell number	$-$
Nu	Nusselt number	$-$
p	partial pressure	Pa
P	ambient pressure	Pa
P_H	hydrostatic pressure	Pa
q	production/ consumption rate	$mmol\, g_{CDW}^{-1}\, h^{-1}$
Q_L	media flow	$m^3\, h^{-1}$
Q_R	back flow of liquid	$m^3\, h^{-1}$
R	gas constant	$kg\, m^2\, s^{-2}\, mol^{-1}\, K^{-1}$
R^2	coefficient of determination	$-$
Re	Reynolds number	$-$
R_R	radius of the reactor	m
s	solubility in water	$kg\, m^3$
Sh	Sherwood number	$-$
t	time	s
T	temperature	K
t_e	surface renewal time	s
u, v, w	velocity components	$m\, s^{-1}$
v_B	bubble rise velocity	$m\, s^{-1}$
$v_{circ,L}$	liquid circulation velocity	$m\, s^{-1}$
$\dot{V}_G$	gas volume flow rate	$m^3\, s^{-1}$
v_L	liquid phase velocity	$m\, s^{-1}$
V_L	liquid working volume	m^3
v_M	velocity magnitude	$m\, s^{-1}$
V_O	volume of the organism	m^3
V_R	liquid volume of the reactor	m^3
v_S	superficial gas velocity	$m\, s^{-1}$
v_T	terminal/ bubble rise velocity	$m\, s^{-1}$
x, y, z	coordinates	m
Y	yield per c-mol CO	$c\text{-}mol\, c\text{-}mol_{CO}^{-1}$
y_m	gas fraction m	$-$
$Y_{P,X}(SS)$	steady state product biomass yield	$c\text{-}mol\, c\text{-}mol^{-1}$

Greek symbols

α	dilution rate of liquid recycling	$-$
β	general mass transfer coefficient	$m\, s^{-1}$

γ	reaction rate	$\mathrm{m\,s^{-1}}$
Δ	gradient or indicated as Laplace operator $\Delta = \nabla^2$	
ε	energy dissipation rate	$\mathrm{m^2\,s^{-3}}$ ($\mathrm{W\,kg^{-1}}$)
ε_G	gas holdup	$-$ (%)
η	dynamic viscosity	$\mathrm{Pa\,s^{-1}}$
η_t	eddy viscosity	$\mathrm{m^2\,s^{-1}}$
λ	thermal conductivity	$\mathrm{W\,m^{-1}\,K^{-1}}$
μ	growth rate	$\mathrm{h^{-1}}$
ρ^*	total molar density	$\mathrm{mol\,m^{-3}}$
ρ_L	liquid density	$\mathrm{kg\,m^{-3}}$
ρ_m	gas density	$\mathrm{kg\,m^{-3}}$
σ	surface tension	$\mathrm{N\,m^{-}1}$
τ	residence time	s

Indices

0	start parameter at time point 0
a	acetate
b	2,3-butanediol
B	bubble
c	carbon monoxide
c2	carbon dioxide
crit	critical value
diff	diffusion
e	ethanol
exp	experimental value
G	gas phase
$\mathrm{h^+}$	hydrogen ion
k	fermentation products $k \in$ [acetate, ethanol, 2,3-butanediol]
L	liquid phase
m	synthesis gas component $m \in [\mathrm{CO,CO_2,H_2}]$
max	maximum value
O	organism
R	reactor
sim	simulated value
w	water
x	biomass

Chapter 1

Introduction

1.1 Challenges of waste gas recycling

In 2015 the United Nations Framework Convention on Climate Change (UNFCCC) signed The Paris Agreement, which was enforced on the 4th of November in 2016. This agreement is built on scientific theories of climate change and the fact that ambitious efforts are necessary to combat these changes as well as to support developing countries to do so. Similar to the Kyoto Protocol of 1992, one of these efforts is reducing man-made greenhouse gas emission. Primarily the release of carbon dioxide has been increasingly moving into political and economic focus (Philip, 2018).

CO_2 emissions are reduced further by the ongoing depletion of fossil resources (Takors et al., 2018). In order to assure the future demand of oil-based industries as well as the supply of transportation fuel, new strategies for carbon-based chemicals and energy sources have to be developed (Phillips et al., 2017). Combining both emission reduction and recirculation of precious carbon would be the best solution and should be the aspiration for future processes (Bengelsdorf and Dürre, 2017). In doing so the climate agreement goals of The Paris Agreement can be met, costly payments for CO_2 emission certificates prevented and carbon recycled.

One way of this so-called circular economy idea uses lignocellulosic waste as renewable resource, which can be converted to biorefinery chemicals such as biofuels or fine chemicals (Liguori and Faraco, 2016). Lignocellulosic feedstock can be agri-residue, agri-processing by-products and energy crops. To make the carbon-based energy available, either fungal, bacterial or enzymatic treatments are used (Liguori and Faraco, 2016). The process itself is technologically and economically very challenging. Industrial scale-up and

microbial performance are key difficulties which need to be dealt with and overcome.

Conventional gasification of biomass (Griffin and Schultz, 2012) or fast pyrolysis (Pfitzer et al., 2016; Arnold et al., 2017) are well applicable processes to use lignocellulosic sources and to produce synthesis gas or short syngas. Another source is the exhaust gas of the steel industry. The main components of this gas mixture are carbon monoxide, carbon dioxide and hydrogen but also hold unwanted compounds such as H_2S or NH_3. Syngas is a common source in chemical processes but can only be exploited in certain composition ratios and without any impurities. Furthermore, these processes demand high temperatures and pressures.

Instead of being used in the chemical applications, syngas can also be converted in bioreactors with fermentative microorganism. Via hydrogenesis, methanogenesis or acetogenesis these bacteria can grow on CO, CO_2 and H_2 and produce economically interesting by-products (Latif et al., 2014; Diender et al., 2015). In general, microbial fermentations are moderate processes which demand usually only low temperatures and pressures, less ecological harmful acids or bases, let alone the use of heavy metals.

For the moderate and ecologically friendly recycling of important carbon sources and the fixation of CO_2, preferably in form of valuable carbohydrates, syngas fermentations with acetogenic microorganism are very promising (Dürre, 2016). However, to be economically superior to conventional chemical approaches, further improvements are needed. This thesis focusses on different aspects of efficient syngas fermentation. In this chapter the motivation and addressed tasks are introduced.

1.2 Motivation of this thesis

In general, gas fermentations mainly need to overcome two limiting factors: (i) low gas solubility and (ii) efficient mass transfer from gas to liquid phase. Aerobic fermentations need oxygen as electron acceptor in the energy metabolism and the carbon source is usually provided in form of a sugar-solutions. In contrast, the carbon source of synthesis gas fermentations is introduced via the gas phase. On the downside, the gas components are only available in their dissolved form making the limiting factors (i) and (ii) even more essential.

This thesis is not only motivated by the previously mentioned physical but also by economic challenges in respect to the desired products and their titres. The profitability of the process sets the framework for potential

scale-up. Product complexity, quantity, purity and stock price are key in this matter which are investigated first. An initial economic assessment of the process narrows down the reactor type and gives information about its general feasibility. However, the first potential assessment is based on assumptions which, if carried out in a reasonable manner, is very helpful.

Scale-up especially for challenging processes such as gas fermentations should be approached from more than one angle. If the economic assessment shows potential for the process, possible maximum titres can be approximated. For this purpose, different *in silico* simulations can be performed to rule out any risks in process up-scaling. As mentioned before, gas fermentations are very difficult to predict since simulating the gas-liquid mass transfer is still very imprecise and thus an estimate. Nevertheless, modelling large-scale fermentations can predict the presumably best operation mode and identify possible inefficiencies in advance.

Spatial resolution is a key aspect in modelling flow behaviours. A reactor can be seen as one evenly mixed vessel or partitioned into several smaller volumes to reflect different spatial properties. The latter allows solving physical flow equations and transport between the reactor partitions. Consequently, the higher the resolution the more information about the process can be derived. Concerning gas fermentations, the complexity for modelling escalates to a multi-phase problem with gas and liquid phase and the above-mentioned crucial mass transfer between these phases.

While the spatial discretisation increases the resolution, an increase can also be seen for the required computing power and solution time. While the general computing power has been changing for the better over the last years high resolution multiphase simulations are still limited. Above all, the chosen simulation approach is specifically tailored to solve a distinct aspect of the system. While dynamic analysis with adequate model assumptions can be executed in rather coarse discretised models, biological impacts due to possible gradient formations require state of the art refinements. Especially in case of synthesis gas fermentations with debated profitability, preliminary studies are advisable. However, only few investigations with regards to *in silico* analysis have been undertaken.

The presented thesis with the title *"Scale-up of gas fermentations - Modelling tools for risk minimisation"* targets the above-mentioned challenges with an overall concept to minimise the risks in scale-up of synthesis gas fermentations by performing essential preliminary investigations as well as pursuing different modelling approaches. The detailed strategy of the objectives and thesis outline can be found in the last section of the introduction.

1.3 Objectives, strategy and thesis outline

The previously mentioned challenges are further described in form of distinct objectives for which solution strategies are introduced (**Chapter 1 - Introduction**). The objectives are formulated as research questions (**RQ**s) alongside which the structure of this thesis is presented. In general, the risk minimisation concept motivated by the up-scaling of synthesis gas fermentations is divided into three parts: a pre-evaluation of reactor geometries and assessment of potential of synthesis gas fermentations (A), a fast low-resolution 1-dimensional (1D) approach (B) and a high-resolution computational fluid dynamic (CFD) approach (C). A schematic overview is given in Figure 1.1.

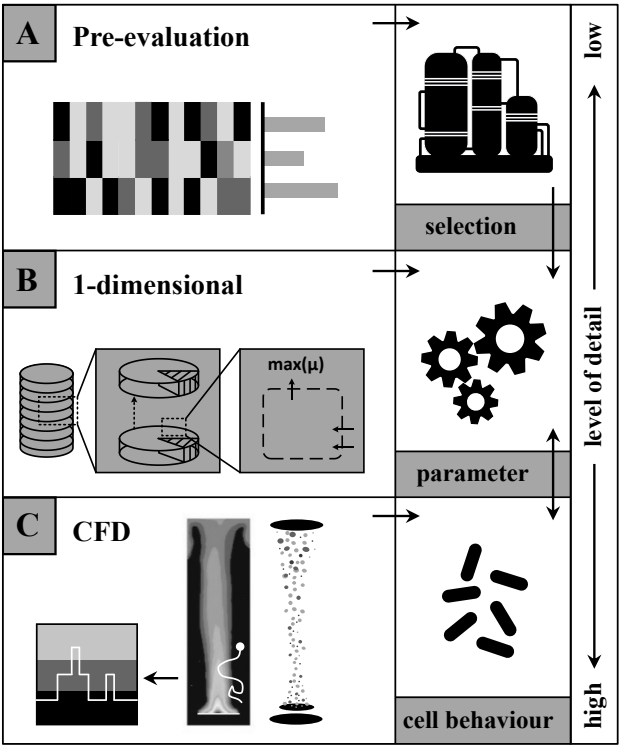

Figure 1.1: Schematic overview of the thesis structure. The thesis is grouped in the evaluation and assessment of industrial reactor geometries (A), and mathematical approaches. The latter are divided in a 1-dimensional approach (B) and computational fluid dynamics (CFD) approach (C).

In **Chapter 2 - Information concerning synthesis gas fermentation** an overview of the state of the art of gas fermentation is given. It includes common information on production, composition and application of synthesis gas, the introduction of strains and metabolism as well as information on the general challenge of gases as substrate. The first part of this thesis, the pre-evaluation section pictured in Figure 1.1 (A), is presented in **Chapter 3 - Evaluation and assessment of industrial reactors** and targets the following research questions (numbering corresponds to the sections of this thesis):

RQ3.1 Which reactor geometries are suitable for synthesis gas fermentations?

RQ3.2 Is the industrial application of synthesis gas fermentations economically feasible?

Answering **RQ3.1** was possible by summarising conventional and non-conventional reactor geometries and comparing them with regard to presumable reactor performance and scale-up costs. The objective of this question is a reactor pre-selection for further *in silico* analysis. The second research question (**RQ3.2**) addresses an assessment of potential. Product stock prices and maximal plant budgets are calculated to assess the profitability of the process.

With the information of the pre-evaluation (A), the modelling parts (B) and (C) are investigated. The model approaches hold the largest share of this study and are organised in three chapters. While **Chapter 4 - Challenges, mathematical methods and approaches** introduces the chosen approaches, **Chapter 5 - Programs and set-up** gives background information concerning programs, simulation parameters and the models. Finally, the results of the simulations are placed in the overall context in **Chapter 6 - Modelling results and discussion**. In the thesis part (B) and (C), the following main research questioned are processed:

RQ4.1 What main characteristics of the chosen reactor must be kept in mind when modelling the process?

RQ4.2 Which models are chosen and why?

RQ4.3 How can a 1-dimensional (1D) model with focus on gas holdup be derived?

RQ4.4 Which numerical approaches are appropriate for modelling multiphase computational fluid dynamics?

RQ6.1 What information is gained by the 1D approach?

RQ6.2 Which statements can be made regarding the computational fluid dynamics results?

RQ6.3 How can the model approaches be complementary?

Detailed background research presented in chapter 4.1 provides an adequate answer to **RQ4.1**. On the other hand, **RQ4.2** is motivated by state of the art models, their application possibilities and desired results. The concept of synthesis gas risk minimisation is built on the development of appropriate modelling tools answering the key issue **RQ4.3**, **RQ4.4**, **RQ6.1** and **RQ6.2**. Deriving of the 1-dimensional model (**RQ4.3**) investigations of possible diffusion limitations follow. In addition, it includes the development of a small kinetic correlation to model microbial growth and production. Since anaerobic acetogenic bacteria are the most researched and promising choice for syngas conversion, a representative acetogenic model strain is used in all approaches. As indicated in Figure 1.1 (B), the main objective of the 1D approach is a parameter space probing (**RQ6.1**) to find a reasonable starting point for the more detailed computational fluid dynamic approach (Figure 1.1 (B) and **RQ4.4**/**RQ6.3**). The CFD approach settings (**RQ4.4**) are derived from the 1D results, extensive literature research and practicability within the constraints of available computing power. Besides higher levels of detail, the objective of the CFD approach (see also Figure 1.1 (C) and **RQ6.2**) is predicting cell behaviour in large scales gas gradients aiming for the biological impacts of possible substrate insufficiencies. While the CFD model is partially built on the 1D model, the latter can also benefit from the high-resolution results (**RQ6.3**).

Chapter 7 - Conclusion and outlook concludes all findings and statements of the developed risk minimisation concept and provides suggestions for future work in up-scaling of synthesis gas fermentations.

Chapter 2

Information concerning synthesis gas fermentation

This chapter gives necessary background information on the production and composition of synthesis gas and its general application, either chemical or biochemical. Additionally, synthesis gas digesting strains and their exceptional Wood-Ljungdahl pathway are introduced as well as possible fermentation products. Finally, the general challenges according to the substrate availability is highlighted in respect to gas-liquid mass transfer.

2.1 Production and composition of synthesis gas

The production of synthesis gas short syngas shows a tremendous feedstock flexibility (Daniell et al., 2012), which leads to a broad variety in the composition of industrial generated syngas (see Table 2.1).Wood, dedicated energy crops, grain wastes, manufacturing or municipal wastes, natural gas, petroleum and chemical wastes, lignin, coal and tires are used as feedstock materials (Phillips et al., 2017). These carbon-rich materials can be gasified to syngas with its main fractions: CO, CO_2 and H_2. The water-gas-shift (WGS) reaction (see equation (2.1)) converts CO and H_2O into CO_2 and H_2 under high pressure and high temperatures and is hereby the key transformation (Takors et al., 2018).

$$CO + H_2O \rightleftharpoons CO_2 + H_2 \qquad \Delta H_R^0 = -41 \text{ kJ mol}^{-1} \tag{2.1}$$

Depending on the type of pollution and its quantity share, potential accumulation of impurities in the fermentation media and associated effects such as cell toxicity, enzymatic inhibition and product distribution can occur

(Xu et al., 2011). Impurities can be H_2S, CH_4, COS, etc. These are summarised as N_2 in Table 2.1. To simplify further steps, the N_2-impurity will have no impact on the fermentation except reducing the other syngas fractions. Nevertheless, impurity effects should be kept in mind if it comes to industrial fermentation processes. Depending on the used syngas, an upstream clean-up process is advisable (Xu et al., 2011) but also an additional source for manufacturing cost.

Table 2.1: Synthesis gas composition. Synthesis gas fractions produced in industrial scale (derived from Wang et al., 2009; U.S. Department of Energy, 2015) and for lab scale purposes (see gas composition in Appendix of Manuscript II).

		CO_2	CO	H_2	N_2
industry	vol.-%	10-15	35-65	27-30	0-5
	mass.-%	12-25	28-68	2	0-5
laboratory	vol.-%	5	55	30	10
	mass.-%	10	73	3	13

There is another source for syngas, too. It is also produced in large volumes as by-product of divers industries for example by the steel industry. During the metallurgical production process (see Figure 2.1), three different gas types are released.

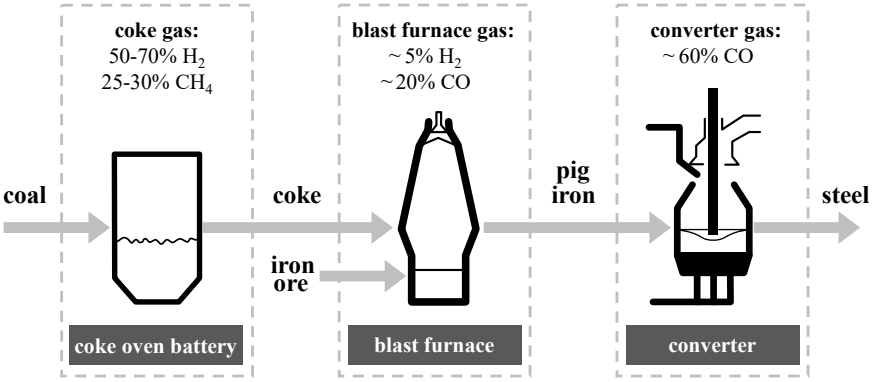

Figure 2.1: Off-gases from metallurgical production process (derived from Clarke Energy®, 2018). The process is divided into three stages with three different off-gas compositions.

Coke gas is produced in the coke oven battery by high-temperature pyrolytic distillation of coking coal. Besides high hydrogen amounts, large quantities of methane gas are produced. In the second process step blast

furnace gas is formed by reducing iron ore with the previous produced coke to metallic pig iron. In the final step the pig iron is converted into the actual steel releasing the converter gas. Is the final step the most common Linz-Donawitz process the converter gas consists of about 65% carbon monoxide, 15% carbon dioxide, 15% nitrogen and small amounts of hydrogen and methane (Clarke Energy®, 2018).

While coke gas is usually recycled in internal processes furnace and converter have low heating values and are difficult and less economical to be completely recycled. Despite the low remaining energy, syngas from the steel industry is a carbon source of the third generation. Energy from substrates of the first generation would be for example sugar and starch which also competes with the food industry. The above-mentioned feedstock for syngas generation would be of the second generation not directly competing with the world's food supply. Feedstock materials such as wood or straw, however, have already important purposes, e.g. paper industry and animal feed, and are therefore also controversially discussed (Basile et al., 2019, p. 320-323). Although carbon sources of the third generation are low in available energy, they are less questionable and often seen as economic burden in terms of CO_2 emission (Takors et al., 2018). For these reasons this thesis addresses mainly the processing of synthesis gas generated by the steel industry.

2.2 General application and advantages

In this section, the chemical application of synthesis is stated, directly followed by the recent biochemical application. For the latter, companies are introduced which have already started syngas fermentation in large scales.

2.2.1 Chemical application

As discussed in the previous chapter syngas can be produced from various sources and is also a by-product of diverse industrial off-gases. In the chemical industry syngas is an important intermediate resource for the production of hydrogen and ammonia via the water-gas-shift reaction, synthetic hydrocarbon fuels via the Fischer-Tropsch synthesis (FTS) and the production of dimethylether via methanol synthesis (van de Loosdrecht and Niemantsverdriet, 2012, p. 443-458). All these processes are strongly endothermic and energy-intensive with pressures of 20-300 bar and temperatures of 200-350 °C (Takors et al., 2018). Additionally, impurities have to be removed and for optimum FTS conversion specific H_2 to CO ratios (>2) need

to be achieved (Abubackar et al., 2011; Griffin and Schultz, 2012). The FTS reaction (see equation (2.2)) is catalysed by metal catalysts such as cobalt, iron and ruthenium.

$$n\,CO + (2n+1)\,H_2O \rightarrow C_nH_{2n+2} + n\,H_2O \tag{2.2}$$

Even though there is a tremendous amount of mechanistic complexity involved the overall reaction is quite straightforward (van de Loosdrecht and Niemantsverdriet, 2012). The oxygen atom is removed from the CO by forming water. For the methanol production a specific ratio of CO_2, CO and H_2 is needed.

$$CO_2 + H_2 \rightleftharpoons CH_3OH + H_2O \qquad \Delta H_R^0 = -47\ \text{kJ mol}^{-1} \tag{2.3}$$

$$CO + 2H_2 \rightleftharpoons CH_3OH \qquad \Delta H_R^0 = -91\ \text{kJ mol}^{-1} \tag{2.4}$$

Equation (2.3) shows the predominant reaction and equation (2.4) the combination of equation (2.1) and (2.3).

An alternative and more moderate syngas application is the fermentative microbial conversion. Nature provides a bunch of these microorganisms which can convert CO_2, CO and H_2 via hydrogenesis, methanogenesis or acetogenesis (Latif et al., 2014; Diender et al., 2015). Especially acetogen organisms are promising for industrial application and potentially economical superior to chemically conversion.

2.2.2 Companies exploring syngas gas fermentation

Until 2012, there were three companies dealing with the commercialisation of synthesis gas fermentation: INEOS Bio, Coskata and LanzaTech (Daniell et al., 2012). Some vanished and some succeeded. This chapter introduces all current industrial initiatives and their main products. Gaddy and Clausen (1992) of the University of Arkansas filed the first patents in this area. INEOS, a major multinational chemical firm, acquired Gaddy's industrial scale-up transfer in 2008 (Daniell et al., 2012).

INEOS Bio (2013) is a subsidiary of INEOS which uses proprietary isolates of *Clostridium ljungdahlii* as biocatalyst. Their pilot plant reports a production rate of 380 L (100 gallons) ethanol per dry ton of feedstock. The feedstock (see chapter 2.1) is gasified to syngas and then fermented to bioethanol (Gaddy et al., 2012). Nowadays, INEOS Bio build two commercial scale plants in the United States (Daniell et al., 2012).

Another company was Coskata (2006) which used technology and organism *Clostridium ragsdalei* and *Clostridium carboxidivorans* licences from Oklahoma. An additional strain, *Clostridium coskatii*, was used for ethanol production. Coskata also produced about 380 L of ethanol per dry ton of softwood in Madison, Pennsylvania. Synata Bio (2016) acquired the technology in 2015 when Coskata went out of business.

LanzaTech (2005) focusses not only on ethanol but on 2,3-butanediol production, too. Besides synthesis gas also CO-rich industrial off-gases are used. To produce chemicals, such as 2,3-butanediol and butanol as well as traditional fuels like ethanol by gas fermentation, is a unique selling point of this company. A pilot plant can be found in Auckland, New Zealand, and a pre-commercial demonstration plant in partnership with BaoSteel is located in Shanghai, China. This demonstration plant produces 380 L ethanol per year from steel mill off-gases. Commercial scale facilities can be found in Caofeidian (China) since 2017 with 16 M gallons per year and in Gent (Belgium) with ArcelorMittal since 2018 with 21 M gallons per year(LanzaTech, 2018). Three additional commercial scale project in South Africa (Swayana) with ferroalloy off-gases, in India (IndianOil) with refinery off-gases and in California (Aemetis) with gasified orchard wood and nutshells (Teixeira et al., 2018).

In 2012, the start-up White Dog Lab (2016) was founded, focussing on mixotrophic fermentation. They use sugars and syngas/CO to produce acetone and isopropanol. The production of both products has also been demonstrated by LanzaTech (2017).

Although there are already existing syngas fermenting companies, efficiency and profitability are not necessarily given and further improvement is advisable. One possibility could be new fermentation products with higher market prices, another would be a more cost-saving scale-up. There is high potential in synthesis gas fermentation with an ever-growing market.

2.3 Synthesis gas digesting strains

In this section the main gas digesting strains are introduced and the specific characteristics of the Wood-Ljungdahl pathway are explained. Finally, the recent main products and their applications are listed.

2.3.1 Acetogenic strains and application

The most relevant syngas digesting strains are acetogenic bacteria. Acetogens can be found in soils, sediments, sludge an intestinal tracts of many animals and are thus anaerobic mircroorganisms (Drake et al., 2008). There are numerous known acetogens but only few serve as model organisms and industrial workhorses (see Table 2.2)). Using the reductive acetyl-CoA pathway, they produce naturally mainly acetate, 2,3-butanediol and ethanol (Daniell et al., 2012). CO and H_2 serve as electron donors enabling the growth on CO_2/H_2, CO or CO/H_2. As the microorgnisms can switch between their educts, they are more flexible and therefore potentially superior to conventional Fisher-Tropsch processes (Munasinghe and Khanal, 2010a; Griffin and Schultz, 2012). Nevertheless, occurrence of off-gas impurities such as sulphur dioxide and hydrogen sulphide may hamper cellular performances (Munasinghe and Khanal, 2010a). Eventually, better fermentation results will be obtained if the fermentation gas is free of impurities and provides a high CO concentration (see also chapter 2.3.2).

In general, the optimal fermentation conditions of acetogenic strains are quite moderate with optimal pH around 7 and usually temperature of 30 °C and 37 °C (see Table 2.2). Thermophilic bacteria such as *Moorella thermoacetica* have much higher optimal operation temperatures, however, not as high as chemical syngas processes (see chapter 2.2.2).

Table 2.2: Main acetogenic model organisms and industrial workinghorses (derived from Takors et al., 2018). DT stands for autotrophic doubling time. If data is not available (n.a.) it is marked as such. References: Balch et al. (1977) [1], Bache and Pfennig (1981) [2], Sharak Genthner and Bryant (1982) [3], Schink and Stieb (1983) [4], Poehlein et al. (2012) [5], Abrini et al. (1994) [6], Köpke et al. (2011) [7], Brown et al. (2014) [8], Tanner et al. (1993) [9], Köpke et al. (2010) [10], Fontaine et al. (1942) [11], Kerby and Zeikus (1983) [12], Andreesen et al. (1973) [13], Daniel et al. (1990) [14], Parekh and Cheryan (1991) [15], Gößner et al. (1999) [16], Bengelsdorf et al. (2015) [17], Poehlein et al. (2015) [18].

Species name	Substrate(s)	Product(s)	Optimum temp.	Optimum pH	DT (CO)	Ref.
Acetobacterium woodii DSM 1030	H_2+CO_2	acetate	30 °C	7.6	n.a.	[1]-[5]
Clostridium autoethanogenum DSM 10061	H_2+CO_2, CO	2,3-butanediol, acetate, ethanol	37 °C	5.8-6.0	4 h	[6]-[8]
Clostridium ljungdahlii DSM 13528	H_2+CO_2, CO	2,3-butanediol, acetate, ethanol	37 °C	6.0	3.8 h	[7],[9], [10]
Moorella thermoacetica DSM 2955	H_2+CO_2, CO	acetate	55 °C	6.9	9-16 h	[11]-[18]

Table 2.2 also lists autotrophic doubling times (DT), which are compared

to for example *Echerichia coli* (Gibson et al., 2018) with up to 20 min and *Vibrio natriegens* with 9.4 min (Hoffart et al., 2017) quite slow. CO is very low in energy compared with other carbon sources. Some reduced sugars offer much more energy and are also digestible by the afore mentioned acetogens. In this thesis, one of the most researched strains, *Clostridium ljungdahlii*, was used as model organism.

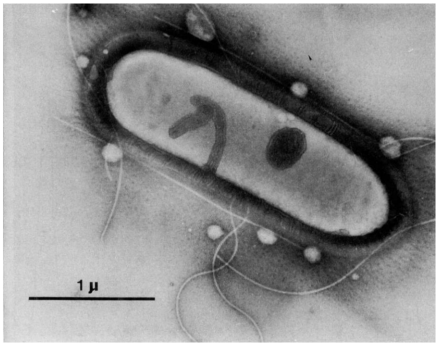

Figure 2.2: *Clostridium ljungdahlii* sp. nov. by Tanner et al. (1993). Picture shows a transmission electron micrograph of the acetogenic strain.

C. ljungdahlii (see Figure 2.2) is anaerobic, rod-shaped, motile, endospore-forming, gram-positive bacterium (Tanner et al., 1993) and highly promising to access not only native products (ethanol, acetate or 2,3-butanediol) but also recombinant compounds such as acetone, butanol etc. (Takors et al., 2018). The organism is completely sequenced and genetically accessible, which was shown by Köpke et al. (2010), who constructed a recombinant butanol producing strain. *C. ljungdahlii* is a model acetogen for proton bioenergetics and CO utilization. With the help of a proton gradient, energy in form of ATP (adenosine triphosphate) can be generated. The following chapter discusses in detail how syngas is metabolised and energy generated.

2.3.2 Wood-Ljungdahl pathway

Acetogens can ferment CO and/or CO_2 and H_2 into acetyl-CoA. The reductive acetyl-CoA pathway is also known as the Wood-Ljungdahl pathway. CO and H_2 are used by these organisms as energy source and CO_2 as an electron acceptor (Daniell et al., 2012). Carbon monoxide enters the Wood-Ljungdahl pathway through two routes and is preferred for electron production over

H_2 (Hu et al., 2011). Phillips et al. (1994) postulate that higher CO concentration result in more product formation (here ethanol and acetate) as well as biomass production.

The two routes are also known as the methyl (eastern) and carbonyl (western) branches. As mentioned before, either CO or CO_2 can serve as carbon source, which can be seen in Figure 2.3 highlighted in blue. When CO is used, it is first oxidised to CO_2 utilising ferredoxin (Fd). Via the methyl branch, CO_2 is then reduced to formate, which is coupled to the coenzyme tetrahydrofolate (CHO-THF) spending one ATP (highlighted in red). After the reduction to methyl-tetrahydrofolate (CH_3-THF), acetyl-CoA is formed with another CO of the carbonyl branch. CO dehydrogenase (CODH) is the key enzyme which catalyses the reaction shown in equation (2.5) and represents the biological version of the water-gas-shift reaction mentioned in chapter 2.1 equation (2.1).

$$CO + H_2O + A \rightarrow CO_2 + AH_2 \tag{2.5}$$

CODH can covert the CO_2 to CO and vis versa and also combines the methyl group of CH_3-THF and the carbonyl group into acetyl coenzyme A (short acetyl-CoA in first and last reaction in Figure 2.3 blue highlighting). In general, the carbonyl or western branch can only be found in anaerobic microorganisms (Ragsdale, 1997). Acetyl-CoA is further metabolised to acetate which yields in one ATP and consequently the preferred by-product (Figure 2.3 yellow highlighting). One ATP is used in the methyl branch and one produced in acetate production leaving no energy for growth so far. Here comes the afore mentioned RNF-complex into focus. RNF comes from *Rhodobacter* nitrogen fixation, which forms with reduced ferredoxin: NAD^+ oxidoreductase a complex and produces as membrane-bound protein a proton gradient. Together with the also membrane-bound ATPase, ADP can be recycled to ATP, which is indicated in Figure 2.3 (highlighted in grey). The coupling with reduction equivalents (Fd_{red}/Fd_{ox}, $NAD^+/NADH$, $NADP^+/NADPH$) is quite complex and catalysed by the bifurcating hydrogenesis. This enzyme oxidise two H_2 and reduce both ferredoxin and NAD^+ (Figure 2.3 in violet). Alcohols such as ethanol (green) and 2,3-butanediol (orange) are produced, too, which generates NAD^+. Lactate (pink) is an overflow product and can only be found in traces. The formation of by-product is needed to keep the RNF-complex running to generate ATP via the ATPase which is needed for growth.

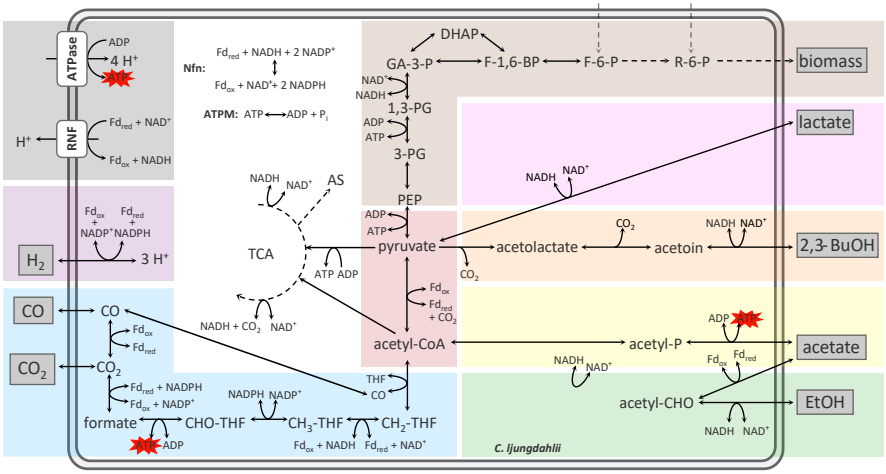

Figure 2.3: Main biochemical pathways of *C. ljungdahlii*. Simplified Wood-Ljungdahl pathway is highlighted in blue. Hydrogenesis reaction to utilise H_2 is highlighted in violet while membrane-bound RNF-complex and ATPase for proton gradient and energy supply is indicated in grey. Important intermediates such as acetyl-CoA and pyruvate are highlighted in red. Product pathways for biomass, lactate, 2,3-butanediol (BuOH), acetate and ethanol (EtOH), are coloured in brown, pink, orange, yellow and green.

How every reaction is intertwined is not completely understood but cell growth depends strongly on the energy providing proton gradient and therefore also on the overall redox potential. Stoichiometric models can give important insight in this matter. There is one genome scale model of *C. ljungdahlii* available so far (Nagarajan et al., 2013). In general, genome scale models are often used for metabolic flux analysis (MFA), an analysis to gain information of the internal fluxes and how to optimise the strain. As mentioned before *C. ljungdahlii* is genetically well accessible giving the opportunity to produce recombinant strains to get new products. Which natural products can be produced with syngas fermentation and are desired by the chemical industry, is discussed in the next chapter.

2.3.3 Possible fermentation products

The most common natural by-product of synthesis gas fermentation is acetate due to the energy generated during the process (see Figure 2.3 in chapter 2.3.2). Acetate is mostly used in the production of polymers, in the textile industry for dyeing and as well as solvent (Cheung et al., 2005). In

many cases, ethanol and 2,3-butanediol are produced, too (see for example Table 2.2 in chapter 2.3.1). Up to 2 mM can be generated by these bacteria from steel mill waste as substrate (Köpke et al., 2011). Ethanol can be used, amongst other things, as precursor of ethyl halides and esters, as biofuel or solvent (Köpke et al., 2010). In addition to acetate, *Clostridium formicoaceticum*, *Clostridium methoxybenzovorans* and *Eubacterium aggregans* produce formate (Andreesen et al., 1970; Lux and Drake, 1992; Mechichi et al., 1998; Mechichi et al., 1999). *Acetonema longum*, *Clostridium drakei*, *Clostridium scatologenes* and *Oxobacter pfennigii* produce innately butyrate (Kane et al., 1991; Chen et al., 2011; Küsel et al., 2000; Liou et al., 2005; Gößner et al., 2008; Jeong et al., 2014; Zhu et al., 2015; Krumholz and Bryant, 1985), which is a precursor in the production of plastics and lacquers, but serves as food flavour, too. (Riemenschneider, 2005). *Butyribacterium methylotrophicum* and *Clostridium carboxidovorans* are able to form butanol (Zeikus et al., 1980; Lynd et al., 1982; Liou et al., 2005), which can be used for surface coatings, plastic production and herbicide esters (Han et al., 2005). Hexanol is naturally formed by *Clostridium caboxidivorans* (Phillips et al., 2015).

Besides these natural products, some strains have been successfully modified to form more desired by-products. New pathways have been introduced via metabolic engineering for butanol and acetone. While *C. ljungdahlii* cannot form butanol naturally Köpke et al. (2010) indicated that 2 mM can be formed after recombinant modifications. Further modifications revealed even higher product yields for *C. ljungdahlii* and *C. autoethanogenum*, which was patented by LanzaTech in 2012 (Daniell et al., 2012; Köpke and Liew, 2012).

This chapter gives only a short overview about synthesis gas fermentation products and their application. In general, strain development and modification will improve production yields and the by-product spectrum in the future. Desired products are mostly determined by their price on the market and application purposes, which is listed in Table 3.1 chapter 3.2.1. Product ratios and titres are influenced by the availability and composition of the educts. Physical challenges for syngas fermentation are summarised in the following chapter.

2.4 General challenges of gas as a substrate

For microorganisms gases are only available in their dissolved form. In syngas fermentations the carbon source is introduced by the gas phase, therefore mass transfer and solubility of the components need to be considered. In this

chapter, biological availability, physical parameters as well as the importance of mass transfer and its modelling approaches are outlined. By comparing different experiments found in literature the specificity and variability of this parameter is indicated.

2.4.1 Solubility and biological availability

While the solubility of CO_2 is rather good, due to its dissociation into carbonic acid, CO and H_2 dissolve poorly which is also indicated by the Henry coefficient and solubility in Table 2.3.

Table 2.3: Physical parameters for synthesis gas components in water. Values are given for ambient pressure (1 atm). Reference temperature is indicated as well as calculated values (calc.) or other sources: Sander (2015) [1], Cussler (2009, p. 127) [2], Fernández-Prini et al. (2003) [3] and Dean (1999, p. 377) [4].

Description	Unit	Temp.	CO_2	CO	H_2	Ref.
density ρ_G	$kg\,m^{-3}$	37 °C	1.71	1.11	$7.97\,e^{-2}$	calc.
molecular weight M	$kg\,mol^{-1}$	–	0.044	0.028	0.002	–
Henry constant H^{cp}	$mol\,Pa^{-1}$	37 °C	$2.14\,e^{-2}$	$7.73\,e^{-4}$	$7.16\,e^{-4}$	[1]
diffusion coefficient $\mathcal{D}$	$m^2\,s^{-1}$	25 °C	$1.95\,e^{-9}$ a)	$2.03\,e^{-9}$ a)	$4.50\,e^{-9}$ b)	a) [2], b) [3]
solubility in water s	$kg\,m^{-3}$	35 °C	1.11	$2.23\,e^{-2}$	$1.43\,e^{-3}$	[4]

The Henry coefficient H^{cp} is a function of the liquid gas concentration c_L^* at the interface and the partial pressure p and can be written as

$$H^{cp} = \frac{c_L^*}{p}. \tag{2.6}$$

The expression in equation (2.6) is valid for equilibrium conditions. The partial pressure is described by Dalton's law. It states that the sum of all partial pressures of the individual gases i in the mixture results in the total pressure of the mixture

$$P = \sum_{i=1}^{N} p_i \qquad \text{with } i = 1, 2, ..., N. \tag{2.7}$$

The ideal gas law is applicable for most gases, relating the pressure P, gas volume V, temperature T and number of moles of gas n using the ideal gas constant $R = 8.314\,J\,mol^{-1}\,K^{-1}$. It concludes the here presented relations

$$PV = nRT. \tag{2.8}$$

The fermentation conditions determine to which degree these physical values can be influenced. While the temperature should be kept in the range of the organism's optimum (see chapter 2.3.1), the partial pressure and total pressure can be varied to a certain amount. In doing so, the solubility of the gases (Najafpour and Younesi, 2006; Mohammadi et al., 2014) as indicated in equation (2.6) is increased.

The overall volumetric mass transfer rate $\dot{n}$ is a function of the the volumetric mass transfer coefficient $k_L a$ and the concentration gradient as driving force Δc which is also known as oxygen transfer rate (OTR) as global average mass transfer rate:

$$\dot{n} = k_L a \Delta c. \tag{2.9}$$

The concentration gradient $\Delta c = (c_\mathrm{L}^* - c_\mathrm{L})$ gives the difference between saturated gas/liquid interface concentration c_L^* and bulk phase concentration c_L. The efficiency of gas-liquid mass transfer in chemical and bioprocess engineering is usually expressed by the volumetric mass transfer coefficient $k_L a$. This transfer is highly specific and mainly depends on medium properties (surface tension, density, viscosity, etc.) as well as on the gas hold-up, flow regime and bubble size. It consists of the liquid mass transfer coefficient k_L and the specific interfacial area:

$$a = \frac{\sum A_\mathrm{B}}{V_\mathrm{L}} = \frac{A_\mathrm{eff}}{V_\mathrm{L}}. \tag{2.10}$$

The specific interfacial area a relates the total surface area of all bubbles $\sum A_\mathrm{B}$ to the liquid volume V_L. As a result, the bubble shape, diameter and number impact the total mass transfer. When this value is modelled, either each bubble can be simulated individually or clustered in different diameter classes. The latter represents bubble size distributions of which a Sauter mean diameter can be derived. Additional population balance models are necessary (Hagesaether et al., 2002; Kumar and Ramkrishna, 1996). On the contrary, in single bubble simulations, coalescence and breakage are calculated individually. However, the mass transfer coefficient k_L is always approximated by a model.

2.4.2 Mass transfer coefficient

According to Huang et al. (2010), there are four categories of k_L-models: (i) correlations derived from dimensional analysis and adjusted by experiments, (ii) spatial models such as the film model, (iii) time models such

as the Higbie's penetration model (Higbie, 1935) and (iv) combined film penetrations models. This work mainly focusses on the most commonly used k_L-correlations derived from Higbie's penetration model:

$$k_L = \frac{2}{\sqrt{\pi}} \sqrt{\frac{\mathcal{D}}{t_e}}. \tag{2.11}$$

The diffusion coefficient $\mathcal{D}$ describes the diffusivity of gas in liquid (see also Table 2.3). The main parameter t_e describes the surface renewal time. Generally, two major approaches are considered. The first relates contact time and bulk liquid flow around the bubble by using the bubble diameter d_B and bubble rise velocity v_T, also referred to as terminal velocity ($t_e = d_B / v_T$):

$$k_L = \frac{2}{\sqrt{\pi}} \sqrt{\frac{\mathcal{D}\, v_T}{d_B}}. \tag{2.12}$$

This first approach is introduced by Higbie. In contrast, the second approach is refined twice. Firstly, the average surface renewal rate results from exposure to eddies with variable contact time as suggested by Danckwerts (1951) leading to $k_L = \sqrt{\mathcal{D}s}$. Secondly, the fractional rate of surface replacement s is calculated as proposed by Lamont and Scott (1970). Their approach uses an eddy cell model and they found that the mass transfer coefficient mainly depends on the motion of small-scale eddies which are in the dissipation range of the spectrum. Considering the Kolmogorov time scale $\tau = (\nu/\varepsilon)^{0.5}$ for t_e, the mass transfer coefficient can be formulated:

$$k_L = C\sqrt{\mathcal{D}} \left(\frac{\varepsilon}{\nu}\right)^{0.25}. \tag{2.13}$$

This isotropic turbulence driven version includes the turbulent energy dissipation rate ε, kinematic viscosity ν and a specific constant C. While equation (2.12) is independent from the energy dissipation rate, the bubble diameter and rise velocity is of utmost importance. In contrast to that, equation (2.13) indicates a decisive influence of the turbulent energy dissipation while being independent of the bubble diameter. While developing reactors, both approaches are considered depending on the type of reactor. In unstirred fermenters such as bubble columns, mainly equation (2.12) is considered. For highly turbulent agitated reactors, equation (2.13) is applied. Both correlations are experimentally validated depending on whether turbulence is generated solely by bubble motion or the existence of another turbulence source (Alves et al., 2006). A downside to equation (2.13) is the

specific constant C which depends on reactor design and set-up. This poses a challenge in respect to mass transfer modelling, because preliminary experimental investigations are required. Especially when scaling up reactors, this is not feasible.

Using published data, Munasinghe and Khanal (2010a) compared different reactor configurations as operation modes for synthesis gas fermentations. In addition, they conducted own experiments (Munasinghe and Khanal, 2010b) providing data for better comparison. The correlation between reactor configuration and parameters such as agitation speed affect the mass transfer rates as listed in Table 2.4.

Table 2.4: Synthesis gas mass transfer rates for different reactor configurations (derived from Munasinghe and Khanal, 2010a). Original sources are indicated as follows: Charpentier (1981) [1], Bouaifi et al. (2001) [2], Datar et al. (2004) [3], Bredwell and Worden (1998) [4], Fadavi and Chisti (2005) [5] and Wu et al. (1992) [6].

Reactor configuration	$k_L a$ in h^{-1}	Parameter of interest	Ref.
stirred tanks	10−500	agitation speed, gas flow rate	[1]
bubble columns	18−860	gas flow rate, bubble size	[1]-[3]
packed bubble columns	18−430	packing media properties, liquid and gas flow rate	[1]
packed columns co-current flow	1.5−3670	packing media, liquid and gas flow rate	[1]
packed columns trickled flow	36−360	packing media, liquid and gas flow rate	[1]
microbubble sparged bubble column	200−1800	bubble size	[4]
internal loop airlift reactor	140−220	aeration rate, pumped liquid flow rate	[5]
airlift reactor with net draft tube	18−160	superficial air velocities, reactor pressure	[6]

While stirred tanks are influenced by agitation speed and gas flow rate, bubble columns only depend on gas flow rate and the sparging systems. Nevertheless, the presented research indicates that bubble columns can reach higher $k_L a$-values than agitated systems. Furthermore, it can be seen that combining them with microbubble generators can enhance the mass transfer. In general, Table 2.4 and the work of Munasinghe and Khanal (2010b) stresses the significance of reactor configuration and also give $k_L a$ ranges for better categorisation. Choosing the most suitable reactor configurations is a crucial step in scale-up and needs to be assessed carefully, which is done in the next chapter in detail.

Chapter 3

Evaluation and assessment of industrial reactors

In this chapter, potential reactor geometries are evaluated and the profitability of synthesis gas fermentations is highlighted. In general, successful, large scale synthesis gas processes need to account for the following main challenges:

- High mass transfer rates respectively high specific bubble surface area (see chapter 2.4.2)
- Evenly distributed gas concentrations reducing substrate gradients
- Preferably simple process transfer into large scale
- Low energy, building and maintenance costs

Since process parameters are dedicated by the biological terms of the microorganism they cannot be influenced (see chapter 2.3.1). Nevertheless, there are some generally valid rules when designing gas fermentation processes: using continuous mode, sparger gassing systems, gas recirculation, additional pressure and surfactants in the medium. Higher mass transfer is reached by reducing the bubble size which increases the specific surface area, as described in chapter 2.4.2. For systems with short retention times, a recirculation of gas may be required, as investigated by Klasson et al. (1991).

3.1 Reactor geometries for gas fermentation

For synthesis gas fermentations, several reactor geometries are worth considering. In Figure 3.1, a collection of common and unconventional geometries

is shown. For each reactor type their advantages and disadvantages are shortly outlined and compared to each other.

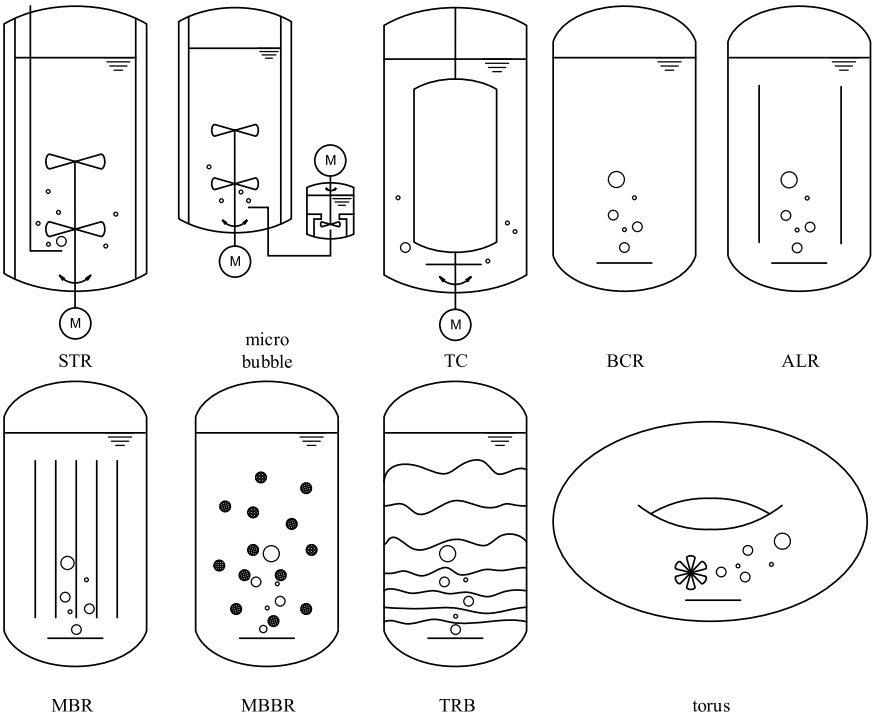

Figure 3.1: Possible reactor geometries for syngas fermentation. Schematically pictured are: stirred tank reactor (STR), micro bubble reactor combined with STR, Taylor-Couette vortex reactor (TC), bubble column reactor (BCR), air lift reactor (ALR), membrane bioreactor (MBR), moving bed biofilm reactor (MBBR), trickled bed bioreactor (TBR) and torus reactor.

The energy requirement of stirred tank (STR) or the Taylor-Couette (TC) reactors, especially in large scales, is very high making the fermentation process very expensive. In addition, it could be necessary to dissipate the heat generated by the power input. In order to reduce the energy consumption, Bredwell and Worden (1998) describe a technique for microbubble formation to overcome the mass transfer limitation of syngas fermentations. Thereby, the average initial bubble diameter is 60 µm and the $k_L a$ ranged from 200 h^{-1} to 1,800 h^{-1}, which is two to three times higher than common reactor systems

(see Table 2.4 in chapter 2.4.2 for comparison). This generated microbubbles by using a spinning disk apparatus and the surface-active substance Tween 20. With such a set-up, the overall energy needed is 100 times less while scaling up STR. Furthermore, the microbubble generator can enhance other reactors.

A rather unusual bioreactor is the Taylor-Couette vortex reactor. Usually, this reactor type is used for mammalian cells and enzymatic reactions. It consists of two cylinders, of which at least one is rotating. These reactors show extraordinary flow patterns that depend on their rotational speed. If Taylor–Couette vortices are formed, higher bubble retention times in comparison to bubble columns can be expected. Ramezani et al. (2015) obtained $k_L a$-values of about $180\,\mathrm{h}^{-1}$ at azimuthal Reynolds numbers $\mathrm{Re_a}$ of 143. Another advantage of this reactor type is the possibility to immobilise microorganisms at the inner cylinder wall. This is discussed more in detail while introducing the membrane bioreactors.

Unstirred systems such as bubble column (BCR) and airlift reactors (ALR) have very low scale-up costs due to their simple architecture. The greatest disadvantage of these reactor types is bubble coalescence which reduces mass transfer rates. Their risk to form unwanted gradients (substrate, pH, etc.) is higher than in stirred systems which can decrease biomass and product yields. Mixing in ALR set-ups with riser and downcomer velocity profiles is usually better than in BCRs. The liquid velocity increase causing a decrease in gas holdup in these set-ups needs to be accounted for. Between both, a perfect balance has to be found. For each reactor type, a long and narrow column allows for longer retention times of the gas phase and higher pressure at the bottom of the reactor.

Membrane bioreactors (MBRs) have two additional performance properties. First, a much easier product recovery. Second, very high microorganism concentrations can be obtained in a continuous fermentation mode. Due to these advantages, cell recycling becomes redundant and the costs for downstream processing is reduced. For synthesis gas fermentations, a moving bed biofilm reactor (MBBR) is introduced by Qureshi et al. (2005). They claim that using carrier materials (plastic nets) increases turbulence and better disperses the gases. They combine a STR with moving biofilm devices and hence achieve ethanol concentrations of $30\,\mathrm{g\,L}^{-1}$ with *Clostridium ragsdalei* in an $18\,\mathrm{m}^3$ fermentation vessel. However, a precondition for membrane bioreactors and MBBRs is that the microorganisms can be immobilised and that they can form biofilms. Nevertheless, the usage of membranes and biofilm carriers can lead to higher acquisition costs.

The next reactor shown in Figure 3.1 is the trickling bed reactor (TBR).

This type is often used for anaerobic processes and has very low cultivation costs. Due to the closely packed beds, a longer gas holdup is obtained and higher cell concentrations can be achieved. Since the organisms are retained in the reactor bed, there is less filter clogging and fewer separation steps are needed. In addition, co-current flow towards the gas flow results in higher $k_L a$-values. These benefits have to be weighted with some disadvantages. Such reactors have a poor gas distribution, can form unwanted gas channel and tend to organism overgrowth. During syngas fermentation, acetic acid is always produced to meet the internal energy demand of the cells (see chapter 2.3.2). In a TBR this acid is more likely to accumulate.

One of the most unconventional reactor geometries is the torus reactor. Similar reactor geometries have been used for methane production by NorFerm (nowadays part of the company Equinor ASA). Recently, Kaiser et al. (2013) introduced an annular shaped travelling wave bioreactor, which is mixed by a shaking platform. This reactor was designed to provide low shear stresses while providing enough oxygen for mammalian cells. As the name implicates, the medium moves through the reactor in waves without additional gassing or optional circular arranged baffles. In the case of synthesis gas fermentation, the torus reactor would be a combination of the NorFerm methane and the travelling wave reactor. The annual shape is very robust and can resist high internal pressures. In addition to that, the gas distribution is very good due to the round shape and its flow field. Like stirred reactors, the greatest disadvantage is the high energy input caused by the agitator.

In general, the most effective syngas bioreactor is one that achieves high cell concentrations, mass transfer rates (Klasson et al., 1991) and additionally has low purchase and operating cost. In order to evaluate synthesis gas reactors, a ranking system is developed. It rates reactor performance and scale-up costs. In Figure 3.2 (A) all requirements for good fermentation results are listed, while in Figure 3.2 (B) the assumed scale-up and process costs are shown. The latter is based on the work of Li et al. (2011) who did an economic assessment of astaxanthin production scale-up including detailed cost predictions. The rating system allows a detailed comparative evaluation including all important strategic matters.

For evaluation, all reactors are compared according to their performance (Figure 3.2 (A)) and rated from low to very good (legend values 0 to 3). The scale-up cost approximation (Figure 3.2 (B)) instead is rated with negative values from -3 to 0 (high to low costs). For both evaluation and each reactor, the total score is calculated leading to positive values for (A) and negative values for (B). To compare each score, they were additionally ranked with

stars while three stars indicated the best reactors of (A) and (B).

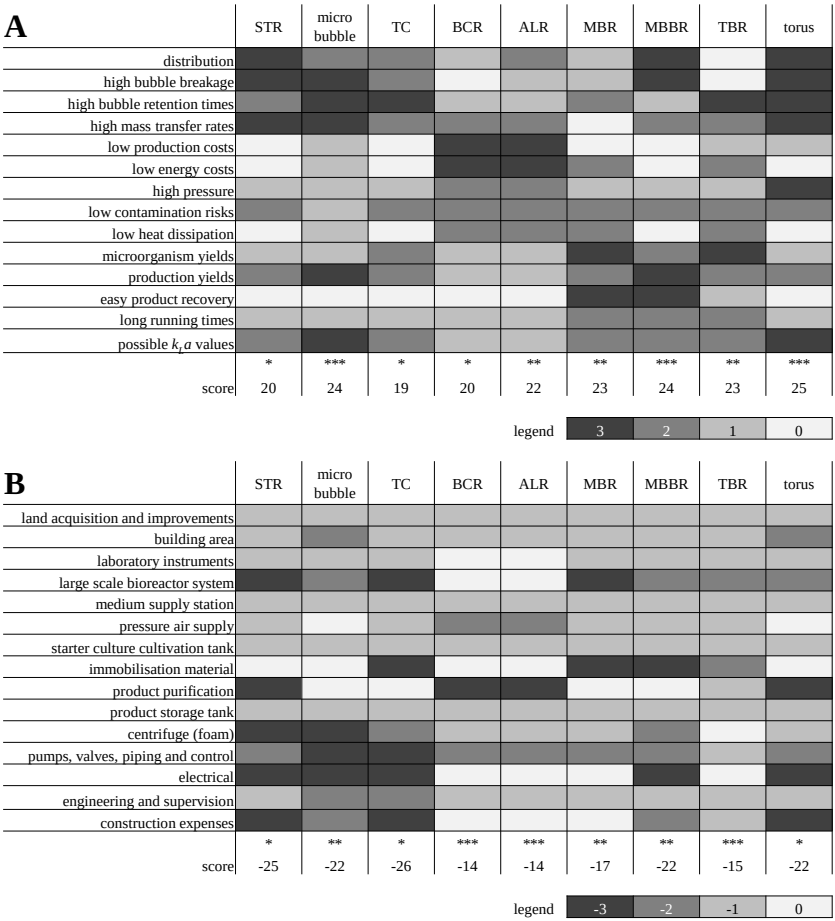

Figure 3.2: Reactor performance (A) and scale-up costs (B) evaluation system (derived from Li et al., 2011). Colour legend is displayed on the bottom of each chart while reactor performance factors rate positive (0-3 from low to very good) and scale-up costs rate negative (-3-0 high to low costs). The score is calculated by the representing value and ranked with stars (*) to indicate the best performing reactors and highest scale-up costs. The reactor abbreviations used correspond to: stirred tank reactor (STR), combination of stirred tank with micro bubble reactor (micro bubble), Taylor-Couette reactor (TC), bubble column reactor (BCR), airlift reactor (ALR), membrane bioreactor (MBR), moving bed biofilm reactor (MBBR), trickled bed reactor (TBR) and torus reactor (torus).

Due to the evaluation system, the best performing reactors for gas fermentations (see Figure 3.2 (A)) are: the micro bubble STR combination, MBBR and torus reactor. The most cost-efficient reactors in scale-up, on the other hand, are BCR, ALR and TBR (see Figure 3.2 (B)). Since both ratings combined give the most efficient gas fermentation reactors, the difference of both is estimated and the offset graphically displayed in Figure 3.2. Accordingly, the most suitable reactor designs for syngas fermentations are BCR, ALR, MBR and TBR.

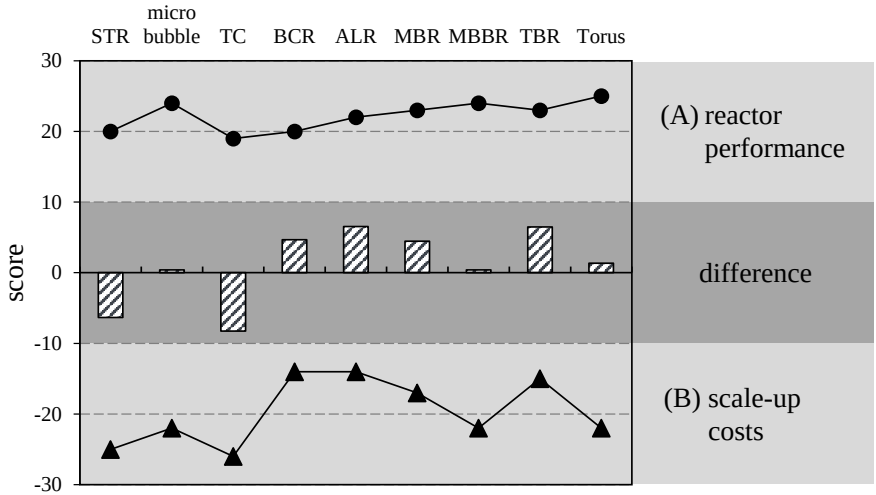

Figure 3.3: Rating results of reactor performance and scale-up costs evaluation (see Figure 3.2). Both scores are of Figure 3.2 (A) and (B) are graphically displayed and their offset illustrated as bars. The reactor abbreviations used correspond to: stirred tank reactor (STR), combination of stirred tank with micro bubble reactor (micro bubble), Taylor-Couette reactor (TC), bubble column reactor (BCR), airlift reactor (ALR), membrane bioreactor (MBR), moving bed biofilm reactor (MBBR), trickled bed reactor (TBR) and torus reactor (torus).

This assessment system is chosen to get a rough direction for possible and feasible synthesis gas bioreactors and to explore and evaluate alternative structural shapes as well as operation modes. The bubble column reactor is chosen due to the fact that it is the second best reactor result of the evaluation. It is already used in industrial plants (see chapter 2.2.2) and a lot of published literature is available for this reactor type. If high operating costs are justified, depends strongly on the product and yield. This aspect is highlighted in the next chapter.

3.2 Assessment of potential of synthesis gas fermentation

A first possible evaluation of a syngas-based production is a general assessment of its potential with the goal to predict the overall margin and plant cost. With this initial investigation the competitiveness, especially when compared with well-established thermochemical conversion routes, can be determined. The first part focuses on the stock prices and application of the products, the second part demonstrates a way to approximate unknown carbon market values and the last part gives an example of maximal budget calculation for industrial plants.

3.2.1 Stock prices and application of fermentation products

Due to energy and redox limitations, *C. ljungdahlii* and other anaerobic acetogenic microorganism are forced to produce large amounts of by-products (see chapter 2.3.2). On the one hand this leads to low growth rates and on the other hand to high product formation. Depending on length and complexity of the carbohydrates, the market prices of the fermentation products show high differences. Table 3.1 lists the most common by-products (Liu et al., 2014a; Liu et al., 2014b; Köpke et al., 2011; Dürre, 2016; Hu et al., 2016) and their stock prices. Ethanol and acetate as C2-body are mainly produced in syngas fermentation and have the lowest market value. They are much cheaper and easier produced in other fermentative processes with organisms like yeasts and acetic acid bacteria of the genus *Acetobacter*.

Nevertheless, first efforts have been made to genetically modify anaerobic acetogenic microorganism towards more attractive product formation (see chapter 2.3.3). Alcohols such as n-butanol are traded with a price of 1.75 USD per kg which is 12 times higher than the ethanol price. Consequently, this product provides a higher financial flexibility for plant design and up-scaling. The more complex the products get, the more profitable they can be traded. Butanediol with two hydroxy groups is a very attractive biocommodity. As C4-body they are often used to produce polyester or epoxy resins.

All in all, the market price depends on the complexity of the manufacturing process and if there are alternative competing processes. Most of the listed molecules can be produced chemically, too. Furthermore, the purity of the product has a great impact on the price as well. The less effort for purification is needed the cheaper the process. Since biological fermentations are quite moderate compared to chemical processes, purification can be easier.

Table 3.1: Possible synthesis gas fermentation products and their prices on the market. Listed are the most common by-products (Liu et al., 2014a; Liu et al., 2014b; Köpke et al., 2011; Dürre, 2016; Hu et al., 2016). The publicly accessible internet sources for the stock prices can be found at the bottom. Some applications of the products are mentioned in the last column.

Name	Formula	M g mol^{-1}	Ox. state	Red. level	USD per kg	Applications
ethanol	C_2H_6O	46.07	6	6	0.14[1)]	precursor of ethyl halides, diethyl ether, acetic acids, medical, fuel, solvent usage
acetate	$C_2H_3O_2^-$	59.04	6	2	0.05[2)]	textile industry (dyeing), rubber production, concrete sealant, food, flavouring,
n-butanol	$C_4H_{10}O$	74.12	-2	6	1.75[3)]	precursor of butyl esters, acetates, pharmaceuticals, polymers, plastics, herbicides
isobutanol	$C_4H_{10}O$	74.12	-2	6	1.65[4)]	food flavour, plasticizer, extractant, gasoline additive
1,4-butanediol	$C_4H_{10}O_2$	90.12	-1.5	5.5	2.52[5)]	polyester resins, plasticizer, α-ketobutyric acid (amino acids precursor)
2,3-butanediol	$C_4H_{10}O_2$	90.12	-1.5	5.5	15.79[5)]	polyurethane production, solvent, glycerine substitute, sanitary products, resins
butyrate	$C_4H_7O_2^-$	87.10	-1.67	5	n.a.	feed supplement, food flavour
hexanol	$C_6H_{14}O$	102.18	-2	6	1.50[5)]	solvent, shellac, resins, hormones
1,6-hexandiol	$C_6H_{14}O_2$	118.18	-1.67	5.7	n.a.	polyester, polyurethane production, acrylics, adhesives and dyestuff

[1)] Börse-Online (2018), [2)] acetic acid (Nasdaq, 2016), [3)] OrbiChem (2013), [4)] Gevo^{TM} (2011), [5)] PR Newswire (2012), not available (n.a.)

All listed by-products show high levels of reduction and therefore high energy levels (Table 3.1). Except acetate with a level of reduction of 2, all other products are highly energetic with values between 5 and 6. This is noteworthy, since the synthesis gas components have very little energy which is discussed in the next paragraph.

3.2.2 Approximation of carbon monoxide price

In this economical approach of synthesis gas as educt, only the carbon sources are considered. Usually, syngas is produced for chemical processes (see chapter 2.2.1), this is why this study focusses on waste gases such as the off-gas of the steel industry. Moreover, reduction of carbon dioxide emission has a positive effect on the ecological reflection.

The stock prices of the educts in the form of synthesis gas are difficult to find. In order to approximate these values, a look at other more common resources can be taken. The idea is to calculate its value by using the available

market prices of other reduced carbon compounds such as crude oil, natural gas or glucose (Table 3.2).

For glucose the market price is about 0.353 USD per kg and the level of reduction per c-mol at complete combustion to H_2O and CO_2 is 4 (Takors, 2014, p. 79). If 1 kg glucose is equivalent to 5.55 mol glucose, thus 1 c-mol glucose costs about 0.0106 USD. That means a C-source with the reduction degree per c-mol of 4 is worth about 0.0106 USD per c-mol, too. CO has a level of reduction of 2 and would consequently costs 0.0053 USD per c-mol. This results in 0.189 USD per kg.

Table 3.2: Calculation of carbon monoxide costs via the glucose stock price. The publicly accessible internet sources for the stock prices can be found at the bottom.

Name	Formula	Ox. state	Red. level	M g mol^{-1}	USD per kg	USD per mol	USD per c-mol
glucose	$C_6H_{12}O_6$	0	4	180.16	0.353[1)]	0.0636	0.0106
carbon monoxide	CO	2	2	28.01	0.189	0.0053	0.0053
carbon dioxide	CO_2	4	0	44.01	0.030[2)]	0.0013	0.0007

[1)] stock price: 0.35 USD per 1 kg sugar (Investing, 2018), [2)] emission certificate 26 EUR per 1 t (EEX, 2019)

CO_2-emissions certificates have to be bought by European companies in order to restrict the annual release of greenhouse gases. The price per kg CO_2 depends on the number of certificates sold by the European Union Emissions Trading System (EU ETS) and how large the demand for certificates is. At present (23/09/2019) it is around 0.03 USD per kg CO_2-emission with rising trend and ecological importance. Compared to 2014 the price is five times higher than today. This fact will reduce the reactant price especially in Europe.

As mentioned in the previous section 3.2.1, there is not necessarily a linear price trend for the products. Figure 3.4 illustrates the connection between price per kg and energy value in form of reduction level and oxidation state for educts and products. Figure 3.4 (A) shows the oxidation states of the different carbon compounds, which differ between -2 and 4. The lower the oxidation state the more the molecule can be oxidized and therefore energy is set free. The same can be said about the reduction level, the higher the better (Figure 3.4 (B)). It can be assumed that the stored energy of a carbon molecule determines the value of the chemical. Furthermore, the complexity of the compound, the purity, demand on the market as well as

the manufacturability plays an important role when it comes to calculating the price (see also Table 3.1).

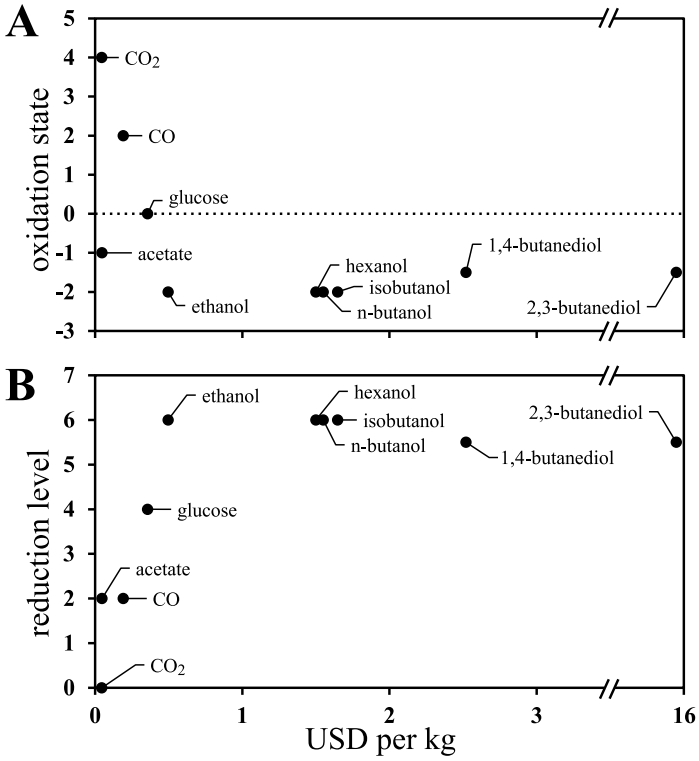

Figure 3.4: Oxidation state (A) and level of reduction (B) as function of USD per kg. According to Table 3.1 and 3.2 the stock prices in USD per kg are graphically shown.

With this stock price research and educt calculations the maximum price range for industrial plant design and scale up can be approximated, which will be exemplary shown in the final sub-chapter of this section.

3.2.3 Maximal budget for industrial plant

The maximum price ranges for the plant and maintenance cost for each product are calculated by the consumption of CO and CO_2. Whereby, carbon monoxide costs as substrate and carbon dioxide does not, due to the CO_2

emission certificate needed in Europe (see section 3.2.2). The costs for the certificates can vary as well, but the tendency is that they will be more expensive in the future, which is advantageous for the whole process and makes synthesis gas fermentations far more attractive.

Exemplary, by taking a closer look at LanzaTech (see also chapter 2.2.2), a synthesis gas fermenting company with an annual production of 60 M gallon ethanol in its biggest plant, a maximum income of 6.4 Mio to 109.2 Mio USD per year can be expected. If the plant, staff and maintenance costs are now subtracted from this value, the profit of this process can be calculated.

From the biotechnological point of view, fermentations with synthesis gas are so far very slow, unproductive and therefore very ineffective. In summary, the performed assessment is a good strategy to make a rough estimation of the economic efficiency of a process. In addition, we know which goal we have to achieve to make these fermentations profitable respectively feasible.

Chapter 4

Challenges, mathematical methods and approaches

4.1 Characteristics of bubble column reactors

In the chemical and biochemical industry bubble columns are widely used due to their simple construction and high energy efficiency according to mass transfer (see also chapter 3.1). Usually, low viscosity fluids are required to assure sufficient mixing, which is the case for the synthesis gas fermentation broth.

Physical parameters such as viscosity have a great impact on performance of the bubble column reactor (BCR), which is schematically shown in Figure 4.1. All these variables interact strongly and can have different impacts on the outcome. For better understanding, these interrelated processes are grouped into three subcategories: (I) given and configurable parameters, (II) dependencies of parameters and (III) effects on important performance parameters.

(I) Specified and configurable parameters: Technical configurations such as sparger type, length and width of the column and other internal installations (e.g. concentric tubes) have a great effect on the whole system. However, these configurable parameters have the advantage to be easily adjustable if needed. Likewise, the superficial gas velocity is adjustable. Medium properties such as liquid density, kinematic viscosity, surface tension and liquid phase diffusivity are not or barely modifiable.

(II) Dependencies of parameters: The interconnectedness of all important factors is complex. Very important are initial bubble sizes and bubble size distributions in the column. They directly depend on the given and configurable parameters as well as the flow regime (Figure 4.2). The latter can be described as a function of superficial gas velocity and column diameter (Figure 4.3 (A)). Ideal is a homogeneous bubbly flow, offering the largest specific surface. Bubble rise or terminal slip velocity together with the mass transfer coefficient depend on the bubble size in the column. In contrast to that, the gas holdup and liquid circulation velocity depend on every condition previously mentioned (Figure 4.3 (B)).

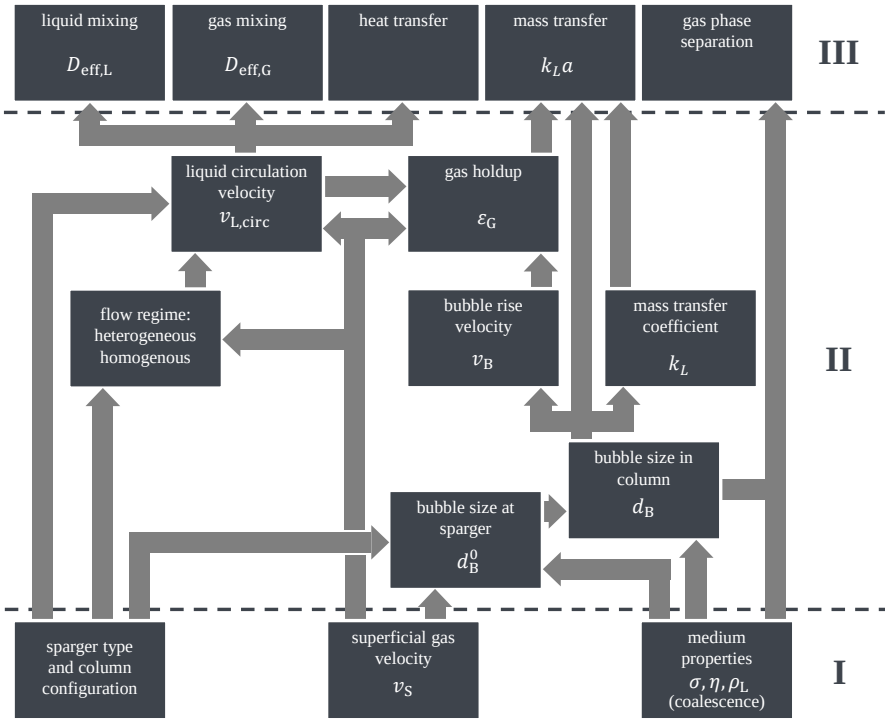

Figure 4.1: Schematic drawing of interrelated processes in a bubble column (derived from Heijnen and Van't Riet, 1984). Artificially divided in three subcategories: (I) specified and configurable parameters, (II) dependencies of parameters and (III) effects on important performance parameters.

(III) Effects on important performance parameters: Reactor performance depends on liquid and gas mixing, heat transfer, mass transfer and gas phase separation. In fact, the first four performance parameters are affected by every other parameter. Various correlations and dependencies have been investigated in the past for certain gas-liquid constellations, which are further described in chapter 6.1.2 (Choosing reasonable parameter ranges).

Several flow regimes for bubble columns have been described. Depending on gassing rate, gassing system and column geometry, two main flow regimes can be observed (Figure 4.2). Perfect bubbly and imperfect bubbly flow are part of the homogeneous flow regime while churn-turbulent and slug flow are defined as heterogeneous flow regime.

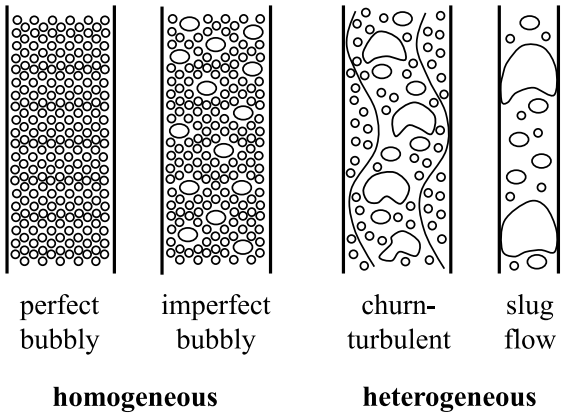

Figure 4.2: Homogeneous and heterogeneous flow regimes. Sown are perfect bubbly flow as most desired homogeneous flow with the transition of imperfect bubbly flow to the most common churn-turbulent flow. Slug flow appears only in smaller columns (derived from Kantarci et al., 2005; Bouaifi et al., 2001; Deckwer et al., 1980).

Perfect bubbly flow can only be achieved in non-coalescent fluids and low column heights. More likely are imperfect bubbly flows with a constant bubble size range and churn-turbulent flows with larger bubbles in the reactor centre. The latter leads to large scale circulation patterns of both liquid and gas (Heijnen and Van't Riet, 1984). Slug flow is only observed in very narrow bubble columns (Figure 4.3 (A)) and is a very particular form of heterogeneous flow, which is not considered further. Between these two

classifications lie a transition area, which varies due to liquid properties, column and sparger configurations.

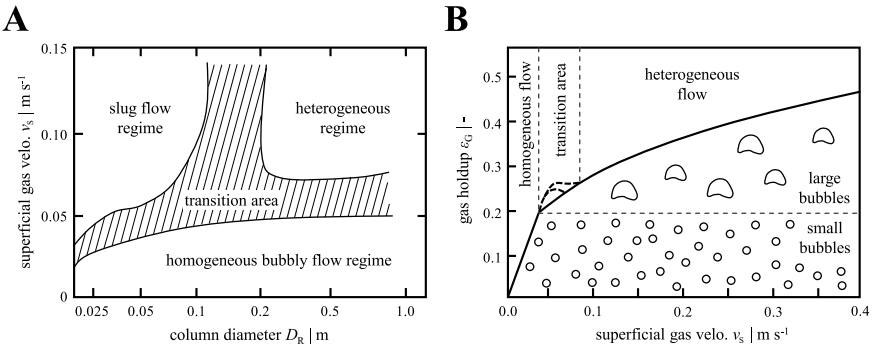

Figure 4.3: Flow regime correlations between superficial gas velocity and column diameter (A) as well as gas holdup (B). In (A) the flow regimes as a function of superficial gas velocity and column diameter for a water/air system is shown (Kantarci et al., 2005; Deckwer et al., 1980). Similar to (A) and for larger column diameters, the homogeneous and heterogeneous flow regimes are illustrated in (B) as well as the transition area of imperfect bubbly flow indicated (Krishna and Sie, 2000).

The gas holdup is a very crucial parameter and can be used to describe the BCR performance. It has a great impact on the mass transfer (implied in Figure 4.1). Additionally, it correlates with the superficial gas velocity, which is outlined in Figure 4.3 (B). Additionally, the flow regimes are indicated in this picture as well. The gas holdup slope decreases significantly in heterogeneous churn-turbulent flows, which occur at high superficial gas velocities. Bailey and Ollis (1986, p. 611) stated that in a water-air system coalescence and therefore heterogeneous flow can be expected when the gas holdup reaches a critical value of $\varepsilon_{crit} = 0.3$. This is an estimated value and differs according to medium properties.

To cover all interrelated processes in a bubble column, high computational power is needed. Moreover, not all interactions are physically described and have to be modelled. However, with higher complexity usually comes a higher need of computing power and simulation time. Two modelling approaches with different resolutions are investigated in this study. Their advantages and disadvantages are discussed in the next chapter.

4.2 Modelling approaches in comparison

Numerous modelling approaches are known for predicting the outcome of bioreactors. The straightforward model would be to assume that everything is well mixed without any spatial differences. In this case, one compartment respectively discretisation volume needs to be considered and temporally solved. This is a valid method for stirred or shaken lab scale scenarios. In scale-up, physical properties such as pressure or power input for sufficient mixing gets more important. Especially for gas fermentations in a bubble column, the hydrostatic pressure can be very advantageous while mixing and circulations times will most likely increase.

As mentioned in the previous chapter, the interrelated processes of a bubble column reactor are very complex and influence each other strongly. For this study two modelling approaches of varying complexity have been chosen. Each model serves a different purpose. In Table 4.1 both approaches are compared to work out their possible application range.

Table 4.1: 1-dimensional approach and computational fluid dynamics in comparison. NSE is short for Navier–Stokes equations. (This table is a reprint of the supplementary files of Siebler et al. (2020) respectively Manuscript III.)

Comparison	1-dimensional approach	Computational fluid dynamics
general level of detail	low	high
solving complex fluid phenomena	simple one-dimensional transport equation for both phases	can solve three dimensional NSE and turbulence as well as complex gas transport
incorporation of kinetics	up to genome-scale models while solving temporal concentration	unstructured model with few kinetic equations
additional bacteria phase	not applicable in one-dimensional flow field	possible for statistical statements
computational effort	adequate (in minutes)	high (in weeks)
applicability and validity	dynamic steady state simulations to find optimal operation parameter	physical properties such as flow field, fermentation 'snap-shots' and to predict cell behaviour

In this case, the 1-dimensional (1D) approach can approximate the pressure gradient in a column. It is easily spatially discretised and allows to solve complex kinetics. Gomez et al. (2014) also combines this approach with genome-scale kinetic models, which was later adapted by Chen et al. (2015) with a *C. ljungdahlii* model. This approach solves in each discretisation volume the genome-scaled model while performing dynamic flux balance analysis (FBA). These models are strongly underestimated and usually need

a lot of constraints to be applicable. With the help of a lexicographical optimisation Gomez et al. (2014) is able to solve this issue. Lexicographic (in order, alphabetically) optimisation means that successively several FBAs are performed with changing optimisation targets. The first target would be to optimise for maximum growth rate with a certain C-source uptake rate as constraint. Afterwards, the growth rate is set as additional boundary condition for the following optimisation (e.g. production rate). This is repeated for all important rates, which finally leads to a more constrained and predictable FBA. This method works fine for well-investigated organisms such as *Escherichia coli* or *Saccharomyces cerevisiae* but is rather imprecise for less researched stoichiometric models such as the *C. ljungdahlii* model. This was also indicated by the findings of Chen et al. (2015). For deriving production kinetics this approach is not suitable, therefore another correlation needs to be found.

The biggest advantage of the 1D model is the short simulation time and the fact that whole fermentation processes can be solved temporally. Hence, it is possible to run various fermentation scenarios with different start conditions. If the optimal result is approximated, the findings can be used for the computational fluid dynamic (CFD) set-up.

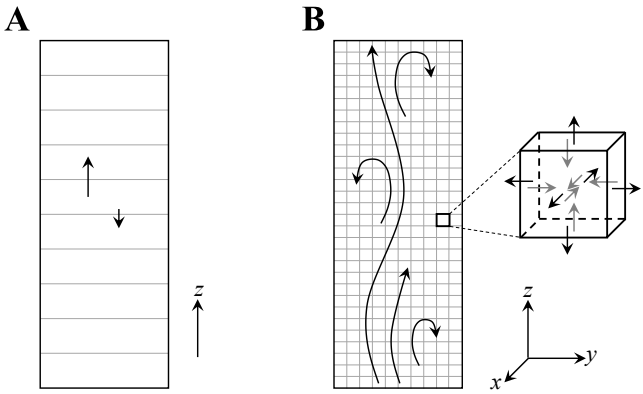

Figure 4.4: Degree of discretisation in case of the applied 1-dimensional approach (A) and computational fluid dynamics approach (B). The 1-dimensional approach (A) is one-dimensional with only linear flow and the computational fluid dynamics approach (B) three-dimensional allowing the resolution of turbulent flow patterns. (Reprinted from Siebler et al., 2020, with permission of © Wiley-VICH Engineering in Life Science.)

In contrast to the dynamic 1-dimensional approach, the CFD approach results in more detailed flow predictions and allows more precise gas holdup

and mass transfer simulations due to the implementation of bubble breakup and coalescence. Figure 4.4 schematically shows the discretisation differences between both approaches. With the three-dimensional discretisation of the CFD approach not only a detailed reproduction of the flow field is possible but also a more profound prediction of the gas phase. Forces, such as drag and lift, can be implemented, too. Additionally, a three-dimensional resolved flow field and gas gradient allow to track massless Lagrange trajectories which represent bacterial lifelines. As the bacteria travel along these lifelines, possible stress conditions can be statistically identified.

The requirement of high computing power as well as rather long simulation times (in the range of weeks) are major disadvantages of CFD simulation. Only simulations of pseudo-stationary gradients which constitute as fermentation 'snap-shot' in combination with statistical lifeline analysis are applicable for the scope of this thesis.

Nevertheless, both methods combined can help to understand and predict the outcome of industrial bioreactors. Therefore, risks in scale-up can be minimised as well as trouble shooting in already existing fermenters can be conducted. The two approaches are introduced in more detail in the following chapters.

4.3 1-dimensional approach

In the 1-dimensional (1D) approach chapter a kinetic correlation is presented, which is derived from element balances. This correlation is also used in the evaluation of the computational fluid dynamics model. Moreover, the possible diffusion limitation is investigated as well as the reactor set-up and operation mode are discussed. Partial and ordinary equations are derived accordingly. Finally, discretisation methods and boundary conditions are outlined. The chapters concerning the 1-dimensional approach are published in Siebler et al. (2020) and chapter 4.3.1 in Siebler et al. (2019). In order to follow the thesis structure and allow important cross references, some of the content is recited and is stated as such.

4.3.1 Deriving a kinetic correlation from element balances

As mentioned before this chapter was published in Siebler et al. (2019) and is recited with the permission of © Elsevier Chemical Engineering Science.

While fermenting *Clostridium ljungdahlii* with synthesis gas as sole carbon source, the following products are formed: carbon dioxide, acetate, ethanol,

2,3-butanediol, traces of lactate and of course biomass. The formation of by-products is quite high, since their biochemical pathway recycles required electron carriers respectively redox equivalents and ATP is produced when acetate is formed (see chapter 2.3.2 Figure 2.3). For this simple kinetic correlation approach, lactate production is neglected. A simple net equation can be formulated as follows:

$$\begin{aligned}\underbrace{1\,\mathrm{CO}}_{q_\mathrm{c}} + \underbrace{Y_{\mathrm{H^+,CO}}\,\mathrm{H^+}}_{q_{\mathrm{h^+}}} \rightleftharpoons\ & \underbrace{Y_{\mathrm{X,CO}}\,\mathrm{CH_{1.8}O_{0.5}}}_{q_\mathrm{x}} + \underbrace{Y_{\mathrm{Ac,CO}}\,\mathrm{CH_{1.5}O}}_{q_\mathrm{a}} \\ & + \underbrace{Y_{\mathrm{EtOH,CO}}\,\mathrm{CH_3O_{0.5}}}_{q_\mathrm{e}} + \underbrace{Y_{\mathrm{2,3But,CO}}\,\mathrm{CH_{2.5}O_{0.5}}}_{q_\mathrm{b}} \\ & + \underbrace{Y_{\mathrm{CO_2,CO}}\,\mathrm{CO_2}}_{q_\mathrm{c2}} + \underbrace{Y_{\mathrm{H_2O,CO}}\,\mathrm{H_2O}}_{q_\mathrm{w}}.\end{aligned} \tag{4.1}$$

Analogously to the yields Y per c-mol CO, the uptake rates are indicated at the bottom with the consumption rate of CO q_c, the production rates for CO_2 q_c2, acetate q_a, ethanol q_e and 2,3-butanediol q_b and the biomass q_x. Water and H^+ ions are used for oxygen and hydrogen compensation. The equation is formulated per c-mol, which leads to the system of element balances:

$$\begin{matrix}\mathrm{C:}\\ \mathrm{H:}\\ \mathrm{O:}\end{matrix}\begin{pmatrix}1 & 0 & 1 & 0 & 1 & 1 & 1 & 1\\ 0 & 1 & 0 & 2 & 1.8 & 1.5 & 3 & 2.5\\ 1 & 0 & 2 & 1 & 0.5 & 1 & 0.5 & 0.5\end{pmatrix}\begin{pmatrix}q_\mathrm{c}\\ q_{\mathrm{h^+}}\\ q_\mathrm{c2}\\ q_\mathrm{w}\\ q_\mathrm{x}\\ q_\mathrm{a}\\ q_\mathrm{e}\\ q_\mathrm{b}\end{pmatrix} = \bar{0}. \tag{4.2}$$

This system of equation is four times under-determined (q_c is given). Therefore, the solution space is restricted as follows:

$$\begin{aligned}\mathrm{lb} &= (q_\mathrm{c}\ \ -100\ \ q_\mathrm{c}/1.7\ \ -100\ \ 0\ \ 0\ \ 0\ \ 0)\\ \mathrm{ub} &= (q_\mathrm{c}\ \ \ 100\ \ q_\mathrm{c}/1.7\ \ \ 100\ \ 2.5\ \ 100\ \ 100\ \ 100).\end{aligned} \tag{4.3}$$

The lower (lb) and upper bound (ub) are described in the same order as the element balance in equation (4.2). Fermentation results with synthesis gas and CO/CO_2 gas mixtures show that always around half of the carbon

source CO is converted into CO_2 (data not shown). In this case, the dividing factor is around 1.7, which gives the ratio for CO_2 production rate per CO consumption rate. Maximum growth for *C. ljungdahlii* is not known and therefore set to $\mu = 0.06\,h^{-1}$, which is slightly higher than the experimental measured rates. The by-products can only be produced while H_2O and H^+ can also be consumed.

To get the most realistic correlation of the solution space, the optimisation function maximises the sum of all relevant products:

$$f(q) = \max\left(q_x + q_a + q_e + q_b\right). \tag{4.4}$$

None of the element balances are violated and the results for carbon monoxide uptakes up to $-40\,mmol\,g_{CDW}^{-1}\,h^{-1}$ are shown in Figure 4.5.

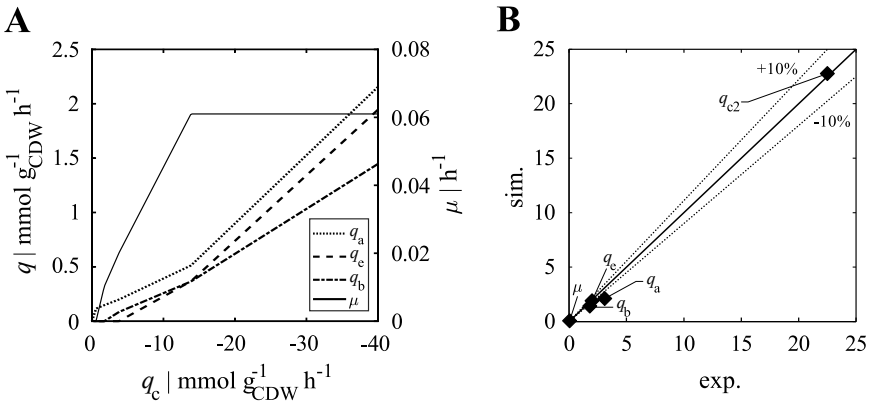

Figure 4.5: Optimisation results for kinetic correlation (A) and comparison with experimental data (B). In (A) the maximisation for product formation results are graphically shown for several possible CO uptake rates q_c. The production rates for acetate q_a, ethanol q_e and 2,3-butanediol q_b are shown as well as the growth rate μ on the left side. The simulation outcome (q_{sim} and μ_{sim}) was compared with experimental data (q_{exp} and μ_{exp}) in (B). All experimental rates were kindly provided by M. Hermann who performed a synthesis gas fermentation with a gas composition of 55/30/5/10% for $CO/H_2/CO_2/Ar$. More details on the experimental set-up can be found in the supplementary of Manuscript II. (Reprinted from Siebler et al., 2019, with permission of © Elsevier Chemical Engineering Science.)

As indicated in Figure 4.5 (A), the by-product formation rates show very similar behaviour. In general, acetate has the highest production rate correlation, then ethanol followed by 2,3-butanediol. The growth rate increases steadily until the maximum growth is reached. All simulation results are in

good agreement with experimental data (Figure 4.5 (B)), hence the correlation between CO consumption rate and production rates will be used for the parameter study.

4.3.2 Investigation of diffusion limitation

Parts of this chapter are recited from the supplementary files of Siebler et al. (2020) with permission of © Wiley-VICH Engineering in Life Science.

In the following chapter, the mass transfer from bubble to cell is analysed. In this context especially the kinetic uptake is compared while possibly being limited by diffusion. As shown in Figure 4.6, diffusion occurs at the laminar layer around a cell or a cell structure. For *Clostridium ljungdahlii* an uptake kinetic with substrate inhibition was determined by Mohammadi et al. (2014). In this chapter, the limitation by diffusive transport is investigated. As a result, a possible uptake kinetic considering both diffusion and the inhibition is derived and presented.

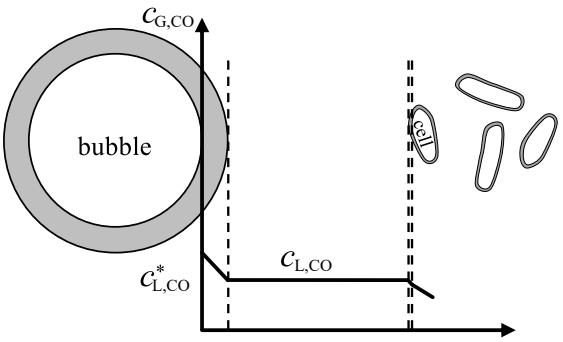

Figure 4.6: Schematic diagram of gas transport from bubble to cell. Modified version of Hass and Pörtner (2011, p. 17) with $c_{G,CO}$ as the gaseous CO concentration, $c^*_{L,CO}$ as the liquid interfacial area concentration and the liquid concentration $c_{L,CO}$.

If the volumetric mass transfer rate $k_L a$ from the gas to liquid phase is the limiting factor as described by the experiments of Mohammadi et al. (2014) the CO mass transfer rate or uptake rate can be expressed as follows:

$$\frac{\mathrm{d}c_{G,CO}}{\mathrm{d}t} = k_L a \, c^*_{L,CO}. \tag{4.5}$$

The CO concentration in the gas phase $c_{G,CO}$ depends on the equilibrium concentration of CO at the interface $c^*_{L,CO}$ and the liquid concentration $c_{L,CO}$. Furthermore, the consumption rate of carbon monoxide in the liquid phase due to the bacteria can be written as:

$$q_c = \frac{1}{c_X} \frac{dc_{L,CO}}{dt}. \tag{4.6}$$

Mohammadi et al. (2014) conducted several syngas fermentations under different pressures. They found that the modified Monod uptake kinetic proposed by Andrews could be fitted in the linear and quadratic regression form with a coefficient of determination of $R^2 = 0.97$:

$$\frac{c^*_{L,CO}}{q_c} = \frac{K_{CO}}{q_{c,max}} + \frac{c^*_{L,CO}}{q_{c,max}} + \frac{{c^*_{L,CO}}^2}{q_{c,max} K_I}. \tag{4.7}$$

The special case of uncompetitive inhibition of the uptake kinetic of CO is in very good agreement with the data of their shaking flasks experiments when growing on CO. Besides the maximum specific uptake rate $q_{c,max} = 34.36\,\mathrm{mmol\,g_{CDW}^{-1}\,h^{-1}}$ they obtained the Monod constant $K_{CO} = 0.02\,\mathrm{mmol\,g_{CDW}^{-1}}$ and the CO inhibition constant $K_I = 0.55\,\mathrm{mmol\,g_{CDW}^{-1}}$ which led to the final formulation:

$$q_c = \frac{q_{c,max}\, c^*_{L,CO}}{K_{CO} + c^*_{L,CO} + \frac{{c^*_{L,CO}}^2}{K_I}}. \tag{4.8}$$

To describe the transport from the liquid phase over the effective mass transfer area A into the microorganisms, the mass transfer rate q_{diff} can be formulated:

$$q_{diff} = \beta A \Delta c. \tag{4.9}$$

Equation (4.9) includes also β as the transfer coefficient and Δc as concentration difference. The transfer coefficient can be derived from the dimensionless Sherwood number $Sh = \beta d_O / \mathcal{D}$ (also called the mass transfer Nusselt number Nu). It represents the ratio of the convective mass transfer to the rate of diffusive mass transport.

Besides the transfer coefficient, d_O as the characteristic length or in this case diameter of the organism and $\mathcal{D}$ as the mass diffusivity are included. According to Ranz and Marshall (1952), the Nusselt number for spheres is 2. When microorganisms are assumed to have spherical shapes equation (4.9) can be combined with the Sherwood equation to a derivation of Fick's first

law:

$$q_{\text{diff}} = \frac{2\mathcal{D}}{d_{\text{O}}} A \Delta c. \tag{4.10}$$

This equation is similar to passive membrane transport formulations but in this case specific for spherical microorganisms and their effective mass transfer area.

In order to decide, whether the gas transport is diffusion limited or limited by internal kinetic reactions, the maximum possible concentration difference should be investigated. All other relevant parameters for carbon monoxide and values for *C. ljungdahlii* are listed in Table 4.2.

Table 4.2: Parameters for carbon monoxide and *C. ljungdahlii*. Poudyal and Adhikari (2014) [1], Tanner et al. (1993) [2] and Mohammadi et al. (2014) [3]. (Reprinted from Siebler et al., 2020, with permission of © Wiley-VICH Engineering in Life Science.)

Parameter	Value	Unit	Description	Reference
$\mathcal{D}_{\text{CO}}$	$2\,\text{e}^{-9}$	$\text{m}^2\,\text{s}^{-1}$	mass diffusivity of CO in water	[1]
d_{O}	$2\,\text{e}^{-6}$	m	diameter of the organism	[2]
A_{O}	$1.26\,\text{e}^{-11}$	m^2	surface of the organism	[2]
V_{O}	$4.2\,\text{e}^{-18}$	m^3	volume of the organism	[2]
V_{L}	$5\,\text{e}^{-5}$	m^3	working volume	[3]
Δc_{max}	0.8	$\text{mol}\,\text{m}^{-3}$	max. concentration difference	[3]
$c_{\text{X,max}}$	0.1	$\text{kg}\,\text{m}^{-3}$	cell density at max. CO conc.	[3]
ρ_{w}	1000	$\text{kg}\,\text{m}^{-3}$	density of water/ organism	–

The effective mass transfer area can be calculated as described in equations (4.11) - (4.13):

$$V_{\text{O,all}} = \frac{c_{\text{X,max}}}{\rho_{\text{w}}} V_{\text{L}} = 5\text{e}^{-9}\ \text{m}^3 \tag{4.11}$$

$$N_{\text{s}} = \frac{V_{\text{O,all}}}{V_{\text{O}}} = 1.2\text{e}^{9} \tag{4.12}$$

$$A = N_{\text{s}} A_{\text{O}} = 1.5\text{e}^{-2}\ \text{m}^2. \tag{4.13}$$

$V_{\text{O,all}}$ is the volume of all cells, V_{L} the working volume. It is assumed that the cell density is similar to water. This leads to the total cell number $N_{\text{s}} = 1.2\,\text{e}^{9}$. The effective mass transfer area is subsequently $1.5\,\text{e}^{-2}\,\text{m}^2$ which leads to $q_{\text{diff}} = 2.4\,\text{e}^{-5}\,\text{mol}\,\text{s}^{-1}$. The effective maximum uptake rate $q_{\text{c,max,eff}} = 24.87\,\text{mmol}\,\text{g}_{\text{CDW}}^{-1}\,\text{h}^{-1}$ as derived by Mohammadi et al. (2014) can be converted as in equation (4.14) assuming the cell dry weight is ten times higher than the aqueous weight.

$$
\begin{aligned}
q_{\mathrm{c,max}} &= 24.87 \frac{1\mathrm{e}^{-3}}{3.6\mathrm{e}^{3} \cdot 1\mathrm{e}^{-3}} \frac{\mathrm{mol}}{\mathrm{kg_{CDW}\,s}} 5\mathrm{e}^{-5}\ \mathrm{m}^3 \cdot 1 \frac{\mathrm{kg_{CDW}}}{\mathrm{m}^3} \\
&= 3.45\mathrm{e}^{-7}\ \frac{\mathrm{mol}}{\mathrm{s}}
\end{aligned}
\tag{4.14}
$$

In this case, q_{CO} at a maximum concentration difference of $\Delta c_{\mathrm{max}} = 0.8\,\mathrm{mol\,m^{-3}}$ is about 10^2 times slower than diffusion, the diffusion is not limiting under these conditions. However, the CO mass transfer rate for the measured cell density is limited by diffusion at a concentration difference Δc of $0.016\,\mathrm{mol\,m^{-3}}$. The higher the cell density the higher the effective mass transfer area and therefore diffusion rate. The concentration difference Δc at which diffusion will limit the mass transfer to the cell is lower.

After all, the carbon monoxide uptake can be affected by diffusion. The switch between kinetic uptake as described in equation (4.8) and 'diffusive uptake' in equation (4.10) can be combined to express the shift between both limitations. In doing so, the mass transport in the surrounding fluid of the microorganism is examined. The fluid is assumed to be unbounded and not turbulent containing the concentration c of liquid CO, CO_2 and H_2 (see also Figure 4.7).

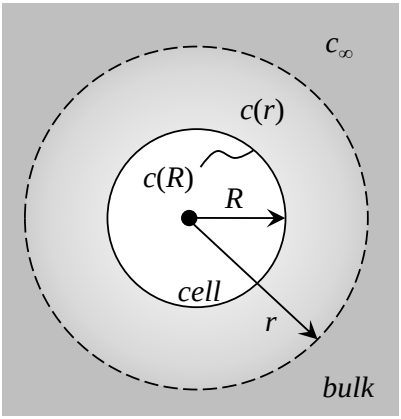

Figure 4.7: Mass transfer of bulk concentration to cell surface. Cell radius R, radial distance r and the bulk concentration c_∞ are given.

In this case, the diffusive mass transport is derived using CO as an example. Starting with Fick's second law in three dimensions with the

Laplace operator (here $\Delta = \nabla^2$):

$$\frac{\partial c}{\partial t} = \mathcal{D}\Delta c. \tag{4.15}$$

The diffusion coefficient $\mathcal{D}$ is isotropic and constant. At steady state conditions ($\partial c/\partial t = 0$), the Laplace equation is derived as $\Delta c = 0$.

Moreover, the problem is assumed to be spherically symmetric, therefore in a spherical polar coordinate system there are no gradients in polar angular and azimuthal coordinates (θ,ϕ). Consequently, the scalar Laplace equation in spherical coordinates can be simplified to

$$\begin{aligned} \Delta c &= \frac{1}{r^2}\frac{\partial}{\partial r}\left(r^2\frac{\partial c}{\partial r}\right) + \frac{1}{r^2\sin\theta}\frac{\partial}{\partial\theta}\left(\sin\theta\frac{\partial c}{\partial\theta}\right) + \frac{1}{r^2\sin^2\theta}\frac{\partial^2 c}{\partial\phi^2} = 0 \\ \Delta c &= \frac{1}{r^2}\frac{\partial}{\partial r}\left(r^2\frac{\partial c}{\partial r}\right) = \frac{\partial^2 c}{\partial r^2} + \frac{2}{r}\frac{\partial c}{\partial r} = 0, \end{aligned} \tag{4.16}$$

and be written in its two equivalent forms. The radial distance r is defined as shown in Figure 4.7. In order to solve this differential equation, two boundary conditions (BC) are needed. With $\partial c/\partial r = u$ the first integration results in

$$\begin{aligned} \frac{\partial u}{\partial r} + \frac{2}{r}u &= 0 \\ \int\frac{1}{u}\partial u &= \int -\frac{2}{r}\partial r \\ \ln u &= -2\ln r + \tilde{a} \\ u\,r^2 &= e^{\tilde{a}} = a \\ u &= \frac{a}{r^2}. \end{aligned} \tag{4.17}$$

The integration constant is given with a. The second inner derivative is integrated as follows:

$$\begin{aligned} \int\partial c &= \int\frac{a}{r^2}\partial r \\ c(r) &= -\frac{a}{r} + b. \end{aligned} \tag{4.18}$$

Here, b is the second integration constant which can be solved using the first BC where $r \to r_\infty$:

$$\begin{aligned} c(r_\infty) = c_\infty &= -\frac{a}{r_\infty} + b \\ b &= c_\infty. \end{aligned} \tag{4.19}$$

The integration constant a is derived applying Fick's first law and the surface reaction at the boundary condition $r = R$ respectively the cell surface (see Figure 4.7).

$$\begin{aligned} J = \mathcal{D} \left.\frac{\partial c}{\partial r}\right|_{r=R} &= \gamma c \\ \mathcal{D} \left.\frac{\partial \left(c_\infty - \frac{a}{R}\right)}{\partial r}\right|_{r=R} &= \gamma \left(c_\infty - \frac{a}{R}\right) \\ \gamma &= \frac{\mathcal{D}\frac{a}{R^2}}{c_\infty - \frac{a}{R}} \\ J = \mathcal{D}\frac{\partial c}{\partial r} = \gamma c &= \frac{\mathcal{D}\frac{a}{R^2}}{c_\infty - \frac{a}{R}} \left(c_\infty - \frac{a}{R}\right) \\ a &= \frac{R^2 J}{\mathcal{D}} \\ \gamma &= \frac{J}{c_\infty - \frac{RJ}{\mathcal{D}}} \end{aligned} \tag{4.20}$$

The surface reaction includes the reaction rate γ and concentration c. The flux J can be expressed as the mass flux $\mathrm{d}M/\mathrm{d}t$ divided by cell number N_s and surface A_O:

$$J = \mathcal{D} \left.\frac{\partial c}{\partial r}\right|_{r=R} = \frac{\frac{\mathrm{d}M}{\mathrm{d}t}}{N_\mathrm{s} A_\mathrm{O}}. \tag{4.21}$$

The volumetric mass flux divided by the cell density c_X gives the biomass specific gas uptake rate q_c and vice versa:

$$q_\mathrm{c} c_\mathrm{X} = \frac{\frac{\mathrm{d}M}{\mathrm{d}t}}{V_\mathrm{L}}. \tag{4.22}$$

The uptake rate, respectively volumetric mass flux, is also the sink term in the CO balance equation described in the following chapter 4.3.4 (Derivation

of partial differential equations). Rearranging equation (4.21) and (4.22) in combination with the cell number calculation leads to:

$$\begin{aligned} N_\mathrm{s} &= V_\mathrm{L}\frac{c_\mathrm{X}}{m_\mathrm{cell}} \\ m_\mathrm{cell} &= V_\mathrm{O}\rho_\mathrm{w} \\ q_\mathrm{c}c_\mathrm{X}V_\mathrm{L} = \frac{\mathrm{d}M}{\mathrm{d}t} &= JN_\mathrm{s}A_\mathrm{O} = JV_\mathrm{L}\frac{c_\mathrm{X}}{m_\mathrm{cell}}A_\mathrm{O} \\ J(\gamma, \mathcal{D}, a, c_\infty) &= q_\mathrm{c}\frac{m_\mathrm{cell}}{A_\mathrm{O}}. \end{aligned} \tag{4.23}$$

V_L is the reaction volume and V_O the volume of the organism. The cell mass m_cell is calculated via the cell density, which is assumed to be similar to the density of water ρ_w. Finally, the flux is expressed through the uptake kinetic introduced by Mohammadi et al. (2014).

$$\begin{aligned} c &= \left(1 - \frac{a}{r}\right)c_\infty \\ J &= \mathcal{D}\left.\frac{\mathrm{d}\left(\left(1-\frac{a}{r}\right)c_\infty\right)}{\mathrm{d}r}\right|_{r=R} = \mathcal{D}\frac{c_\infty a}{R^2} \\ JA_\mathrm{O}\frac{N_\mathrm{s}}{V_\mathrm{L}} = J4\pi R^2\frac{c_\mathrm{X}}{m_\mathrm{cell}} &= \mathcal{D}\frac{c_\infty a}{R^2}4\pi R^2\frac{c_\mathrm{X}}{m_\mathrm{cell}} = \frac{34.36c_\infty}{0.02 + c_\infty + \frac{{c_\infty}^2}{0.55}}c_\mathrm{X} \\ \mathcal{D}a4\pi\frac{1}{m_\mathrm{cell}} &= \frac{34.36}{0.02 + c_\infty + \frac{{c_\infty}^2}{0.55}} \\ a &= \frac{34.36}{0.02 + c_\infty + \frac{{c_\infty}^2}{0.55}}\frac{m_\mathrm{cell}}{\mathcal{D}4\pi} \end{aligned} \tag{4.24}$$

$$\begin{aligned} J = \mathcal{D}\frac{\partial c}{\partial r} = \mathcal{D}\frac{c_\infty a}{R^2} &= \gamma\left(1 - \frac{a}{r}\right)c_\infty \\ \gamma &= \frac{\mathcal{D}a}{R(R-a)} \end{aligned} \tag{4.25}$$

With $c^*_\mathrm{L,CO} = c_\infty$, the combination of equation (4.20) and the boundary condition in equation (4.23), the uptake rate describing inhibition kinetic and limitation by diffusion can now be expressed as

$$q_\mathrm{c} = \frac{A_\mathrm{O}}{m_\mathrm{cell}}J = \frac{A_\mathrm{O}}{m_\mathrm{cell}}\gamma c. \tag{4.26}$$

Finally, the new uptake kinetic is plotted over the bulk concentration to display the effect of diffusion in comparison to the previous kinetic as shown in Figure 4.8. Furthermore, the reaction rate γ shows, that diffusion has the highest impact at low gas concentrations as previously indicated.

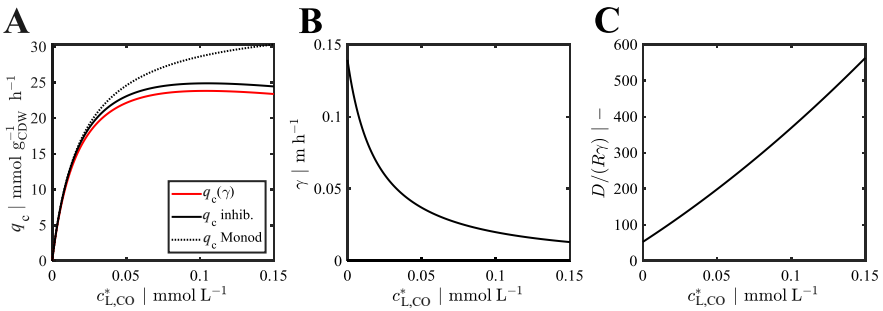

Figure 4.8: Volumetric uptake kinetic with diffusion limitation. Volumetric uptake rate q_c over concentration $c^*_{L,CO}$ (A). Dotted line shows Monod-like kinetic as relation to inhibition kinetic (black line) by Mohammadi et al. (2014) and the new uptake rate including limitation by diffusion (red line). Reaction rate γ as a function of $c^*_{L,CO}$ (B) as well as the dimensionless correlation of diffusion coefficient, radius and γ (C).

The here presented derivation is duo to equation (4.19) similar to the one used for the Thiele module. Likewise, a dimensionless number can be formulated with $\mathcal{D}/(R\,\gamma)$. The closer it is to zero the more impact diffusion has on the new reaction rate γ. The final impact of possible diffusion limitation is discussed in chapter 6.1.3 (Steady state results) in greater detail.

4.3.3 Reactor set-up and operation mode

As established in chapter 3 (Evaluation and assessment of industrial reactors), the bubble column reactor is chosen for economical synthesis gas fermentation. The 1-dimensional approach is developed for a cylindrical reactor with a liquid height of 25 m and diameter of $D_R = 2.52$ m resulting in a H_L/D_R-ratio of around 10. With this set-up a high hydrostatic pressure gradient is achieved.

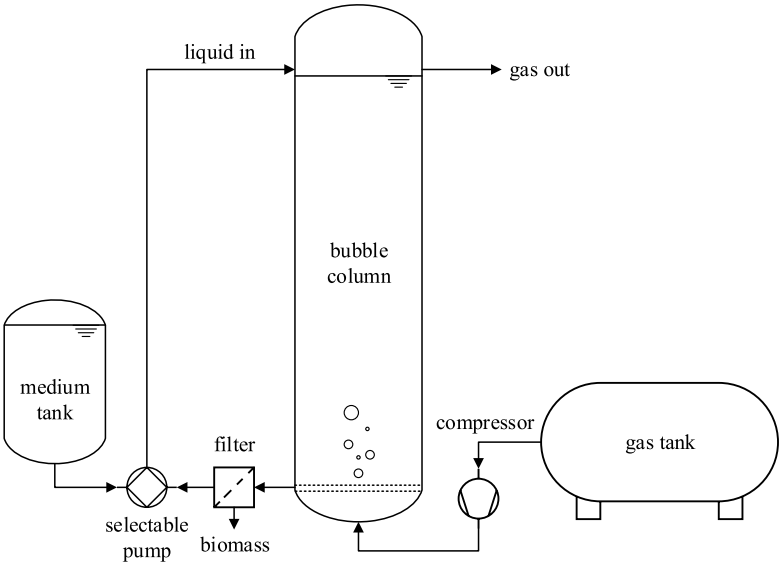

Figure 4.9: Bubble column reactor set-up. Bubble column reactor in continuous counter current mode with liquid recycling and medium feed. Synthesis gas is provided by a gas compressor at the bottom of the reactor.

As described in Figure 4.9, the bubble column was simulated in a continuous counter current mode with liquid recycling and medium feed at the top of the reactor. Synthesis gas is continuously provided at the bottom of the reactor via the whole cross-sectional area A_R. No additional pressure is applied, the optimum temperature of *Clostridium ljungdhalii* is used and the medium density equals the density of water (see also Table 4.3).

Table 4.3: Reactor dimensions and physical properties. Liquid height and physical properties are assumed to be constant during the fermentation.

Parameter	Value	Unit	Description
A_R	5	m^2	cross sectional area of the reactor
D_R	2.52	m	diameter of the reactor
H_L	25	m	liquid height
V_R	125	m^3	liquid volume of the reactor
P	$1.013\,25\,e^5$	Pa	operation pressure equals ambient pressure
T	310.15	K	operation temperature
ρ_L	1000	$kg\,m^{-3}$	density equals density of water

These physical properties as the liquid height are assumed to not change during the fermentation. All other changing values as for example the gassing rate are described in chapter 6.1.2 (Choosing reasonable parameter ranges).

The most important values such as gas concentrations and gas holdup are partially differentiated. The derivation of these equations is presented in the following chapter.

4.3.4 Derivation of partial differential equations

The derivation of the 1-dimensional approach is published in Siebler et al. (2020) and is recited in this chapter to follow the thesis structure and allow important cross-references.

According to the previously outlined reactor set-up, partial differential equations (PDE) and ordinary differential equations (ODE) are derived. Dissolved and gaseous synthesis gas components and the gas holdup are local and time dependent variables serving as input values for calculating dynamics of growth and product formation.

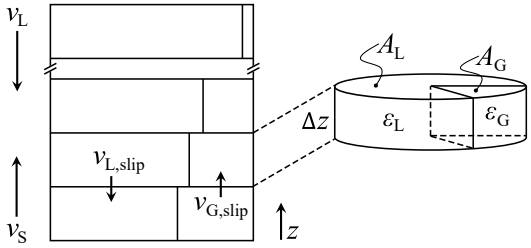

Figure 4.10: Schematic drawing of compartments and volume fractions. For better understanding the liquid v_L and superficial gas velocity v_S, slip velocity $v_{G/L,slip}$, volume fractions $\varepsilon_{G/L}$, the cross-sectional area of the reactor $A_R = A_L + A_G$, direction z and discretisation volume height Δz are visualised. (Reprinted from Siebler et al., 2020, with permission of © Wiley-VICH Engineering in Life Science.)

The mass balance for the liquid phase in one discretisation volume is derived including convective and diffusive transport, phase-to-phase mass transfer and consumption terms. The volume of each compartment is $\Delta V_L = \Delta z A_L$ with Δz as compartment height and A_L as liquid surface area between the compartments. The cross-sectional area of the reactor A_R is the sum of A_L and the gaseous interface A_G (see Figure 4.10). The gaseous and liquid volume fractions are indicated by ε_G and ε_L. It follows

$$\begin{aligned}\Delta z \frac{\mathrm{d}c_\mathrm{L} A_\mathrm{L}}{\mathrm{d}t} = &\underbrace{A_\mathrm{L} c_\mathrm{L} v_{\mathrm{L,slip}}\Big|_{z+\Delta z} - A_\mathrm{L} c_\mathrm{L} v_{\mathrm{L,slip}}\Big|_{z}}_{\text{transport}} + \underbrace{A_\mathrm{slice} k_L \left(c_\mathrm{L}^* - c_\mathrm{L}\right)}_{\text{mass transfer}} \\ &- \underbrace{\Delta z A_\mathrm{L} q c_\mathrm{X}}_{\text{consumption}} + \underbrace{\mathcal{D}_\mathrm{L} A_\mathrm{L} \frac{\mathrm{d}c_\mathrm{L}}{\mathrm{d}z}\Big|_{z+\Delta z} - \mathcal{D}_\mathrm{L} A_\mathrm{L} \frac{\mathrm{d}c_\mathrm{L}}{\mathrm{d}z}\Big|_{z}}_{\text{diffusion}}\end{aligned} \tag{4.27}$$

with A_slice as the mass transfer area between the liquid and gaseous phase, which leads to $a = A_\mathrm{slice}/(\Delta z A_\mathrm{L})$ and the well-known $k_L a$ term for modelling the mass transfer term with the equilibrium concentration c_L^* and the soluble gas concentration c_L. The liquid slip velocity $v_{\mathrm{L,slip}}$ multiplied by $\varepsilon_\mathrm{L} = 1 - \varepsilon_\mathrm{G}$ provides the liquid velocity v_L, which can be assumed to be constant. The diffusion term with the liquid phase dispersion coefficient $\mathcal{D}_\mathrm{L}$ is included as well as the consumption term consisting of the uptake kinetic q_c and biomass concentration c_X. By dividing equation (4.27) by A_R and Δz and using the correlation $1 - \varepsilon_\mathrm{G} = A_\mathrm{L}/A_\mathrm{R}$ the final PDEs for the dissolved gases ($m \in$ [CO,CO_2,H_2]) can be formulated:

$$\begin{aligned}\frac{\partial c_{\mathrm{L},m} \varepsilon_\mathrm{L}}{\partial t} =& v_{\mathrm{L,slip}} \frac{\partial c_{\mathrm{L},m} \varepsilon_\mathrm{L}}{\partial z} + k_{\mathrm{L},m} a \left(c_{\mathrm{L},m}^* - c_{\mathrm{L},m}\right) \\ &- q_m c_\mathrm{X} \varepsilon_\mathrm{L} + \mathcal{D}_\mathrm{L} \frac{\partial^2 c_{\mathrm{L},m} \varepsilon_\mathrm{L}}{\partial z^2}.\end{aligned} \tag{4.28}$$

Each balance of the gas phase only needs to consider convective mass transport and phase-to-phase mass transfer, which leads to the following equation:

$$\frac{\partial c_{\mathrm{G},m} \varepsilon_\mathrm{G}}{\partial t} = v_{\mathrm{G,slip}} \frac{\partial c_{\mathrm{G},m} \varepsilon_\mathrm{G}}{\partial z} - k_{\mathrm{L},m} a \left(c_{\mathrm{L},m}^* - c_{\mathrm{L},m}\right). \tag{4.29}$$

Because the gas phase is compressible, the gas holdup depends on the local pressure which correlates ε_L and ε_G with the liquid height H_L. The total molar density ρ^* is introduced using the ideal gas law $PV = nRT$ and the hydrostatic pressure $P_\mathrm{H} = P_0 + \rho g h$ with $h = H_\mathrm{L} - z$ leading to

$$\rho^* = \sum_{m=1}^{3} \frac{\rho_m(z)}{M_m} = \frac{P_0 + (H_\mathrm{L} - z) g \rho_\mathrm{L} \varepsilon_\mathrm{L}}{RT} \tag{4.30}$$

with the gravitational acceleration g, liquid density ρ_L, universal gas constant R and the operating temperature T. The index $m = 1, 2, 3$ always represents the synthesis gas composition with CO, CO_2 and H_2. Considering the total molar gas density, the following equation can be derived:

$$\frac{\partial \varepsilon_G \rho^*}{\partial t} = v_{G,slip} \frac{\partial \varepsilon_G \rho^*}{\partial z} - \sum_{m=1}^{3} k_{L,m} a \left(c^*_{L,m} - c_{L,m} \right). \tag{4.31}$$

It is further assumed that the number density n_G, i.e. the number of bubbles N_B divided by the reactor volume V_R, only depends on convection:

$$\begin{aligned} \frac{\partial n_G}{\partial t} &= v_{G,slip} \frac{\partial n_G}{\partial z} \\ n_G(t,z) &= \frac{N_B}{V_R} = \frac{\varepsilon_G}{\frac{4}{3}\pi R_B^3}. \end{aligned} \tag{4.32}$$

No further bubble breakage or coalescence occurs. Nevertheless, the bubble radius R_B is a function of the gas hold-up and hydrostatic pressure. If the number of bubbles in a discretisation volume i is multiplied with the bubble volume $V_{B,i}$, the gas holdup $\varepsilon_{G,i}$ is derived. Therefore, all balance equations are intertwined by the gas hold-up. Noteworthy, this also affects the volumetric surface area a

$$a = \frac{\sum A_B}{V_R} = \frac{3}{R_B} \varepsilon_G \tag{4.33}$$

which is the sum of all bubble surfaces A_B divided by the reactor volume (see also equation (2.10)).

Product formation and growth are formulated as ordinary differential equations

$$\begin{aligned} \frac{\mathrm{d}c_X}{\mathrm{d}t} &= \mu c_X - D c_X \\ \frac{\mathrm{d}c_k}{\mathrm{d}t} &= M_k q_k c_X - D c_{L,k} \end{aligned} \tag{4.34}$$

using the growth rate μ and the dilution rate $D = 0.055\,\mathrm{h}^{-1}$.

Because biomass and product concentrations c_k are in $\mathrm{g\,L^{-1}}$, the molecular weight M_k is needed with $k \in$ [acetate, ethanol, 2,3-butanediol]. For the sake of simplicity, individual production rates q_k represent mean values of the compartment-specific $q_{k,i}$, which consider local gas uptake kinetics $q_{m,i}$ (see chapter 4.3.1).

Finally, four ($m = 1$) to eight ($m = 1, 2, 3$) PDEs (equations (4.28), (4.29) and (4.31)) and four ODEs (equation (4.34)) are derived. They are spatially and temporally discretised and their start and boundary conditions are chosen, which is described in the following subsection.

4.3.5 Spatial and temporal discretisation

The spatial and temporal discretisation is published in Siebler et al. (2020) and is recited in this chapter. In general, similar discretisation methods as described by Chen et al. (2016; 2018) are applied.

In order to solve the partial differential equations numerically, spatial and temporal discretisation methods have to be chosen. For this reason, the bubble column reactor is divided into N compartments with $n = N + 1$ interpolation points of the liquid height $H_L = \Delta z N$ (see Figure 4.11). In each discretisation volume the balance equations (4.28), (4.29), (4.31) and (4.34) are solved temporally.

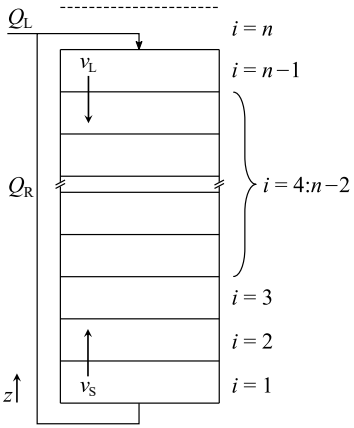

Figure 4.11: Scheme of discretisation steps and back flow. The column is fragmented in N compartments with $n = N + 1$ numerical volumes. Back flow Q_R, media flow Q_L, liquid v_L and superficial gas velocity v_S are depicted.

For the liquid phase PDE (see equation (4.28)) a first order upwind scheme is depicted

$$
\begin{aligned}
\frac{\partial c_{\mathrm{L}}\varepsilon_{\mathrm{L}}(t,z_n)}{\partial z} &= 0 \\
\frac{\partial c_{\mathrm{L}}\varepsilon_{\mathrm{L}}(t,z_{n\text{-}1})}{\partial z} &\approx \frac{c_{\mathrm{L}}\varepsilon_{\mathrm{L}}(t,z_n) - c_{\mathrm{L}}\varepsilon_{\mathrm{L}}(t,z_{n\text{-}1})}{\Delta z} \\
&\vdots \\
\frac{\partial c_{\mathrm{L}}\varepsilon_{\mathrm{L}}(t,z_i)}{\partial z} &\approx \frac{c_{\mathrm{L}}\varepsilon_{\mathrm{L}}(t,z_{i+1}) - c_{\mathrm{L}}\varepsilon_{\mathrm{L}}(t,z_i)}{\Delta z} \\
&\vdots \\
\frac{\partial c_{\mathrm{L}}\varepsilon_{\mathrm{L}}(t,z_3)}{\partial z} &\approx \frac{c_{\mathrm{L}}\varepsilon_{\mathrm{L}}(t,z_4) - c_{\mathrm{L}}\varepsilon_{\mathrm{L}}(t,z_3)}{\Delta z} \\
\frac{\partial c_{\mathrm{L}}\varepsilon_{\mathrm{L}}(t,z_2)}{\partial z} &\approx \frac{c_{\mathrm{L}}\varepsilon_{\mathrm{L}}(t,z_3) - c_{\mathrm{L}}\varepsilon_{\mathrm{L}}(t,z_2)}{\Delta z} \\
\frac{\partial c_{\mathrm{L}}\varepsilon_{\mathrm{L}}(t,z_1)}{\partial z} &\approx \frac{c_{\mathrm{L}}\varepsilon_{\mathrm{L}}(t,z_2) - c_{\mathrm{L}}\varepsilon_{\mathrm{L}}(t,z_1)}{\Delta z},
\end{aligned}
\tag{4.35}
$$

and a central difference approximation with second order accuracy for the diffusion term. An upwind finite difference approximation with third order accuracy is chosen for the convection term in the case of the gas phase PDE (see equation (4.29)), which is described as follows for each node point:

$$
\begin{aligned}
\frac{\partial c_{\mathrm{G}}\varepsilon_{\mathrm{G}}(t,z_n)}{\partial z} &\approx \frac{c_{\mathrm{G}}\varepsilon_{\mathrm{G}}(t,z_n) - c_{\mathrm{G}}\varepsilon_{\mathrm{G}}(t,z_{n\text{-}1})}{\Delta z} \\
\frac{\partial c_{\mathrm{G}}\varepsilon_{\mathrm{G}}(t,z_{n\text{-}1})}{\partial z} &\approx \frac{2c_{\mathrm{G}}\varepsilon_{\mathrm{G}}(t,z_n) + 3c_{\mathrm{G}}\varepsilon_{\mathrm{G}}(t,z_{n\text{-}1}) - 6c_{\mathrm{G}}\varepsilon_{\mathrm{G}}(t,z_{n\text{-}2}) + c_{\mathrm{G}}\varepsilon_{\mathrm{G}}(t,z_{n\text{-}3})}{6\Delta z} \\
&\vdots \\
\frac{\partial c_{\mathrm{G}}\varepsilon_{\mathrm{G}}(t,z_i)}{\partial z} &\approx \frac{2c_{\mathrm{G}}\varepsilon_{\mathrm{G}}(t,z_{i+1}) + 3c_{\mathrm{G}}\varepsilon_{\mathrm{G}}(t,z_i) - 6c_{\mathrm{G}}\varepsilon_{\mathrm{G}}(t,z_{i\text{-}1}) + c_{\mathrm{G}}\varepsilon_{\mathrm{G}}(t,z_{i\text{-}2})}{6\Delta z} \\
&\vdots \\
\frac{\partial c_{\mathrm{G}}\varepsilon_{\mathrm{G}}(t,z_3)}{\partial z} &\approx \frac{2c_{\mathrm{G}}\varepsilon_{\mathrm{G}}(t,z_4) + 3c_{\mathrm{G}}\varepsilon_{\mathrm{G}}(t,z_3) - 6c_{\mathrm{G}}\varepsilon_{\mathrm{G}}(t,z_2) + c_{\mathrm{G}}\varepsilon_{\mathrm{G,in}}}{6\Delta z} \\
\frac{\partial c_{\mathrm{G}}\varepsilon_{\mathrm{G}}(t,z_2)}{\partial z} &\approx \frac{c_{\mathrm{G}}\varepsilon_{\mathrm{G}}(t,z_2) - c_{\mathrm{G}}\varepsilon_{\mathrm{G,in}}}{\Delta z} \\
\frac{\partial c_{\mathrm{G}}\varepsilon_{\mathrm{G}}(t,z_1)}{\partial z} &= 0.
\end{aligned}
\tag{4.36}
$$

At the reactor boundaries, a first order backward difference approximation is set. The accuracy of the chosen discretisation methods is tested in a mesh refining study in which the compartment number N is varied between 3 and 200. Incoming and outgoing mass is compared in a scenario without any organism and consumption term (see chapter 6.1.1). Starting values and

boundary conditions are discussed in the next subchapter.

4.3.6 Start values and boundary conditions

A start biomass concentration $c_X(t_0)$ of 0.1 g L^{-1} and a start product concentration $c_k(t_0)$ of 0.0 g L^{-1} are chosen. The PDEs described in chapter 4.3.2 equation (4.28) and (4.29) are initialised with the following correlation based on the absolute pressure P (ambient pressure plus hydrostatic pressure), Henry coefficient H_m^{cp} and gas fraction y_m ($m = 1, 2, 3$ respectively CO, CO_2 and H_2 fraction):

$$\begin{aligned} c_{G,m}\varepsilon_G\,(t_0, z) &= \frac{y_m P(z)\varepsilon_{G,0}}{RT} \\ c_{L,m}\varepsilon_L\,(t_0, z) &= \frac{c_{G,m}\varepsilon_G\,(t_0, z)}{\varepsilon_{G,0}} RT H_m^{cp} \frac{1000}{1.01325e^5}\varepsilon_L. \end{aligned} \tag{4.37}$$

The bubble column reactor is used in counter current mode and with a liquid recycling port (see chapter 4.3.3). Hence, a Robin boundary condition is implemented at the top of the reactor for the liquid phase:

$$\begin{aligned} v_{L,slip} c_{L,m}\varepsilon_L(t, z_n) + \mathcal{D}_L \frac{\partial c_{L,m}\varepsilon_L}{\partial z}(t, z_n) &= v_{L,slip} c_{L,m}\varepsilon_L(t, z_1)\alpha \\ c_{L,m}\varepsilon_L(t, z_n) &= \frac{\frac{\Delta z}{\mathcal{D}_L} v_{L,slip} c_{L,m}\varepsilon_L(t, z_1)\alpha - c_{L,m}\varepsilon_L(t, z_{n\text{-}1})}{\frac{\Delta z}{\mathcal{D}_L} v_{L,slip} - 1}. \end{aligned} \tag{4.38}$$

As indicated in Figure 4.11 the fermentation broth is continuously recycled with the back flow Q_R, which also comprises media. The back flow and media flow Q_L are combined in $\alpha = Q_R/(Q_R + Q_L)$. A zero slope boundary condition with a constant gas feed $c_{G,m}\varepsilon_{G,in}(t, z_1) = y_m P(z_1)\varepsilon_{G,0}/(RT)$ is set at the bottom of the reactor (see also equation (4.36)). The initial number density $n_G(t_0, z)$ is derived from equation (4.32) with initial gas holdup $\varepsilon_{G,0}$ and bubble radius $R_{B,0}$, which accounts for the start gas holdup $\varepsilon_G\rho^*(t_0, z) = \varepsilon_{G,0}\rho^*(z)$ as well. In that regard, the liquid dispersion coefficient $\mathcal{D}_L$ is set to 4.5 m^2 h^{-1} and the liquid phase velocity v_L to 50 m h^{-1}.

The initial values of y, $R_{B,0}$, k_L, $\varepsilon_{G,0}$ and superficial gas velocity v_S are varied as discussed in chapter 6.1.2 (Choosing reasonable parameter ranges).

4.4 Computational fluid dynamics

While the 1-dimensional approaches (Chen et al., 2015; Vrábel et al., 2001; Heins et al., 2015; Pigou and Morchain, 2015) inherently offer high simulation speed even in combination with complex kinetics (Mantzaris et al., 1999; Henson, 2003), computational fluid dynamics allows higher resolution in flow behaviour and mass transfer approximations by including important bubble effects. Some 1-dimensional approaches even need general information of the flow behaviour obtained from CFD (Pigou and Morchain, 2015). CFD offer for each level of complexity a computing solution which solves the basic flow equations in combination with different modelled values. In this chapter, the governing equations are pointed out as well as which values are approximated by models. The importance of bubble breakage and coalescence is noted as well as forces which act on bubbles are mentioned. All effects are crucial to get a reliable gas gradient and finally investigate the impact of microbial activity as they impose fluctuating concentration in the cell environment. In this chapter parts of Manuscript I are presented and summarised. The research of Kuschel et al. (2017) is conducted in a collaborative effort and presents the Lagrange trajectory method for a large-scale *Pseudomonas putida* fermentation.

4.4.1 Turbulent incompressible flow

In the early 19$^{\text{th}}$ century, Claude Louis Marie Henri Navier, Siméon Denis Poisson, Barré de Saint-Venant and George Gabriel Stokes independently formulated the principle of linear momentum of Newtonian fluids and thereby completed the Eulerian equations of motion. The resulting Navier-Stokes equations (NSE) include five non-linear partial differential equation: the continuity equation (4.39), three impulse equations (4.40) in each direction in space x, y, z and the energy conservation equation (4.41). The NSE are given for incompressible fluids.

The three dimensional velocity u, v, w is part of each term, whereby the impulse equations also include the fluid density ρ, pressure P and dynamic viscosity η. In the energy conservation equation the specific thermal capacity c_{T}, temperature T and thermal conductivity λ are needed. However, the process is assumed to be isothermal, thus equation (4.41) will be neglected from now on.

$$\frac{\partial u}{\partial x} + \frac{\partial v}{\partial y} + \frac{\partial w}{\partial z} = 0 \tag{4.39}$$

$$\rho\left(\frac{\partial u}{\partial t} + u\frac{\partial u}{\partial x} + v\frac{\partial u}{\partial y} + w\frac{\partial u}{\partial z}\right) = -\frac{\partial p}{\partial x} + \eta\left(\frac{\partial^2 u}{\partial x^2} + \frac{\partial^2 u}{\partial y^2} + \frac{\partial^2 u}{\partial z^2}\right)$$

$$\rho\left(\frac{\partial v}{\partial t} + u\frac{\partial v}{\partial x} + v\frac{\partial v}{\partial y} + w\frac{\partial v}{\partial z}\right) = -\frac{\partial p}{\partial y} + \eta\left(\frac{\partial^2 v}{\partial x^2} + \frac{\partial^2 v}{\partial y^2} + \frac{\partial^2 v}{\partial z^2}\right) \tag{4.40}$$

$$\rho\left(\frac{\partial w}{\partial t} + u\frac{\partial w}{\partial x} + v\frac{\partial w}{\partial y} + w\frac{\partial w}{\partial z}\right) = -\frac{\partial p}{\partial z} + \eta\left(\frac{\partial^2 w}{\partial x^2} + \frac{\partial^2 w}{\partial y^2} + \frac{\partial^2 w}{\partial z^2}\right)$$

$$\rho \cdot c_{\mathrm{T}}\left(\frac{\partial T}{\partial t} + u\frac{\partial T}{\partial x} + v\frac{\partial T}{\partial y} + w\frac{\partial T}{\partial z}\right) = \lambda\left(\frac{\partial^2 T}{\partial x^2} + \frac{\partial^2 T}{\partial y^2} + \frac{\partial^2 T}{\partial z^2}\right) \tag{4.41}$$

The incompressible NSE with constant liquid properties and gravity g_i ($g_1 = g_2 = 0$ and $g_3 = -9.81\,\mathrm{m\,s^{-1}}$) can under isothermal conditions be simplified in tensor form as shown in equation (4.43). The notation implies summation over the indices $i, j = 1, 2, 3$ analogous to x, y, z respectively u, v, w:

$$\frac{\partial u_i}{\partial x_i} = 0 \tag{4.42}$$

$$\rho\frac{\partial u_i}{\partial t} + \rho u_j\frac{\partial u_i}{\partial x_j} = g_i - \frac{\partial p}{\partial x_i} + \eta\frac{\partial}{\partial x_j}\frac{\partial u_i}{\partial x_j}. \tag{4.43}$$

A bubble column has a turbulent flow pattern. Turbulence is three dimensional and transient. It also consists of strongly fluctuating vortex structures with large and small eddies (see Figure 4.12). When geometry and Reynolds number are not changing, the image of a turbulent flow is only in average the same. The instantaneous images on the other hand can differ a lot. Only a Direct Numerical Simulation (DNS) with a sufficient fine grid can solve the accurate eddy structure but is usually not suitable in most cases (see Figure 4.12 (A)). DNS is primarily used for academic purposes to validate averaged model approaches such as Large-Eddy-Simulations (LES) and the Reynolds-averaged Navier-Stokes (RANS) method (Figure 4.12 (B) and (C)). LES models eddy structures which are smaller in size than the mesh size (sub-grid scale modelling) and directly solves for the dynamics of those structures that can be resolved spatially by the employed mesh. For the RANS approach the vortex structure is not resolved. In general, the higher the resolution the more computing power and time is needed. In the case of

an industrial scale bubble column reactor (see Figure 4.10), a RANS approach for turbulence is chosen due to time efficiency and sufficient accurate results.

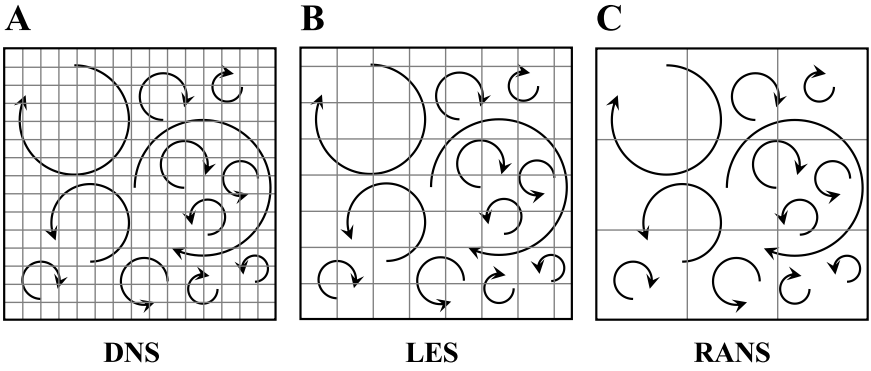

Figure 4.12: Resolution of turbulence with three mesh sizes according to their approach (derived from Paschedag, 2004, p. 33). In (A) Direct Numerical Simulation (DNS) with a very fine grid, solving each eddy. The Large-Eddy-Simulation approach (LES) in (B) solves only the large eddies directly, therefore showing a coarser grid, while the Reynolds-averaged Navier-Stokes (RANS) method uses the average of turbulence fluctuations.

In the RANS approach, it is assumed that the time scales of the main flow and the turbulent transport differ strongly from each other. For this reason, the temporal average value $\overline{u}_i$ and fluctuation u_i' can be defined with $\overline{u_i'} = 0$. Potential temporal fluctuations of the main flow are covered by the average value, while oscillation caused by turbulence are given by the fluctuation variable $u_i = \overline{u}_i + u_i'$. This averaged expression $\overline{\overline{u}_i + u_i'}$ can now be inserted into equation (4.42) and (4.43) and transformed to the following equations:

$$\frac{\partial \overline{u}_i}{\partial x_i} = 0 \tag{4.44}$$

$$\rho \frac{\partial \overline{u}_i}{\partial t} + \frac{\partial \overline{u}_i \overline{u}_j}{\partial x_j} = g_i - \frac{\partial \overline{p}}{\partial x_i} + \frac{\partial}{\partial x_j}\left(\eta \frac{\partial \overline{u}_i}{\partial x_j} - \rho \overline{u_i' u_j'}\right). \tag{4.45}$$

Calculating two times the average leads to $\overline{\overline{u_i}} = \overline{u}_i$ and $\overline{\overline{u_i}\overline{u_j}} = \overline{u}_i\overline{u}_j$ However, it is different for $\overline{\overline{u_i'}\overline{u_j'}} = \overline{u_i'}\overline{u_j'}$ and $\overline{\overline{u_i}u_j'} = 0$. As a result, the product of fluctuations does not disappear and lead to the introduction of six Reynolds stress terms $\tau_{ij}^{\mathrm{Re}} = -\rho\overline{u_i' u_j'}$ $(i, j = 1, 2, 3)$. These fluctuations are unknown and have to be modelled.

There are several classic model approaches which can be grouped by the number of employed modelling equations:

- Zero equation model: mixing length model
- One equation model: Spalart-Almaras model
- Two equation models: k-ε style models, k-ω model and algebraic stress model
- Seven equation model: Reynolds stress model.

If the model is more complex, additional partial differential equations need to be solved. The underlined models can predict the turbulent (respectively eddy) viscosity μ_t, which can be linked with the Reynolds stress terms:

$$\tau_{ij}^{\mathrm{Re}} = -\rho\overline{u_i' u_j'} = \mu_t \left(\frac{\partial \overline{u}_i}{\partial x_i} + \frac{\partial \overline{u}_j}{\partial x_j} \right). \tag{4.46}$$

Equation (4.46) is based on the Boussinesq eddy viscosity assumption and only valid for incompressible fluids.

The standard k-ε-model by Launder and Spalding (1974) is briefly introduced due to its reasonable predictions for certain cases and stable calculation. It is a model which renders the characteristics for turbulent flow conditions by means of two transport equations. As the name implies, the first transported variable is the turbulent kinetic energy k and the second the dissipation rate of turbulent energy ε:

$$\frac{\partial \rho k}{\partial t} + \frac{\partial \rho k u_i}{\partial x_i} = \frac{\partial}{\partial x_j}\left(\frac{\mu_t}{\sigma_k} \frac{\partial k}{\partial x_j} \right) + 2\mu_t E_{ij} E_{ij} - \rho\varepsilon \tag{4.47}$$

$$\underbrace{\frac{\partial \rho \varepsilon}{\partial t}}_{\text{rate of change}} + \underbrace{\frac{\partial \rho \varepsilon u_i}{\partial x_i}}_{\text{convection}} = \underbrace{\frac{\partial}{\partial x_j}\left(\frac{\mu_t}{\sigma_\varepsilon} \frac{\partial \varepsilon}{\partial x_j} \right)}_{\text{diffusion}} + \underbrace{C_{1\varepsilon} \frac{\varepsilon}{k} 2\mu_t E_{ij} E_{ij}}_{\text{production}} - \underbrace{C_{2\varepsilon} \rho \frac{\varepsilon^2}{k}}_{\text{destruction}}. \tag{4.48}$$

Both equations include the component of deformation rate E_{ij} and the eddy viscosity with $\mu_t = \rho C_\mu k^2/\varepsilon$. The adjustable constants have been derived from numerous iterations of data fitting for a wide range of flows with $\sigma_k = 1.00$, $\sigma_k = 1.30$, $C_\mu = 0.09$, $C_{1\varepsilon} = 1.44$ and $C_{2\varepsilon} = 1.92$.

Not all kinds of turbulence can be reliably modelled by the standard k-ε-model. For special fields of application, derivations of the standard form

are available. The RNG (Re-Normalisation Group) k-ε-model, for example, is very stable even for strongly bent streamlines and high stress gradients. Another derivation would be the realisable k-ε-model which improves, for example, solving planar and round jets or boundary layers. The final choice of turbulent a model depends on the purpose and also simulation stability.

Since the governing equations for turbulent flow have been shortly introduced, the next chapter addresses the complexity of multiphase flows.

4.4.2 Modelling two-phase flow

The continuous phase is usually simulated as Eulerian phase while for the disperse phase either an Eulerian or a Lagrangian approach can be chosen. While the Euler-Euler approach treats the different phase mathematically as interpenetrating continua, the Euler-Lagrange approach treats the dispersed gas phase as Lagrangian elements by individually tracking them on their way through the reactor. Both multiphase approaches and their variations are summarised in Figure 4.13.

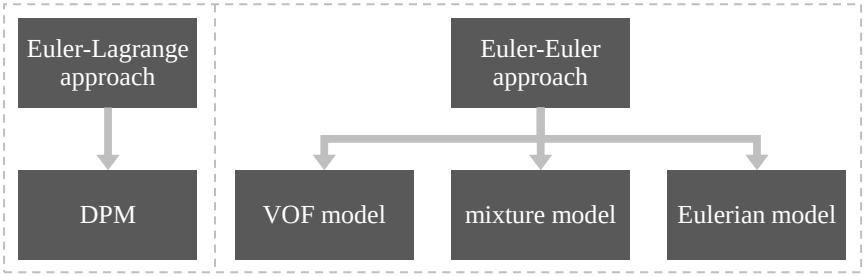

Figure 4.13: Two approaches for the numerical calculation of multiphase flows in ANSYS Fluent. For the Euler-Lagrange approach a discrete phase model (DPM) for the disperse Lagrange phase is available and for the Euler-Euler approach the volume of fluid (VOF), mixture and Eularian model can be chosen.

Even though, there are various two-phase systems the main focus in this thesis will be on gas-liquid bubbly flow. This excludes volume of fluid (VOF) simulations, which are often used for free-surface flows. Commercial computational fluid dynamic tools such as ANSYS Fluent offer besides the VOF model, simple mixture, Eulerian and discrete phase models (DPM). The mixture model solves only one momentum equation for n phases while the Eulerian multiphase model solves N momentum equations for n phases, which requires for the latter more computing power. They also address the

interaction between the phases differently. While the mixture model uses a simple algebraic relationship, the Eulerian multiphase model incorporates source terms which contain, for example, a drag function of usually empirical nature.

As the following chapter points out, forces such as the drag force are important for realistic bubble column calculations which limit the available models to Eulerian and DPM. In respect to the specific interfacial area (see chapter 2.4.1) and therefore volumetric mass transfer rate, the Eulerian model allows to solve bubble sizes as distributions and the Lagrange approach can solve each bubble individually. However, to apply the DPM formulation, the discrete phase, here gas phase, must be present at a rather low volume fraction with usually less than 10-12%. Since gas volume fractions up to 30% are to be expected, the Eulerian multiphase approach is used.

4.4.3 Forces acting on a bubble

As introduced in chapter 2.4.2, a critical variable is the specific interfacial area a. The more and smaller the bubbles the higher the effective surface and therefore desired mass transfer from gas to liquid. For this reason, bubble breakage and coalescence are the most important bubble effects, dictating this value. Both effects are not completely understood and various models are available on this subject. Nevertheless, bubbles not only coalesce and break but can also change their shape or move according to different forces acting on them.

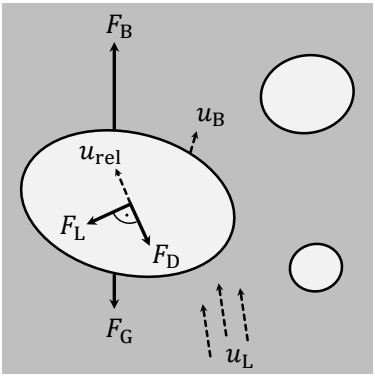

Figure 4.14: Forces acting on a bubble. The relative velocity u_{rel} is the difference between bubble velocity u_B and liquid velocity u_L. In opposite to the relative velocity is the drag force F_D which is orthogonal to the lift force F_L.

One of these forces is the drag force F_D acting opposite to the relative bubble motion u_{rel}, which is also graphically shown in Figure 4.14. The lift force F_L acts perpendicularly to this fluid resistance. Together, they build the total hydrodynamic force. Both forces depend strongly on the form of the bubble. The drag and lift coefficient are also values which need to be modelled.

To classify the bubble from, three dimensionless numbers have to be introduced. The bubbles Reynolds number Re, giving the ratio between inertia and viscosity force (equation (4.49)), then the Eötvös number Eo, describing the ratio of buoyancy to surface tension (equation (4.50)), and the Morton number Mo, which characterises the properties of the two phases (equation (4.51)):

$$\mathrm{Re} = \frac{\rho_L v_T d_B}{\eta} \tag{4.49}$$

$$\mathrm{Eo} = \frac{g\left(\rho_L - \rho_G\right) d_B^2}{\sigma} \tag{4.50}$$

$$\mathrm{Mo} = \frac{g\eta^4\left(\rho_L - \rho_G\right)}{\rho_L^2 \sigma^3}. \tag{4.51}$$

Of importance are the gravitational acceleration g, characteristic length or in this case bubble diameter d_B, surface tension σ, density of liquid ρ_L and gas phase ρ_G, velocity of the fluid with respect to the object, here terminal velocity v_T and dynamic viscosity of the fluid η. With various experiments, correlations between all three dimensionless numbers have been derived in respect to their bubble shape, which is shown in Figure 4.15.

In general, for low Reynolds and Eötvös numbers spherical bubbles can be assumed. While higher Reynolds and Eötvös numbers show ellipsoidal and wobbling shapes, low Reynolds and high Eötvös numbers have skirted and dimpled bubble shapes. Spherical-caps are formed when both Reynolds and Eötvös numbers are very high. As the equations indicate, the Morton number only depends on material properties and does not vary as much as equation (4.49) and (4.50). In bioreactors, bubble diameter and terminal velocity vary with a wider range affecting both Reynolds and Eötvös number.

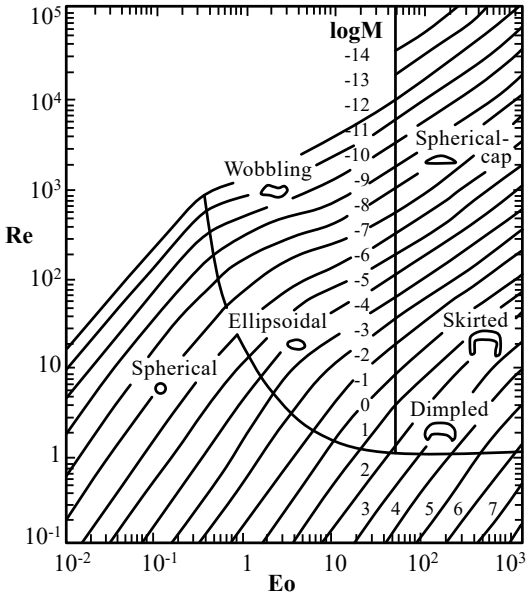

Figure 4.15: Graphical correlation between dimensionless numbers and bubble shape (derived from Grace, 1973). Reynolds number Re, Eötvös number Eo and Morton number Mo determine the bubble shape in liquid flow.

To get back to the point, the specific interfacial area a also shifts according to the bubble shape because the surface to volume ratio changes. All in all, drag and lift force are very important, especially in unstirred systems such as bubble columns.

4.4.4 Pseudo-stationary gas gradient

As mentioned before, the occurrence of substrate gradients is inevitable in process scale-up (Enfors et al., 2001). These gradients can be modelled to locate process inefficiencies and possible heterogeneity formations to finally guide design changes and reduce performance losses in up-scaling (Kuschel et al., 2017; Haringa et al., 2016; Haringa et al., 2018a). While gradients for highly soluble substrates like glucose can easily be simulated in a single phase CFD approach, gases as substrate require more complex and computationally expensive multiphase approaches (see also chapter 4.4.2).

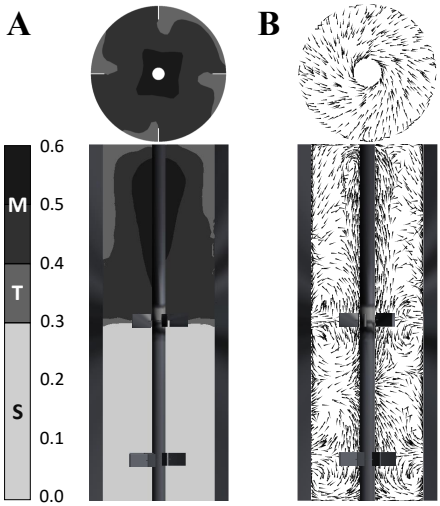

Figure 4.16: Pseudostationary glucose gradient of an industrial fed batch fermentation (derived from Kuschel et al., 2017). The averaged substrate gradient is colour by regime classifications (standard S, transient T and multifork M) which were set according to the replication strategy of *Pseudomonas putida* (A). Additionally, the averaged flow field is shown in (B). The stirred tank reactor had four baffles and a stirrer with two Rushton agitators installed. Aeration, gas transfer, and oxygen uptake were neglected. (Reprinted and modified from Kuschel et al., 2017, with permission of © MDPI Bioengineering.)

In Figure 4.16 an exemplary glucose gradient is depicted as the corresponding flow field (Kuschel et al., 2017). It is a pseudo-stationary substrate gradient in a stirred tank reactor. The gradient is simulated by setting a constant mass flow at the top of the reactor as feed and in each numerical cell a sink term as glucose uptake rate. However, aeration, gas transfer, and oxygen uptake, are neglected in this case. Pseudo-stationary gradient means that only a time point respectively 'snap-shot' of a real large-scale simulation is chosen with a temporary constant biomass concentration. No cell multiplication is considered. This assumption can be made since mixing and mass flow (feed) are much smaller than time scales for bacterial growth.

The procedure is similar to simulating a gas gradient. However, the feed source would be the gas liquid mass transfer mentioned in chapter 2.4.1 and 2.4.2. In order to simulate realistic gas to liquid mass transfers, a valid two-phase approach should be chosen as well as important bubble effects such as breakage and coalescence enabled. As examined in chapter 4.4.2 and 2.4.1, an Euler-Euler approach is advisable combined with a population balance

model (PBM). The latter allows the modelling of bubble size distributions (BSD) caused by bubble expansion due to hydrostatic pressure, breakage and coalescence. As mentioned in chapter 2.4.1, the BSD has a great effect on the specific interfacial area a and therefore the overall mass transfer. The impact on the gas transfer can be pictured by looking at the change in the surface size with increasing depth. This correlates with the rising interfacial area concentration at the gas side as well as the resulting mass transfer. Figure 4.17 shows these effects for three different bubble diameters. The greater the bubble the more significant is the impact of hydrostatic pressure. Smaller bubbles with a diameter of for example 2.5 mm seem not to be affected by rising pressure while the mass transfer of bubbles with large diameters are strongly influenced by hydrostatic pressure.

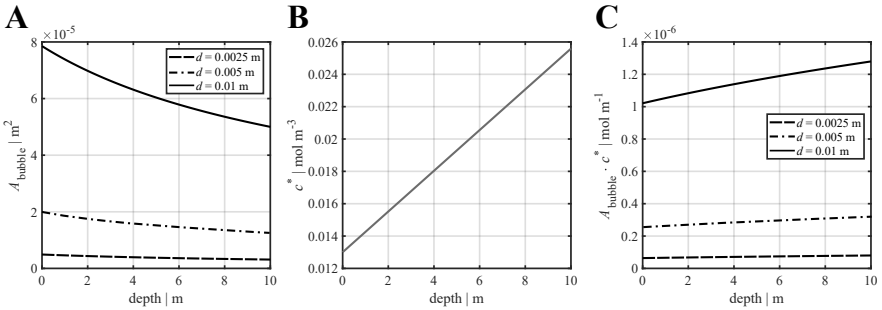

Figure 4.17: Effects on mass transfer by increasing hydrostatic pressure. For three diameters of spherical bubbles the bubble surface (A), interfacial concentration (B) and mass transfer correlation (C) are plotted over the depth of water.

For breakage and coalescence several models are available, which are more or less applicable depending on their scope. Since these are only modelled dimensions, they serve only as approximations. Often cited and applied models are derived from Luo (1993) and Luo and Svendsen (1996), but there are many more. Usually, they strongly depend on the energy dissipation, which is also modelled by the k-ε-model (see chapter 4.4.1). Nevertheless, they give a adequate prediction of a possible large-scale gas gradients, which is more accurate than assuming no breakage and coalescence at all.

4.4.5 Lagrange trajectories as bacterial lifelines

Gradients impact the microbial activity as they impose fluctuating concentration in the cell environment. One way to investigate this issue is the bacterial

'lifeline'-analysis. First introduced by Lapin et al. (2004), this method has gained momentum in numerous continuing works (Haringa et al., 2016; Kuschel et al., 2017; Haringa et al., 2018a; Siebler et al., 2019). Besides the Euler-Euler phases a third phase, the bacteria phase is introduced as massless Lagrange particles. The Euler-Euler phase is not further simulated and set as 'frozen' while a statistically relevant amount of Lagrange particles representing the bacteria is tracked. The particle ID, corresponding substrate concentration and position are recorded for further analysis.

Before the statistical conclusions of the Lagrange trajectories are listed, the general principle of ergodicity is explained. If the trajectories are ergodic, a statistically relevant number of lifelines has been tracked. The average of a dynamic system is ergodic when its time average is the same as its space average or average over the probability space. In this case the bubble column can be divided into smaller volumes to check if each location of the reactor was crossed by the bacteria with the same probability. Additionally, the average continuum concentration can be compared to the average Lagrange concentration, which should also be the same. In other words, it does not matter if only one bacteria is tracked for a very long time or if millions are tracked for a short time period (at least twice the circulation time). How many massless Lagrange particles are recorded and for how long, depends on the computing power and time as well as the chosen computational fluid dynamic program.

In Figure 4.18 (A) 2,000 magnified bacteria are shown for a random time point in a 54 m^3 stirred tank reactor. They are a proportion of the 30,000 Lagrange particles originally introduced at a vertical line and coloured in shades of grey according to their ID to indicate their even distribution (Kuschel et al., 2017). To display the movement, two lifelines are depicted in Figure 4.18 (B). They are tracked for 20 s respectively the average mixing-time of the reactor. While the black lifeline is located between the two Rushton turbines, the light grey transverses the reactor from the top to the bottom stirrer.

While the glucose gradient (see Figure 4.16 (A)) gives the volume fraction of each critical substrate amount, the analysis of the Lagrange trajectories takes the flow field (see Figure 4.16 (B)) and individual bacteria movement into account (see Figure 4.18 (B)). Information about the concentration fluctuations a bacteria endures and for how long they are exposed to this critical environment can be derived. On this basis, statistical and spacial predictions of bacterial behaviour can be made to identify insufficiencies and maybe adapt the industrial set-up.

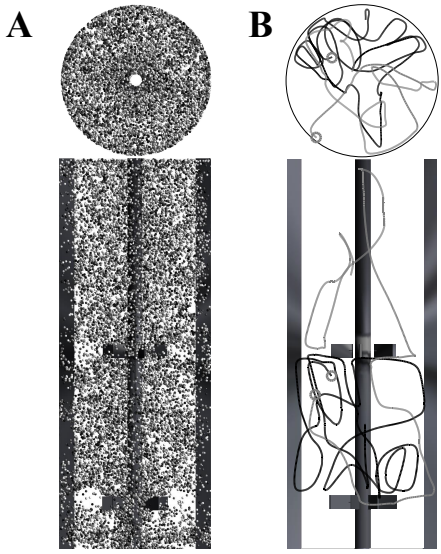

Figure 4.18: Lagrange trajectories for bacterial 'lifeline'-analysis (derived from Kuschel et al., 2017). Representative magnified bacteria particles (around 2,000) at a certain time step in (A). Examples for two bacterial lifelines are depicted in (B). Starting positions are indicated by grey circles. (Reprinted and modified from Kuschel et al., 2017, with permission of © MDPI Bioengineering.)

These kinds of *in silico* analyses need scale-down experiments or adequate mostly literature-based assumptions. Usually, critical concentrations which are linked to metabolic or transcriptional changes of the organism are needed to make reliable statements. These changes can be triggered by physical forces (e.g. shear stress), extremes in pH, oxygen, temperature, nutrient concentration and toxic compounds (Neubauer et al., 2013). Besides the fast metabolic and transcriptional responses long time adaptation to repeated exposer can occur as well (Neubauer and Junne, 2010; Löffler et al., 2016). The more biological data is available for a strain the more beneficial and faster the scale-up. As listed in Neubauer and Junne (2010), possible scale-down devices are single pulse simulators with (i) rapid sampling device after a pulse addition into the bioreactor or (ii) with a stop-flow sampling device (plug-flow) with different sampling positions which represent different incubation times. Furthermore, there are experiments with permanent changes such as (iii) oscillatory feeding or two compartment reactors with (iv) two stirred tank reactors, with (v) a simple plug-flow reactor or with (vi) a plug-flow reactor which contains static mixers which can be aerated (Neubauer

and Junne, 2010). Usually, the samples taken are examined for changes in the metabolome and the transcriptome of the organism. The gathered data give for example insight in threshold values for cell adaptation and critical exposure times as well as concentrations. Unfortunately, complex processes such as the anaerobic fermentation of *C. ljungdahlii* are only basically researched and still in the early stages of development. Nevertheless, data of other comparable strains can be used for early bioprocess development (Neubauer et al., 2013) and first *in silico* approximations or scale-up risk minimisation.

To investigate possible insufficiencies in syngas fermentations with *C. ljungdahlii* on a cellular level, the bacterial 'lifeline'-analysis with Lagrange trajectories is chosen and applied for a pseudo-stationary carbon monoxide gradient.

Chapter 5

Programs and set-up

This chapter combines all further model set-ups and is divided into four sections. The optimisation tool and setting for the kinetic correlation derived in chapter 4.3.1 is outlined directly followed by the 1-dimensional model and computational fluid dynamics set-ups. The latter is divided into the Euler-Euler settings to generate a pseudo-stationary gas gradient and the integration of Lagrange trajectories as bacterial lifelines. The settings for the statistical evaluation of such lifelines is then further explained in the final chapter. All simulations were performed on a local tower PC with the following specifications: Intel i7-5820K (six cores), 32GB RAM, NVIDIA GeForce GT 730, ASRock X99M Extreme4, Windows 7 64 Bit.

5.1 Optimisation approach for substrate kinetics

The optimisation function described in chapter 4.3.1 equation (4.4) was constrained by the element balances, lower and upper bounds for each flux and finally solved with the commercially available modelling tool MATLAB® version R2016b (file name: **fluxopt_fmincon.m**). MATLAB® offer diverse functions for optimisation. In this case `fmincon` was chosen which finds the minimum of nonlinear multivariable function. As optimisation algorithm `sqp` for sequential quadratic programming was set. As indicated in Figure 4.5, optimisations for different possible carbon monoxide uptake rates ($0 \leq q_c \leq -40$) are solved and the c-balance checked. The results are saved as matrix **q_opt.mat** which serves as lookup table and can be interpolated with `interp1`. This is a one-dimensional interpolation function provided by MATLAB®.

5.2 1-dimensional model

All partial (PDE) and ordinary differential equations (ODE) of chapter 4.3.4 were temporally solved with the stiff ODE solver `ode15s` of MATLAB® version R2016a (file name: **main_eG.m**). A simple backward Euler method, the `BDF1` (backward differentiation formula of first order), was used with variable step size and absolute and relative tolerance of $1\,e^{-4}$. To assure that the concentrations are not smaller than zero the `ode15s` option `NonNegative` for each differential equation was enabled.

Table 5.1: 1-dimensional approach set-up for parameter study. Listed are boundary conditions, physical properties, initial values and parameter ranges of **A** to **F** also described in chapter 6.1.2.

	Boundary condition	**Equation**
bottom	Robin boundary for liquid phase	(4.38)
	constant gas feed	(4.36)
top	Robin boundary for liquid phase	(4.38)
	zero slope for gas phase	(4.36)
	Physical properties	**Unit**
column diameter D_R	2.5	m
column height H_R	25	m
media surface tension σ_L	0.072	$N\,m^{-1}$
liquid phase dispersion coefficient $\mathcal{D}_L$	4.5	$m^2\,h^{-1}$
ambient pressure H_{CO}^{cp}	$7.73\,e^{-4}$	$mol\,L^{-1}\,atm^{-1}$
media density ρ_L	1,000	$kg\,m^{-3}$
gas density ρ_G	1.1	$kg\,m^{-3}$
temperature T	310.15	K
ambient pressure P	$1.01325\,e^{-5}$	Pa
	Initial values	**Unit**
liquid phase velocity u_L	50	$m\,h^{-1}$
dilution rate D	0.055	h^{-1}
biomass concentration $c_X(t_0)$	0.1	$g\,L^{-1}$
product concentration $c_k(t_0)$	0.0	$g\,L^{-1}$
initial gas $c_{G,m}\varepsilon_G\,(t_0, z)$ and liquid concentration $c_{L,m}\varepsilon_L\,(t_0, z)$	by hydrostatic pressure gradient described in equation (4.37)	$mmol\,L^{-1}$
	Variable parameters	**Reference**
CO gas fraction y_{CO}	$0 \leq y_{CO} \leq 0.9$	**A**
different gassing rates v_S	$0.004 \leq v_S \leq 0.063\,m\,s^{-1}$	**B**
initial k_La	$40 \leq k_La \leq 180\,h^{-1}$	**C**
	$100 \leq k_La \leq 425\,h^{-1}$	**F**
initial gas holdup (k_La = const)	$0.02 \leq \varepsilon_{G,0} \leq 0.19$	**D**
initial gas holdup (variable k_La)	$0.02 \leq \varepsilon_{G,0} \leq 0.19$	**E**

The code for the spatial discretisation of the PDEs can be found in

DRHS_eG.m and the production rate interpolation mentioned in the previous chapter in **RHS_eG.m**. Since diffusion limitation occurs as described in chapter 4.3.2, a modified version of the latter function can be found in **RHS_eG_diff.m**. The final results are plotted with the plotting function also embedded in the main file (file name: **plotting.m**). About 120 different start parameters were simulated and their steady state results compared with the Microsoft Office program EXCEL (file name: **variations_steady_state_fixC.xlsx**).

Table 5.1 summarises the general 1-dimensional approach set-up as well as parameter variations. The sensitivity of this model was analysed in EXCEL (file name: **sensitivity_analsysis.xlsx**), too. Variations in total production biomass yields, carbon fixation, bubble number density, overall gas holdup, mass transfer and mean bubble diameter were compared. Each value was normalised to the overall maximum (1) and minimum (-1).

5.3 Computational fluid dynamics

This chapter is based on Siebler et al. (2019) and recited with the permission of © Elsevier Chemical Engineering Science.

The multiphase approach was conducted by an Euler-Euler simulation and solved with the commercial computational fluid dynamics (CFD) program ANSYS Fluent 18.0. The reactor volume of 125 m^3 was discretised into 125,000 numerical cells. By solving the Reynolds-averaged Navier-Stokes equations (RANS) combined with the RNG (Re-Normalization Group) k-ε-model the gas gradient was approximated. ANSYS Fluent states that the RNG model is the most suitable turbulence model for bubble column simulation. All simulations were calculated on four cores with double precision. The flow field in a bubble column is only developed when liquid and dispersed phase are coupled and a bubbly flow is reproduced. Coupling is achieved through the pressure and interphase exchange coefficients set by the chosen phase interaction correlations. The ideal gas law was applied. All other settings are listed in Table 5.2.

The flow equations were solved every 10 ms and the maximum iterations per time step were set to 25. However, only ten or less iterations per time step were needed. The gas holdup was tracked via the simple output file **UDF_Execute1.c** which was execute at the end of each time step. After 1,000 s a constant gas holdup was reached which corresponds to approximately 10 simulation days. Likewise, the mass balance of gas in- and outflow converged in a steady state and the second modelling set-up was started.

Table 5.2: Computational fluid dynamics simulation set-up for pseudo-stationary gas gradient. Listed are boundary conditions, physical properties, phase set-up and solution methods. Details on the mesh can be found in chapter 6.2.1. (Reprinted from Siebler et al., 2019, with permission of © Elsevier Chemical Engineering Science.)

	Boundary condition	**Unit**
inlet	velocity inlet with 0.0625 m s^{-1} ($\varepsilon_G = 1$)	m s^{-1}
outlet	degassing	
wall	non-slip conditions	
initial	bubble size 4	mm
	Physical properties	**Unit**
column diameter D_R	2.5	m
column height H_R	25	m
media viscosity η_L	0.001	Pa s^{-1}
media surface tension σ_L	0.072	N m^{-1}
media density ρ_L	1,000	kg m^{-3}
gas density ρ_G	1.1	kg m^{-3}
temperature T	310.15	K
CO/N_2 composition	55/45	vol-%
	Models and phase set-up	**Reference**
multiphase	Euler-Euler (implicit)	
population balance model	discrete with 16 bins and a diameter range of $0.001 \leq d_B \leq 0.032$ m	
turbulence	RNG k-ε-model + differential viscosity model	
phase interactions	drag	Grace drag force or universal drag law (Clift et al., 1978)
	lift	Tomiyama et al. (2002)
	wall Lubrication	Antal et al. (1991)
	turbulent Dispersion (cd = 0.8)	Burns et al. (2004)
	turbulent Interaction	Sato and Sekoguchi (1975)
	surface tension coefficient	specified
	Solution methods	
pressure-velocity coupling	phase coupled SIMPLE	
spatial discretisation	gradient	least square cell based
	momentum	QUICK
	volume fraction	QUICK
	turbulent kinetic energy	first order upwind
	turbulent dissipation rate	first order upwind
	phase 1 (liquid) and 2 (gas) species	first order upwind
	phase 2 bin	first order upwind
transient formulation	bounded second order implicit	
under-relaxation factors	between 0.3 and 1 (mostly default)	
transient regime	time step size	0.01 s
	iterations per time step	maximum 25 (usually >10)
simulation time	flow field	1,000 s
	gradient	500 s
	Lagrange trajectories	500 s

The computational fluid dynamics mesh of the 125 m^3 bubble column

reactor was also generated with the commercial program ANSYS Fluent 18.0. Therefore, the reactor was divided into three parts: the inner rectangular section with uniform grid cells, the outer cylinder cut with inflating grid cells as well as the area in-between both geometries. Mainly rectangular grid cells are generated giving a good minimal orthogonal quality of 0.66 and maximum aspect ratio of 4.1. All in all, about 125,000 numerical cells are used for the simulation (approx. 1,000 per $1\,m^3$).

Simulations with higher spatial resolution (250,000 and 1,000,000 numerical cells) and the same set-up repeatedly revealed severe numerical instabilities. Solving Euler-Euler multiphase combined with population balance model turned out to be not only computationally intensive but also very sensitive with respect to the multiphase interactions per cell. Poor approximations of the flow dynamics in a single cell turned out to be easily propagated (and amplified) to other cells finally causing cessation of the whole simulation. Nevertheless, this set-up ensured that global parameters such as gas holdup are within the expected range of heterogeneous churn-turbulent bubbly flows (Krishna and Sie, 2000). Besides, satisfying flow fields and gas gradients were achieved giving a first glimpse on their effect on bacterial movements and lifelines.

In general, it should be stated that the k-ε-model represents a promising, commonly applied approach for estimating turbulent flow. However, because of its basic nature, non-accuracies of turbulence predictions may propagate further, e.g. affecting bubble breakage when applying the Luo models (Luo, 1993; Luo and Svendsen, 1996). Furthermore, Haringa et al. (2018b) indicated that 1st order upwind has the tendency of under-estimating turbulence quantities which may further affect the discrepancy between e.g. power input estimations using superficial gas velocity measurements and k-ε-derived predictions.

5.3.1 Pseudo-stationary gas gradient

This chapter is based on Siebler et al. (2019) and recited with the permission of © Elsevier Chemical Engineering Science. Modifications have been made to relate to the attached simulation scripts indicated in bold letters.

The next step to reach a pseudo-stationary gas gradient is to include breakage, coalescence and bubble expansion. Therefore, different bubble sizes were introduced by the population balance model (PBM) also available in ANSYS Fluent 18.0. All in all, 16 bubble classes with a diameter range of $0.001\,m \leq d_B \leq 0.032\,m$ were chosen and for both - breakage and

coalescence - the Luo-model (Luo, 1993; Luo and Svendsen, 1996) was applied. In addition, two user defined functions (UDF) for mass transfer (file name: **UDF_Mass_Transfer.c**) and the dissolved carbon monoxide uptake (file name: **UDF_Reaction.c**) were included. For the simulation of mass transfer from gas to liquid phase in non-agitated bubble column reactors, the conform Higbie correlation (see also chapter 2.4.2 equation (2.12)) for the mass transfer rate k_L was chosen and solved in each numerical cell (Higbie, 1935). Instead of the bubble diameter d_B the Sauter mean bubble diameter d_{32} was used, a diffusion coefficient of CO $\mathcal{D}_{CO} = 2\,e^{-9}\,m^2\,s^{-1}$ and relative bubble velocity v_{rel} (respectively terminal velocity v_T) of the numerical cell. While the Sauter mean bubble diameter is applied, the effects of PBM bubble distribution is neglected in this case. Henry's law was used to estimate solubility with the coefficient $H^{cp}_{CO} = 7.7\,e^{-4}\,mol\,L^{-1}\,atm^{-1}$. The pressure gradient was also accounted for in this UDF (**UDF_Mass_Transfer.c**), giving the equilibrium concentration of carbon monoxide $c^*_{L,CO}$. The interfacial area concentration a is calculated assuming a spherical bubble shape which finally leads to the expression

$$\dot{m}_{GL} = k_L \left(c^*_{L,CO} - c_{L,CO}\right) \frac{6\varepsilon_G}{d_{32}} \tag{5.1}$$

for the mass transfer $\dot{m}_{GL}$ solved at each time step in each discretisation volume.

The Higbie correlation for the mass transfer and spherical bubble shapes are rough simplifications. The reader must be aware that dimensionless numbers for the bubbles, such as Eötvös ($\approx$ 60), Morton (log(Mo) = -10) and Reynolds number ($\approx$ 5,000) rather pinpoint to transient wobbling to spherical cap geometries (see chapter 4.4.3 equations (4.49) - (4.51) and Figure 4.15). Additionally, gas holdup and superficial gas velocity also indicate transition between homogeneous bubbly flow to heterogeneous churn-turbulent flow (see chapter 4.1 Figure 4.2 and 4.3). Nevertheless, the Higbie correlation was used, not only for the sake of simplicity but also because profound mass transfer studies with the said biological matrix would have been needed which are far beyond the scope of this lifeline analysis.

The reaction UDF (**UDF_Reaction.c**) was written to describe the CO uptake kinetic q_c of *C. ljungdahlii* described in equation (4.8) in chapter 4.3.2 (Investigation of diffusion limitation). The dissolved carbon monoxide uptake takes place in each numerical cell at each time step. After another 500 s a new steady state for the gas hold-up and dissolved CO concentration was reached which does not account for the constantly changing periodic flow

field (tracked via **UDF_Execute2.c**). Pseudo-stationary gradient means that only a time point respectively 'snap-shot' of a real large scale simulation is chosen with a temporary constant biomass concentration of $10\,g\,L^{-1}$ and no cell multiplication. This assumption can be made since mixing and mass transfer time scales are much smaller than time scales for bacterial growth. The second simulation part lasted more than ten simulation days since 16 bubble classes instead of one, breakage, coalescence, bubble expansion, mass transfer and a reaction needed to be solved as well. Detailed changes in the volumetric mass transfer rate after 1,000 s and 1,500 s can be found in the Appendix of Manuscript II (Siebler et al., 2019).

5.3.2 Lagrange trajectories

This chapter is based on Siebler et al. (2019) and recited with the permission of © Elsevier Chemical Engineering Science. Modifications have been made to relate to the attached simulation scripts indicated in bold letters.

The final CFD simulation uses the generated pseudo-stationary gas gradient and flow field to analyse cell lifelines, movement patterns and circulation time. Beside the Euler-Euler phases, a third phase, the bacteria, were introduced as massless Lagrange particles as well as the discrete random walk (DRW) model was enabled. The DRW model was used to superimpose turbulent motions on the convective velocity (Haringa et al., 2016). The gradient and flow field were set as frozen and not further calculated. With another user defined function every 30 ms, the particle ID, the corresponding CO concentration and position were recorded (file name: **UDF_Execute_Bacteria.c**). In total, 120,000 bacteria were tracked for 500 s. More precisely, four simulations were started with 30,000 mass less Lagrange particles to speed the simulations process up. The trajectories were checked for ergodicity (see chapter 4.4.5). The results can be found in chapter 6.2.3. Further evaluations of the lifelines were conducted with the program MATLAB®.

5.4 Statistical evaluation of Lagrange trajectories

About 70,000 (**teilchen_bacteria_*.txt**) files are generated by ANSYS Fluent described in the previous chapter. These files need to be loaded and processed. MATLAB® version R2016b offers big data functions such as `datastore` which reads the files and creates a datastore for the accumulated information too large to fit in memory (file name: **cs_read_tex_files_cs.m**). With this script, a rearranged and sorted matrix **cs_all_*.mat** is generated,

which is in this case 30,000 particle IDs long and 16,670 time steps wide. The statistical relevance can be checked by the **quality_evaluation.m** script (see also chapter 6.2.3. How the **cs_all_*.mat** matrices can be further analysed is described in the following chapters.

5.4.1 Evaluation of regime transition events

This chapter is based on Siebler et al. (2019) and slightly modified to relate to the attached simulation scripts indicated in bold letters.

For the evaluation of the regime transition events (see chapter 4.4.5 and 6.2.3) the **evaluation_script_main.m** script is needed with the sub-functions **move_av.m**, **kinetic.m**, **sort_reg.m** and **reg_class.m**.

As described in Kuschel et al. (2017), the moving-average filter was applied to erase unrealistic, turbulent fluctuations caused by the standard discrete random walk (DRW) model. With the **kinetic.m** function the CO concentration is directly translated into CO uptake rate (see equation (4.8) in chapter 4.3.2) and then sorted with **sort_reg.m** according to the resulting product biomass yield (see equation (6.4) in chapter 6.2.2). Finally, the regime transition events and their duration time are counted with the **reg_class.m** function and saved as **Sim*.mat**. With **evaluation_tau_main.m** and **plot_tau.m** all four **Sim1.mat-Sim4.mat** are collected and plotted. Additionally, total frequency of the six regime transition events, average and maximum retention times are calculated, too (results are shown in Figure 6.18 and Table 6.1 in chapter 6.2.4).

5.4.2 Evaluation of short- and long-term responses

This chapter is based on Siebler et al. (2019) and recited with the permission of © Elsevier Chemical Engineering Science.

With the **short_long_term.m** script short- and long-term responses can be investigated (see Figure 6.19 and 6.20 in chapter 6.2.5). The concentration profiles $c_{\mathrm{L,CO}}(t)$ of the bacterial lifelines were processed according to the Nassi-Shneiderman diagram in Figure 5.1 for each critical time periods $\tau^{\mathrm{crit}} = 10\,\mathrm{s}$, $\tau^{\mathrm{crit}} = 40\,\mathrm{s}$ and $\tau^{\mathrm{crit}} = 70\,\mathrm{s}$.

If both thresholds, $c^{\mathrm{crit}}_{\mathrm{L,CO}}$ and τ^{crit}, are true, the average concentration respectively uptake rate (see equation (4.8) in chapter 4.3.2) of the real time period is calculated. Mean concentration and retention time are saved in two arrays $c^{\mathrm{vec}}_{\mathrm{L,CO}}$ and Δt^{vec}. For each critical time period the resulting arrays were clustered into histograms with 100 bins and normalized to the highest total

percentage of the average occurrence ($\tau^{\mathrm{crit}} = 10\,\mathrm{s}$). To take the actual duration of each average concentration respectively uptake rate into account, histograms with weighted distribution (weighting factor $\alpha_{\tau i} = \Delta t_i^{\mathrm{vec}} / \sum \Delta t^{\mathrm{vec}}$) are also visualised (see Figure 6.19 in chapter 6.2.5).

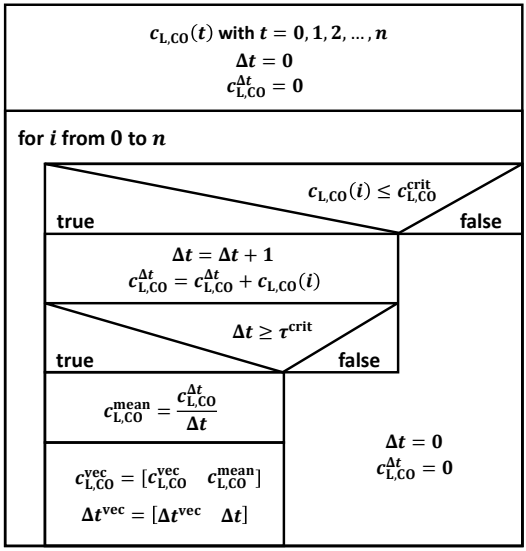

Figure 5.1: Nassi-Shneiderman diagram of short- and long-term response evaluation. For three critical periods $\tau^{\mathrm{crit}} = 10\,\mathrm{s}$, $\tau^{\mathrm{crit}} = 40\,\mathrm{s}$ and $\tau^{\mathrm{crit}} = 70\,\mathrm{s}$ the evaluation of the concentration profiles $c_{\mathrm{L,CO}}(t)$ was performed. As a result, the averaged concentrations $c_{\mathrm{L,CO}}^{\mathrm{mean}}$ and corresponding time periods Δt are summarised in two arrays $c_{\mathrm{L,CO}}^{\mathrm{vec}}$ and Δt^{vec}. (Reprinted from Siebler et al., 2019, with permission of © Elsevier Chemical Engineering Science.)

Chapter 6

Modelling results and discussion

6.1 1-dimensional approach

The 1-dimensional (1D) approach was performed to get a feeling about the behaviour of gas fermentation in a large scale bubble column reactor. Due to its simplicity, most parameter have to be set in advance. These parameters should be chosen carefully and according to values in published literature which is done in the first part of this section. Mesh study, steady state results, sensitivity investigations and final simulation set-up is also shown.

Most of the results mentioned in chapter 6.1 are published in Siebler et al. (2020). The following sub-chapters are either a summary or contain more detailed unpublished results. The structure deviates from Siebler et al. (2020) and all recited pictures, listings and tables are stated as such.

6.1.1 Mesh refinement study

In order to get reasonable and sufficient flow results, the spatial discretisation respectively the mesh has to be fine enough but not too highly resolved. The finer the discretisation the more time consuming but accurate the flow prediction. There are several ways to verify the mesh quality. In any case, the mass needs to be conserved. The numerical approximation not always reaches the true physical value. However, the error should be negligible small (at least smaller than 5%).

The mass balances for different spatial discretisations with compartment slices N between 3 and 200 steps were monitored. As described in chapter 4.3.2, equations (4.28), (4.29) and (4.31) were solved for each refinement.

In Figure 6.1 the results for four spatial discretisation steps (N = 10, 20, 100 and 200) are shown.

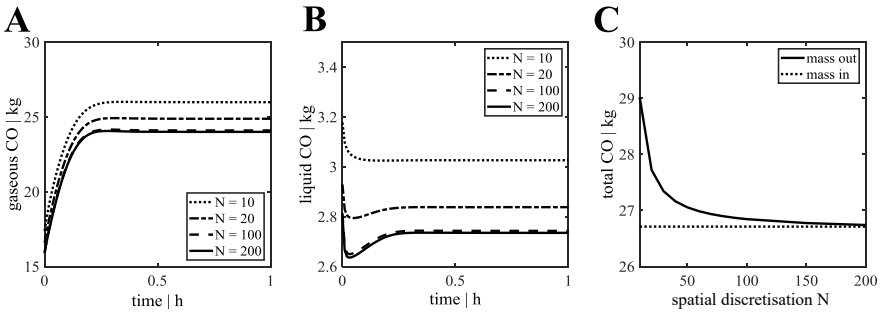

Figure 6.1: Compartment refinement study. In (A) and (B) the gaseous and dissolved (liquid) mass of CO over times is shown. Exemplary, four discretisation steps are depicted N = 10, 20, 100 and 200. In (C) the relation between total CO leaving and entering the column is illustrated revealing that N = 100 closes the mass balance with less than 5% gap. (Reprinted from Siebler et al., 2020, with permission of © Wiley-VICH Engineering in Life Science.)

In Figure 6.1 (C) it can be seen that the mass balance for the chosen discretisation steps does not completely close. Nevertheless, results for $N \geq 100$ are adequate with an imbalance of even less than 3%. In respect to computational efforts, increasing N from 100 to 200 (respectively 4 min to 20 min simulation time) is not in relation to the gained accuracy, therefore all 1-dimensional simulations were performed with $N = 100$. More information on this topic can be found in Siebler et al. (2020).

6.1.2 Choosing reasonable parameter ranges

As mentioned in chapter 4.1 the initial gassing rate respectively superficial velocity, gas composition, liquid velocity, initial bubble diameter, mass transfer coefficient and initial gas holdup need to be set for the 1-dimensional approach. All these parameters strongly interact with each other (see chapter 4.1, Figure 4.1) and not all of these interrelated processes are implemented in the dynamic model. Nevertheless, key impact factors defining the performance of a biotechnological bubble column need to be specified.

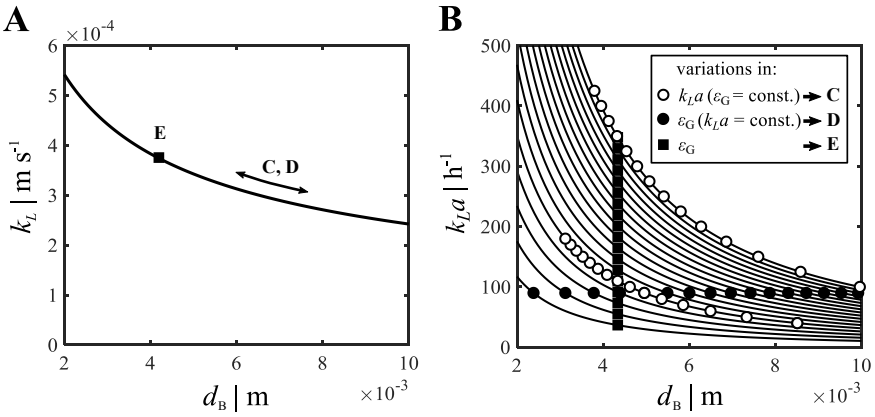

Figure 6.2: Mass transfer rate, bubble diameter and gas holdup correlation. The Higbie mass transfer rate k_L to bubble diameter d_B correlation (A) is valid in the range of $2\,e^{-3} \leq d_B \leq 10^{-3}$m when using the terminal bubble velocity $v_T = 0.23\,m\,s^{-1}$ described in Tomiyama et al. (1998). (B) According to k_La and $\varepsilon_{G,0}$ variations the initial bubble diameter $d_{B,0}$ and mass transfer coefficient k_L can be adjusted.

The well-known Higbie correlation (Higbie, 1935) is used for estimating k_L as described in chapter 2.4.2 equation (2.12) and graphically shown in Figure 6.2 (A) which is valid for bubbles larger than $2\,e^{-3}\,m$. It can be assumed that the bubble surface is always mobile and surface active materials have no influence (Heijnen and Van't Riet, 1984). According to Tomiyama et al. (1998) the steady-state uprising bubble velocity v_T can be estimated as

$$v_T = \sqrt{2}\left(\frac{\sigma g\,(\rho_L - \rho_G)}{\rho_L^2}\right)^{0.25} \tag{6.1}$$

which accounts for $2\,e^{-3} \leq d_B \leq 10\,e^{-3}\,m$ and an Eötvös number $Eo \leq 16$ (see equation (4.50) in chapter 4.4.3).

The measured surface tension σ of the cultivation medium is 0.0724 $\pm$ 0.0063 N m (identified via bubble pressure tensiometer), the medium density ρ_L is 1,000 kg m^{-3} and the air density ρ_G is 1.2 kg m^{-3}. The bubble velocity with $0.23\,m\,s^{-1}$ is calculated and very similar to the distilled water value with $v_T = 0.25\,m\,s^{-1}$ (Heijnen and Van't Riet, 1984). The interfacial

area concentration a was estimated assuming spherical bubbles:

$$a = \frac{6}{d_B}\varepsilon_G. \tag{6.2}$$

For spherical bubbles the specific surface a correlates directly with the diameter and gas holdup. Three variation scenarios can be derived from this interaction (Figure 6.2 (B)). Changes in the k_La value by adjusting $d_{B,0}$ and k_L, varying the $\varepsilon_{G,0}$ range and keeping the k_La constant by also adjusting $d_{B,0}$ and k_L and finally only adjusting $\varepsilon_{G,0}$ by keeping $d_{B,0}$ and k_L constant at an average initial k_La of $110\,h^{-1}$.

However, not only initial diameter and gas holdup need to be set in the model but also the gassing rate and gas composition. Schügerl et al. (1977) tested several liquid compositions according to their gas holdup behaviour by applying different superficial gas velocities (selection shown in Figure 6.3 (A)). Due to similar properties of the medium to water another correlation was chosen as reference (Figure 6.3, dashed lines). In the case of distilled water and a bubble diameter larger than $10\,e^{-3}$ m the following equation can be used with $v_T = 0.25\,m\,s^{-1}$ (Heijnen and Van't Riet, 1984):

$$\varepsilon_G = \frac{v_S}{v_T}. \tag{6.3}$$

By applying equation (6.3) a superficial gas velocity of $0.025\,m\,s^{-1}$ respectively 0.06 vvm equals a mean gas holdup $\overline{\varepsilon_G}$ of around 10% (Figure 6.3 (A), dashed lines). Combining the gas velocity with $\overline{k_La}$ and again consider water as reference (Figure 6.3 (C) dashed lines) a $\overline{k_La}$ of around $130\,h^{-1}$ can be assumed. This is in accordance with the interrelation by Akita and Yoshida (1973) illustrated in Figure 6.3 (C) and (D). They found for a certain bubble column diameter ($D_R > 0.08$ m) the mass transfer rate correlates linearly with the gas holdup and has always a slope of one.

While taking a closer look at Figure 6.3, a grey overlay is used to highlight the parameter ranges chosen for this study. The superficial gas velocity range is set in order to assure homogeneous bubbly flow (see chapter 4.1, Figure 4.2). However, superficial gas velocities above $0.05\,m\,s^{-1}$ reach into the transition area with different bubble behaviour. Nevertheless, this range is set to show the limits of this simple model compared with the more detailed computational fluid dynamics approach.

Also the gas holdup range is chosen according to literature with 30% as maximum gas holdup which can not be achieved with a pure demineralised

water system as shown in Figure 6.3 (A). On the contrary, yeast and alcohol solutions decrease the surface tension and therefore bubble diameter as well as bubble rise velocity (interaction illustrated in chapter 4.1 Figure 4.1) which results in higher gas holdups. The ethanol plot of Figure 6.3 (A) is chosen since *C. ljungdahlii* additionally produces alcohols such as ethanol and 2,3-butanediol.

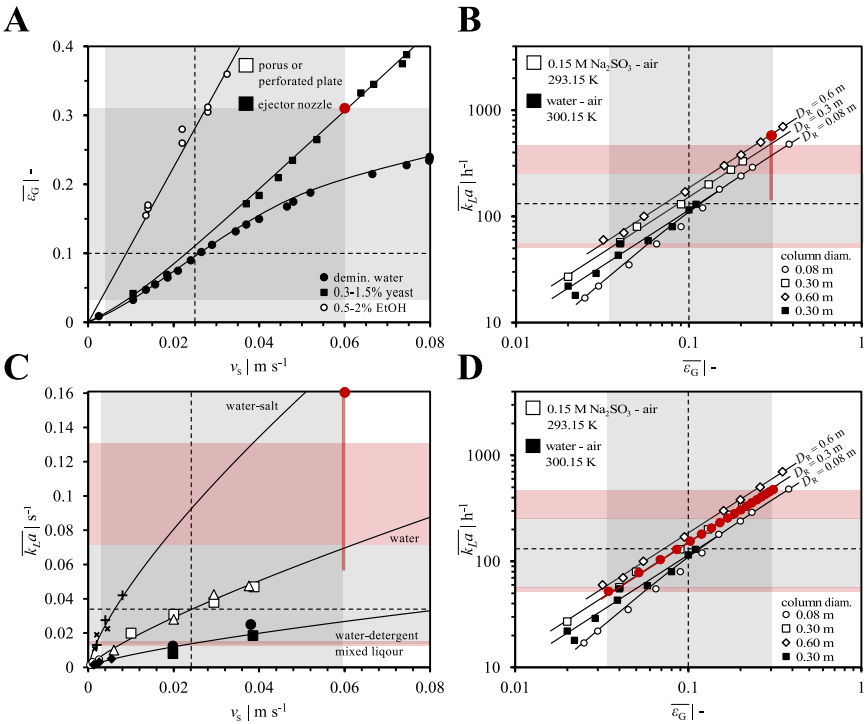

Figure 6.3: Comparing parameter variation ranges with literature. (A) Gas holdup in relation to superficial gas velocity for demineralised water, yeast solution and ethanol solution (Schügerl et al., 1977). (B) and (D) Mass transfer correlated with gas holdup for different column diameters (Akita and Yoshida, 1973). (C) Mass transfer rate over superficial gas velocity for water-slat solution, pure water and water detergent mix (Heijnen and Van't Riet, 1984). Highlighted in grey are the parameter variation areas, in red the additional k_La range due to gas holdup variations with variable mass transfer (red dots and balance line in (D)). Dashed black line indicates the first fix parameter set. Sole red dot in (A) to (C) is the final parameter set after the variation study with the red line accentuating the second k_La variation study. (Reprinted and modified from Siebler et al., 2020, with permission of © Wiley-VICH Engineering in Life Science.)

The final reference settings (Figure 6.3, dashed black line) are: $y_{CO} = 0.55$, 0.06 vvm, $\overline{\varepsilon_G} = 0.1$ ($\varepsilon_{G,0} = 0.06$) and $\overline{k_L a} = 130\,h^{-1}$ ($k_L a = 90\,h^{-1}$ with $d_{B,0} = 5\,e^{-3}$ m and $k_L = 3.4\,e^{-3}\,m\,s^{-1}$). The simulation scenarios **A** – **E** (Figure 6.3, grey highlighting) are performed using the following settings (list is recited from Siebler et al., 2020):

- **A:** Variation in CO gas fraction with $0 \leq y_{CO} \leq 0.9$
- **B:** Different gassing rates with $0.004 \leq v_S \leq 0.063\,m\,s^{-1}$ (0.01 - 0.15 vvm, $15 \leq \dot{V}_G \leq 225\,m^3\,s^{-1}$)
- **C:** Variations of $k_L a$ (ε_G = const.) with initial settings of 40 - 180 h^{-1} resulting in mean steady state values ($\overline{k_L a}$) of 60 - 250 h^{-1}
- **D:** Variation in initial gas holdup $0.02 \leq \varepsilon_{G,0} \leq 0.19$ with a fixed $k_L a$ resulting in $0.03 \leq \overline{\varepsilon_G} \leq 0.31$ (and variable d_B, see Figure 6.4 for explanation)
- **E:** Same variation as in **D** but considering variable $k_L a$ yielding equal $\overline{\varepsilon_G}$ as in **D** and constant d_B (see Figure 6.4 for explanation)
- **F:** Final parameter study with new reference set-up according to findings in **A** to **E**: $y_{CO} = 0.55$, 0.15 vvm and $\overline{\varepsilon_G} = 0.31$ ($\varepsilon_{G,0} = 0.19$). initial $k_L a$ settings ranged from 100 h^{-1} to 425 h^{-1} finally reaching mean steady state $\overline{k_L a}$ between 140 h^{-1} to 580 h^{-1}

For the final parameter study **F**, the reference setting is adjusted according to the results of **A** – **E**, which will be described in chapter 6.1.5 in detail. As the previous Figure 6.2, Figure 6.4 helps to understand how variations **D** and **E** affect different parameters and why a differentiation for the gas holdup variation was made in the first place.

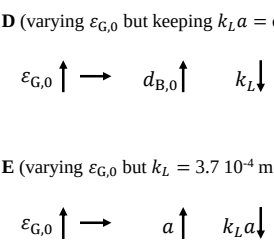

Figure 6.4: Analysing the impact of gas holdup on simulation performance. **D**: Yielding to keep constant $k_L a$ while increasing gas holdup $\varepsilon_{G,0}$ leads to increasing bubble diameters and lowering k_L values. **E**: Increasing gas holdup $\varepsilon_{G,0}$ with constant k_L and d_B immediately increases $a = 6\varepsilon_G/d_B$ proportionally which leads to increasing $k_L a$ values. (Reprinted from Siebler et al., 2020, with permission of © Wiley-VICH Engineering in Life Science.)

The gas fraction variation range is chosen according to Clarke Energy® (2018) syngas composition as described in chapter 2.1 and the laboratory gas mixture with y_{CO} of 0.55 (also reference value). For the final parameter study **F** the CO fraction is not adjusted since this value is rarely exceeded. The red overlay in Figure 6.3 (B) to (D) indicates that the resulting $\overline{k_L a}$ range was wider, due to variation **E** which had a great effect on the mass transfer rate. The final $\overline{k_L a}$ values of study **E** are illustrated in Figure 6.3 (D) as red dots. As the first reference set-up is graphically displayed with black dashed lines, the final result of study **F** is marked with a red dot in Figure 6.3 (A) to (C). In addition, the last variation **F** is also indicated by the red line. With this appropriate parameter variation set-up, the simulations were performed and the results are shown in the following subsections.

Further informations on the parameter ranges can be found in Manuscript III under *3.2. Probing the parameter space*.

6.1.3 Steady state results

The 1-dimensional model solves five partial differential equations (CO and CO_2 in gas and liquid phase as well as the gas holdup) and four ordinary differential equations (see equation (4.28) and equation (4.29) in chapter 4.3.4). After 800 h a steady state is reached for all simulations.

To compare the outcome for every variation, the steady state results are shown in Figure 6.5. Each point is the result of one simulation run. Figure 6.5 (A) shows the concentrations of products and gases for different CO gas fractions, which let to a wash-out scenario when the CO share is less den 10 vol-%. In general, the higher the CO fraction the more product is produced. The soluble CO gas increases as well. The grey symbols in Figure 6.5 (A) are the results without the implementation of a liquid diffusion therm (see chapter 4.3.2). Especially in the second picture the effect is clearly visible and a diffusion limitation can be observed. For every further study the limitation therm of equation (4.26) is included.

Variations in gassing rate (Figure 6.5 (B)) show at low superficial gas velocities less CO_2 removal and therefore higher concentrations. This gas accumulation effect decreases the higher the gas throughput is. With this simulation set-up and by increasing the gassing rate even further, the product formation is relatively unaffected. In this context it should be stated that at very high superficial gas velocities the assumption of a homogeneous flow regime in a bubble column is probably not supported anymore (see chapter 4.1 Figure 4.3).

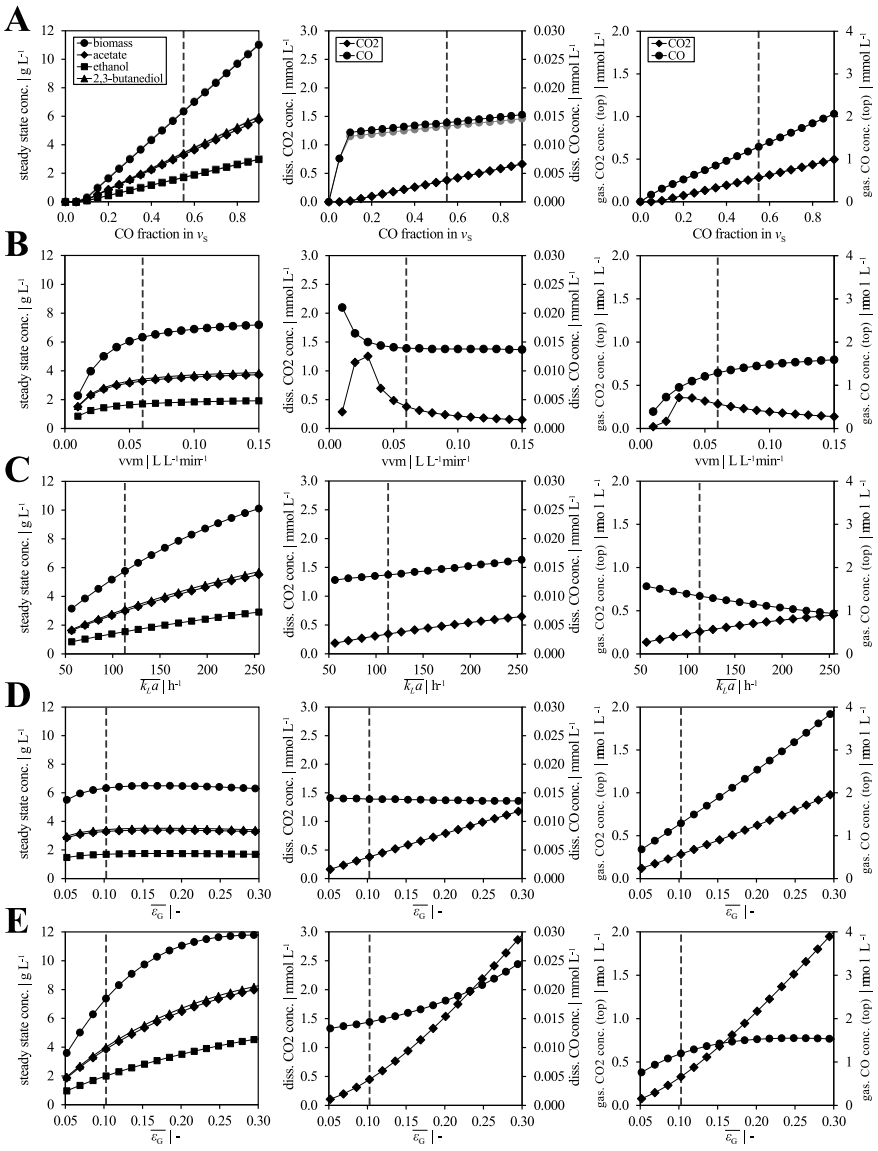

Figure 6.5: Steady state results of parameter study. Variation results are shown as follows: Variation in (A) gas composition, in (B) gassing rate, of (C) initial k_La value, of (D) initial gas holdup $\varepsilon_{G,0}$ with constant k_La value and of (E) initial gas holdup $\varepsilon_{G,0}$ with variable k_La value. Grey points in (A) are simulation results without consideration of diffusion. (Reprinted from Siebler et al., 2020, with permission of © Wiley-VICH Engineering in Life Science.)

By increasing the $k_L a$ value (Figure 6.5 (C)), production and CO consumption increases as well. The initial mass transfer value changes during the simulation. This is due to the fact that the model initialisation does not include consumption and production kinetic as well as the vertical transport (see equation (4.37) in chapter 4.3.6). The same accounts for the gas holdup and bubble diameter.

In Figure 6.5 (D) and (E) the effect and importance of mass transfer are clearly visible. The production rates are limited by the CO consumption, which in turn depends on the mass transfer. The parameter study **D** demonstrates that the gas holdup of 10% is not limiting. Only at a very small gas holdup ($\overline{\varepsilon_G} \leq 0.08$), a decline in productivity can be noted. With a fix $k_L = 3.7\,\mathrm{e}^{-4}\,\mathrm{m\,s}^{-1}$ and $d_{B,0} = 4.3\,\mathrm{e}^{-3}\,\mathrm{m}$ as in **E**, the gas holdup has a much greater impact on the steady state result because it affects directly the specific bubble surface a and therefore the $\overline{k_L a}$ value. Although the product formation stays almost constant, the CO_2 concentration increases. More gas is hold up respectively dissolved in the bubble column. The gas amount increases linearly with the increasing $\overline{\varepsilon_G}$. The superficial gas velocity v_S is directly affected by changes in $\overline{\varepsilon_G}$ (see chapter 4.3.4, $v_S = v_{G,slip}\varepsilon_G$) as well. It seems the product concentration reaches a plateau even though the dissolved CO concentration increases. The reason for this can be found in the uptake kinetic of Mohammadi et al. (2014) and the set dilution rate of $D = 0.055\,\mathrm{h}^{-1}$.

All in all, the steady state concentration results provide information about the model behaviour. However, there are better ways to show the sensitivity of this model and the impact of the parameter variations, which can be found in the next subsections.

6.1.4 Sensitivity and impact of parameter variations

To show the sensitivity of certain parameter changes on the model, radar charts have been chosen. Figure 6.6 illustrates the observed sensitivities of the simulation scenarios **A** to **E** (see declaration in chapter 6.1.2, p. 86) focussing on the readouts: mean gas holdup $\overline{\varepsilon_G}$, final $\overline{k_L a}$, mean bubble diameter $\overline{d_B}$, bubble number density n_G, total carbon fixation C_{fix}(SS) and production biomass yields $Y_{P,X}$(SS). Values are normalised with respect to the maximum (1) and the minimum (-1). The black solid line indicates the baseline (0) respectively reference.

Variations in CO fraction and gassing rate (Figure 6.6 (A) and (B)) have no significant effect on gas holdup, mass transfer, mean bubble diameter and bubble number density. However, low CO fraction cause poor CO fixation

and production biomass yields. On the contrary, at high CO fractions the carbon is fixated mainly as product and biomass. Whereas, low gassing rates have high production biomass yields due to longer gas dwell times.

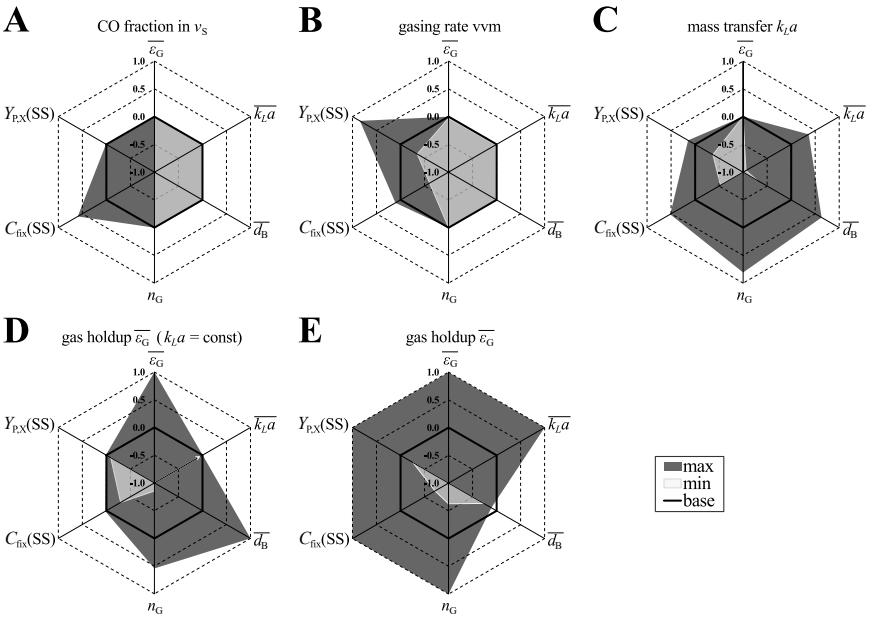

Figure 6.6: Parameter sensitivity analysis for conceptual design. The following scenarios are studied with variations of: (A) gas composition (excluding wash-out results), (B) gassing rate, of (C) initial k_La value, (D) initial gas hold-up $\varepsilon_{G,0}$ with constant k_La and (E) initial gas hold-up $\varepsilon_{G,0}$ with variable k_La. Variables with a bar indicate the average steady state value. Additionally, the steady state production biomass yields $Y_{P,X}(SS)$, total steady state carbon fixation $C_{fix}(SS)$ and bubble number density n_G are depicted. All values are normalised to the overall maximum (1) as well as minimum (-1) value to allow comparability. The black solid line indicates the first parameter set, thereby defining the baseline (0) of each radar graph. Areas of light grey (as well as small arrow in (D)) contour the set of minimum values, dark grey areas highlight maximum values. (Reprinted from Siebler et al., 2020, with permission of © Wiley-VICH Engineering in Life Science.)

The mass transfer rate (Figure 6.6 (C)) has been adjusted with different $d_{B,0}$ and k_L values. Changing the initial bubble diameter consequential changes the average bubble diameter and number density (see equation (4.32) in chapter 4.3.4 and equation (6.2) in chapter 6.1.2). Higher mass transfer rates allow higher dissolved gas concentration and therefore CO fixation. Additionally, the product biomass yield increases slightly and declines with

lower $\overline{k_L a}$ values. There is no significant effect on the mean gas holdup for the parameter variation **C**.

Figure 6.6 (D) shows the gas holdup variation with constant $\overline{k_L a}$ (indicated with an arrow). Consistent with the modification of the initial gas holdup $\varepsilon_{G,0}$ and diameter $d_{B,0}$, the average steady state gas holdup $\overline{\varepsilon_G}$ and diameter $\overline{d_B}$ vary (applies for Figure 6.6 (D) and (E)). Both parameter also affect the number density according to the correlation in equation (4.32) in chapter 4.3.4. The CO_2 production increases in **D** and **E**, which causes a drop in CO fixation.

The last variation has the greatest impact on the outcome of the model (Figure 6.6 (E)). This underlines again the importance of including the gas holdup into the systems of partial differentiated equations. Almost all parameters show maximum deviations, especially the $\overline{k_L a}$ value is affected. In this case, the mass transfer coefficient and initial diameter are constant (see also Figure 6.4). The diameter for an initial $k_L a$ of $110\,h^{-1}$ is smaller than the one of the reference state, therefore both maximum and minimum value are lower than the baseline. It should be noted that changing the specific bubble surface by adapting the initial gas holdup has a greater effect on the average mass transfer than changing k_L and $d_{B,0}$.

The sensitivity of the parameter can be used to describe the outcome of the model. However, besides the general CO fixation $C_{fix}(SS)$, it is also economically interesting how much of the carbon goes into biomass and how much into product formation. This examination is presented in chapter 6.1.5.

6.1.5 Carbon flow and final parameter set-up

The carbon flow in gas fermentations is very difficult to predict. On the basis of the CO uptake kinetic described by Mohammadi et al. (2014) and the simple kinetic correlation outlined in chapter 4.3.1 the steady state carbon share for each variation can be calculated (Figure 6.7). It is of interest how the carbon flows within a parameter variation (Figure 6.7) and in comparison with the other variations (Figure 6.8).

In Figure 6.7 all identification letters are analogue to the variation description **A** - **F** determined in chapter 6.1.2. The percentage carbon share is generally very similar. With more than 95% in each simulation, the CO is converted mainly into product (grey area) and biomass (white area). The product share is slightly higher than the biomass share and shows the highest variations in study **B**, **C** and **E**. This is also indicated with the product biomass yields $Y_{P,X}(SS)$ in the radar charts (Figure 6.6). The final parameter

study **F**, which is based on **A** - **E**, is also included and elaborated in this chapter.

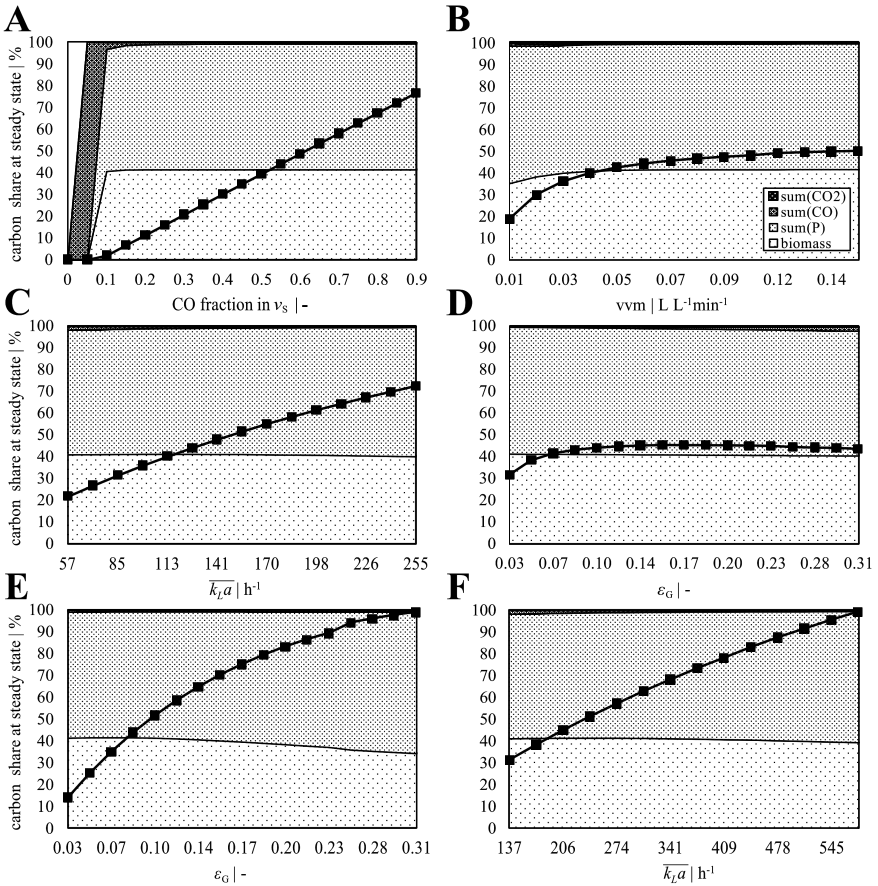

Figure 6.7: Steady state carbon share of parameter study. Variation results are shown as follows with variations in: (A) gas composition, (B) gassing rate, (C) initial k_La value, (D) initial gas holdup $\varepsilon_{G,0}$ with constant k_La value and (E) initial gas holdup $\varepsilon_{G,0}$ with variable k_La value. In (A) the first two volume fraction of CO in the gas are two low and the continuous fermentation results in a wash out scenario. The black dashed line indicates the reference, while the interconnected black squares in (A) to (E) describe the maximum CO fixation normalised to the overall maximum in (E). However, (F) is normalised to the maximum in the final k_La study.

In all three cases high dissolved CO concentrations are reached, either

due to longer dwell times as in case **B** or due to higher mass transfer rates as in **C** and **E**. High CO concentrations result in better consumption rates and according to the kinetic correlation in higher local product formation rates.

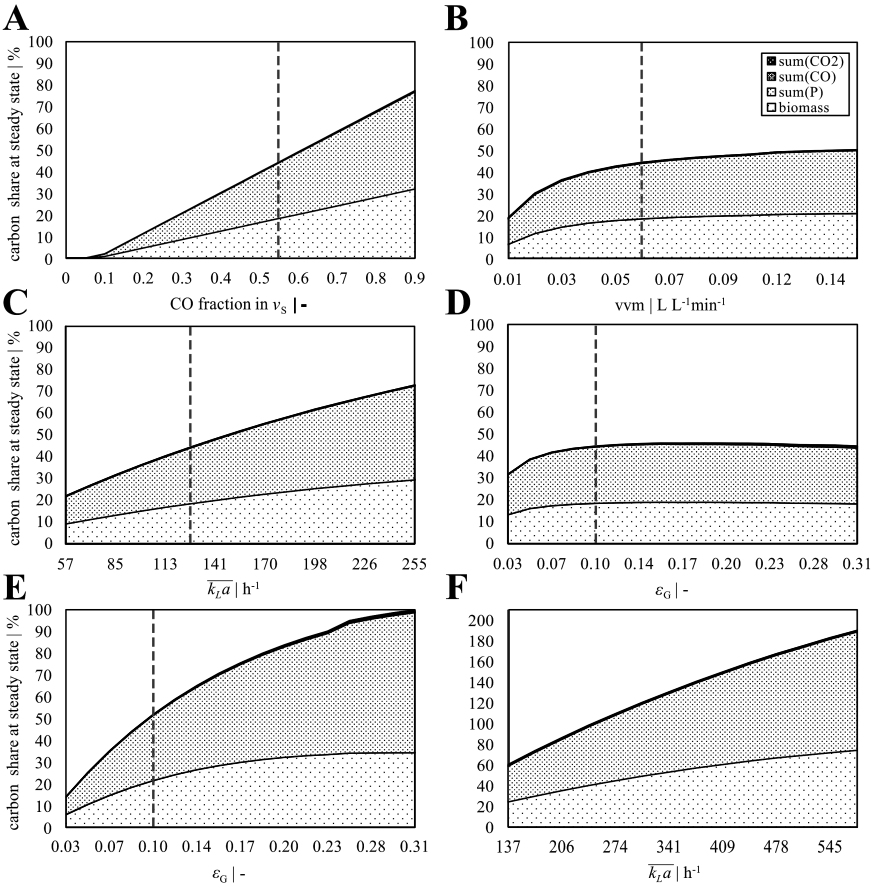

Figure 6.8: Total steady state carbon share in comparison. Variation results are shown as follows with variations in: (A) gas composition, (B) gassing rate, (C) initial k_La value, (D) initial gas holdup $\varepsilon_{G,0}$ with constant k_La value and (E) initial gas holdup $\varepsilon_{G,0}$ with variable k_La value. The black dashed line indicates the reference, while the maximum CO conversion for each parameter is normalised to the maximum in (E) of the first parameter study series **A** - **E**.

Since the dilution rate is constant at $D = 0.055\,\mathrm{h}^{-1}$, changes in carbon share respectively product formation rates can only be achieved by increasing

the CO concentration locally. In addition, the wash-out scenario at low CO fractions is clearly visible in Figure 6.7 (A). Consequently, the dilution rate respectively growth rate can only be met with CO fractions larger than 10 vol-%.

Figure 6.7 not only displays the carbon share within the parameter variation but also the maximum CO fixation normalised to the maximum in the first parameter study **A** - **E**, which is analogue to the C_{fix}(SS) mapping in Figure 6.6.

Figure 6.7 and Figure 6.8 show similar results in two different ways. While Figure 6.7 displays the carbon share of each steady state in a more comparable manner, Figure 6.8 outlines the total carbon amount of the fermentation normalised to the maximum in **E** of the first parameter study series. Biomass (white area) and sum(P) (grey area) together result in the same quantity displayed in Figure 6.7 as interconnected black squares.

The highest fixated amount of carbon with the greatest product biomass yield of the first parameter study is achieved with a mean gas holdup of about 30% (equals $\varepsilon_{\mathrm{crit}}$ see also chapter 4.1) and $\overline{k_L a}$ of 480 h^{-1}. For the final study, new starting parameters are chosen according to the findings of the first run. Besides, an initial gas holdup $\varepsilon_{\mathrm{G},0}$ of 19% ($\overline{\varepsilon_{\mathrm{G}}}$ = 0.31) the CO fraction of 55% is not changed, since the amount of CO rarely exceeds this value in converter gas of the steel production (Clarke Energy®, 2018) and it is the same amount used in the experiments (in the supplementary files of Siebler et al., 2019, respectively Manuscript II). According to published literature (Figure 6.3 (A)), $\overline{\varepsilon_{\mathrm{G}}}$ can only be increased by also increasing the superficial gas velocity, which was set for **F** to the maximum of the first study (0.15 vvm).

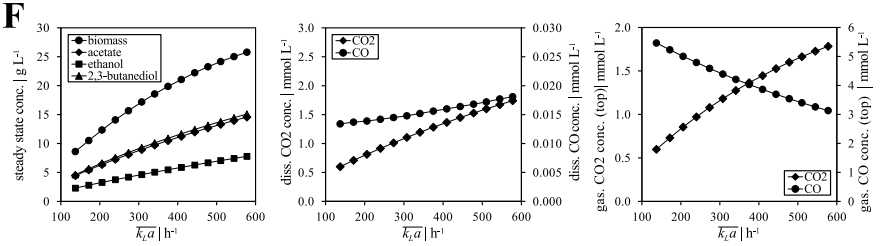

Figure 6.9: Steady state results of $k_L a$ variations of final parameter set-up. The new parameter set has a CO fraction of 55 vol-%, gas holdup $\overline{\varepsilon_{\mathrm{G}}}$ of 0.3 and superficial gas velocity of 0.0625 m s^{-1} (0.15 vvm) as new reference. According to Figure 6.11, the results of a second and final mass transfer variation is pictured in (F).

With this new parameter set-up a final k_La study was modelled as displayed in Figure 6.9. The behaviour is similar to the first mass transfer study **C**. However, much higher product and biomass yields are reached (Figure 6.10).

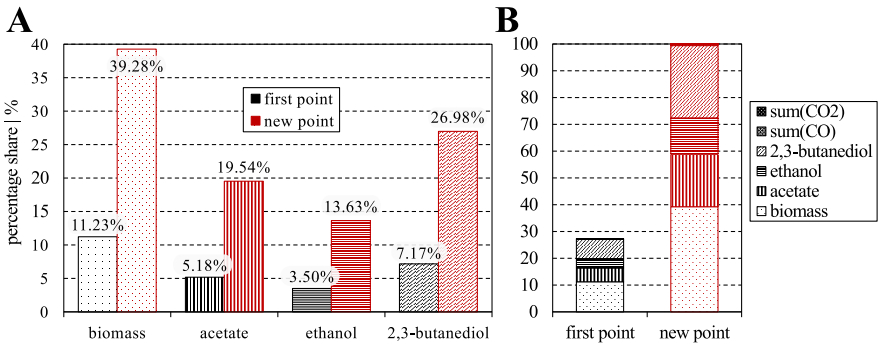

Figure 6.10: Comparison of old reference point with the final result. The pictures show the percentage carbon share of the first parameter set (coloured black) with a $\overline{k_La}$ of around 130 h^{-1}, CO fraction of 55 vol-%, gas holdup $\overline{\varepsilon_G}$ of 0.1 and superficial gas velocity of 0.025 $m\,s^{-1}$ (0.06 vvm). The new parameter set (coloured red) has a $\overline{k_La}$ of around 580 h^{-1}, CO fraction of 55 vol-%, gas holdup $\overline{\varepsilon_G}$ of 0.3 and superficial gas velocity of 0.0625 $m\,s^{-1}$ (0.15 vvm). In (A) the products of both parameter sets are comparatively shown. The percentage share is normalised to the maximum carbon amount of both simulations (see (B)). Note: Percentage share is given for c-mol.

In Figure 6.10 the reference of the first study is compared with the final k_La study **F** respectively the simulation result of the last k_L and $d_{B,0}$ set. A final mass transfer of 580 h^{-1} is reached, which leads to high local CO uptake and therefore production rates (see kinetic correlation in chapter 4.3.1). This means that in comparison three times more CO is converted to biomass and product (Figure 6.10 (B)). The percentage share within each setting stays almost the same (around 40/60% – biomass/sum(P) with remaining carbon always < 1%). The final fermentation set-up has only 2% more carbon converted into product than biomass. A significant change in product share can only be expected for two substrate growth with different gas solubilities as for example CO_2/H_2 gas fermentations. Nevertheless, the product can be divided into 32/23/45% – acetate/ethanol/2,3-butanediol (percentage share is given for c-mol).

Each steady state result can be displayed as concentration over time and for each time step the local concentration can be plotted over the height of the

reactor. In Figure 6.11, the final scenario was selected to show the temporal (A) and spatial results (B). The spatial results of the steady state (at 1,200 h) have also been translated into consumption, production and growth rates (Figure 6.11 (B), right side). For the temporal results in Figure 6.11 (A) the biomass and product concentrations (left), the gas concentration at the top (middle) and mean soluble gas concentration of the whole bubble column (right) was depicted. As mentioned before, the steady state is reached after around 800 h.

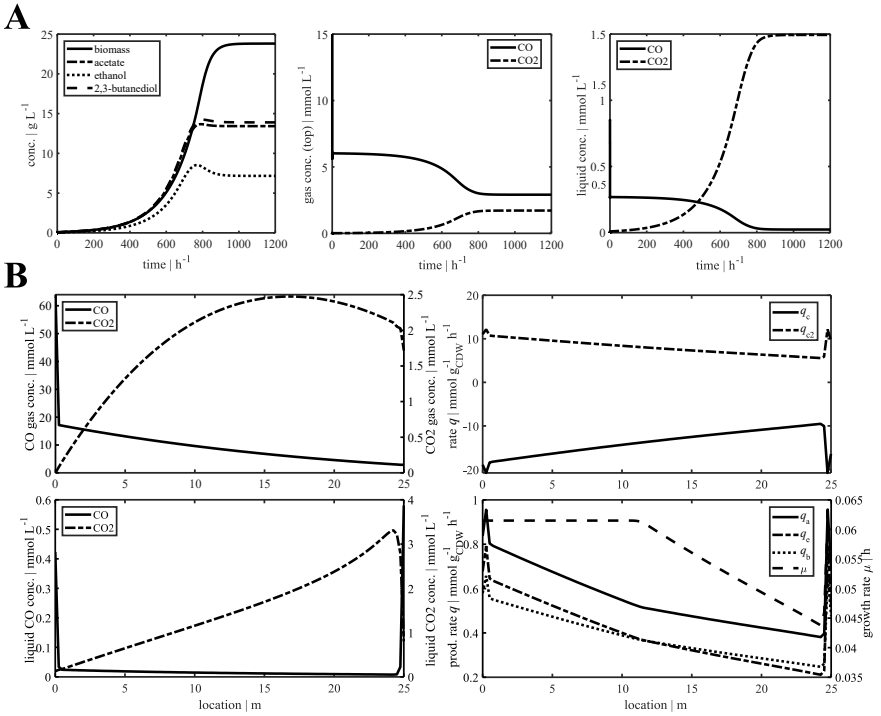

Figure 6.11: Temporal and spatial results for final parameter set-up. In (A) the average concentrations are pictured over time until the process reaches a steady state. (B) Spatially resolved steady state results of the liquid and gaseous concentrations are shown in on the left side. The right side illustrates the related consumption and production rates (acetate q_a, ethanol q_e and 2,3-butanediol q_b and the growth rate μ). (Reprinted from Siebler et al., 2020, with permission of © Wiley-VICH Engineering in Life Science.)

The gas composition changes over the height (Figure 6.11 (B) top left). As CO dissolves and is consumed CO_2 is produced. The dissolved gasses

behave accordingly. In Figure 6.11 (B) top right, it can be seen that the kinetic correlation determines a CO consumption proportional to the CO_2 production as defined in equation 4.3 (chapter 4.3.1). CO limitations described by Mohammadi et al. (2014) only occur at CO concentration higher than $0.1\,\mathrm{mmol\,L^{-1}}$. This is only the case at the bottom of the reactor respectively in the first compartment and thereby negligible. When the gas enters the reactor it almost immediately dissolves due to high hydrostatic pressure (around 3.5 atm) and is consumed at once by the organism.

The sudden changes in the growth and production rates occur when $q_c \leq -14\,\mathrm{mmol\,g_{CDW}^{-1}\,h^{-1}}$. This happens at a column height of around 12 m. In this scenario the growth rate is not at its maximum as it can be seen in chapter 4.3.1 Figure 4.5. The production rates are lower as well. Since the maximum growth rate of around $0.06\,\mathrm{h^{-1}}$ is not the same as the dilution rate $D = 0.055\,\mathrm{h^{-1}}$, the growth rate can change locally. Nevertheless, the mean steady state growth rate always equals the dilution rate, except the two wash-out scenarios at low CO gas fractions. At which height this effect occurs for growth and production rates depends on the gas availability, which in turn depends mostly on gas holdup and mass transfer. This can also cause changes in the product biomass yield respectively carbon flow (see Figure 6.6 and 6.10).

In summary, the most important properties of a gas fermentation are gas holdup and mass transfer. Unfortunately, they are very difficult to predict and most likely to change during the fermentation. Nevertheless, the 1-dimensional approach gives an overview of possible fermentation scenarios and their carbon flow. This helps to find an optimal parameter set for further analysis with computational fluid dynamics focusing on the cell behaviour. The results also give a recommendation of how the fermentation has to be run in order to obtain the best yields and therefore minimise risks in scale-up.

6.2 Computational fluid dynamics

The second modelling part focuses on more detailed flow behaviour and bacteria tracking. With the help of computational fluid dynamics (CFD) and therefore more detailed spatial discretisation, a pseudo-stationary gas gradient is achieved. In this chapter, the classification of the gas gradient as processing and the interpretation of the bacterial lifelines are also presented and discussed. How predictions according to short and long-term responses of the microorganism can be made is also shown.

This chapter is a summary of Siebler et al. (2019, respectively Manuscript II). The structure deviates from Manuscript II and all recited pictures and tables are stated as such.

6.2.1 Mesh, flow field and pseudo-stationary gas gradient

To solve the flow equations mentioned in chapter 4.4.1 (Turbulent incompressible flow), both spatial and temporal discretisation need to be chosen carefully. As stated in the 1-dimensional approach, the mass needs to be conserved. Additionally, the general flow behaviour of a bubble column should be represented as well as possible. As mentioned before, the finer the numerical grid the more accurate the eddies are reproduced and therefore the two phase flow. However, the equations to be solved increase the higher the spatial resolution. Accordingly, the simulation time also increases.

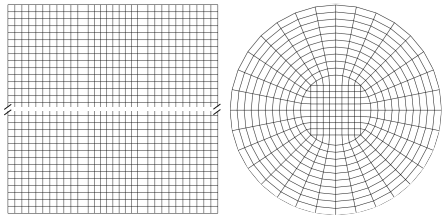

Figure 6.12: Computational fluid dynamic grid. Top and bottom section of grid in side and top view. (Reprinted from Siebler et al., 2019, with permission of © Elsevier Chemical Engineering Science.)

The final mesh with around 125,000 numerical cells is shown in Figure 6.12 in side and top view (further information can be found in chapter 5.3). The mean gas holdup is tracked (Figure 6.13 (A)) to determine whether incoming and outgoing gas flow is approximately the same and a steady state is reached. The mass flow at the bottom and top of the reactor is also analysed in ANSYS Fluent (data not shown). In bubble column reactors the flow field is developed by the bubble movement. For simulation stability reasons, in the first 1,000 s only one constant bubble size is used until the flow field with a gas holdup of 0.34 is developed. An initial diameter of 4 mm is set to keep the simulation comparable to the 1-dimensional approach. After 1,000 s, different bubble sizes are enabled by using the population balance model with sixteen discrete size classes ranging from 0.001 m to 0.032 m. Breakage, coalescence, expansion, mass transfer from gas to liquid phases and the gas uptake in each numerical cell are enabled as well (Figure 6.13

(A) dashed line). The incoming bubble size is kept at 4 mm (bubble diameter bin 7).

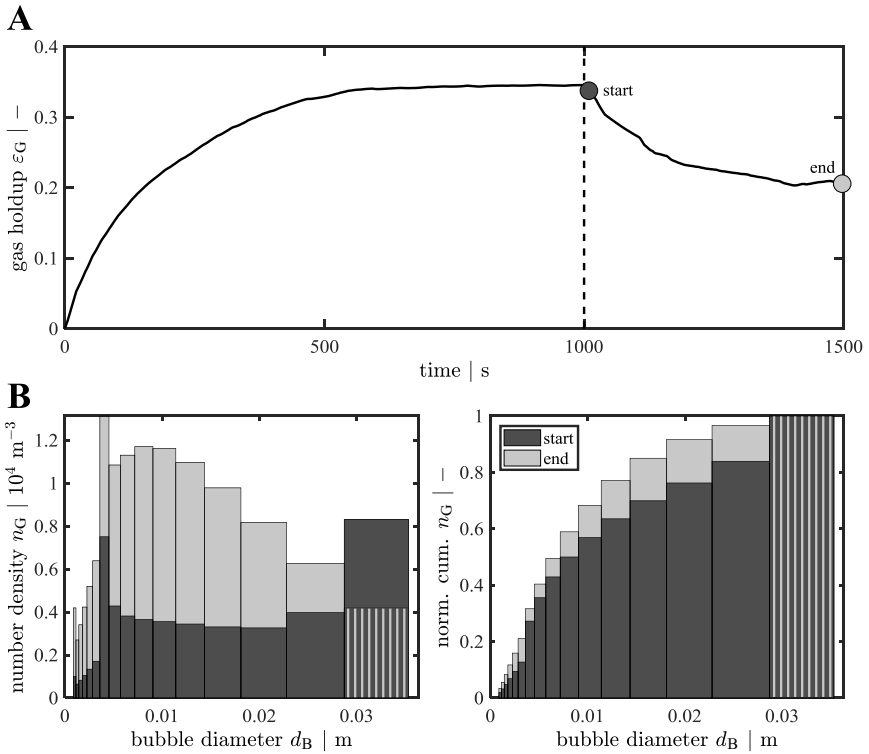

Figure 6.13: Simulation development to reach pseudo-stationary gas gradient. In (A) the average gas holdup in the bubble column reactor is plotted against time. During the first 1,000 s the flow field was developed with one bubble size and no mass transfer from gas to liquid phase. From 1,000 to 1,500 s breakage and coalescence and effects of hydrostatic pressure are enabled by including the population balanced model. The average bubble size distribution for start (dark grey) and end point (light grey) are shown in (B). The number density over diameter bin is given as normal and cumulative distributions. Similar to 1-dimensional approach the start parameter is always 4 mm (bin 7). (Adapted from Siebler et al., 2019, with permission of © Elsevier Chemical Engineering Science.)

Figure 6.13 (B) shows the number density n_G of each bubble diameter class on the left side and the normalised cumulative number density on the right side. To show how the bubble size distribution (BSD) changes, start (dark grey) and final (light grey) distributions are depicted, which is

also indicated in Figure 6.13 (A) as dots. The gas holdup decreases when coalescence is enabled and a new steady state is reached after 500 s with ε_G of 0.21. The trend of the final BSD is similar to observations with water-air experiments of Lehr et al. (2002). However, longer bubble dwell times are obtained in the six times larger bubble column of this study. The probability for coalescence is much higher compared to Lehr et al. (2002) leading to larger bubbles classes up to 3.2 cm (bin 16). This causes the lower average gas holdup after 1,500 s.

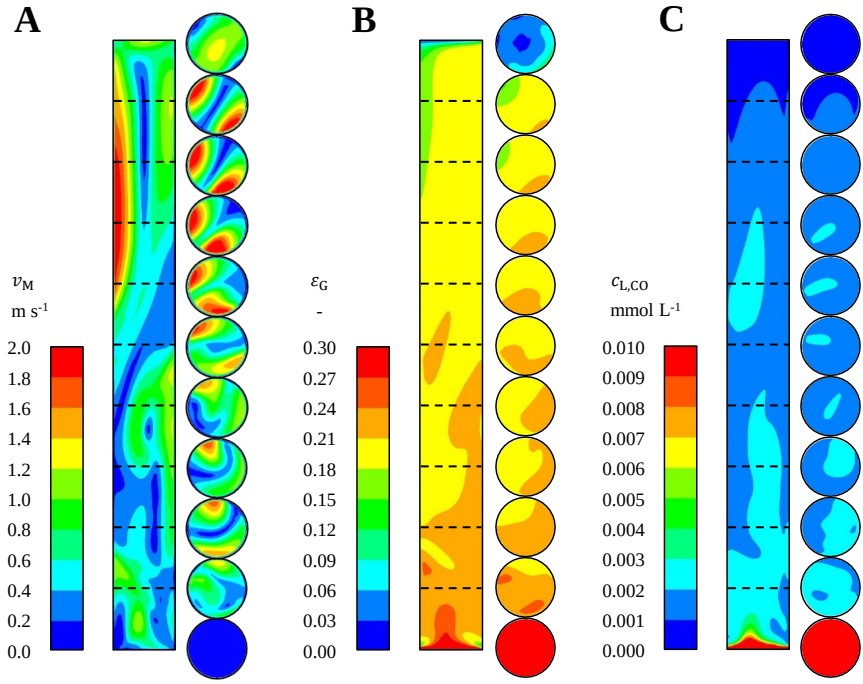

Figure 6.14: Flow field (A), gas holdup (B) and concentration profile (C) of the CFD simulation. Colour scale and unit is given on the left side. Shown are side profiles in yz-direction and eleven section planes in xy-direction indicated by the dashed lines as well as reactor top and bottom. In (A) the velocity magnitude $v_M = \sqrt{u^2 + v^2 + w^2}$ as defined by Fluent is depicted. (Reprinted and modified from Siebler et al., 2019, with permission of © Elsevier Chemical Engineering Science.)

With the same bubble diameter and gas input as in the 1-dimensional approach the first steady state of the gas holdup is 3% higher. More accurate

flow behaviour with recirculation patterns and eddies are factored in which cause more gas retention in the liquid. However, if bubble breakage, coalescence and expansion are enabled, the average bubble diameter of 4 mm is increased to 9.7 mm (number length mean) or more important a Sauter bubble diameter of 20.9 mm (surface area mean). This indicates that bubble expansion and coalescence are the governing effects in bubble column. Additionally, larger bubbles experience more buoyancy and rise faster which is in accordance to Figure 6.14 (A) with higher velocities at the top of the reactor. Simultaneously, the overall gas holdup decreases, because higher velocities mean lower bubble dwell times. Therefore, the gas holdup declines, which corresponds to heterogeneous churn-turbulent flow behaviour and not perfect bubbly flow as described in chapter 4.1 Figure 4.3 on page 36 (Kantarci et al., 2005; Deckwer et al., 1980; Krishna and Sie, 2000).

In conclusion, computational fluid dynamics allow to cover important physical properties such as drag, lift, expansion, breakage and coalescences, which give a more realistic flow behaviour in large scale bubble column reactors. Therefore, mass transfer calculations are more accurate and a pseudo-stationary gas gradient with flow field can be derived for further studies on the microbial level. Information on the overall changes in mass transfer before and after the population balance model is enabled can be found in the supplementary files of Siebler et al. (2019, respectively Manuscript II).

In addition to that, the mixing time with 27.3 ± 4.3 s and the circulation time with 14.7 ± 1.4 s is demerited. Since the circulation velocity is approximately two times the reactor height divided by the circulation time, the bacteria travel through the reactor with an average speed of $3.4\,\mathrm{m\,s^{-1}}$. This is within the range of Pandit and Joshi (1983). Further, information on the determination of these values can be found in the supplementary files of Siebler et al. (2019, respectively Manuscript II).

Finally, with the gas gradient, hydrodynamics and mixing time the Lagrange trajectories can be simulated. However, before the data of this CFD simulation can be processed, reasonable classification criteria have to be found, which is discussed in the next chapter.

6.2.2 Classification of regimes by product biomass yields

For the statistical evaluation, the Lagrange trajectories were sorted and the CO concentration profiles filtered as described in Kuschel et al. (2017). As the title of this chapter implies, the classification criteria of the lifeline interpretation is the productivity of the organism, more precisely the steady state product biomass yield $Y_{P,X}$. This crucial biological value is also mentioned

in the 1-dimensional approach (chapter 6.1.4: Sensitivity and impact of parameter variations). As discussed in chapter 3 (Evaluation and assessment of industrial reactors), synthesis gas fermentations are not highly productive and should be low in plant, operation and maintenance cost. The more product is produced the more economical the process. Therefore, the product per biomass yield is a good indicator and choice for the regime classification.

In order to do so, the dissolved CO concentration needs to be connected to the product biomass yield $Y_{P,X}$. From chapters 4.3.1 and 4.3.2 the CO uptake kinetic of Mohammadi et al. (2014) and element balance correlation can be used to approximate the product biomass yield as a function of CO uptake q_c, which is given in equation (6.4) and illustrated in Figure 6.15 (A).

$$Y_{P,X}(q_c) = \begin{cases} \frac{1.51\, q_c}{q_c - 2.29} & -14 < q_c \leq 0 \\ -\frac{q_c}{6} - 1 & q_c \leq -14 \end{cases} \tag{6.4}$$

Since the product yields per c-mol CO can be derived from the rates $Y_{\text{product,CO}} = q_{\text{product}}/q_c$, the product biomass yield is the sum of all product substrate yields divided by the biomass per carbon monoxide yield.

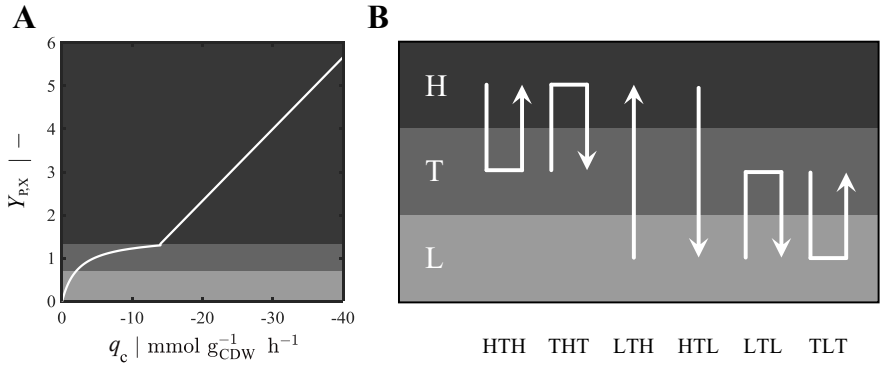

Figure 6.15: Regime classification as function of productivity. In (A) the product biomass yield $Y_{P,X}$ is given in c-mol per c-mol as a function of CO uptake rate (see also equation (6.4)). From q_c of 0 to $-14\,\text{mmol}\,g_{CDW}^{-1}\,h^{-1}$ the $Y_{P,X}$ function behaves Monod-like with a half-maximum value of $-2.29\,\text{mmol}\,g_{CDW}^{-1}\,h^{-1}$ which is also the first regime transition value. The second transition value is at $-14\,\text{mmol}\,g_{CDW}^{-1}\,h^{-1}$ when the $Y_{P,X}$ function is linear ascending. All six regime transition strategies are illustrated in (B). (Reprinted from Siebler et al., 2019, with permission of © Elsevier Chemical Engineering Science.)

The higher the $Y_{P,X}$ value the more carbon flows in the formation of the desired by-product. High product biomass yields indicate a strong metabolism of growing cells. As described in chapter 5.3.2 and pictured in Figure 6.15 (B), the movement patterns of the individual cell is analysed by this translation. In doing so, critical thresholds need to be defined to divide the gas gradient in gradient segments. Considering the function for $Y_{P,X}$, the first part of the equation ($0 \leq q_c < -14\,\mathrm{mmol\,g_{CDW}^{-1}\,h^{-1}}$) shows Monod-like behaviour with a half-maximum yield $K_{Y_{P,X}}$ of $-2.29\,\mathrm{mmol\,g_{CDW}^{-1}\,h^{-1}}$. With this value also the first threshold from low to high yields is set. At $q_c \leq -14\,\mathrm{mmol\,g_{CDW}^{-1}\,h^{-1}}$ the $Y_{P,X}$-function turns into a linear correlation. This indicates that the maximum of CO conversion into biomass formation is achieved and all additional carbon is used in by-product formation. The switch to linear function behaviour is used as second threshold leading to three regimes: **L** for low yields from 0 to $-2.29\,\mathrm{mmol\,g_{CDW}^{-1}\,h^{-1}}$ ($0 \leq Y_{P,X} < 0.75$), **T** for transition area between -2.29 and $-14\,\mathrm{mmol\,g_{CDW}^{-1}\,h^{-1}}$ ($0.75 \leq Y_{P,X} < 1.33$) and **H** for high yields starting from $-14\,\mathrm{mmol\,g_{CDW}^{-1}\,h^{-1}}$ ($1.33 \leq Y_{P,X}$).

This classification is also implied in Figure 6.15. Six movement patterns (Figure 6.15 (B)) can be derived characterising the shift between three gradient zones. The regime transition events are described in the following list (recited from Siebler et al., 2019, with permission of © Elsevier Chemical Engineering Science.):

HTH: Event from high to transition and back to high product per biomass yield areas.

THT: Reverse movement starting from the transition area with retention in the high yield area and back to transition.

LTH: Crossing all regimes from low to high and with dwelling in the transition area.

HTL: Reverse event from low to high product biomass yields.

LTL: Analogous to HTH but from low to higher and back to low yield areas with residence time in the transition domain.

TLT: Same regimes but with a stay in the lower domain with little product biomass yields and start in the transition class.

The second letter of the regime transition events also indicates the residence time τ for each movement pattern.

Finally, the Lagrange trajectories representing the bacterial lifelines can be processed in a statistical manner. Statistical relevance, translation and processing of the data will be shown in the following chapter.

6.2.3 Processing bacterial lifelines

Four times 30,000 massless Lagrange particles are tracked for 500 s which results in 120,000 bacteria for 2,000 s (see chapter 5.3.2). The statistical relevance of the space and time dependent trajectories are checked for ergodicity. As described in chapter 4.4.5, the Lagrange trajectories are ergodic when the time average is the same as the average over the probability space. For this reason, the reactor was horizontally divided into ten uniform columns (Figure 6.16 (A) $z_0 - z_9$). In each subdivision the particles were superimposed at each time step ($t_0 - t_{end}$). More precisely, at each recorded time step the amount of bacteria in one volume is counted and then compared to the expected amount (see Figure 6.16 (B)). As indicated in Figure 6.16 (B) all volumes show deviations lower then 2%. Consequently, both, the amount of particles and tracking time, can be assumed to be ergodic and statistically relevant. In addition to that, the average carbon monoxide concentration of the Lagrange trajectories ($c_{L,CO} = 0.0020\,\mathrm{mmol\,L^{-1}}$) is approximately the same as of the liquid phase ($c_{L,CO} = 0.0018\,\mathrm{mmol\,L^{-1}}$).

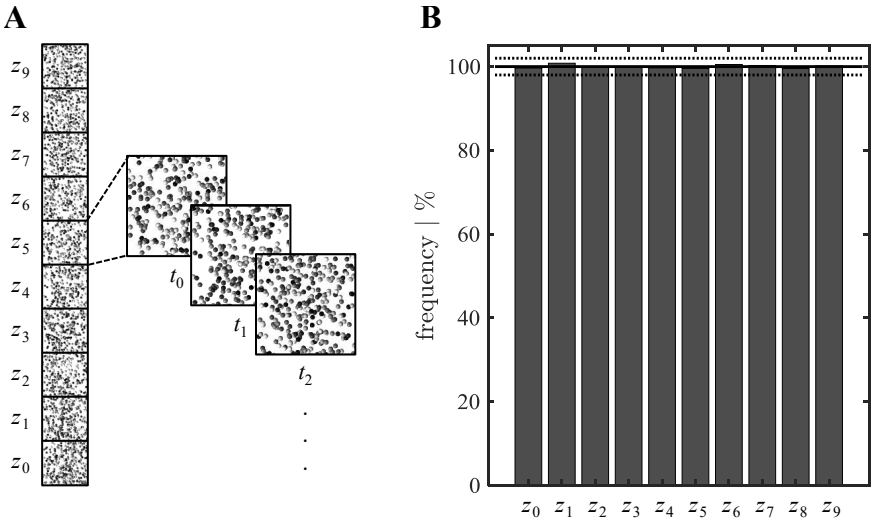

Figure 6.16: Statistical relevance of Lagrange trajectories. In (A) 3,000 representative enlarged bacteria are depicted to illustrate the spatial ($z_0 - z_9$) and temporal ($t_0 - t_{end}$) residence of the bacteria. For each spatial segment z the probability with respect to expected value (black line) is shown in (B) as frequency in percentage. Dotted black lines indicate the $\pm 2\%$ deviation limit. (Reprinted from Siebler et al., 2019, with permission of © Elsevier Chemical Engineering Science.)

The representative 120,000 bacteria lifelines need to be further processed in order to gain insight into the effects of substrate gradients on the cellular level. The gradient classification and movement pattern introduced in the previous chapter are applied to the recorded trajectories. In general, the longer a bacterium stays in one regime the more likely it adapts to its surroundings leading to demanding adaptations of the regulatory programs of the organism (Löffler et al., 2016).

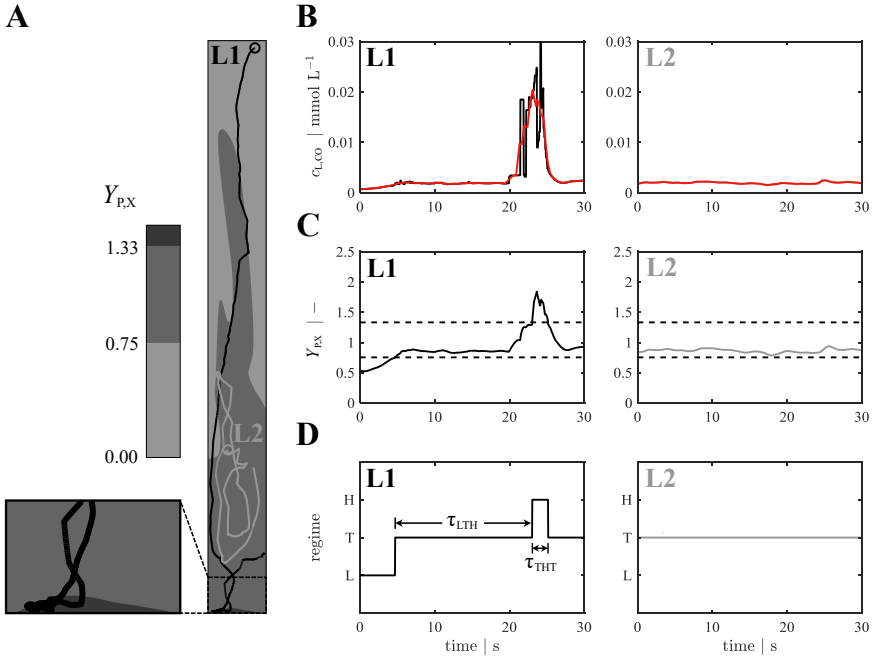

Figure 6.17: Processing of bacterial lifelines. Exemplary two 30 s lasting bacterial lifelines L1 (black) and L2 (grey) are shown in spatial resolution in (A). The related CO concentration profiles are given in (B) also indicating the results of the moving-average filter (red line) (see also Kuschel et al., 2017). The concentration is translated into the uptake rate q_c finally yielding the total product biomass yield $Y_{P,X}$ presented in (C). The black dashed lines indicate the regime transition boundaries which are used to translate the lifelines into regime switch diagrams with transient stays τ of each regime switching event (D). The regimes are divided into high (H), transition (T) and low (L) product biomass yields. For lifeline L1 two strategies are shown (LTH and THT) with different durations of stay τ. (Reprinted from Siebler et al., 2019, with permission of © Elsevier Chemical Engineering Science.)

In Figure 6.17 (A), the CO gradient of Figure 6.14 (C) is translated into the

three product biomass yield dependent regimes: **H** encoding high product biomass yields (zoomed detail in dark grey) located in the lowest column zone, **T** the transition regime (in grey) spreads along the column height and **L** the low product biomass yield regime (in light grey) mainly at the top of the reactor. Figure 6.17 (B) to (D) shows two lifelines tracked for 30 s as well as their translation process from concentration profile (B) to product biomass yield (C) and finally regime transition (D). Their movement is spatially shown in Figure 6.17 (A) as well. The first lifeline L1 (black) passes all three gradient regimes while the second L2 (grey) stays only in the transition area. This leads to only two transition events for L1 with residence times of $\tau_{\mathrm{LTH}} = 18.3\,\mathrm{s}$ and $\tau_{\mathrm{THT}} = 2.1\,\mathrm{s}$ (Figure 6.17 (D)).

Both frequency of the six regime transition strategies as retention time depend on the substrate gradient, regime classification and flow field respectively velocity of the bacteria. The next chapter focuses on these properties and points out a possible way of interpreting the Lagrangian trajectories.

6.2.4 Frequency of regime transition strategies

The classification into three regimes for different product biomass yields allows the assessment of bacteria passing through a gradient. This evaluation encompasses counting of transition events and grouping them with respect to the retention time in the transient regime (Figure 6.18). From this evaluation, maximum and average time of stays in a certain regime can be derived and listed (Table 6.1).

Table 6.1: Total frequency, average and maximum retention time. For each regime transition event the total frequency, the average retention $\overline{\tau}$ and maximum retention time τ_{max} is listed. A confidence level of 99% for τ_{max} is chosen. (Reprinted from Siebler et al., 2019, with permission of © Elsevier Chemical Engineering Science.)

Regime transition strategy	Total frequency in %	$\overline{\tau}$ in s	τ_{max} in s
LTL	44.6	12.1	86.6
TLT	46.0	7.2	28.4
THT	3.6	3.4	15.3
HTH	1.2	17.4	80.4
LTH	2.4	29.6	107.5
HTL	2.2	32.8	109.8

In Figure 6.18 the frequency patterns of all possible regime transition strategies are given. The regime transitions are listed on page 103 in chapter 6.2.2. With an overall probability of 46.0%, the TLT movement pattern

is the most common event, directly followed by the LTL regime transition event with 44.6% (see also Table 6.1). The overall probability of the other events is less than 4%. In contrast to that, the average retention times $\overline{\tau}$ range from 3.4 s to 32.8 s, whereas maximal regime durations τ_{max} go up to 109.8 s. LTH and HTL include all regimes and show besides the maximum retention time also a minimum time of about 10 s (see Figure 6.18).

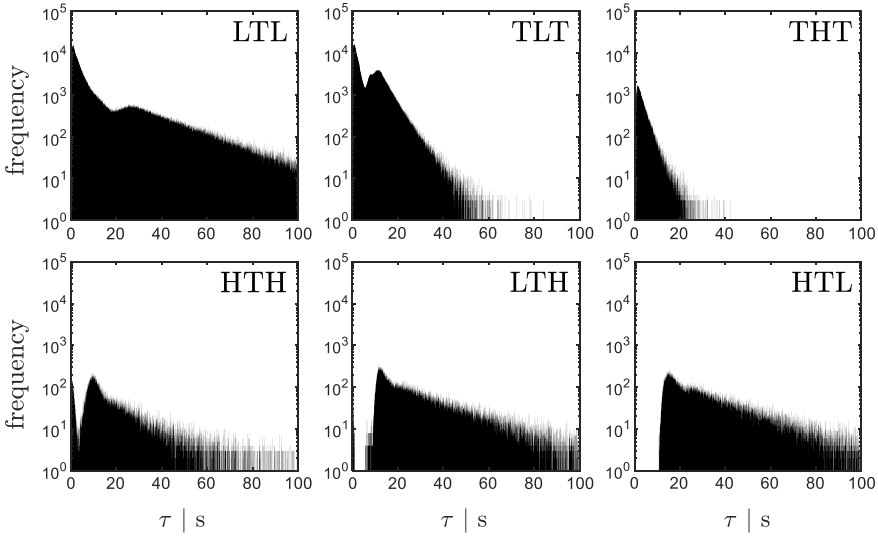

Figure 6.18: Regime transition strategies over retention time. The frequency of all six regime transition strategies are given (log scale) and plotted against their duration of stay τ in the second (transient) regime. For each histogram 600 bins have been chosen. (Reprinted from Siebler et al., 2019, with permission of © Elsevier Chemical Engineering Science.)

The volume of each regime reflects the total event frequency. On the other hand, the retention time and frequency of a transition event depend on the gradient profile and the flow field. When comparing Figure 6.14 (A) with Figure 6.17 (A) (flow field and gradient in regimes), the difference in $\overline{\tau}$ and τ_{max} between LTL and TLT can be explained. Higher velocities close to the wall and on top of the reactor cause lower average and maximum retention times for the TLT regime transition event. In a biological context this means that a high turnover of cells is passing the low product biomass yield zone in less time (TLT) than it is staying in the transition regime (LTL).

Between the high and low regime areas (see Figure 6.17 (A)) the rather wide transition area is located leading to the low event frequencies of LTH

and HTL. For each event the T area has to be passed, which lasts at least 10 s. These maximum shifts from low to high rarely happen ($\leq 5\%$), thus the organisms are not often exposed to very extreme environmental changes. Haringa et al. (2017) observed similar behaviour in their stirred tank investigations.

The H zone represents less than 1% of the total bubble column. This leads to the conclusion that only in this small area the CO supply for the organisms is optimal. Kinetic inhibition of the CO uptake is not an issue in the major part of the reactor.

Moreover, by weighting the average residence time of each regime transition event with its overall probability, an average circulation time of a bacterium with 10.5 s can be estimated. This value is similar to the circulation time derived from the mixing time estimation (see supplementary files of Siebler et al., 2019). Compared to stirred tank observations with circulation times of 20 s (Haringa et al., 2017; Kuschel et al., 2017), the mixing of the reactor is rather good with a much lower power input (Siebler et al., 2019). Bubble column reactors allow for axial flow patterns while stirred tank reactors with Rushton blades mostly reveal radial velocities with typical eddy formations along the stirrer. This also leads to hard transitions zones between the vortices. Bacteria often dwell in these eddies for a longer period of time and cause therefore longer circulation times.

The next chapter focuses on short- and long-term responses which can be derived from the Lagrangian trajectories as well.

6.2.5 Short- and long-term responses

How microorganisms react to environmental changes depends on external stress stimuli and the period of exposure to this stimulus. A short-term stress indicator can be a critical substrate concentration, while the long-term response to this critical change are usually transcriptional adaptations of the organism. The longer the exposure the more severe the internal changes of the cell. The indicators respectively thresholds for short- and long-term responses can be identified with plug-flow experiments (Löffler et al., 2016).

Unfortunately, for *C. ljungdahlii* no comparable experimental studies are published and their development is not in the scope of this study. However, thresholds from well-investigated organisms such as *Escherichia coli* can be used. With a maximum glucose uptake rate $q_{\max}$ of $1.8\,\mathrm{g_{gluc}\,g_{CDW}^{-1}\,h^{-1}}$ this strain has a maintenance demand m_s of $0.057\,\mathrm{g_{gluc}\,g_{CDW}^{-1}}$ (Taymaz-Nikerel et al., 2010; Michalowski et al., 2017). In other words, under optimum

growth conditions 3.2% of the maximum uptake are needed for maintenance. In the case of *C. ljungdahlii*, this would be a critical CO concentration of $c_{\mathrm{L,CO}}^{\mathrm{crit}} = 0.003\,\mathrm{mmol\,L^{-1}}$ derived from $q_{\mathrm{c,max}}^{\mathrm{real}} = q_{\mathrm{c}}\left(\sqrt{K_{\mathrm{M}}K_{\mathrm{I}}}\right)$, which results in $24.87\,\mathrm{g_{gluc}\,g_{CDW}^{-1}\,h^{-1}}$ ($0.1\,\mathrm{mmol\,L^{-1}}$). This value consequently marks the metabolic short-term stress response.

The second threshold marks transcriptional and translational responses which occur only after longer exposure. For *E. coli* after 30-40 seconds first transcriptional changes can be measured (Löffler et al., 2016). Major transcriptom adaptations can be found after 70 s. In comparison with *E. coli*, three minimum critical residence times in stress-inducing zones are derived: $\tau^{\mathrm{crit}} = 10\,\mathrm{s}$, $\tau^{\mathrm{crit}} = 40\,\mathrm{s}$ and $\tau^{\mathrm{crit}} = 70\,\mathrm{s}$.

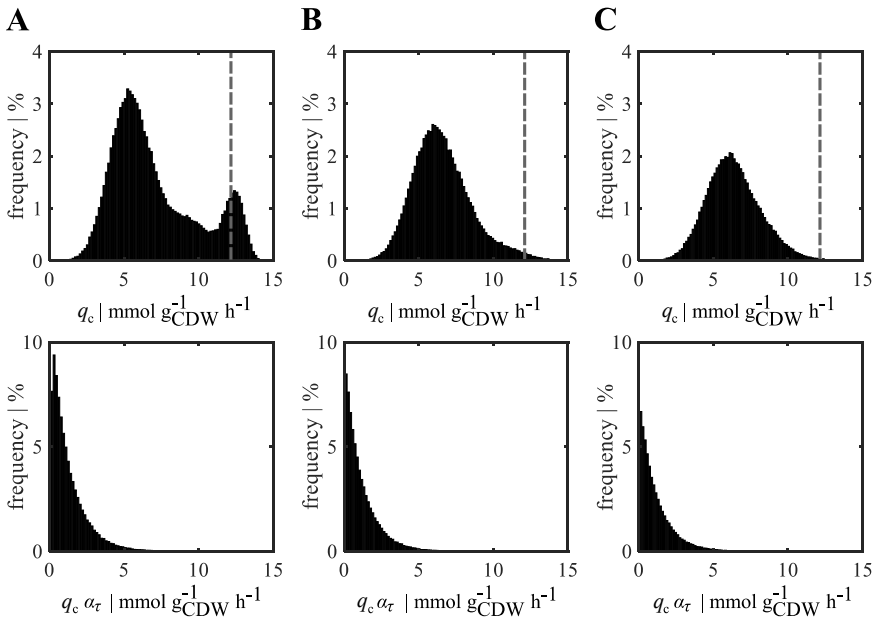

Figure 6.19: Expected bacterial responses while experiencing limitation for different exposure periods. As described in chapter 5.4.2 three critical time points $\tau^{\mathrm{crit}} = 10\,\mathrm{s}$ in (A), $\tau^{\mathrm{crit}} = 40\,\mathrm{s}$ in (B) and $\tau^{\mathrm{crit}} = 70\,\mathrm{s}$ in (C) have been chosen to show the distribution of uptake rates (first row) and the weighted distribution by actual duration τ_i indicated by the case-specific weighting factor $\alpha_{\tau,i}$ (second row). Histograms are normalized to the highest total percentage of the average occurrence ($\tau^{\mathrm{crit}} = 10\,\mathrm{s}$) and divided into 100 bins. The average uptake rate $q_{\mathrm{c}} = 12.26\,\mathrm{mmol\,g_{CDW}^{-1}\,h^{-1}}$ is indicated as a grey dotted line. (Reprinted from Siebler et al., 2019, with permission of © Elsevier Chemical Engineering Science.)

The Lagrange trajectories are processed as described in chapter 5.4.2 and resulted in Figure 6.19 and 6.20 for the short- and long-term responses. For each stress exposure period, the distribution of uptake rates (Figure 6.19 (A) - (C), first row) is depicted. Since the frequency of different uptake rates does not include the actual duration, each count is additionally weighted by its average residence time (Figure 6.19 (A) - (C), last row). The abstract visualisation of the distributions in Figure 6.19 is summarised in Figure 6.20 in form of total percentage shares.

In Figure 6.19, heterogeneous cellular population with a bimodal distribution can be identified for short residence times of at least $\tau^{\mathrm{crit}} = 10\,\mathrm{s}$. Since the carbon uptake rates can be correlated with the product biomass yields, also bimodal production zones can be expected in this case. The very short retention in high CO concentration areas such as for the THT regime transition event (Table 6.1 with $\overline{\tau}_{\mathrm{THT}} = 3.4\,\mathrm{s}$) is reflected by the normalised distribution. They indicate that long residence times in high CO concentration areas respectively high q_{c} do not happen frequently. On the other hand, longer exposure periods ($\tau^{\mathrm{crit}} = 40\,\mathrm{s}$ and $\tau^{\mathrm{crit}} = 70\,\mathrm{s}$) show homogeneous unimodal distributions (Figure 6.19 (B) and (C)). However, the overall uptake rate q_{c} with $12.26\,\mathrm{mmol\,g_{CDW}^{-1}\,h^{-1}}$ (Figure 6.19, dashed grey line) deviates from all three critical time period. This is an indication that time-dependant bacterial adaptation caused by substrate limitation will have a major negative effect on the overall production of this fermentation process.

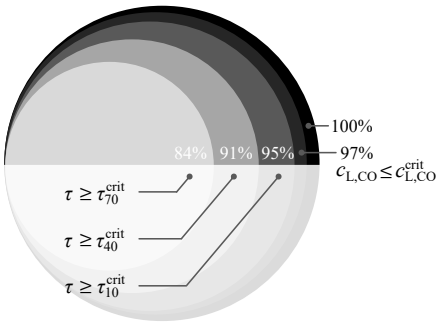

Figure 6.20: Percentage share for three critical residence time points. From black to light grey the overall probability (100%), percentage of all possible dissolved CO concentrations smaller than the critical value $c_{\mathrm{L,CO}}^{\mathrm{crit}} = 0.003\,\mathrm{mmol\,L^{-1}}$ (97%), amount of residence times with at least 10 s (95%), not less than 40 s (91%) and with a critical residence time point of 70 s (84%) are shown. (Reprinted from Siebler et al., 2019, with permission of © Elsevier Chemical Engineering Science.)

As indicated in Figure 6.20, 97% of all bacteria experienced severe CO limitation at least once ($c_{L,CO} \leq c_{L,CO}^{crit}$) while 95% are likely to show immediate metabolic changes ($\tau^{crit} = 70\,s$). When taking *E. coli* as a reference, 84% of all cells react to external CO limitation and start transcriptional adaptations by inducing starvation programs. This causes additional energy demand in the organism. The additional maintenance is most likely to reduce the product biomass yields and the growth rate. To confirm these findings, experimental scale-up studies with *C. ljungdahlii* are necessary.

6.3 Computation results in comparison

In this chapter both approaches are compared. The results and discussion is mainly given in Manuscript III (Siebler et al., 2020). Not only the key findings are summarised, but also the results of one additional pursuing simulation is included.

Even though, the 1-dimensional (1D) approach has a low spatial resolution, it can resolve local heterogeneities. Moreover, it reduces the model complexity and simulation time. In contrast to that, the computational fluid dynamics (CFD) approach has a much higher resolution, which allows for better flow behaviour prediction and the integration of bacterial lifeline analysis. The CFD simulation needs much more computational power and can only represent certain states (snap-shots) of a large scale fermentations. Consequently, less computationally challenging frameworks such as the 1D model are advisable to narrow down optimal operation modes.

Table 6.2: Average results of both simulations as well as iteratively adjusted 1-dimensional approaches. Both approaches, 1D (1D(F), (G) and *) and computational fluid dynamics (CFD) simulation used the same initial conditions with superficial gas velocity of $0.0625\,m\,s^{-1}$ and initial bubble diameter of 4 mm. 1D(G) used the Sauter mean diameter of the CFD simulation as mean bubble diameter. In the final simulation 1D*, besides the Sauter diameter, the gas holdup and mass transfer rate were adjusted accordingly. (Recited from Siebler et al., 2020, with permission of © Wiley-VICH Engineering in Life Science.)

Average	Variable	1D(F)	CFD	1D(G)	1D*	Unit
CO concentration	$\overline{c}_{L,CO}$	0.018	0.002	0.0016	0.0015	$mmol\,L^{-1}$
gas holdup	$\overline{\varepsilon}_G$	0.31	0.34/0.21[1)]	0.31	**0.21**	–
diameter	$\overline{d}_B$	4.4	20.9[2)]	**20.9**	**20.9**	mm
bubble surface	$\overline{a}$	408.3	61.8	86.9	59.1	m^{-1}
mass transfer rate	$\overline{k_L}$	3.93	1.75	3.93	**1.75**	$e^{-4}\,m\,s^{-1}$
vol. mass transfer rate	$\overline{k_L a}$	578	39	123	37	h^{-1}
product biomass yield	$\overline{Y}_{P,X}$	1.5	0.9	1.3	1.4	–

[1)] second value with breakage, coalescence, bubble expansions and mass transfer, [2)] Sauter mean for CFD

Initially both models are used for different purposes. However, it might be interesting to compare and discuss their results. In Table 6.2 the most important average results of the 1D simulation **F** is compared with the CFD outcome. Additionally, two further 1D simulations were subsequently performed and listed.

In the first two columns of Table 6.2 the final results of both models are listed. Almost every value except the mean diameter $\overline{d}_B$ of the 1D(F) simulation is much higher than the CFD results. Besides the average values of Table 6.2 also the spatial differences are illustrated in Figure 6.21.

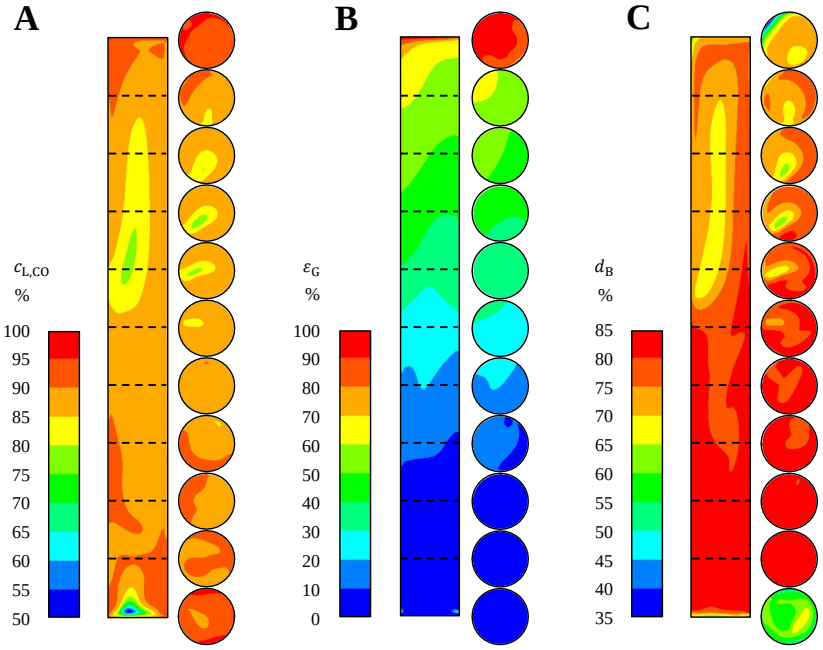

Figure 6.21: Differences between 1D and CFD simulation over reactor height. Pictured are concentration $c_{L,CO}$ (A), gas hold-up ε_G (B) and mean diameter d_B (C) deviations in percentage. In (A) $100\%-c^{CFD}_{L,CO}(z)/c^{1D}_{L,CO}(z)\cdot 100\%$ is shown which translates high similarity into low values. By analogy, graphic (B) is set. In (C) the criterion $100\%-d^{1D}_B(z)/d^{CFD}_B(z)\cdot 100\%$ was applied to avoid negative values. Still, high percentages encode large deviations. (Reprinted and modified from Siebler et al., 2020, with permission of © Wiley-VICH Engineering in Life Science.)

In Figure 6.21 the difference in percentage of both approaches between dissolved CO concentration, gas holdup and bubble diameter are illustrated.

In general, the deviation is rather high for each comparison. CO levels are almost everywhere overestimated (Figure 6.21 (A)) while the gas holdups of 1D(F) and CFD are similar in at least the lower parts of the bubble column reactor (Figure 6.21 (B)). The strongest deviation occurs for the diameter (Figure 6.21 (C)), which is also reflected by the average values of Table 6.2. Moreover, Figure 6.21 not only visualises discrepancies over the reactor height but also in the radial direction (section planes).

According to these findings, the initial diameter of the 1-dimensional model is adjusted to reach the same average value as for the CFD simulation (Table 6.2 1D(G)). Besides the underestimated diameter with the greatest deviation in Figure 6.21, another 1D simulation is performed by adjusting also the gas holdup $\bar{\varepsilon}_G$ and mass transfer rate k_L (Table 6.2 1D*). These adjustments are graphically compared and displayed in Figure 6.22.

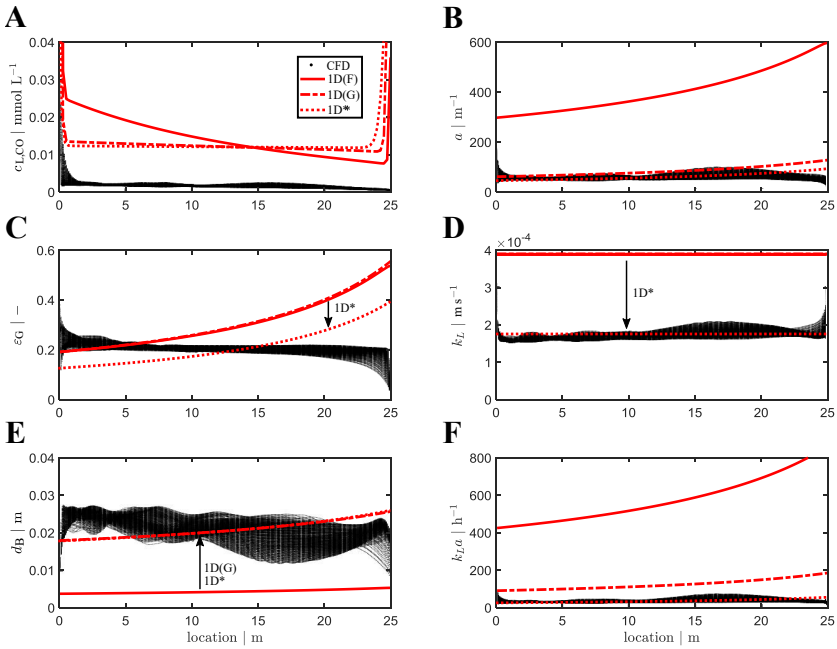

Figure 6.22: Profiles over reactor height in comparison. Each graph depicts profiles of CFD (dots) and 1D (red lines) simulation. In case of CFD, each dot represents values of individual numerical cells, thereby visualising the varying conditions at each column height. (A) to (F) compare dissolved CO concentration $c_{L,CO}$, bubble area a, gas hold-up ε_G, mass transfer rate k_L, bubble diameter d_B and volumetric mass transfer $k_L a$. (Reprinted from Siebler et al., 2020, with permission of © Wiley-VICH Engineering in Life Science.)

In Figure 6.22 the same representation method as in Figure 6.11 (B) is chosen. Besides the 1D results over reactor height, also the CFD results are shown as scatter plot while each dot represents values of individual numerical cells. By adjusting the average diameter as in 1D(G), the interfacial area concentration a also decreases and consequently the volumetric mass transfer rate $k_L a$ (see Figure 6.22 (B), (E) and (F)). The gas holdup ε_G and mass transfer rate k_L are still far from the CFD results. In a final 1D* simulation, these values are adjusted as well (see Figure 6.22 (C) and (D)). The gas holdup adjustment affects a directly and together with k_L they cause a lower $k_L a$ with $37\,h^{-1}$, which is almost the same value as for the CFD simulation ($39\,h^{-1}$). However, the general gas holdup and diameter trends of the 1D simulations are spatially very different from the CFD results.

The 1D approach clearly lacks mechanistic details of modelling bubble size distributions. Important bubble functions for breakage and mainly coalescence are not considered. This leads to severe overestimation of the volumetric mass transfer rate which is reflected in the small bubble diameters d_B. In other words, 1D(G) predicts too high CO concentrations and therefore product biomass yields. When bubble size distributions and functions for breakage and coalescence are not included, a proper average bubble diameter should be considered to give reasonable mass transfer predictions.

As mentioned previously in chapter 4.1, churn-turbulent heterogeneous bubbly flow occurs when a critical gas holdup value is reached (for water $\varepsilon_{crit} = 0.3$). This heterogeneous flow regime is rendered by the CFD simulation, which is indicated by the bubble size distributions in Figure 6.22 (E). Moreover, turbulent flow patterns in combination with different bubble sizes cause locally changing gas holdups. These effects can not be reproduced by the one dimensional 1D model. Homogeneous bubbly flow and gas holdup assumption up to $\bar{\varepsilon}_G = 0.31$ are too optimistic but can be adapted by the high resolution CFD results.

In summary, both models have their advantages and disadvantages. Together, they complement each other and enable large-scale bubble column prediction to narrow down the optimum industrial scale scenario.

Chapter 7

Conclusion and outlook

A summary of all results, a reflection on their implications and their research contribution is presented in this chapter. The conclusion is structured in the same three main parts which are outlined at the beginning of the thesis (1.3. Objectives, strategy and thesis outline). All research questions are addressed in this context followed by suggestions concerning future research. Some information of this chapter was also published in Siebler at al. (2019; 2020).

(A) Pre-evaluation of industrial reactor design

In scale-up as in many other disciplines, the technically possible needs to be balanced with the economically reasonable. The first part of the thesis deals exactly with this estimation by pre-evaluating the synthesis gas process. Two research questions have been formulated (see chapter 1.3) addressing this topic. Their research answers (RA) can be summarised as follows:

RA3.1 Based on the developed rating system, bubble column, airlift, membrane and trickled bed reactors are most suitable for synthesis gas fermentations.

RA3.2 The industrial application of synthesis gas fermentation is economically feasible if sufficient amounts of complex and high energy carbon hydrates are produced.

In chapter 3 both questions are analysed in detail. First, an overview of reactors used in syngas fermentations, including some unconventional reactors variations/ designs, is given. A rating system is developed to compare and finally assess each reactor for industrial application. Additionally, a focus was set on expected reactor performance and expenses in scale-up.

The evaluation results in bubble columns being one of the most feasible reactor types. That is why they are investigated in greater detail. Nevertheless, the final choice can be adjusted depending on the products and their yields. In case of the second question, possible fermentation products are listed and analysed according to their conserved energy and market price. While products with higher complexity such as isobutanol or 2,3-butanediol currently achieve very high stock prices, more common products such as acetate and ethanol are comparatively cheap. Long chain carbon hydrates are usually high-energy products. However, the stored energy is not necessarily proportional to the rates. In addition, product purity and general complexity of the production have a great influence on the price. With both values for educts and products as well as the annual production, expected profits per year can be estimated. An example of this assessment of potential was calculated for an already existing industrial process from LanzaTech producing ethanol with up to 109.2 Mio USD profit per year. The model strain *Clostridium ljungdahlii* produces, 2,3-butanediol besides its main products acetate and ethanol. Alongside the general recycling aspect, the additional product makes synthesis gas fermentations lucrative.

The next research questions are answered by further investigating the chosen bubble column reactor. This resulted in the following statements:

RA4.1 Crucial characteristics of bubble column reactor are the possible occurrence of bubble coalescence and the overall gas holdup.

RA4.2 A fast 1-dimensional (1D) approach for parameter probing and a high-resolution computational fluid dynamics approach for cell behaviour evaluation seem to be appropriate scale-up tools.

Fortunately, in the case of bubble column reactors, a lot of information is available in published literature. Generally, gas-liquid two-phase systems are very complex. Some parameters have a greater impact on performance than others. Their dependencies and importance were stated as well as parameters highlighted which can be adjusted in order to achieve the best performance outcome (see chapter 4.1). Additionally, background information was given about flow behaviour and flow regimes. In summary, the most desired flow regime would be the homogeneous bubbly flow which not necessarily forms when the gas holdup exceeds 30%. Small uniform bubbles assure high mass transfer areas and thorough mixing of the liquid.

The two model approaches were chosen according to currently available computing power and their scope of applicability. While computational fluid dynamic (CFD) analysis can solve physical multi-phase problems with an

adequate level of detail, simplified models are potentially faster and less computationally demanding. During the selection process, the applicability of biological behaviour in addition to the fluid flow models was taken into account, too (see chapter 4.2). Simple one-dimensional 1-dimensional (1D) approaches can even include genome-scale kinetic models, which is still challenging with CFD. Besides the computing speed, 1D models can temporally solve the whole fermentation process within minutes. It is for this reason that 1D model was chosen to scan different start conditions for an optimal parameter set which then was used in the more detailed CFD simulation. The latter not only models the gas fermentation more properly but also allows statistical cell behaviour analysis. Combining both modelling approaches narrows down the most efficient scale-up scenario and therefore reduces the risk of performance loss.

Both modelling tools make use of existing approaches but are adjusted or derived in a more suitable way while targeting the issues of gas fermentations. It is for this reason that both the model derivation, model set-up and the simulation findings are equally important steps of this thesis. The summary of the last RAs is therefore grouped according to the risk minimisation concept and finally concluded by the last RA. In both cases, the chosen reactor volume is 125 m^3 with a high to diameter ratio of around 10 reaching a pressure of 3.5 atm at the bottom of the bubble column.

(B) 1-dimensional approach

In general, models are used for predictions and reducing experimental efforts. The more physical equations are solved, the more accurate the prediction. However, model reduction can have important advantages. The 1-dimensional approach includes a kinetic correlation maintaining the element balances of carbon, hydrogen and oxygen of the overall chemical reaction. After a brief excursus whether diffusion is limiting or not, the next two research answers can be summarised as follows:

RA4.3 By considering an additional partial differential equation, the focus of the 1-dimensional model is set on the gas holdup as well. The equation takes the total molar density of the gas mixture into account.

RA6.1 The 1-dimensional approach revealed that for the chosen set-up inhibition due to carbon monoxide excess is not an issue but the mass transfer from gas to liquid phase. In addition, the performed

parameter probing provided the optimal start conditions for the CFD simulations.

In chapter 4.3, the model approach is described in detail, resulting in partial differential equations for bacterial growth on carbon monoxide in synthesis gas mixture: CO and CO_2 in gas and liquid phase as well as the gas holdup. Assuming an ideally mixed liquid phase, four ordinary differential equations are solved, too. Spatial and temporal discretisation are chosen appropriately with simulation times under five minutes and a resolution of 100 numerical volumes respectively compartments. The code was written and executed in Matlab®. With this set-up, about 120 different start parameters are investigated within a reasonable probing space derived from published experimental values (see chapter 6.1).

The sensitivity of the 1-dimensional model is examined highlighting the importance of proper start parameters. The additional modelling of the gas holdup proves to be of importance and should not be disregarded. It even turned out to be the parameter with the widest influence on process performance directly followed by mass transfer. With this set-up, variations of the carbon monoxide fraction and the gassing rate have no effect on physical parameters such as gas holdup, mass transfer and bubble diameter. On the contrary, they change the biological performance index of total bound carbon and product biomass yields. As mentioned before, this analysis indicates the best operation mode for the chosen parameter ranges. In addition to that, the kinetic inhibition due to carbon monoxide excess will not occur under these conditions. However, the mass transfer from gas to liquid phase is the limiting factor. Besides a better understanding of the process and general operation suggestions, the results are mainly used in the next refinement step: the computational fluid dynamics analysis.

(C) Computational fluid dynamics approach

As mentioned before, computing power still restricts direct simulations of physical multiphase flows. For this reason, models are used which approximate some of these physical effects. Models usually are limited within a certain range of parameters in which they are valid. This is proven by either experimental or numerical validation with direct numerical simulations. Even though a validation of the applied models is beyond the scope of this thesis, they raise valid and important questions concerning computational fluid dynamics. Their answers can be summarised as follows:

RA4.4 An Euler-Euler multiphase approach including breakage and coalescence is appropriate for bubble column CFD simulations. Lagrangian trajectories are a suitable tool for bacterial lifelines analysis to predict biological effects.

RA6.2 The CFD results reveal mixing and circulation time, the gas gradient and substrate limitation zones as well as the bacterial short- and long-term responses under these CO limiting conditions.

Background information on the main models is given in chapter 4.4 from which the final modelling set-up is selected: The turbulence is modelled using the RANS equations combined with the RNG- k-ε-model, all within the Euler-Euler multiphase approach. Mainly pre-programmed models and functions of ANSYS Fluent are combined, self-implemented code as well as adjustments are introduced in chapter 5.3. It is noteworthy that meshing allows solving breakage and coalescence, which have a great effect on the mass transfer. Both have a significant influence on the gas holdup and substrate availability. The Lagrangian trajectories method was chosen to predict the effect of CO insufficiencies on *Clostridium ljungdahlii*. In a previous study, this method was established with another strain (see chapter 4.4.5 and Manuscript I).

While the CFD results are already published in Siebler et al. (2019), the conclusion is only a short repetition thereof (more information can be found in Manuscript II). The CFD simulation revealed a well-mixed bubble column with average circulation times of about 10 seconds. Compared to conventional stirred tank reactors, less power is needed for similar circulation times. In respect to that, the bubble column reactor a good alternative to additionally agitated processes. On the other hand, strong coalescence of the bubbles lead to an average Sauter mean bubble diameter of about 2.1 cm reducing the overall mass transfer. For the first time, a pseudo-stationary gas gradient was successfully examined with the statistical Lagrangian trajectories method for *Clostridium ljungdahlii* in an anaerobic, synthesis gas operated bubble column. The regime transition analysis as well as short- and long-term responses indicate that most of microorganisms suffer from an insufficient CO supply. Improvements in CO mass transfer as well as engineering the strains to cope with these stress conditions are advisable. For higher biomass concentrations and even more active cells, the CO gradient is most likely intensified making further engineering studies necessary in order to improve the synthesis gas process.

Initially, the 1D and CFD model were chosen for different purposes but in the end, they solve similar problems with different resolutions. For this

reason, the last research question was formulated which can be answered as follows:

RA6.3 Properly estimated parameters from CFD simulations help to improve 1D model predictions, especially for highly relevant biological readouts such as product-biomass yields.

In respect to Figure 1.1 of the thesis introduction, the results of the risk minimisation concept is concluded in Figure 7.1. With the real scale-up optimum as goal, the presented concept narrows down all possible results (abstract parameter spaces of Figure 7.1) towards the best solution.

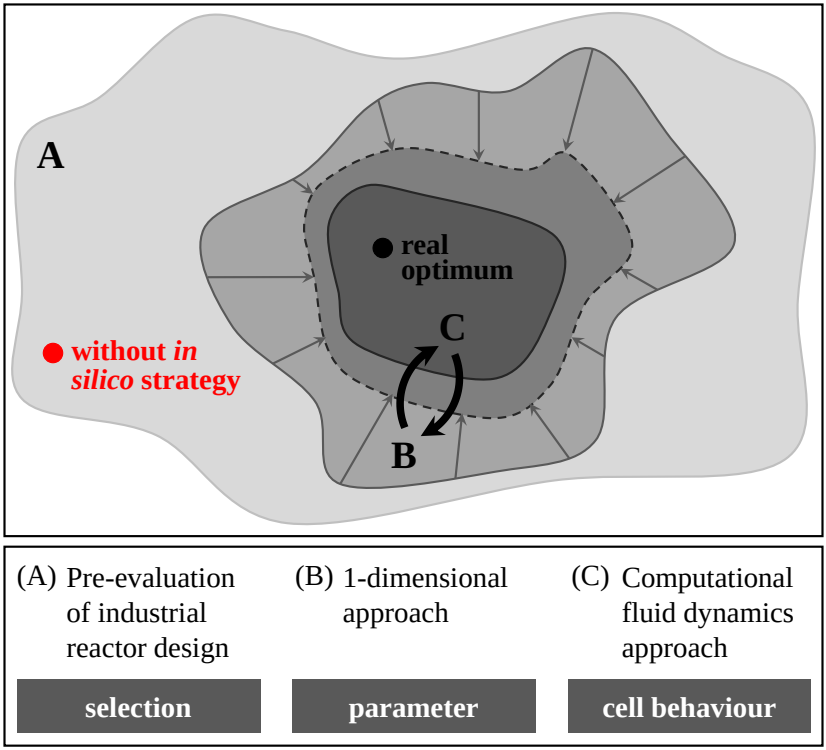

Figure 7.1: Result abstraction of the risk minimisation concept. The real scale-up optimum (black circle) is unknown and approximated by the presented concept (A)-(C). In red the possible scale-up solution without the presented *in silico* strategy is indicated. The grey areas indicate their abstract parameter spaces. The arrows between (B) and (C) indicate the synergistic potential of both methods with the final adaptation (dashed line) of the solution space of (B).

CFD simulations offer the most accurate solution for the prediction of physical and biological readouts in large-scale bioreactor fermentations (see Figure 7.1 (C) in dark grey). However, they are comparatively complex and computationally expensive and therefore limited to solve only pre-evaluated problems. Conceptual design approaches such as the 1-dimensional approach can search through parameter spaces of putative operational windows (see Figure 7.1 (A)) and thus narrow down the initial values and operation mode for CFD (see Figure 7.1 (B)). Without doubt, physical readouts of the 1D model are most likely overestimated but can be adjusted by considering the results of CFD (see Figure 7.1 adaptation of solution space of (B)). Finally, combining the advantages of both models improve their respective accuracy resulting in reliable findings, obtainable with reasonable effort.

Focus of future work

The models and work of this thesis provide a sound foundation for future research. A first step could be to establish a kinetic correlation for the growth of *Clostridium ljungdahlii* in an CO_2/H_2 environment. This then could be combined with the presented correlation for CO and finally be implemented into the models as a multi-substrate kinetic. By doing so, all carbon of the synthesis gas is bound as product and biomass, reducing the carbon emissions. The multi-substrate kinetic should be validated by further experiments. Especially, the critical CO concentration needs to be found when the organism switches form the preferred CO consumption to the CO_2/H_2 consumption.

With this new kinetic correlation, further possibilities for additional investigation using the 1-dimensional model arise. First of all, produced CO_2 can additionally be converted and secondly, off-gas circulation strategies can be investigated. It is recommended to use gas recycling ports at different reactor heights for optimum carbon exploitation. Besides the simple kinetic correlation, it is also possible to include profound stoichiometric models. These models exist for *C. ljungdahlii* but need further improvements to be of use for the 1D model.

As for the CFD approach, future work should focus on properly predicting physical and biological effects since the lifeline analysis depends strongly on them. In general, multiphase simulations are still very challenging. While the k-ε-model is a commonly applied approach for estimating turbulent flow, it is not impeccable. Moreover, inaccuracies while calculating the energy

dissipation can propagate affecting the prediction of breakage and coalescence respectively the volumetric mass transfer. It is for this reason, that these models need ongoing improvement in form of fundamental research while considering particularities of biotechnological applications (e.g. media compositions). With the help of experimental bubble size distribution and volumetric mass transfer measurements, their accuracy can be examined. Additionally, the effect of the mesh resolution on a pseudo-stationary substrate gradient is worth investigating.

Lifeline analysis is a very promising investigation tool. This method depends on the real stress response of *C. ljungdahlii*, which so far has not been investigated experimentally so far. Scale-down fermentations with plug-flow and cascade reactors can be conducted to find critical concentrations and retention times for this strain. As the gradient is pseudo-stationary, the flow filed for bubble column reactors is fluctuating, thus numerical studies seem to be appropriate to identify the effect of different frozen flow fields on the statistical analysis.

As indicated while comparing both models, iteratively apply their results to the other model show synergistic potential. The 1D model is used for the high-resolution simulation set-up and benefits subsequently from the CFD results. This iterative 'model-training' can be continued to further narrow down the real scale-up optimum. Furthermore, the risk minimisation concept can be applied to other reactor geometries and set-ups. Depending on the complexity of the reactor only few adjustments are required. The airlift reactor for example only needs the implementation of a reverse flow in the 1D model for the downcomer. On the other hand, membrane and trickle bed reactors are more complex and required further adaptations or even other model approaches. When the best performing reactor and set-up is approximated, a final budget calculation can be performed.

Chapter 8

Bibliography

Articles

Abrini, J., Naveau, H., and Nyns, E.-J. (1994). "*Clostridium autoethanogenum*, sp. nov., an anaerobic bacterium that produces ethanol from carbon monoxide." In: *Archives of Microbiology* 161.4, pp. 345–351.

Abubackar, H. N., Veiga, M. C., and Kennes, C. (2011). "Biological conversion of carbon monoxide: rich syngas or waste gases to bioethanol." In: *Biofuels, Bioproducts and Biorefining* 5.1, pp. 93–114.

Akita, K. and Yoshida, F. (1973). "Gas Holdup and Volumetric Mass Transfer Coefficient in Bubble Columns. Effects of Liquid Properties." In: *Industrial & Engineering Chemistry Process Design and Development* 12.1, pp. 76–80.

Alves, S. S., Vasconcelos, J. M. T., and Orvalho, S. P. (2006). "Mass transfer to clean bubbles at low turbulent energy dissipation." In: *Chemical Engineering Science* 61.4, pp. 1334–1337.

Andreesen, J. R., Gottschalk, G., and Schlegel, H. G. (1970). "*Clostridium formicoaceticum* nov. spec. Isolation , Description and Distinction from *C . aceticum* and *C . thermoaceticum*." In: *Archives of Microbiology* 72.2, pp. 154–174.

Andreesen, J. R., Schaupp, A., Neurauter, C., Brown, A., and Ljungdahl, L. G. (1973). "Fermentation of glucose, fructose, and xylose by *Clostridium thermoaceticum*: effect of metals on growth yield, enzymes, and the synthesis of acetate from CO_2." In: *Journal of Bacteriology* 114.2, pp. 743–751.

Antal, S. P., Lahey Jr, R. T., and Flaherty, J. E. (1991). "Analysis of phase distribution in fully developed laminar bubbly two-phase flow." In: *International Journal of Multiphase Flow* 17.5, pp. 635–652.

Arnold, S., Moss, K., Henkel, M., and Hausmann, R. (2017). "Biotechnological Perspectives of Pyrolysis Oil for a Bio-Based Economy." In: *Trends in Biotechnology* 35.10, pp. 925–936.

Bache, R. and Pfennig, N. (1981). "Selective Isolation of *Acetobacterium woodii* on Methoxylated Aromatic Acids and Determination of Growth Yields." In: *Archives of Microbiology* 130.3, pp. 255–261.

Balch, W. E., Schoberth, S., Tanner, R. S., and Wolfe, R. S. (1977). "*Acetobacterium*, a New Genus of Hydrogen-Oxidizing, Carbon Dioxide-Reducing, Anaerobic Bacteria." In: *International Journal of Systematic Bacteriology* 27.4, pp. 355–361.

Bengelsdorf, F. R. and Dürre, P. (2017). "Gas fermentation for commodity chemicals and fuels." In: *Microbial Biotechnology* 10.5, pp. 1167–1170.

Bengelsdorf, F. R., Poehlein, A., Esser, C., Schiel-Bengelsdorf, B., Daniel, R., and Dürre, P. (2015). "Complete Genome Sequence of the Type Strain of the Acetogenic Bacterium *Moorella thermoacetica* DSM 2955^T." In: *Genome Announcements* 3.5, e01157–15.

Bouaifi, M., Hebrard, G., Bastoul, D., and Roustan, M. (2001). "A comparative study of gas hold-up, bubble size, interfacial area and mass transfer coefficients in stirred gas-liquid reactors and bubble columns." In: *Chemical Engineering and Processing* 40.2, pp. 97–111.

Bredwell, M. D. and Worden, R. M. (1998). "Mass-transfer properties of microbubbles. 1. Experimental studies." In: *Biotechnology Progress* 14.1, pp. 31–38.

Brown, S. D., Nagaraju, S., Utturkar, S., De Tissera, S., Segovia, S., Mitchell, W., Land, M. L, Dassanayake, A., and Köpke, M. (2014). "Comparison of single-molecule sequencing and hybrid approaches for finishing the genome of *Clostridium autoethanogenum* and analysis of CRISPR systems in industrial relevant Clostridia." In: *Biotechnology for Biofuels* 7. 40.

Burns, A. D., Frank, T., Hamill, I., and Shi, J.-M. (2004). "The Favre Averaged Drag Model for Turbulent Dispersion in Eulerian Multi-Phase Flows." In: *Fifth International Conference on Multiphase Flow, ICMF* 392, pp. 1–17.

Charpentier, J.-C. (1981). "Mass-transfer rates in gas-liquid absorbers and reactors." In: *Advances in chemical engineering* 11, pp. 1–133.

Chen, J., Gomez, J. A., Höffner, K., Barton, P. I., and Henson, M. A. (2015). "Metabolic modeling of synthesis gas fermentation in bubble column reactors." In: *Biotechnology for biofuels* 8. 89.

Chen, J., Gomez, J. A., Höffner, K., Phalak, P., Barton, P. I., and Henson, M. A. (2016). "Spatiotemporal modeling of microbial metabolism." In: *BMC Systems Biology* 10. 21.

Chen, J., Daniell, J., Griffin, D., Li, X., and Henson, M. A. (2018). "Experimental testing of a spatiotemporal metabolic model for carbon monoxide fermentation with *Clostridium autoethanogenum*." In: *Biochemical Engineering Journal* 129, pp. 64–73.

Chen, S., Beeby, M., Murphy, G. E., Leadbetter, J. R., Hendrixson, D. R., Briegel, A., Li, Z., Shi, J., Tocheva, E. I., Müller, A., Dobro, M. J., and Jensen, G. J. (2011). "Structural diversity of bacterial flagellar motors." In: *The EMBO Journal* 30, pp. 2972–2981.

Danckwerts, P. V. (1951). "Significance of liquid-film coefficients in gas adsorption." In: *Industrial and Engineering Chemistry* 43.6, pp. 1460–1467.

Daniel, S. L., Hsu, T., Dean, S. I., and Drake, H. L. (1990). "Characterization of the H_2- and CO-dependent chemolithotrophic potentials of the acetogens *Clostridium*

thermoaceticum and *Acetogenium kivui*." In: *Journal of Bacteriology* 172.8, pp. 4464–4471.

Daniell, J., Köpke, M.l, and Simpson, S. D. (2012). "Commercial biomass syngas fermentation." In: *Energies* 5.12, pp. 5372–5417.

Datar, R. P., Shenkman, R. M., Cateni, B. G., Huhnke, R. L., and Lewis, R. S. (2004). "Fermentation of biomass-generated producer gas to ethanol." In: *Biotechnology and Bioengineering* 86.5, pp. 587–594.

Deckwer, W. D., Louisi, Y., Zaidi, A., and Ralek, M. (1980). "Hydrodynamic Properties of the Fischer-Tropsch Slurry Process." In: *Industrial and Engineering Chemistry Process Design and Development* 19.4, pp. 699–708.

Diender, M., Stams, A. J M., and Sousa, D. Z. (2015). "Pathways and Bioenergetics of Anaerobic Carbon Monoxide Fermentation". In: *Frontiers in Microbiology* 6. 1275.

Drake, H. L., Gößner, A. S., and Daniel, S. L. (2008). "Old Acetogens , New Light". In: *Annals of the New York Academy of Sciences* 1125.1, pp. 1–54.

Dürre, P. (2016). "Butanol formation from gaseous substrates." In: *FEMS Microbiology Letters* 363.6, fnw040.

Enfors, S.-O., Jahic, M., Rozkov, A., Xu, B., Hecker, M., Jürgen, B., Krüger, E., Schweder, T., Hamer, G., O'Beirne, D., Noisommit-Rizzi, N., Reuss, M., Boone, L., Hewitt, C., McFarlane, C., Nienow, A., Kovacs, T., Trägårdh, C., Fuchs, L., Revstedt, J., Friberg, P. C., Hjertager, B., Blomsten, G., Skogman, H., Hjort, S., Hoeks, F., Lin, H.-Y., Neubauer, P., van der Lans, R., Luyben, K., Vrabel, P., and Manelius, Å. (2001). "Physiological responses to mixing in large scale bioreactors." In: *Journal of Biotechnology* 85.2, pp. 175–185.

Fadavi, A. and Chisti, Y. (2005). "Gas–liquid mass transfer in a novel forced circulation loop reactor." In: *Chemical Engineering Journal* 112.1-3, pp. 73–80.

Fernández-Prini, R., Alvarez, J. L., and Harvey, A. H. (2003). "Henry's Constants and Vapor–Liquid Distribution Constants for Gaseous Solutes in H_2O and D_2O at High Temperatures." In: *Journal of Physical and Chemical Reference Data* 32.2, pp. 903–916.

Fontaine, F. E., Peterson, W. H., McCoy, E., Johnson, M. J., and Ritter, G. J. (1942). "A New Type of Glucose Fermentation by *Clostridium thermoaceticum*." In: *Journal of bacteriology* 43.6, pp. 701–715.

Gibson, B., Wilson, D. J., Feil, E., and Eyre-Walker, A. (2018). "The distribution of bacterial doubling times in the wild." In: *Proceedings of the Royal Society B: Biological Sciences* 285.1880, p. 20180789.

Gomez, J. A., Höffner, K., and Barton, P. I. (2014). "DFBAlab: a fast and reliable MATLAB code for dynamic flux balance analysis." In: *BioMed Central bioinformatics* 15. 409.

Gößner, A. S., Devereux, R., Ohnemüller, N., Acker, G., Stackebrandt, E., and Drake, H. L. (1999). "*Thermicanus aegyptius* gen. no.v, sp. nov., isolated from oxic soil, a fermentative microaerophile that grows commensally with the thermophilic acetogen *Moorella thermoacetica*." In: *Applied and Environmental Microbiology* 65.11, pp. 5124–5133.

Gößner, A. S., Picardal, F., Tanner, R. S., and Drake, H. L. (2008). "Carbon metabolism of the moderately acid-tolerant acetogen *Clostridium drakei* isolated from peat." In: *FEMS Microbiology Letters* 287.2, pp. 236–242.

Grace, J. R. (1973). "Shapes and velocities of bubbles rising in infinite liquids." In: *Transactions of the Institution of Chemical Engineers* 51, pp. 116–120.

Griffin, D. W. and Schultz, M. A. (2012). "Fuel and Chemical Products from Biomass Syngas: A Comparison of Gas Fermentation to Thermochemical Conversion Routes." In: *Environmental Progress and Sustainable Energy* 31.2, pp. 219–224.

Hagesaether, L., Jakobsen, H. A., and Svendsen, H. F. (2002). "A model for turbulent binary breakup of dispersed fluid particles." In: *Chemical Engineering Science* 57.16, pp. 3251–3267.

Haringa, C., Tang, W., Deshmukh, A. T., Xia, J., Reuss, M., Heijnen, J. J., Mudde, R. F., and Noorman, H. J. (2016). "Euler-Lagrange computational fluid dynamics for (bio)reactor scale-down: an analysis of organism life-lines." In: *Engineering in Life Sciences* 16.7, pp. 652–663.

Haringa, C., Deshmukh, A. T., Mudde, R. F., and Noorman, H. J. (2017). "Euler-Lagrange analysis towards representative down-scaling of a 22 m^3 aerobic *S. cerevisiae* fermentation." In: *Chemical Engineering Science* 170, pp. 653–669.

Haringa, C., Tang, W., Wang, G., Deshmukh, A. T., van Winden, W. A., Chu, Ju, van Gulik, W. M., Heijnen, J. J., Mudde, R. F., and Noorman, H. J. (2018a). "Computational fluid dynamics simulation of an industrial *P. chrysogenum* fermentation with a coupled 9-pool metabolic model: Towards rational scale-down and design optimization." In: *Chemical Engineering Science* 175, pp. 12–24.

Haringa, C., Vandewijer, R., and Mudde, R. F. (2018b). "Inter-compartment interaction in multi-impeller mixing part II : Experiments, Sliding mesh and Large Eddy Simulations." In: *Chemical Engineering Research and Design* 136, pp. 886–899.

Heijnen, J. J. and Van't Riet, K. (1984). "Mass Transfer, Mixing and Heat Transfer Phenomena in Low Viscosity Bubble Column Reactors." In: *The Chemical Engineering Journal* 28.2, B21–B42.

Heins, A.-L., Lencastre Fernandes, R., Gernaey, K. V., and Lantz, A. E. (2015). "Experimental and *in silico* investigation of population heterogeneity in continuous *Sachharomyces cerevisiae* scale-down fermentation in a two-compartment setup." In: *Journal of Chemical Technology and Biotechnology* 90.2, pp. 324–340.

Henson, M. A. (2003). "Dynamic modeling of microbial cell populations." In: *Current Opinion in Biotechnology* 14.5, pp. 460–467.

Higbie, R. (1935). "The rate of absorption of a pure gas into a still liquid during short periods of exposure." In: *Transactions of the American Institute of Chemical Engineers* 31, pp. 365–389.

Hoffart, E., Grenz, S., Lange, J., Nitschel, R., Müller, F., Schwentner, A., Feith, A., Lenfers-Lücker, M., Takors, R., and Blombach, B. (2017). "High Substrate Uptake Rates Empower *Vibrio natriegens* as Production Host for Industrial Biotechnology." In: *Applied and Environmental Microbiology* 83.22. e01614-17.

Hu, P., Bowen, S. H., and Lewis, R. S. (2011). "A thermodynamic analysis of electron production during syngas fermentation." In: *Bioresource Technology* 102.17, pp. 8071–8076.

Hu, P., Chakraborty, S., Kumar, A., Woolston, B., Liu, H., Emerson, D., and Stephanopoulos, G. (2016). "Integrated bioprocess for conversion of gaseous substrates to liquids." In: *Proceedings of the National Academy of Sciences* 113.14, pp. 3773–3778.

Huang, Q., Yang, C., Yu, G., and Mao, Z.-S. (2010). "CFD simulation of hydrodynamics and mass transfer in an internal airlift loop reactor using a steady two-fluid model." In: *Chemical Engineering Science* 65.20, pp. 5527–5536.

Jeong, Y., Song, Y., Shin, H. S., and Cho, B.-K. (2014). "Draft Genome Sequence of Acid-Tolerant *Clostridium drakei* $SL1^T$, a Potential Chemical Producer through Syngas Fermentation." In: *Genome Announcements* 2.3, e00387–14.

Kaiser, S. C., Kraume, M., and Eibl, D. (2013). "Development of the travelling wave bioreactor - A concept study." In: *Chemie Ingenieur Technik* 85.1-2, pp. 136–143.

Kane, M. D., Bauman, A., and Breznak, J. A (1991). "*Clostridium mayombei* sp. nov., an H_2/CO_2 acetogenic bacterium from the gut of the African soil-feeding termite, *Cubitermes speciosus*." In: *Archives of Microbiology* 156.2, pp. 99–104.

Kantarci, N., Borak, F., and Ulgen, K. O. (2005). "Bubble column reactors". In: *Process Biochemistry* 40, pp. 2263–2283.

Kerby, R. and Zeikus, J. G. (1983). "Growth of *Clostridium thermoaceticum* on H_2/CO_2 as Energy Source." In: *Current Microbiology* 8.1, pp. 27–30.

Klasson, K. T., Ackerson, M. D., Clausen, E. C., and Gaddy, J. L. (1991). "Bioreactors for synthesis gas fermentations." In: *Resources, Conservation and Recycling* 5.2-3, pp. 145–165.

Köpke, M., Held, C., Hujer, S., Liesegang, H., Wiezer, A., Wollherr, A., Ehrenreich, A., Liebl, W., Gottschalk, G., and Dürre, P. (2010). "*Clostridium ljungdahlii* represents a microbial production platform based on syngas." In: *Proceedings of the National Academy of Sciences of the United States of America* 107.29, pp. 13087–13092.

Köpke, M., Mihalcea, C., Liew, F. M., Tizard, J.H., Ali, M. S., Conolly, J. J., Al-Sinawi, B., and Simpson, S. D. (2011). "2,3-Butanediol production by acetogenic bacteria, an alternative route to chemical synthesis, using industrial waste gas." In: *Applied and Environmental Microbiology* 77.15, pp. 5467–5475.

Krishna, R. and Sie, S. T. (2000). "Design and scale-up of the Fischer–Tropsch bubble column slurry reactor." In: *Fuel Processing Technology* 64, pp. 73–105.

Krumholz, L. R. and Bryant, M. P. (1985). "*Clostridium pfennigii* sp. nov. Uses Methoxyl Groups of Monobenzenoids and Produces Butyrate." In: *International Journal of Systematic Bacteriology* 35.4, pp. 454–456.

Kumar, S. and Ramkrishna, D. (1996). "On the solution of population balance equations by discretization - I. A fixed pivot technique." In: *Chemical Engineering Science* 51.8, pp. 1311–1332.

Kuschel, M., Siebler, F., and Takors, R. (2017). "Lagrangian Trajectories to Predict the Formation of Population Heterogeneity in Large-Scale Bioreactors." In: *Bioengineering* 4.2. 27.

Küsel, K., Dorsch, T., Acker, G., Stackebrandt, E., and Drake, H. L. (2000). "*Clostridium scatologenes* strain SL1 isolated as an acetogenic bacterium from acidic sediments." In: *International Journal of Systematic and Evolutionary Microbiology* 50.2, pp. 537–546.

Lamont, J. C. and Scott, D. S. (1970). "An eddy cell model of mass transfer into surface of a turbulent liquid." In: *American Institute of Chemical Engineers* 16.4, pp. 513–519.

Lapin, A., Mü1ller, D., and Reuss, M. (2004). "Dynamic Behavior of Microbial Populations in Stirred Bioreactors Simulated with Euler-Lagrange Methods: Traveling along the Lifelines of Single Cells." In: *Industrial and Engineering Chemistry Research* 43.16, pp. 4647–4656.

Latif, H., Zeidan, A. A., Nielsen, A. T., and K., Zengler (2014). "Trash to treasure: production of biofuels and commodity chemicals via syngas fermenting microorganisms." In: *Current opinion in biotchnology* 27, pp. 79–87.

Launder, B. E. and Spalding, D. B. (1974). "The numerical computation of turbulent flows." In: *Computer Methods in Applied Mechanics and Engineering* 3.2, pp. 269–289.

Lehr, F., Millies, M., and Mewes, D. (2002). "Bubble size distributions and flow fields in bubble columns." In: *American Institute of Chemical Engineers Journal* 48.11, pp. 2426–2443.

Li, J., Zhu, D., Niu, J., Shen, S., and Wang, G. (2011). "An economic assessment of astaxanthin production by large scale cultivation of *Haematococcus pluvialis*." In: *Biotechnology Advances* 29.6, pp. 568–574.

Liguori, R. and Faraco, V. (2016). "Biological processes for advancing lignocellulosic waste biorefinery by advocating circular economy." In: *Bioresource Technology* 215, pp. 13–20.

Liou, J. S. C., Balkwill, D. L., Drake, G. R., and Tanner, R. S. (2005). "*Clostridium carboxidivorans* sp. nov., a solvent-producing clostridium isolated from an agricultural settling lagoon, and reclassification of the acetogen *Clostridium scatologenes* strain SL1 as *Clostridium drakei* sp. nov." In: *International Journal of Systematic and Evolutionary Microbiology* 55.5, pp. 2085–2091.

Liu, K., Atiyeh, H. K., Stevenson, B. S., Tanner, R. S., Wilkins, M. R., and Huhnke, R. L. (2014a). "Continuous syngas fermentation for the production of ethanol, n-propanol and n-butanol." In: *Bioresource Technology* 151, pp. 69–77.

— (2014b). "Mixed culture syngas fermentation and conversion of carboxylic acids into alcohols." In: *Bioresource Technology* 152, pp. 337–346.

Löffler, M., Simen, J. D., Jäger, G., Schäferhoff, K., Freund, A., and Takors, R. (2016). "Engineering *E. coli* for large-scale production – Strategies considering ATP expenses and transcriptional responses." In: *Metabolic Engineering* 38, pp. 73–85.

Luo, H and Svendsen, H F (1996). "Theoretical Model for Drop and Bubble Breakup in Turbulent Dispersions." In: *The Global Home of Chemical Engineers* 42.5, pp. 1225–1233.

Lux, M. F. and Drake, H. L. (1992). "Re-examination of the metabolic potentials of the acetogens *Clostridium aceticum* and *Clostridium formicoaceticum*: chemolithoautotrophic and aromatic-dependent growth." In: *FEMS Microbiology Letters* 95.1, pp. 49–56.

Lynd, L. H., Kerby, R., and Zeikus, J. G. (1982). "Carbon monoxide metabolism of the methylotrophic acidogen *Butyribacterium methylotrophicum*." In: *Journal of Bacteriology* 149.1, pp. 255–263.

Mantzaris, N. V., Liou, J.-J., Daoutidis, P., and Srienc, F. (1999). "Numerical solution of a mass structured cell population balance model in an environment of changing substrate concentration." In: *Journal of Bacteriology* 71.1-3, pp. 157–174.

Mechichi, T., Labat, M., Woo, T. H. S., Thomas, P., Garcia, J.-L., and Patel, B. K. C. (1998). "*Eubacterium aggregans* sp. nov., a New Homoacetogenic Bacterium from Olive Mill Wastewater Treatment Digestor." In: *Anaerobe* 4.6, pp. 283–291.

Mechichi, T., Labat, M., Patel, B. K. C., Woo, T. H. S., Thomas, P., and Garcia, J.-L. (1999). "*Clostridium methoxybenzovorans* sp. nov., a new aromatic o-demethylating homoacetogen from an olive mill wastewater treatment digester." In: *International Journal of Systematic Bacteriology* 49.3, pp. 1201–1209.

Michalowski, A., Siemann-Herzberg, M., and Takors, R. (2017). "*Escherichia coli* HGT: Engineered for high glucose throughput even under slowly growing or resting conditions." In: *Metabolic Engineering* 40, pp. 93–103.

Mohammadi, M., Mohamed, A. R., Najafpour, G. D., Younesi, H., and Uzir, M. H. (2014). "Kinetic studies on fermentative production of biofuel from synthesis gas using *Clostridium ljungdahlii*." In: *The Scientific World Journal* 2014. 910590.

Munasinghe, P. C. and Khanal, S. K. (2010a). "Biomass-derived syngas fermentation into biofuels: Opportunities and challenges." In: *Bioresource Technology* 101.13, pp. 5013–5022.

— (2010b). "Syngas fermentation to biofuel: Evaluation of carbon monoxide mass transfer coefficient ($k_L a$) in different reactor configurations." In: *Biotechnology Progress* 26.6, pp. 1616–1621.

Nagarajan, H., Sahin, M., Nogales, J., Latif, H., Lovley, D. R., Ebrahim, A., and Zengler, K. (2013). "Characterizing acetogenic metabolism using a genome-scale metabolic reconstruction of *Clostridium ljungdahlii*." In: *Microbial cell factories* 12. 118.

Najafpour, G. and Younesi, H. (2006). "Ethanol and acetate synthesis from waste gas using batch culture of *Clostridium ljungdahlii*." In: *Enzyme and Microbial Technology* 38.1-2, pp. 223–228.

Neubauer, P. and Junne, S. (2010). "Scale-down simulators for metabolic analysis of large-scale bioprocesses." In: *Current Opinion in Biotechnology* 21.1, pp. 114–121.

Neubauer, P., Cruz, N., Glauche, F., Junne, S., Knepper, A., and Raven, M. (2013). "Consistent development of bioprocesses from microliter cultures to the industrial scale." In: *Engineering in Life Sciences* 13.3, pp. 224–238.

Pandit, A. B. and Joshi, J. B. (1983). "Mixing in mechanically agitated gas-liquid contactors, bubble columns and modified bubble columns." In: *Chemical Engineering Science* 38.8, pp. 1189–1215.

Parekh, S. R. and Cheryan, M. (1991). "Applied Microbiology Bioteclmology Production of acetate by mutant strains of *Clostridium thermoaceticum*." In: *Applied microbiology and biotechnology* 36.3, pp. 384–387.

Pfitzer, C., Dahmen, N., Tröger, N., Weirich, F., Sauer, J., Günther, A., and Müller-Hagedorn, M. (2016). "Fast Pyrolysis of Wheat Straw in the Bioliq Pilot Plant." In: *Energy and Fuels* 30.10, pp. 8047–8054.

Philip, J. (2018). "The bioeconomy, the challenge of the century for policy makers." In: *New Biotechnology* 40.Part A, pp. 11–19.

Phillips, J. R., Clausen, E. C., and Gaddy, J. L. (1994). "Synthesis gas as substrate for the biological production of fuels and chemicals." In: *Applied Biochemistry and Biotechnology* 45.1, pp. 145–157.

Phillips, J. R., Atiyeh, H. K., Tanner, R. S., Torres, J. R., Saxena, J., Wilkins, M. R., and Huhnke, R. L. (2015). "Butanol and hexanol production in *Clostridium carboxidivorans* syngas fermentation: Medium development and culture techniques." In: *Bioresource Technology* 190, pp. 114–121.

Phillips, J. R., Huhnke, R. L., and Atiyeh, H. K. (2017). "Syngas Fermentation: A Microbial Conversion Process of Gaseous Substrates to Various Products." In: *Fermentation* 3.2. 28.

Pigou, M. and Morchain, J. (2015). "Investigating the interactions between physical and biological heterogeneities in bioreactors using compartment, population balance and metabolic models." In: *Chemical Engineering Science* 126, pp. 267–282.

Poehlein, A., Schmidt, S., Kaster, A. K., Goenrich, M., Vollmers, J., Thürmer, A., Bertsch, J., Schuchmann, K., Voigt, B., Hecker, M., Daniel, R., Thauer, R. K., Gottschalk, G., and Müller, V. (2012). "An ancient pathway combining carbon dioxide fixation with the generation and utilization of a sodium ion gradient for ATP synthesis." In: *PLoS ONE* 7.3. e33439.

Poehlein, A., Bengelsdorf, F. R., Esser, C., Schiel-Bengelsdorf, B., Daniel, R., and Dürre, P. (2015). "Complete Genome Sequence of the Type Strain of the Acetogenic Bacterium *Moorella thermoacetica* DSM 521^T." In: *Genome Announcements* 3.5. e01159-15.

Poudyal, I. and Adhikari, N. P. (2014). "Temperature dependence of diffusion coefficient of carbon monoxide in water: A molecular dynamics study." In: *Journal of Molecular Liquids* 194, pp. 77–84.

Qureshi, N., Annous, B. A., Ezeji, T., Karcher, P., and Maddox, I. S. (2005). "Biofilm reactors for industrial bioconversion processes: employing potential of enhanced reaction rates." In: *Microbial cell factories* 4. 24.

Ragsdale, S. W. (1997). "The Eastern and Western branches of the Wood/Ljungdahl pathway: how the East and West were won." In: *BioFactors* 6.1, pp. 3–11.

Ramezani, M., Kong, B., Gao, X., Olsen, M. G., and Vigil, R. D. (2015). "Experimental measurement of oxygen mass transfer and bubble size distribution in an air–water multiphase Taylor–Couette vortex bioreactor." In: *Chemical Engineering Journal* 279, pp. 286–296.

Ranz, W. E. and Marshall, W. R. (1952). "Evaporation from drops." In: *Chemical Engineering Progress* 48.3, pp. 141–146.

Sander, R. (2015). "Compilation of Henry's law constants (version 4.0) for water as solvent." In: *Atmospheric Chemistry and Physics* 15.8, pp. 4399–4981.

Sato, Y. and Sekoguchi, K. (1975). "Liquid velocity distribution in two-phase bubble flow." In: *International Journal of Multiphase Flow* 2.1, pp. 79–95.

Schink, B. and Stieb, M. (1983). "Fermentative Degradation of Polyethylene Glycol by a Strictly Anaerobic, Gram-Negative, Nonsporeforming Bacterium, *Pelobacter venetianus* sp. nov." In: *Applied and Environmental Microbiology* 45.6, pp. 1905–1913.

Schügerl, K., Lücke, J., and Oels, U. (1977). "Bubble column bioreactors: tower bioreactors without mechanical agitation." In: *Advances in Biochemical Engineering* 7, pp. 1–84.

Sharak Genthner, B. R. and Bryant, M. P. (1982). "Growth of *Eubacterium limosum* with Carbon Monoxide as the Energy Source." In: *Applied and Environmental Microbiology* 43.1, pp. 70–74.

Siebler, F., Lapin, A., Hermann, M., and Takors, R. (2019). "The impact of CO gradients on *C. ljungdahlii* in a 125 m^3 bubble column: Mass transfer, circulation time and lifeline analysis." In: *Chemical Engineering Science* 207, pp. 410–423.

Siebler, F., Lapin, A., and Takors, R. (2020). "Synergistically applying 1-D modelling and CFD for designing industrial scale bubble column syngas bioreactors." In: *Engineering in Life Science*, pp. 1–13.

Takors, R., Kopf, M., Mampel, J., Blümke, W., Blombach, B., Eikmanns, B., Bengelsdorf, F. R., Weuster-Botz, D., and Dürre, P. (2018). "Using gas mixtures of CO, CO_2 and H_2 as microbial substrates: the do's and don'ts of successful technology transfer from laboratory to production scale." In: *Microbial Biotechnology* 11.4, pp. 606–625.

Tanner, R. S., Miller, L. M, and Yang, D. (1993). "*Clostridium ljungdahlii* sp. nov., an acetogenic species in clostridial rRNA homology group I." In: *International Journal of Systematic and Evolutionary Microbiology* 43.2, pp. 232–236.

Taymaz-Nikerel, H., Borujeni, A. E., Verheijen, P. J. T., Heijnen, J. J., and van Gulik, W. M. (2010). "Genome-derived minimal metabolic models for *Escherichia coli* MG1655 with estimated in vivo respiratory ATP stoichiometry." In: *Biotechnology and bioengineering* 107.2, pp. 369–381.

Teixeira, L. V., Moutinho, L. F., and Romão-Dumaresq, A. S. (2018). "Gas fermentation of C1 feedstocks: commercialization status and future prospects." In: *Biofuels, Bioproducts and Biorefining* 12.6, pp. 1103–1117.

Tomiyama, A., Kataoka, I., Zun, I., and Sakaguchi, T. (1998). "Drag Coefficients of Single Bubbles under Normal and Micro Gravity Conditions." In: *Japan Society of Mechanical Engineers International Journal* 41.2, pp. 472–479.

Tomiyama, A., Celata, G. P., Hosokawa, S., and Yoshida, S. (2002). "Terminal velocity of single bubbles in surface tension force dominant regime." In: *International Journal of Multiphase Flow* 28.9, pp. 1497–1519.

Vrábel, P., van der Lans, R. G. J. M., van der Schot, F. N., Luyben, K. C. A. M., Xu, B., and Enfors, S.-O. (2001). "CMA : integration of fluid dynamics and microbial kinetics in modelling of large-scale fermentations." In: *Chemical Engineering Journal* 84.3, pp. 463–474.

Wang, Z., Yang, J., Li, Z., and Xiang, Y. (2009). "Syngas composition study." In: *Frontiers of Energy and Power Engineering in China* 3.3, pp. 369–372.

Wu, W. T., Wu, J. Y., and Jong, J. Z. (1992). "Mass transfer in an air-lift reactor with a net draft tube." In: *Biotechnology Progress* 8.5, pp. 465–468.

Xu, D., Tree, D. R., and Lewis, R. S. (2011). "The effects of syngas impurities on syngas fermentation to liquid fuels." In: *Biomass and Bioenergy* 35.7, pp. 2690–2696.

Zeikus, J. G., Lynd, L. H., Thompson, T. E., Krzycki, J. A., Weimer, P. J., and Hegge, P. W. (1980). "Isolation and characterization of a new, methylotrophic, acidogenic anaerobe, the marburg strain." In: *Current Microbiology* 3.6, pp. 381–386.

Zhu, Z., Guo, T., Zheng, H., Song, T., Ouyang, P., and Xie, J. (2015). "Complete genome sequence of a malodorant-producing acetogen, *Clostridium scatologenes* ATCC 25775^T." In: *Journal of Biotechnology* 212, pp. 19–20.

Books

Bailey, J. E. and Ollis, D. F. (1986). *Biochemical engineering fundamentals.* 2nd. McGraw-Hill. ISBN: 0-07-003212-2.

Basile, A., Cassano, A., and Figoli, A. (2019). *Current trends and future development on (bio-) membranes: Renewable energy integrated with membrane operations.* 1st. Elsevier Inc., pp. 320–323. ISBN: 9780128135457.

Cheung, H., Tanke, R. S., and Torrence, G. P. (2005). "Acetic acid". In: *Ullmann's Encyclopedia of Industrial Chemistry.* Ed. by B. Elvers. WILEY-VCH. ISBN: 9783527306732.

Clift, R., Grace, J. R., and Weber, M. E. (1978). *Bubbles, drops, and particles.* 3rd. Academic press. ISBN: 9780121769505.

Cussler, E. L. (2009). *Diffusion: Mass Transfer in Fluid Systems.* 3rd. Cambrige University Press. ISBN: 978-0-521-87121-1.

Dean, J. A. (1999). *Lange's Handbook of Chemistry.* 15th. McGRAW-HILL, INC. ISBN: 0-07-016384-7.

Han, H., Dämbkes, G., and Rupprich, N. (2005). "Butanols". In: *Ullmann's Encyclopedia of Industrial Chemistry.* Ed. by B. Elvers. WILEY-VCH. ISBN: 9783527306732.

Hass, V. C. and Pörtner, R. (2011). *Praxis der Bioprozesstechnik.* 2nd. Springer Verlag. ISBN: 978-3-8274-2828-8.

Paschedag, A. R. (2004). *CFD in der Verfahrenstechnik: Allgemeine Grundlagen und mehrphasige Anwendungen.* Ed. by Wiley-VCH. 1st. ISBN: 3-527-30994-2.

Riemenschneider, W. (2005). "Carboxylic acids". In: *Ullmann's Encyclopedia of Industrial Chemistry.* Ed. by B. Elvers. WILEY-VCH. ISBN: 9783527306732.

Takors, R. (2014). *Kommentierte Formelsammlung Bioverfahrenstechnik.* 1st. Springer Verlag. ISBN: 978-3-642-41902-7.

van de Loosdrecht, J. and Niemantsverdriet, J. W. H. (2012). "Synthesis Gas to Hydrogen, Methanol, and Synthetic Fuels." In: *Chemical Energy Storage*. Ed. by R. Schlögel. De Gruyter. ISBN: 978-3-11-026407-4.

Thesis

Luo, H. (Dec. 1993). "Coalescence, Breakup and Liquid Circulation in Bubble Column Reactors." Ph.D. dissertation. University of Trondheim.

Patents

Gaddy, J. L. and Clausen, E. C. (Dec. 22, 1992). "*Clostridium ljungdahlii*, an Aerobic Ethanol and Acetate Producting Microorganism." Pat. US 005173429 A.

Gaddy, J. L., Arora, D. K., Ko, C.-W., Phillips, J. R., Basu, R., Wikstrom, C. V., and Clausen, E. C. (May 17, 2012). "Methods for Increasing the Production of Ethanol from Microbial Fermentation". Pat. US 2012/0122173 A1.

Köpke, M. and Liew, F. (Apr. 26, 2012). "Production of butanol from carbon monoxide by a recombinant microorganism." Pat. WO 2012/053905 A1.

Internet sources

Börse-Online (2018). *Aktueller Ethanolpreis in USD je Gallone.* URL: `https://www.boerse-online.de/rohstoffe/ethanolpreis` (visited on 10/14/2018).

Clarke Energy® (2018). *Furnace Gas for Power Production: Gases from Metallurgical Production Processes.* URL: `https://www.clarke-energy.com/furnace-gas/` (visited on 07/02/2019).

Coskata (2006). URL: `http://www.coskata.com` (visited on 05/12/2015).

EEX (2019). *European Emission Allowances (EUA).* URL: `https://www.eex.com/de/marktdaten/umweltprodukte/spotmarkt/european-emission-allowances` (visited on 09/23/2019).

Gevo™ (2011). *Gateway to Renewable Chemicals and Hydrocarbon Fuels.* URL: `https://www.sec.gov/Archives/edgar/data/1392380/000119312511176342/dex991.htm` (visited on 10/13/2018).

INEOS Bio (2013). *First facility in the world using new advanced bioenergy technology to convert waste to renewable fuel and electricity.* URL: `https://www.ineos.com/news/ineos-group/ineos-bio-produces-cellulosic-ethanol-at-commercial-scale/` (visited on 07/22/2019).

Investing (2018). *London Sugar Futures Overview.* URL: `https://www.investing.com/commodities/london-sugar` (visited on 10/16/2018).

LanzaTech (2005). *Capturing carbon. Fuelling growth.* URL: https://www.lanzatech.com/ (visited on 07/22/2019).

— (2017). *Pollution to Products!* URL: https://www.lanzatech.com/2017/11/16/pollution-products/ (visited on 07/22/2019).

— (2018). *Presentation: Waste Carbon Streams as a Resource for Gas Fermentation..* URL: https://www.energy.gov/sites/prod/files/2017/07/f35/BETO_2017WTE-Workshop_SeanSimpson-LanzaTech.pdf (visited on 07/22/2019).

Nasdaq (2016). *Celanese (CE) Raises Selling Prices of Acetic Acid in Europe.* URL: https://www.nasdaq.com/article/celanese-ce-raises-selling-prices-of-acetic-acid-in-europe-cm711034 (visited on 10/15/2018).

OrbiChem (2013). *Chemical market insights and foresight - on a single page: n-butanol.* URL: http://www.orbichem.com/userfiles/CNF%20Samples/nbt_13_11.pdf (visited on 10/15/2018).

PR Newswire (2012). *Butanediol and 1,3-butadiene markets are expected to reach 2,357.3 kilo tons, 74.4 kilo tons and 14,799.3 kilo tons respectively in 2018.* URL: https://www.prnewswire.com/news-releases/global-1-4-butanediol-2-3-butanediol-and-1-3-butadiene-markets-are-expected-to-reach-23573-kilo-tons-744-kilo-tons-and-147993-kilo-tons-respectively-in-2018-transparency-market-research-174540991.html (visited on 10/14/2018).

Synata Bio (2016). *Coskata's technology re-emerges as Synata Bio.* URL: http://www.biofuelsdigest.com/bdigest/2016/01/24/coskatas-technology-re-emerges-as-synata-bio/ (visited on 07/22/2019).

U.S. Department of Energy (2015). *Syngas Composition.* URL: http://www.netl.doe.gov/research/coal/energy-systems/gasification/gasifipedia/syngas-composition (visited on 10/13/2018).

White Dog Lab (2016). URL: https://www.whitedoglabs.com/ (visited on 07/22/2019).

Appendix A

Authors contribution

This chapter summarises my (Flora Siebler) contribution to the manuscripts which are already published. The content of the manuscripts are supplementary provided as well.

Manuscript I

Kuschel†, M., Siebler†, F., and Takors, R. (2017). "Lagrangian Trajectories to Predict the Formation of Population Heterogeneity in Large-Scale Bioreactors". In: *Bioengineering* 4.27, pp. 1-13.

† These authors contributed equally to this work.

Both, Maike Kuschel and Flora Siebler, equally conducted all parts of the simulations, evaluations, and preparations of the manuscript.

Manuscript II

Siebler, F., Lapin, A., Hermann, M., and Takors, R. (2019). "The impact of CO gradients on *C. ljungdahlii* in a 125 m^3 bubble column: Mass transfer, circulation time and lifeline analysis". In: *Chemical Engineering Science* 207, pp. 410-423.

All simulations, evaluations, and the writing of the manuscript was conducted by Flora Siebler.

Manuscript III

Siebler, F., Lapin, A., and Takors, R. (2020). "Synergistically applying 1-D modeling and CFD for designing industrial scale bubble column syngas bioreactors". In: *Engineering in Life Science*, pp. 1-13.

Both, simulations and evaluations, were performed by Flora Siebler. The manuscript was written by Flora Siebler in cooperation with Ralf Takors.

A.1 Manuscript I

Lagrangian Trajectories to Predict the Formation of Population Heterogeneity in Large-Scale Bioreactors

bioengineering

MDPI

Article

Lagrangian Trajectories to Predict the Formation of Population Heterogeneity in Large-Scale Bioreactors

Maike Kuschel †, Flora Siebler † and Ralf Takors *

Institute of Biochemical Engineering, University of Stuttgart, 70569 Stuttgart, Germany; Maike.Kuschel@ibvt.uni-stuttgart.de (M.K.); Flora.Siebler@ibvt.uni-stuttgart.de (F.S.)

* Correspondence: takors@ibvt.uni-stuttgart.de; Tel.: +49-711-685-64535

† These authors contributed equally to this work.

Academic Editor: Christoph Herwig

Received: 23 February 2017; Accepted: 24 March 2017; Published: 29 March 2017

Abstract: Successful scale-up of bioprocesses requires that laboratory-scale performance is equally achieved during large-scale production to meet economic constraints. In industry, heuristic approaches are often applied, making use of physical scale-up criteria that do not consider cellular needs or properties. As a consequence, large-scale productivities, conversion yields, or product purities are often deteriorated, which may prevent economic success. The occurrence of population heterogeneity in large-scale production may be the reason for underperformance. In this study, an *in silico* method to predict the formation of population heterogeneity by combining computational fluid dynamics (CFD) with a cell cycle model of *Pseudomonas putida* KT2440 was developed. The glucose gradient and flow field of a 54,000 L stirred tank reactor were generated with the Euler approach, and bacterial movement was simulated as Lagrange particles. The latter were statistically evaluated using a cell cycle model. Accordingly, 72% of all cells were found to switch between standard and multifork replication, and 10% were likely to undergo massive, transcriptional adaptations to respond to extracellular starving conditions. At the same time, 56% of all cells replicated very fast, with $\mu \geq 0.3\ h^{-1}$ performing multifork replication. The population showed very strong heterogeneity, as indicated by the observation that 52.9% showed higher than average adenosine triphosphate (ATP) maintenance demands (12.2%, up to 1.5 fold). These results underline the potential of CFD linked to structured cell cycle models for predicting large-scale heterogeneity *in silico* and *ab initio*.

Keywords: computational fluid dynamics; cell cycle model; Lagrange trajectory; scale-up; stirred tank reactor; population dynamics; energy level

1. Introduction

The physiological state of bacterial cells is strongly dependent on the surrounding conditions. As outlined in Müller et al. [1], external stress is a key factor inducing the formation of population heterogeneity, which differs according to growth phenotypes and cell cycle patterns. Moreover, concentration fluctuations occurring under large-scale mixing conditions have a measurable influence on growth and production yield [2–4]. Accordingly, homogeneity of the bacterial population may be affected, yielding subpopulations that co-exist next to each other [1]. Makinoshima et al. [5] observed five and ten cell populations of *Escherichia coli* during exponential growth and the subsequent stationary phase, respectively. For *Pseudomonas putida*, steady-state chemostat cultivation revealed that industry-like stress conditions induced changes in the cell cycle process. Under stress, deoxyribonucleic acid (DNA) replication was accelerated in a dose-dependent manner, yielding subpopulations with different DNA contents [6].

To investigate whether nutrient gradients of large-scale conditions foster the occurrence of population heterogeneity, the following concept was formulated. First, large-scale substrate gradients of a bioreactor should be simulated. Next, the path of bacterial cells through the gradients need to be tracked, and the resulting growth phenotypes monitored. Then, a cell cycle model can be used to translate changing growth conditions into cell cycle patterns. Apparently, this approach requires (i) a sound simulation of large-scale substrate gradients that trigger 'stress' in the cells and (ii) the translation of nutrient availability in growth patterns as a basis of cell cycle modelling. For the latter, the findings of Cooper and Helmstetter [7] were applied. They specified a relationship between chromosome content and cell cycle phase duration for *E. coli B/r* and showed that the amount of DNA varies continuously with the growth rate and substrate availability. Consequently, the durations of the cell cycle phases are strongly dependent on the environmental conditions.

The cell cycle of bacteria using binary fission can be divided into three parts: the time for initiation of replication (B-period), the time required for replication (C-period), and the time between replication and completed cell division (D-period). C-periods are the longest for slow-growing cells but decrease to constant values under elevated growth conditions [8]. In order to grow faster, replication and segregation are separated in time. Most bacteria initiate replication during a previous generation, leading to multifork replication.

Single-cell analysis by fluorescence-activated cell scanning has proven to be a valuable method to measure the DNA content from thousands of bacteria and to generate DNA content histograms for the population [9]. Also, latest lab on a chip techniques are a feasible method for measuring population heterogeneity [10,11]. Subpopulations with one, two, or more chromosomes can be detected. Skarstad [12] extended the model of Cooper and Helmstetter to calculate the number of individuals of *E. coli B/r* comprising a subpopulation with a specific DNA content from flow cytometry data. Furthermore, Skarstad determined the duration of the cell cycle periods for various growth rates. This was proven to be applicable for *P. putida* KT2440 as well [6].

It is still challenging to capture the magnitude and frequency of fluctuations in large scale bioprocesses and to predict the extent of the intracellular response. Several authors have suggested computational fluid dynamics (CFD) as a tool to provide detailed information of environmental conditions inside a fermenter. The gas, liquid, and bio phases are often modeled as a continuum by the Euler-Euler approach [13–15]. Typically, microorganisms react individually to different environmental conditions; therefore, a continuum description may not be advantageous. An extension of the Euler-Euler approach for the liquid phase is the use of population balance equations to model the heterogeneity of a population [16,17]. The incorporation of a detailed intracellular reaction network, however, demands a high computational effort to solve the complex distribution functions [18,19].

Since the pioneering work of Lapin et al. [20], environmental fluctuations have been studied from the perspective of microorganisms. The applied Euler-Lagrange approach uses a continuous representation of the fluid phase (Euler), combined with a segregated description of the cell population (Lagrange). The bacteria are simulated as particles, which are tracked on their way through the reactor. Statistical evaluation of these trajectories, denoted as bacterial lifelines, provide valuable information about substrate fluctuation frequencies experienced by microorganisms [21].

The influence of these fluctuations on cell cycle dynamics and energy levels has not been demonstrated yet. Thus, in this study, based on the work of Haringa et al. [21], an extensive statistical evaluation of bacterial lifelines was performed. Rather conservative operating conditions for the industrially relevant strain *P. putida* KT2440 were assumed to investigate the occurrence of and impact on population homogeneity. The Euler-Lagrange approach was combined with a cell cycle model of Lieder et al. [6] to gain deeper insights into the behaviors of cell cycle dynamics and individual distributions during large-scale fermentation.

These findings present a method to better analyze and understand the heterogeneity caused by scale up-induced stress stimuli.

2. Materials and Methods

2.1. Cell Cycle Model

Flow cytometry data ranging from $\mu = 0.1\ h^{-1}$ to $0.6\ h^{-1}$ for *P. putida* KT2440 were obtained by Lieder et al. [6] and processed as shown in Figure 1. The data were channeled and displayed as the frequency distribution of DNA content. The durations of cell cycle phases C (DNA replication) and D (period between replication and completed cell division) were determined iteratively by minimizing the deviation between experimental and theoretical DNA histograms. The theoretical DNA content of an asynchronous, ideal culture in which all cells have equal growth parameters was derived from the age distribution according to Cooper and Helmstetter [7]. Using this probability density function for cells of a specific cell age, Cooper and Helmstetter further calculated the theoretical chromosome content per cell at a specific cell age. This model was extended by Skarstad et al. [12] to calculate the frequency of the occurrence of a specific DNA content in an interval of ongoing DNA synthesis. The durations of phases C and D are decisive for the distribution of DNA content. Different values for C were obtained to fit the experimental histograms for various growth rates. Based on the work of Lieder [22], a function for C-phase duration, dependent on the growth rate of *P. putida* KT2440, was derived. A correlation for C proposed by Keasling et al. [23] was used.

$$C = C_{min}\left(1 + a\, e^{b\,\mu}\right) \quad (1)$$

where C is the length of the C period, C_{min} is the minimal length of the C period, μ represents the growth rate and a and b are parameters that fit the experimental data. Based on the experimental data of Lieder et al. [6], the parameter estimation resulted in $C_{min} = 0.77$ h, a = 1.83, and b = 4.88.

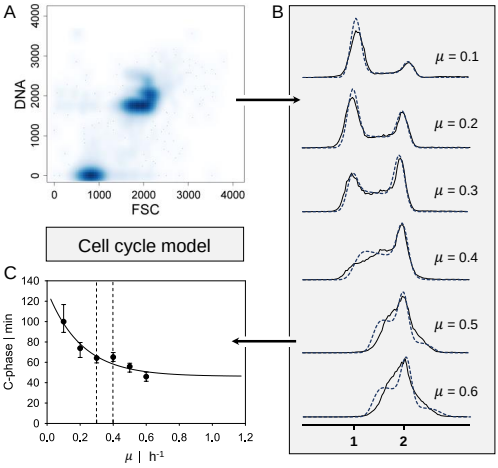

Figure 1. Approach for the cell cycle dynamics model. (**A**) Representative flow cytometry scatter plot for deoxyribonucleic acid (DNA) content of the growth rate $\mu = 0.3\ h^{-1}$. (**B**) DNA content over counts for growth rates ranging from $\mu = 0.1\ h^{-1}$ up to $\mu = 0.6\ h^{-1}$. A single genome is indicated by 1, and double chromosomes by 2. Black lines present experimental data, and blue dashed lines present the calculation of the cell cycle model. (**C**) Approximated C-phase duration over growth rate estimated by the cell cycle model (1% parameter covariance). Black dashed lines indicate the transition regime from single-forked to multiforked replication. Flow cytometry data obtained by Lieder et al. [6].

2.2. Numerical Simulation

2.2.1. Geometry and Reactor Setup

In order to generate a pseudostationary glucose gradient of an industrial fed batch fermentation, a large-scale stirred tank bioreactor was chosen. Precise dimensions and information about the inner geometry can be found in Appendix A (Figure A1 and Table A1). The main geometry was derived from Haringa et al. [21] and only slightly modified for the purpose of this study. With an H/D ratio of 2.57, the total volume was about 54,000 L. The reactor setup included four baffles and a stirrer with two Rushton agitators. The lower stirring unit was equipped with eight blades, and the middle unit with six blades. With a stirring rate of 100 rpm, a tip speed of 5–8 m s^{-1} was reached. The impeller Reynolds number was 1.8×10^6, the power number 13.15, and the needed power was 226 kW.

The feeding rate was set as half of the maximum uptake rate $q_{s,max}$ of *P. putida* with 0.738 $kg_{glc} \cdot kg_{CDW}^{-1} \cdot h^{-1}$. Aeration, gas transfer, and oxygen uptake were neglected in this study. Therefore, no gassing system was installed. A cell concentration of 10 $kg_{CDW} \cdot m^{-3}$ was assumed, and a simple Monod-like kinetic was used to simulate the substrate uptake q_s:

$$q_s = q_{s,max} \cdot \frac{c_s}{K_s + c_s} \quad (2)$$

where $q_{s,max}$ is the maximum uptake rate, c_s is the glucose concentration, and the approximated substrate specific uptake constant K_s with 10 $mg \cdot L^{-1}$. The maximum uptake rate was calculated with the biomass substrate yield Y_{XS} = 0.40 $g_s \cdot g_{CDW}^{-1}$ and the maximum growth rate μ = 0.59 h^{-1} [22,24].

2.2.2. Simulation Setup

For the numerical simulation, the commercial calculation tool ANSYS Fluent version 17.0 was used. Using this finite volume-based fluid dynamic analysis program, the virtual geometry was built, and spatial discretization was performed. A total of 445,000 numerical cells yielded the same circulation time as achieved by Haringa et al. [21]. The flow field was approximated by solving the Reynolds-averaged Navier-Stokes (RANS) equations in combination with the standard k-ε model for turbulence. All surfaces were set as slip boundaries, except for the frictionless top area, which implied the reactor filling height. Both impeller units were set to sliding mesh motion to generate a more realistic flow field.

For glucose feed, a separate volume at the top of the reactor was defined, and a constant mass flow was set. The feed was inserted as mass percentage, with constant pressure and volume. The hydrodynamic and kinetic was calculated every 10 ms until the overall glucose concentration was constant and a pseudostationary gradient was reached. Finally, an average flow field and glucose gradient were obtained over 150 s. In further simulations, the hydrodynamic and glucose gradient were set as frozen.

Bacteria lifelines were simulated as massless Lagrangian particles with a discrete random walk (DRW) model passing through the flow field. Every 30 ms, the position and glucose concentration for each bacterium were recorded. In total, 120,000 bacterial cells were tracked over 260 s. According to the ergodic theorem, the same average values are obtained by tracking 1,560,000 bacteria for 20 s (the approximate circulation time). The simulation would yield even more precise statistical evaluations by increasing the number of lifelines.

2.3. Statistical Evaluation

All bacterial lifelines were evaluated statistically and grouped according to the regime borders. The growth rate was calculated for each bacterial cell and each time interval. The regimes were classified as follows: standard forked replication S for $\mu \leq 0.3\ h^{-1}$, the transition area T ($0.3 < \mu < 0.4\ h^{-1}$), and multifork replication M for $\mu \geq 0.4\ h^{-1}$ derived by the cell cycle model (see Section 2.1.). By evaluating

the cell history, further classifications were made. Six regime transitions follow when two transitions and one retention time were considered:

- **STM**: transition from standard forked to multiforked with a retention time in the transition area.
- **STS**: standard forked, retention in the transition area, and back to standard forked
- **TST**: starting from the transition area with retention in a single forked area and back to transition
- **MTS**: multiforked replication regime to single forked replication with a retention time in the transition area
- **MTM**: beginning in the multifork regime with retention in the transition area and back to the multifork regime
- **TMT**: circulation from transition back to transition area with retention time in the multifork replication regime

The second capital letter always indicates the area in which the retention time τ was measured. Before the bacterial lifelines were grouped in regimes, a moving-average filter was applied to filter unrealistic, turbulent fluctuations caused by the standard DRW model (see Appendix B). A second one-dimensional (1D) filter was conducted to erase rapid sequential regime transitions smaller than 0.09 s. Both filtering steps caused deviations from the raw data of less than 5%.

The distribution of the growth rates was derived by calculating the mean growth rate for the whole reactor and the mean growth rate for 20 s for each bacterium. This distribution combined with the cell cycle approach resulted in a distribution of different C-phase durations using Equation (1). Additionally, the energy level distribution was obtained based on Pirt's law [25]:

$$q_{ATP} = \frac{\mu}{Y_{x/ATP}} + m_{ATP} \tag{3}$$

with the *Pseudomonas putida* properties of nongrowth-associated maintenance $m_{ATP} = 3.96\ mmol_{ATP} \cdot g_{CDW}^{-1} \cdot h^{-1}$ and the growth-associated maintenance $Y_{XATP} = \frac{1}{85}\ g_{CDW} \cdot mmol_{ATP}^{-1}$ [24].

3. Results and Discussion

In order to investigate heterogeneity in large-scale bioreactors, a pseudostationary glucose gradient occurring during fed batch fermentation of *P. putida* was simulated. Therefore, a biomass of 10 $kg \cdot m^{-3}$ was assumed, which remained constant within the time observed. For higher biomass concentrations, stronger gradients can be expected.

3.1. Gradient and Flow Field

In a 54,000 L stirred tank reactor, a pseudostationary glucose gradient was obtained with CFD simulations. The average glucose concentration was monitored until no further changes could be observed. The residual steady state glucose concentration was 20.7 $mg \cdot L^{-1}$. The theoretical growth rate for every numerical cell was computed (Eulerian approach), resulting in an average growth rate of $\mu = 0.294\ h^{-1}$. Ideal mixing was assured by comparing the average growth rate in the reactor (Eulerian approach) and the expected growth rate for the set feed rate $\mu = 0.295\ h^{-1}$. In the fed batch fermentation, the feeding rate amounted to half the maximum uptake rate of *P. putida*. The objective of the simulation was to generate a realistic glucose gradient with concentrations for which theoretical growth rates ranging from 0.0 h^{-1} to 0.59 h^{-1} could be approximated. Moreover, the distribution of bacteria that were introduced from different vertical positions in the reactor at the start of the simulation is displayed.

In Figure 2, three reactor cross sections are depicted to describe (A) the growth rate regimes (see also Section 2.3), (B) the flow field, and (C) the bacterial distribution. Due to asymmetric reactor geometry (see Section 2.2.1), the mean flow field and mean glucose gradient showed periodic changes. Accordingly, the averages of the flow field and gradients over 150 s were computed to track the bacteria (Figure 2C) as lifelines. Bacteria moved faster when approaching the stirrer. This clearly indicated

zones with different residence times. However, tracking the bacterial paths showed that they evenly crossed every part in the reactor.

The underlying gradient was not expected to perfectly reflect the real experiment. Several assumptions had to be made. For simplicity, bubbling flow and oxygen transfer were neglected. The kinetic reaction of substrate consumption following a Monod-like kinetic was assumed to take place in every numerical cell. This implied that the bacterial cells were distributed homogeneously at each time step, which is only a simplified scenario (Figure 2C). However, to examine the effects of cell history or lag phases of the bacteria on the gradient itself, an existing gradient had to be installed with the stated simplifications. In the following sections, a detailed statistical analysis is provided to study the influence of the gradient on the bacteria and reverse in a realistic manner.

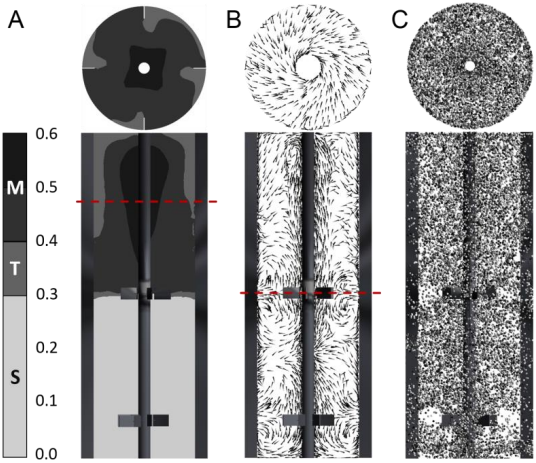

Figure 2. Simulation of gradients and bacterial lifelines. (**A**) Averaged substrate gradient calculated for 150 s, colored by regime classification: standard replication S ($\mu < 0.3$) in light gray, transition regime T ($0.3 \leq \mu \leq 0.4$) in gray, and multifork replication M ($\mu > 0.4$) in dark gray. (**B**) Average flow field estimated for 150 s. (**C**) Representative magnified bacteria particles (around 2000) at a certain time step (colored by particle ID; low numbers in dark gray represent a starting point close to the reactor bottom, high numbers in light gray represent a starting point close to the reactor top). Horizontal section planes are indicated by dashed red lines; otherwise, the top view is shown.

3.2. *Lagrangian Trajectory*

For 260 s, 120,000 bacteria were tracked on their paths crossing different substrate concentrations. Figure 3 depicts growth rate profiles of two organisms for 20 s, referred to as lifelines L1 and L2. Figure 3C shows the related paths.

According to the regime thresholds (see Section 2.3 and Figure 3A, dashed lines), the growth rate trajectories could be transferred to replication modus curves, as described in Figure 3B). The lifeline L1 revealed high variations in glucose concentrations that were likely to induce strong metabolic changes. In contrast, environmental shifts along L2 were moderate, and there were no effects on metabolism or the cell cycle. The first lifeline L1 gave information regarding five regime transition strategies (STS, TST, STM, TMT, and MTS) and the individual residence times. Lifelines L1 and L2 started from different positions in the reactor and were unequal in length because they moved according to the

predominant velocity field. Within 20 s, L2 did not approach the feed zone, remaining in an area of reduced substrate concentration and increased shear stress, owing to the higher velocity of L2.

As shown in Figure 3B,C, within a defined timescale, bacteria completely sensed different environmental conditions. Whereas L2 seemed to remain in the same environment, L1 passed different glucose concentrations and performed several replication strategies. Each metabolic adjustment will cost energy and could have an impact on the production yield.

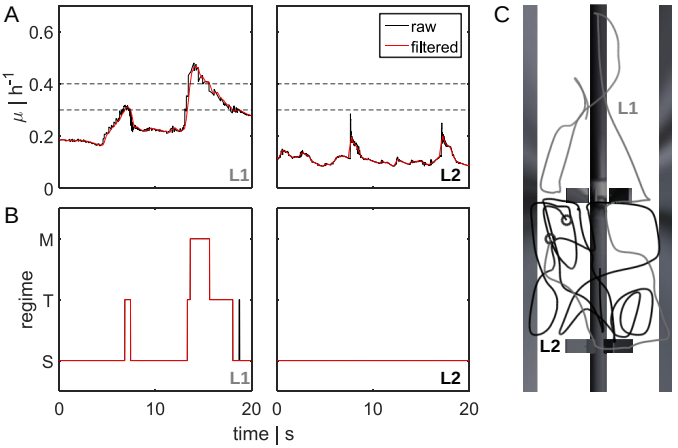

Figure 3. Bacterial lifeline and regime transition classification. (**A**) Two-dimensional (2D) bacterial lifeline for different growth rates μ over time. The black line represents raw data, and the red line represents filtered data (moving average filter to correct discrete random walk (DRW) fluctuations). Black dashed lines indicate the transition regime from single-forked to multiforked replication. (**B**) Translation of filtered (one-dimensional (1D) filter) growth rate curves for the three regimes: multifork replication regime M, transition between standard forked and multiforked T, and standard replication S. Examples for two bacterial lifelines L1 and L2 are depicted. For L1, five regime transitions (STS, TST, STM, TMT, and MTS; see Section 2.3) were analyzed. (**C**) Bacterial movement patterns for two bacterial lifelines (L1 in gray and L2 in black). Starting positions are indicated by black circles.

3.3. *Statistical Evaluation*

3.3.1. Regime Transition Frequency

All bacterial lifelines were scanned for regime transitions and retention times in order to obtain the frequency distributions as a function of τ. Thus, six transition strategies were evaluated in a statistical manner to gain insights into cell histories and possible cell behaviors (see also Section 2.3).

Figure 4 shows the counts for each regime transition at a certain retention time. All regime transition statistics, except the TST transition, exhibited a decay after at least 10 s. Bacteria starting from the transition regime T could remain in an area of low concentration for up to 73.5 s (data not shown), where they could grow regularly (standard forked S), before changing back to the T regime. This could be explained by the flow field and gradient pictured in Figure 2A,B. The critical concentrations representing possible growth rates for the regime transition ($\mu \geq 0.3\,h^{-1}$ and $\mu > 0.4\,h^{-1}$) were located in the upper half of the reactor. Rushton turbines usually cause flow patterns moving away from the blades to the wall, where they circulate up or down, thereby forming large eddies for each stirrer set (Figure 2B). Consequently, cells will often circulate in this segment and do not pass other areas of the

reactor. The lower part of the reactor, which does not provoke a regime transition and, therefore, badly supplies the organisms with substrate, consisted of three segments. As a result, the average retention time in the TST transition was the longest ($\overline{\tau}_{TST}$ = 8.54 s). All other average and maximum retention times are listed in Table 1. The shapes of the distributions follow a Poisson distribution. The maximal retention time was defined as the limit, within which 99% of the values were located.

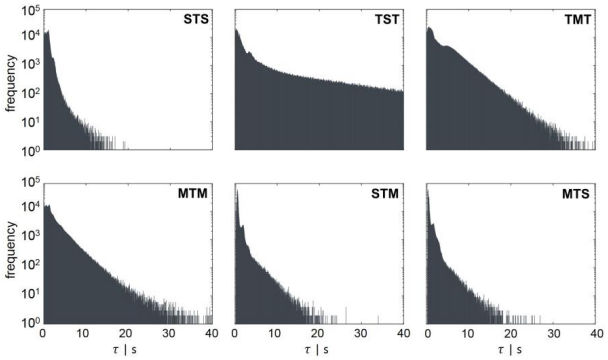

Figure 4. Regime transition frequency as a function of the retention time τ. Regime transition classifications are indicated in the left corner of each panel. The second capital letter always indicates the area, in which the retention time τ was measured. The regime transition count for each retention time was scaled logarithmically.

Table 1. Average and maximal retention time in a specific regime. For the six regimes (STS, TST, TMT, MTM, STM, and MTS), the average ($\overline{\tau}$) and maximal retention times (τ_{max}) are displayed in seconds. The maximum τ was defined as the limit, within which 99% of the values were located.

Regime Transition	$\overline{\tau}$ [s]	τ_{max} [s]
STS	0.99	3.7
TST	8.54	73.5
TMT	3.53	16.25
MTM	2.45	13
STM	0.95	6.6
MTS	0.88	5.5

Lifeline statistics provide insights into the frequency of regime transitions and residence times. Depending on the cell history, i.e., the concentrations of bacteria encountered before the bacteria passed the actual concentration, the cells will adapt accordingly. Although metabolic adaptation is known to be very rapid, the initiation of regulatory programs involving transcriptional changes is slower. Investigating the impact of large-scale conditions for *E. coli*, Löffler et al. [26] showed that fundamental transcriptional programs were initiated after 70 s of glucose shortage. After 30 s, metabolic consequences were measured, and the first transcriptional changes were detected. In total, about 600 genes were found to be up- or downregulated repeatedly, indicating a strong adaption.

Considering this finding during the regime analysis, it is assumed that all cells travelling from high (M) to low (S) substrate availability should be influenced. Being prepared for multifork replication in M, the cells must adapt to standard replication (S). By analogy, this also includes travelers from T to S. Such cells can have a growth rate of about 0.4 h^{-1} before they adapt to growth rates of less than 0.3 h^{-1}. During the observation window of 260 s, 72.6% of all cells were expected to carry out this move at least once and to linger more than 30 s in regime S. About 14.7% of all cells were expected

to stay more than 70 s in regime S after experiencing higher glucose concentrations in regime T. Furthermore, if a regime transition from maximal to moderate growth conditions (MTS) with the retention time in regime T and S is assumed, 55.5% of all cells performed this move for more than 30 s. A retention time of 70 s was calculated for 10.4% of all cells. The time scales of 30 s and 70 s were shown to significantly influence the transcriptional response of *E. coli* [26], leading to the assumption that changes in adenosine triphosphate (ATP) and guanosine triphosphate (GTP) levels of *P. putida* KT2440 could also be expected.

3.3.2. Energy and C-Phase Duration Distribution

For the observation window of 260 s, the growth rate profiles of 120,000 bacteria were calculated. Given the set feed rate, the average μ of 0.295 h^{-1} was expected. Using the Lagrangian approach, an average growth rate of μ = 0.269 h^{-1} was computed, indicating an adequate deviation of 8.5% compared to the Eulerian approach with μ = 0.294 h^{-1} (see Section 3.1).

The distribution of the ATP consumption rate q_{ATP} is presented in Figure 5A. The growth rate μ and q_{ATP} were not evenly distributed compared to the mean value, but exhibited individual distributions according to the gradient. The ATP consumption rate was calculated applying Pirt's law (see Equation (3)). While only 6.3% of all cells had a mean ATP consumption rate of $q_{ATP,mean}$ = 29.31 ± 2 $mmol_{ATP} \cdot g_{CDW}^{-1} \cdot h^{-1}$, 40.8% showed a reduced consumption rate of less than 27.31 $mmol_{ATP} \cdot g_{CDW}^{-1} \cdot h^{-1}$, and 52.9% showed an increased energy demand of 31.31 $mmol_{ATP} \cdot g_{CDW}^{-1} \cdot h^{-1}$ in comparison to the average consumption rate. Moreover, 12.2% show an energy demand that was more than 1.5 times that of the mean value in the reactor.

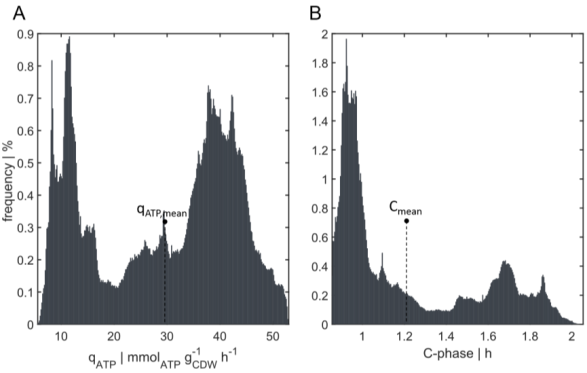

Figure 5. Distribution of C-phase duration and energy level. (**A**) Frequencies of cells with a specific adenosine triphosphate (ATP) consumption rate (q_{ATP}) tracked for 20 s. Average value of $q_{ATP,mean}$ = 29.31 $mmol_{ATP} \cdot g_{CDW}^{-1} \cdot h^{-1}$. Range of the x-axis from $q_{ATP,min}$ = 5.57 $mmol_{ATP} \cdot g_{CDW}^{-1} \cdot h^{-1}$ to $q_{ATP,max}$ = 52.98 $mmol_{ATP} \cdot g_{CDW}^{-1} \cdot h^{-1}$. (**B**) Frequency of cells having a specific duration of replication (C-phase). Average C-phase duration of C_{mean} = 1.21 h. Range of the x-axis from C_{min} = 0.86 h to C_{max} = 2.05 h. Counts were divided into 300 bins.

The distribution will differ if increased nongrowth-associated maintenance m_{ATP} is considered. As outlined by Löffler et al. [26], m_{ATP} increases by 40–50% when cells are exposed to large-scale substrate gradients.

The individual growth profiles of the cells are the basis for deducing cell cycle patterns using the cell cycle model (see Section 2.3). Distributions of the C-length (encoding DNA replication) could be derived for the population of 120,000 bacteria. Figure 5B shows the average duration of

replication of 1.21 h and the frequency of cells with a C-phase duration ranging from C_{min} = 0.86 h to C_{max} = 2.05 h. Clearly, the bacteria were not evenly distributed according to the mean value, and there was a large heterogeneity in the reactor. Although only 22.3% of all cells had a replication phase of 1.21 ± 0.2 h, about 30% possessed a C-period of more than 1.41 h. In contrast, 47.7% displayed a shorter replication phase than the average time for replication (less than 1.01 h). Moreover, approximately 56.1% of the cells were rapidly replicating cells with a growth rate higher than $\mu = 0.3\ h^{-1}$. For these cells, it can be assumed that they already started to completely adjust their metabolism to achieve multifork replication. As shown in Figure 5B, the bioreactor population was strongly heterogeneous, characterized by a nonequal distribution of bacteria in different cell cycle states. Three different growth phenotypes are shown: C-phase durations of (i) 0.94 ± 0.08 h, (ii) 1.68 ± 0.1 h, and (iii) a transition state of C-phases ranging from 1.1 to 1.5 h. Previously, subpopulations resulting from chemostat experiments have been categorized in populations containing one, two, or more than two chromosomes [27]. With this simulation setup, a model-based superposition of subpopulations containing different growth rates to mimic the scenario in a (fed)batch fermentation was shown. For the underlying gradient, new categories of subpopulations according to the C-phase durations mentioned above can be formulated.

4. Conclusions

The existence of population heterogeneity in industrial fermenters has been demonstrated, but it still not completely understood. Improvements in fermenter operation, reactor design, and strain engineering can be achieved as more information of cell behaviors during large-scale production becomes available. In this study, the formation of heterogeneity by combining CFD with a cell cycle model of *P. putida* was investigated. With this method, heterogeneity can be interpreted from the bacterial point of view, particularly with respect to the growth phase durations and energy demands of the cell.

Average and maximum residence times for each transition strategy have been approximated and can be linked to scale-down experiments using STR-PFR setups. Moreover, distributions of growth rates, ATP consumptions, and C-phase durations could be generated. Such findings provide important insights into the intracellular mechanisms that determine growth phenotypes. These mechanisms may become a crucial part of strain and process engineering to predict *ab initio* and *in silico* whether and how large-scale performance will meet expectations. Realistic large-scale cultivation can be simulated by investigating the "subpopulations" individually. Specifically, it may be possible to elucidate whether the total drop in production performance during large-scale production is caused by all cells or by individual "subpopulations" that underperform.

To further investigate such problems, heterogeneity studies need to be coupled with single-cell product kinetics. Moreover, research will need to focus on the quantitative measurement of the impact of stress intensity on the m_{ATP} level. This will enable prediction of the total energy demand for a given setup.

Acknowledgments: The research could not have been conducted without the previous work on the cell cycle model of Sarah Lieder and the flow cytometry analysis of Susann Müller. We also thank Alexei Lapin and Alexander Nieß for their advice and support during this study. This work was supported by the German Research Foundation (DFG; GZ: TA241/5-2) and the Federal Ministry of Education and Research (BMBF; FKZ031A468B).

Author Contributions: Ralf Takors initiated the study and provided important advice during the entire investigation. Maike Kuschel and Flora Siebler equally conducted all parts of the simulation, evaluation, and writing of the manuscript as a team.

Conflicts of Interest: The authors declare no conflicts of interest.

Appendix A

More precise information of the reactor setup and geometry can be found in Table A1 and Figure A1.

Table A1. Dimensions of the reactor setup pictured in Figure A1.

Description	Symbol	Relation
Reactor diameter	D_R	3.00 m
Impeller diameter	D_I	0.43 D_R
Impeller height	H_I	0.21 D_I
Bottom clearance	C_1	0.30 D_R
Impeller spacing	ΔC	1.00 D_R
Upper clearance	C_2	1.27 D_R
Baffle width	B	0.10 D_R
Liquid height	H_L	$C_1 + \Delta C + C_2$

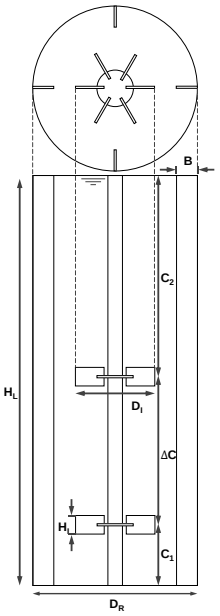

Figure A1. Schematic diagram of reactor geometry derived from Haringa et al. [21]. The stirred tank reactor contains four baffles and two Rushton turbines with eight blades (**bottom**) and six blades (**top**). Dimensions indicated by capital letters are explained in Table A1.

Appendix B

The standard moving average filter of MATLAB is a linear filter (low pass filter), which removes high frequency components such as fluctuations caused by the DRW model. It is formulated as:

$$m(t) = \sum_{j=-q}^{q} y_{t+j} \quad q < t < N - q \tag{A1}$$

with:

$$q = \frac{\overline{\tau} - 1}{2} \tag{A2}$$

where N is the total number of measured time points and $\overline{\tau}$ the filter timescale.

References

1. Müller, S.; Harms, H.; Bley, T. Origin and analysis of microbial population heterogeneity in bioprocesses. *Curr. Opin. Biotechnol.* **2010**, *21*, 100–113. [CrossRef] [PubMed]
2. Bylund, F.; Collet, E.; Enfors, S.; Larsson, G. Substrate gradient formation in the large-scale bioreactor lowers cell yield and increases by-product formation. *Bioprocess Eng.* **1998**, *18*, 171–180. [CrossRef]
3. Enfors, S.; Jahic, M.; Rozkov, A.; Xu, B.; Hecker, M.; Ju, B. Physiological responses to mixing in large scale bioreactors. *J. Biotechnol.* **2001**, *85*, 175–185. [CrossRef]
4. Takors, R. Scale-up of microbial processes: Impacts, tools and open questions. *J. Biotechnol.* **2012**, *160*, 3–9. [CrossRef] [PubMed]
5. Makinoshima, H.; Nishimura, A.; Ishihama, A. Fractionation of *Escherichia coli* cell populations at different stages during growth transition to stationary phase. *Mol. Microbiol.* **2002**, *43*, 269–279. [CrossRef] [PubMed]
6. Lieder, S.; Jahn, M.; Koepff, J.; Müller, S.; Takors, R. Environmental stress speeds up DNA replication in *Pseudomonas putida* in chemostat cultivations. *Biotechnol. J.* **2016**, *11*, 155–163. [CrossRef] [PubMed]
7. Cooper, S.; Helmstetter, C.E. Chromosome replication and the division cycle of *Escherichia coli*. *J. Mol. Biol.* **1968**, *31*, 519–540. [CrossRef]
8. Girault, M.; Kim, H.; Arakawa, H.; Matsuura, K.; Odaka, M.; Hattori, A.; Terazono, H.; Yasuda, K. An on-chip imaging droplet-sorting system: A real-time shape recognition method to screen target cells in droplets with single cell resolution. *Sci. Rep.* **2017**, *7*, 1–10. [CrossRef] [PubMed]
9. Cheng, Y.H.; Chen, Y.C.; Brien, R.; Yoon, E. Scaling and automation of a high-throughput single-cell-derived tumor sphere assay chip. *Lab Chip* **2016**, *16*, 3708–3717. [CrossRef] [PubMed]
10. Helmstetter, C.E. Timing of Synthetic Activities in the Cell Cycle. In *Escherichia coli and Salmonella. Cellular and Molecular Biology*; Neidhardt, F.C., Ed.; American Society for Microbiology (ASM) Press: Washington, DC, USA, 1996; pp. 1627–1639.
11. Müller, S. Modes of cytometric bacterial DNA pattern: A tool for pursuing growth. *Cell Prolif.* **2007**, *40*, 621–639. [CrossRef] [PubMed]
12. Skarstad, K.; Steen, H.B.; Boye, E. *Escherichia coli* DNA distributions measured by flow cytometry and compared with theoretical computer simulations. *J. Bacteriol.* **1985**, *163*, 661–668. [PubMed]
13. Larsson, G.; Törnkvist, M.; Ståhl Wernersson, E.; Trägårdh, C.; Noorman, H.; Enfors, S.O. Substrate gradients in bioreactors: Origin and consequences. *Bioprocess Eng.* **1996**, *14*, 281–289. [CrossRef]
14. Noorman, H.; Morud, K.; Hjertager, B.H.; Traegaardh, C.; Larsson, G.; Enfors, S.O. CFD modeling and verification of flow and conversion in a 1 m^3 bioreactor. *BHR Gr. Conf. Ser. Publ.* **1993**, *5*, 241–258.
15. Schmalzriedt, S.; Jenne, M.; Mauch, K.; Reuss, M. Integration of physiology and fluid dynamics. *Adv. Biochem. Eng.* **2003**, *80*, 19–68.
16. Morchain, J.; Gabelle, J.-C.; Cockx, A. A coupled population balance model and CFD approach for the simulation of mixing issues in lab-scale and industrial cioreactors. *Am. Inst. Chem. Eng.* **2014**, *60*, 27–40. [CrossRef]
17. Bezzo, F.; Macchietto, S.; Pantelides, C.C. General hybrid multizonal/CFD approach for bioreactor modeling. *AIChE J.* **2003**, *49*, 2133–2148. [CrossRef]
18. Mantzaris, N.V.; Liou, J.; Daoutidis, P.; Srienc, F. Numerical solution of a mass structured cell population balance model in an environment of changing substrate concentration. *J. Biotechnol.* **1999**, *71*, 157–174.
19. Henson, M.A. Dynamic modeling of microbial cell populations. *Curr. Opin. Biotechnol.* **2003**, *14*, 460–467. [CrossRef]
20. Lapin, A.; Müller, D.; Reuss, M. Dynamic behavior of microbial populations in stirred bioreactors simulated with Euler-Lagrange methods: Traveling along the lifelines of single cells. *Ind. Eng. Chem. Res.* **2004**, *43*, 4647–4656. [CrossRef]
21. Haringa, C.; Tang, W.; Deshmukh, A.T.; Xia, J.; Reuss, M.; Heijnen, J.J.; Mudde, R.F.; Noorman, H.J. Euler-Lagrange computational fluid dynamics for (bio)reactor scale-down: An analysis of organism life-lines. *Eng. Life Sci.* **2016**, *16*, 652–663. [CrossRef] [PubMed]
22. Lieder, S. *Deciphering Population Dynamics as a Key for Process Optimization*; University of Stuttgart: Stuttgart, Germany, 2014.
23. Keasling, J.D.; Kuo, H.; Vahanian, G. A Monte Carlo simulation of the *Escherichia coli* cell cycle. *J. Theor. Biol.* **1995**, *176*, 411–30. [CrossRef] [PubMed]

24. Van Duuren, J.B.J.H.; Puchałka, J.; Mars, A.E.; Bücker, R.; Eggink, G.; Wittmann, C.; Dos Santos, V.A.P.M. Reconciling in vivo and *in silico* key biological parameters of *Pseudomonas putida* KT2440 during growth on glucose under carbon-limited condition. *BMC Biotechnol.* **2013**, *13*, 93. [CrossRef] [PubMed]
25. Pirt, S.J. The maintenance energy of bacteria in growing cultures. *Proc. R. Soc. Lond. Ser. B. Biol. Sci.* **1965**, *163*, 224–231. [CrossRef]
26. Löffler, M.; Simen, J.D.; Jäger, G.; Schäferhoff, K.; Freund, A.; Takors, R. Engineering *E. coli* for large-scale production—Strategies considering ATP expenses and transcriptional responses. *Metab. Eng.* **2016**, *38*, 73–85. [CrossRef] [PubMed]
27. Lieder, S.; Jahn, M.; Seifert, J.; von Bergen, M.; Müller, S.; Takors, R. Subpopulation-proteomics reveal growth rate, but not cell cycling, as a major impact on protein composition in *Pseudomonas putida* KT2440. *AMB Express* **2014**, *4*, 71. [CrossRef] [PubMed]

A.2 Manuscript II

The impact of CO gradients on *C. ljungdahlii* in a 125 m^3 bubble column: Mass transfer, circulation time and lifeline analysis

---

Chemical Engineering Science 207 (2019) 410–423

Contents lists available at ScienceDirect

Chemical Engineering Science

journal homepage: www.elsevier.com/locate/ces

The impact of CO gradients on *C. ljungdahlii* in a 125 m^3 bubble column: Mass transfer, circulation time and lifeline analysis

Flora Siebler [a], Alexey Lapin [b], Maria Hermann [a], Ralf Takors [a,*]

[a] Institute of Biochemical Engineering, University of Stuttgart, Allmandring 31, 70569 Stuttgart, Germany
[b] Stuttgart Research Centre Systems Biology, University of Stuttgart, Nobelstraße 15, 70569 Stuttgart, Germany

HIGHLIGHTS

- Risks in scale-up of gas fermentations can be minimized by CFD simulations.
- Circulation time and lifeline analysis give insight in reactor performance.
- CO limiting conditions will occur in bubble column reactor.
- Short- and long-term response can be expected for syngas fermentations.

ARTICLE INFO

Article history:
Received 7 February 2019
Received in revised form 7 June 2019
Accepted 14 June 2019
Available online 15 June 2019

Keywords:
Pseudo-stationary gas gradient
Two-phase Euler-Euler simulation
Lagrange trajectories
Bubble column reactor
Computational fluid dynamics (CFD)

ABSTRACT

Successful scale-up of biological fermentations requires the prevention of any performance losses from lab to production scale. Modelling large-scale conditions, in particular, so-called lifeline analysis, is a proper approach to unravel potential risks and to guide the way for preventing non-wanted underperformance. This study focuses on synthesis gas fermentations in bubble columns which are particularly challenging because of poor carbon (C) -source solubility and low bacterial energy availability under such anaerobic conditions. As a model case, *Clostridium ljungdahlii* DSM 13528 is studied in a 125 m^3 bubble column reactor investigating bacterial motion patterns, circulation time, short- and long-term responses. A pseudo-stationary gas gradient respectively fermentations 'snap-shot' was conducted with computational fluid dynamics in an Euler-Euler approach while the movement of the microorganism was simulated as Lagrangian massless particles. Cells were assigned uptake and product formation kinetics. Statistical lifeline analysis revealed that 97% of all cells experienced substrate limitations, whereas 84% were likely to undergo transcriptional changes after exposure in stress-inducing zone longer than 70 s. Bacteria movements predominately occurred between low and moderate product biomass yield regions with longer residence times in the latter. The circulation time derived from mixing time analysis is similar to the mean circulation time of a single bacterium. The latter was deduced from regime transition studies. Maximum residence times over 100 s as minimum regime crossing times of 10 s could also be identified. These findings show the high potential of Lagrange trajectories analysis in bubble column gas gradients which can be used for performance prediction and therefore risk minimization in scale-up.

1. Introduction

Supported by worldwide agreed resolutions such as the Paris Climate Agreement 2015, politicians and decision-makers in the industry more and more evaluate possibilities for establishing a CO_2 neutral bioeconomy (Philp, 2018). Accordingly, the use of synthesis gas (also called syngas) as a CO_2, CO and H_2 containing substrate gets in the focus to supply bacterial fermentations. Via syngas fermentations, said substrates can be converted through microbial routes to high-grade hydrocarbons (Köpke et al., 2010; Daniell et al., 2012) finally representing drop-in chemicals for the existing industrial infrastructure (Takors et al., 2018). From the engineering perspective, the main issue of this process is the poor mass transfer and equally low solubility of the gas components, since only dissolved carbon monoxide, carbon dioxide and hydrogen can be utilized by the acetogenic bacteria. Several reactor concepts have been investigated to overcome this challenge (Abubacker et al., 2011). As syngas fermentations typically yield commodities, i.e. low value, large volume products with small

* Corresponding author.
E-mail address: takors@uni-stuttgart.de (R. Takors).

https://doi.org/10.1016/j.ces.2019.06.018
0009-2509/

Nomenclature

A_R	reactor cross section, m^2
a	interfacial area concentration, m^{-1}
$c_{L,CO}$	dissolved CO concentration, mmol g_{CDW}^{-1}
d_{32}	Sauter mean bubble diameter
d_B	bubble diameter, m
D_R	reactor diameter, m
$D_{L,CO}$	diffusion coefficient of CO, $m^2\ s^{-1}$
H_R	reactor height, m
$k_{H,cp}$	Henry coefficient, mol L^{-1} atm^{-1}
K_I	inhibition constant, mmol g_{CDW}^{-1}
k_L	mass transfer coefficient, m s^{-1}
K_M	Monod constant, mmol g_{CDW}^{-1}
$K_{Y_{P,X}}$	half-maximum yield, mmol g_{CDW}^{-1} h^{-1}
lb	lower bound
$\dot{m}_{GL}$	mass transfer from gas to liquid phase, kg m^{-3} s^{-1}
q	consumption/production rate, mmol g_{CDW}^{-1} h^{-1}
T	temperature, K
ub	upper bound
v_{rel}	relative velocity, m s^{-1}

Greek

ε_G	gas hold-up, –
η_L	media viscosity, Pa s^{-1}
μ	growth rate, h^{-1}
ρ_L	liquid density, kg m^{-3}
σ_L	surface tension, N m^{-1}
τ	residence time, s

Subscripts

*	equilibrium concentration of gas in liquid phase
a	acetate
b	2,3-butanediol
B	bubble
c	carbon monoxide
c2	carbon dioxide
CDW	cell dry weight
e	ethanol
h^+	proton
L	liquid
R	reactor
w	water
max	maximum value

Abbreviations

BSD	bubble size distribution
CFD	computational fluid dynamics
DRW	discrete random walk
MS	mass spectrometry
PBM	population balance model
RANS	Reynolds-averaged Navier-Stoke equations
RNG	Re-Normalization Group
UDF	User-defined function

margins of economic benefit, large-scale gas fermentations should run with low operation costs. Furthermore, any loss of microbial production performance in large-scale should be prevented which is a challenging task (Takors, 2012). To minimize energy input and expenses, bubble columns are typically preferred. Compared to the conventional biotechnical set-up using stirred tanks they offer low operating costs and show high gas solubility because of their slim design and consequently high hydrostatic pressure.

However, the set-up or more precisely the competition between mixing and bioreaction creates gradients of dissolved substrates. In return, gradients impact the microbial activity as they impose fluctuating concentration in the cell environment. Various formulation of the same idea is to be found in Enfors et al. (2001); Schmalzriedt et al. (2003); Lapin et al. (2006); Morchain et al. (2014). This study will investigate related consequences focusing on the impact of a pseudo-stationary carbon monoxide gas gradient that will serve as the background of fluctuating bacteria. Pseudo-stationary gas gradient means that only a time point respectively 'snap-shot' of a large-scale bioreactor is simulated with a fixed biomass concentration. In this case, the gas holdup, as well as the liquid gas gradient, is stationary which does not account for the locally changing flow field. CO has been chosen as a model case because of the growth inhibition that is created by high levels (Mohammadi et al., 2014). Concentration changes that cells experience while flowing along the so-called 'lifelines' will be recorded. Apparently, (*i*) a sound large-scale gas gradient in a bubble column with representative flow structures in form of a motion 'snap-shot' and (*ii*) the translation of nutrient availability into product and biomass formation are essential prerequisites of such simulations.

The latter (*ii*) requires a thorough understanding of the intracellular metabolic network which interacts with the cellular environment. A comprehensive genome-scale stoichiometric model of *Clostridium ljungdahlii* has been published by Nagarajan et al. (2013). Chen et al. (2015) succeeded to apply the genome-scale model with the dynamic flux balancing technique of Gomez et al. (2014) to resolve the spatiotemporal distributions of *C. ljungdahlii* fluxes in a bubble column reactor. For minimizing computational efforts, the bioreactor was discretized in a set of compartments each assuming homogenous conditions. In general, compartment-based bioreactor simulations are quite common (Vrábel et al., 2001; Heins et al., 2015; Pigou and Morchain, 2015) because they inherently offer high simulation speed even in combination with complex kinetics (Mantzaris et al., 1999; Henson, 2003). Challenging flow patterns may be well approximated. However, important bubble characteristics such as coalescence and breakup are rarely (Nauha et al., 2018) or not at all considered which have a great impact on mass transfer especially in large scales (Akita and Yoshida, 1973).

To fulfil the constraint (*i*) compartment-based approaches need to be replaced by improved spatial resolution applying computational fluid dynamics (CFD). For gas–liquid multiphase flows, either the Euler-Euler or the Euler-Lagrange approach can be used (Noorman et al., 1993; Larsson et al., 1996; Schmalzriedt et al., 2003). The latter allows more detailed bubble simulation but is not recommended for large-scale simulations with gas hold-ups higher than 10%. Solving the Euler-Euler approach combined with a population balance model (PBM) enables the implementation of important bubble physics such as bubble expansion, breakage and coalescence. Gas hold-up and mass transfer get more realistic as well as the simulation of a pseudo-stationary gas gradient.

This study aims to predict the impacts of large-scale bubble column fermentations through the 'eyes' of *C. ljungdahlii* DSM 13528 (Tanner et al., 1993) which was chosen as a promising acetogenic strain of industrial interest. So-called 'lifelines' will be calculated, i.e. fluctuation profiles of individual cells recording extracellular impacts of biological relevance. To fulfil the constraints (*i*) and (*ii*) Euler-Lagrange multi-phase simulations will be linked to metabolic models. Accordingly, the study follows the original approach

of Lapin et al. (2004) which is gaining momentum by numerous continuing works (Haringa et al., 2016a; Haringa et al., 2016b; Haringa et al., 2017; Kuschel et al., 2017). The statistical interpretation of bacterial lifelines was initially shown by Haringa et al. (2016b) and will also be applied in this study. The framework will be used to investigate the challenging design of large-scale bubble columns as a prerequisite of successful syngas fermentations. Conclusions will be drawn not only with respect to mass transfer and hydrodynamics but particularly regarding the expected impact of time-varying concentrations on the metabolic behaviour of *C. ljungdahlii* in a 125 m^3 bubble column.

2. Materials and methods

2.1. Geometry, reactor set-up and biological system

For the computational investigation of a large-scale synthesis gas gradient, a bubble column reactor of 25 m in height and 2.5 m in diameter has been chosen. *Clostridium ljungdahlii* DSM 13528 (Tanner et al., 1993) serves as a model organism using as carbon (C) source carbon monoxide provided by synthesis gas. The gas inflow was set to 0.15 vvm at the whole bottom surface area of the reactor (A_R = 5 m^2) and contained a CO/N_2-mixture of 55/45 vol-%. The initial bubble diameter was 4 mm. Media viscosity η_L, density ρ_L and surface tension σ_L was assumed to be similar to the properties of water with η_L = 0.001 Pa s^{-1}, ρ_L = 1000 kg m^{-3} and surface tension σ_L = 0.072 N m^{-1}. The process was assumed to be isotherm with an operating temperature of 310.15 K. No additional pressure was applied beside the ambient pressure of 1 atm and the hydrostatic pressure due to the column height. All values can also be found in Table 1.

2.2. Mathematical method and computational set-up

The multiphase approach was conducted by an Euler-Euler simulation and solved with the commercial computational fluid dynamics (CFD) program ANSYS Fluent 18.0. The reactor volume of 125 m^3 was discretised into 125,000 numerical cells (see also Appendix A: Mesh). By solving the Reynolds-averaged Navier-Stokes equations (RANS) combined with the RNG (Re-Normalization Group) k-ε-model the gas gradient was approximated. The flow field in a bubble column is only developed when the liquid and dispersed phase are coupled and a bubbly flow reproduced. Coupling is achieved through the pressure and interphase exchange coefficients set by the chosen phase interaction correlations. The ideal gas law was applied. All other settings are listed in Table 1.

The flow equations were solved every 10 ms and the maximum iterations per time step were set to 25. However, only ten or fewer iterations per time step were needed. After 1000 s a constant gas hold-up was reached which corresponds to approximately 10 sim-

Table 1
Computational fluid dynamics simulation set-up for the pseudo-stationary gas gradient. Listed are boundary conditions, physical properties, phase set-up and solution methods. Details on the mesh can be found in Appendix A.

	Boundary condition	Units
Inlet	Velocity inlet with 0.0625 m s^{-1} (ε_G = 1)	m s^{-1}
Outlet	Degassing	
Wall	Non-slip conditions	
Initial bubble size	4	mm
	Physical properties	**Units**
Column diameter D_R	2.5	m
Column height H_R	25	m
Media viscosity η_L	0.001	Pa s^{-1}
Media surface tension σ_L	0.072	N m^{-1}
Media density ρ_L	1000	kg m^{-3}
Gas density ρ_L	1.1	kg m^{-3}
Temperature T	310.15	K
CO/N_2 composition	55/45	vol-%
	Models and phase set-up	**Source**
Multiphase	Euler-Euler (implicit)	
Population balance model	Discrete with 16 bins and a diameter range of 0.001 ≤ d_B ≤ 0.032 m	
Turbulence	RNG k-ε-model + differential viscosity model	
Phase interactions	Drag	Grace drag force or universal drag law (Clift et al., 1978)
	Lift	Tomiyama et al. (2002)
	Wall Lubrication	Antal et al. (1991)
	Turbulent Dispersion (cd = 0.8)	Burns et al. (2004)
	Turbulent Interaction	Sato and Sekoguchi (1975)
	Surface tension coefficient	Specified
	Solution methods	
Pressure-velocity coupling	Phase coupled SIMPLE	
Spatial discretization	Gradient	Least square cell based
	Momentum	QUICK
	Volume fraction	QUICK
	Turbulent kinetic energy	First order upwind
	Turbulent dissipation rate	First order upwind
	Phase 1 (liquid) and 2 (gas) species	First order upwind
	Phase 2 bin	First order upwind
Transient formulation	Bounded second order implicit	
Under-relaxation factors	Between 0.3 and 1 (mostly default)	
Transient regime	Time step size	0.01 s
	ITERATIONS per time step	Maximum 25 (usually > 10)
Simulation time	Flow field	1000 s
	Gradient	500 s
	Lagrange trajectories	500 s

ulation days with four cores and double precision. Likewise, the mass balance of gas in- and outflow converged in a steady state and the second modelling set-up was started.

In general, it should be stated that the k-ε-model represents a promising, commonly applied approach for estimating turbulent flow. However, because of its basic nature, non-accuracies of turbulence predictions may propagate further, e.g. affecting bubble breakage when applying the Luo model (Luo, 1993; Luo and Svendsen, 1996). Furthermore, Haringa and Mudde (2018) indicated that 1st order upwind has the tendency of underestimating turbulence quantities which may further affect the discrepancy between e.g. power input estimations using superficial gas velocity measurements and k-ε-derived predictions.

2.2.1. Pseudo-stationary gas gradient

The next step to reach a pseudo-stationary gas gradient is to include breakage, coalescence and bubble expansion. Therefore, different bubble sizes were introduced by the population balance model (PBM) also available in ANSYS Fluent 18.0. All in all, 16 bubble classes with a diameter range of $0.001\ \text{m} \leq d_B \leq 0.032\ \text{m}$ were chosen and for both - breakage and coalescence - the Luo-model (Luo, 1993; Luo and Svendsen, 1996) was applied. In addition, two user defined functions (UDF) for mass transfer and the dissolved carbon monoxide uptake were included. For the simulation of mass transfer from gas to the liquid phase in non-agitated bubble column reactors the conform Higbie correlation for the mass transfer rate k_L was chosen and solved in each numerical cell (Higbie, 1935).

$$k_L = \frac{2}{\sqrt{\pi}}\sqrt{\frac{D_L v_{rel}}{d_{32}}} \tag{1}$$

The correlation depends only on the Sauter mean bubble diameter d_{32}, the diffusion coefficient of CO $D_{L,CO} = 2\ \text{e}^{-9}\ \text{m}^2\ \text{s}^{-1}$ and relative bubble velocity v_{rel} of the numerical cell. While the Sauter mean bubble diameter is applied, the effects of PBM bubble distribution is neglected in this case. Henry's law was used to estimate solubility with the coefficient $k_{H,cp} = 7.7\ \text{e}^{-4}\ \text{mol}\ \text{L}^{-1}\ \text{atm}^{-1}$. The pressure gradient was also accounted for in this UDF, giving the equilibrium concentration of carbon monoxide $c^*_{L,CO}$. The interfacial area concentration a is calculated assuming a spherical bubble shape which finally leads to the expression in Eq. (2) for the mass transfer $\dot{m}_{GL}$ solved at each time step in each discretisation volume.

$$\dot{m}_{GL} = k_L\left(c^*_{L,CO} - c_{L,CO}\right)\frac{6\varepsilon_G}{d_{32}} \tag{2}$$

The Higbie correlation for the mass transfer and spherical bubble shapes are rough simplifications. The reader should be aware that dimensionless numbers for the bubbles, such as Eötvös (~60), Morton ($\log(\text{Mo}) = -10$) and Reynolds number (~5000) rather pinpoint to transient wobbling to spherical cap geometries (Grace, 1973). Additionally, gas hold-up and superficial gas velocity also indicate the transition between homogeneous bubbly flow to heterogeneous churn-turbulent flow (Deckwer et al., 1980; Krishna and Sie, 2000; Kantarci et al., 2005). Nevertheless, the Higbie correlation was used, not only for the sake of simplicity but also because profound mass transfer studies with the said biological matrix would have been needed which are far beyond the scope of this lifeline analysis.

The second UDF was written to describe the CO uptake kinetic q_c of *C. ljungdahlii* published by Mohammadi et al. (2014). With a maximum uptake of $q_{c,max} = 34.36\ \text{mmol}\ g^{-1}_{CDW}\ h^{-1}$ and a Monod constant of $K_M = 0.02\ \text{mmol}\ g^{-1}_{CDW}$ the equation also includes a substrate ($c_{L,CO}$) inhibition modification by Andrews with an inhibition coefficient $K_I = 0.55\ \text{mmol}\ g^{-1}_{CDW}$.

$$q_c = \frac{q_{c,max} c_{L,CO}}{c_{L,CO} + K_M + \frac{c^2_{L,CO}}{K_I}} \tag{3}$$

The dissolved carbon monoxide uptake takes place in each numerical cell at each time step. After another 500 s a new steady state for the gas hold-up and dissolved CO concentration was reached which does not account for the constantly changing periodic flow field. Pseudo-stationary gradient means that only a time point respectively 'snap-shot' of a real large-scale simulation is chosen with a temporary constant biomass concentration of 10 g L^{-1} and no cell multiplication. This assumption can be made since mixing and mass transfer time scales are much smaller than time scales for bacterial growth. The second simulation part lasted more than ten simulation days since 16 bubble classes instead of one, breakage, coalescence, bubble expansion, mass transfer and a reaction needed to be solved as well. Detailed changes in the volumetric mass transfer rate after 1000 s and 1500 s can be found in Appendix E.

2.2.2. Lagrange trajectories

The final CFD simulation uses the generated pseudo-stationary gas gradient and flow field to analyse cell lifelines, movement patterns and circulation time. Therefore, besides the Euler-Euler phases a third phase, the bacteria were introduced as massless Lagrange particles as well as the discrete random walk (DRW) model was enabled. The gradient and flow field were set as frozen and not further calculated. With another user defined function every 30 ms the particle ID, the corresponding CO concentration and position were recorded. In total, 120,000 bacteria were tracked for 500 s. The trajectories were checked for ergodicity which can be found in Appendix B: Statistical relevance. Further evaluations of the lifelines were conducted with the program MATLAB®.

2.3. Uptake kinetic and product formation correlation

C. ljungdahlii prefers CO over CO_2 because the substrate equally serves as a carbon and electron source. However, the consumption of CO_2 requires additional electrons originating from the crucial co-uptake of H_2. For the sake of simplicity, this case is omitted in the current study which focuses on the impact of CO gradients only. The growth of *C. ljungdahlii* coincides with the formation of the by-product's acetate, ethanol, 2,3-butanediol and maybe even carbon dioxide (under distinct conditions). Clearly, the latter may only be produced under ample CO conditions when the carbon drain to targeted products such as ethanol and 2,3-butanediol is limited (e.g. because of non-optimum strain engineering). Linking metabolic modelling with large-scale CFD represents a trade-off between crucial metabolic complexity and computational efforts necessary to solve the large-scale simulation problem. Because the use of genome-scale network models is computationally expensive a minimum stoichiometry model was formulated mirroring the essentials of *C. ljungdahlii* metabolism. With the help of a simple net Eq. (4) and the element balances for carbon C, hydrogen H and oxygen O (Eq. (5)) the correlation can be derived.

$$\underbrace{1\ \text{CO}}_{q_c} + \underbrace{Y_{H^+,CO}H^+}_{q_{h^+}} \rightleftharpoons \underbrace{Y_{X,CO}CH_{1.8}O_{0.5}}_{q_x} + \underbrace{Y_{Ac,CO}CH_{1.5}O}_{q_a} + \underbrace{Y_{EtOH,CO}CH_3O_{0.5}}_{q_e}$$
$$\underbrace{Y_{2.3But,CO}CH_{2.5}O_{0.5}}_{q_b} + \underbrace{Y_{CO_2,CO}CO_2}_{q_{c2}} + \underbrace{Y_{H_2O,CO}H_2O}_{q_b} \tag{4}$$

The net reaction includes all relevant products such as biomass (x), acetate (a), ethanol (e), 2,3-butanediol (b) and carbon dioxide (c2). Water (w) and hydroxide ion (h^+) are needed for H- and

O-balance. Analogous to the yields Y per c-mol CO the uptake and production rates q are indicated at the bottom in Eq. (4).

$$\begin{matrix} C: \\ H: \\ O: \end{matrix}\begin{pmatrix} 1 & 0 & 1 & 0 & 1 & 1 & 1 & 1 \\ 0 & 1 & 0 & 2 & 1.8 & 1.5 & 3 & 2.5 \\ 1 & 0 & 2 & 1 & 0.5 & 1 & 0.5 & 0.5 \end{pmatrix} \begin{pmatrix} q_c \\ q_{h^+} \\ q_{c2} \\ q_w \\ q_x \\ q_a \\ q_e \\ q_b \end{pmatrix} = \bar{0} \tag{5}$$

Eq. (4) can also be transformed into Eq. (5) which is five times under-determined. Therefore, the resulting solution space is restricted by lower (lb) and upper bounds (ub) as described in Eq. (6). The ratio qc/1.7 is motivated by own experimental observations (data not shown) studying the by-product formation of *C. ljungdahlii* wildtype under ample CO conditions.

$$\begin{matrix} \text{lb} & = & (q_c & -100 & q_c/1.7 & -100 & 0 & 0 & 0 & 0) \\ \text{ub} & = & (q_c & 100 & q_c/1.7 & 100 & 2.5 & 100 & 100 & 100) \end{matrix} \tag{6}$$

Maximum growth for *C. ljungdahlii* is set to $\mu = 0.06\ h^{-1}$. H_2O and H^+ can either be consumed or produced and the by-products only produced.

$$f(q_c) = \max(q_x + q_a + q_e + q_b) \tag{7}$$

The optimal result can be derived by maximizing the sum of all production rates (Eq. (7)) which is graphically shown in Fig. 1(A) for different possible uptake rates. In each case, the element balances are not violated.

Fig. 1(B) compares experimental findings with the simulation results. How the experiment was conducted can be found in Appendix D: Experimental values. As the predictions are the result of elementary flux balance analysis, instantaneous 'pseudo-steady-state' transitions are intrinsically assumed which translate local q_c to growth and production rates. Accordingly, time-resolved metabolic or transcriptional dynamics as seen in Chen et al. (2015) and Löffler et al. (2016) are not covered by the simple modelling approach.

2.4. Statistical evaluation

2.4.1. Evaluation of regime transition events

For the statistical evaluation, the Lagrange trajectories were sorted and the CO concentration profiles filtered as described in Kuschel et al. (2017). The filtered concentration is translated into uptake kinetics and total product-biomass yields. The latter can be derived from the optimization results of the element balances which leads to Eq. (8) also shown in Fig. 2(A). The total product-biomass yield describes the carbon share between all products and biomass as a function of the carbon uptake rate. High $Y_{P,X}$ values indicate that more carbon flows in the formation of the desired by-product. Accordingly, high $Y_{P,X}$ values can be considered as a proxy for strong metabolism in growing cells. The aim of this translation is to investigate how the cells move. From which gradient segment they come, where they go and for how long they stay in a certain environment defined by the surrounding dissolved CO concentration. Therefore, conditions have to be classified in high and low total product-biomass yields and in a transition phase between both regimes.

$$Y_{P,X}(q_c) = \begin{cases} \frac{1.51 q_c}{q_c - 2.29} & -14 < q_c \le 0 \\ -\frac{q_c}{6} - 1 & q_c \le -14 \end{cases} \tag{8}$$

The first functional segment ranging from $q_c = 0$ to $q_c < -14$ mmol $g_{CDW}^{-1}\ h^{-1}$ shows Monod-type kinetics with a half-maximum yield at $K_{Y_{P,X}} = 2.29$ mmol $g_{CDW}^{-1}\ h^{-1}$. This value was also used to mark the beginning regime transition from low to higher yields. Translating the yield limits into CO concentrations transfers the yield regime into a CO regime, respectively. When $q_c \le -14$ mmol $g_{CDW}^{-1}\ h^{-1}$ the function turns into a linear correlation. The maximum of CO conversion into biomass formation is achieved. Additional uptake directly fuels by-product formation. This switch was used as the second regime transition criterion indicating the high yield zone. Thus, three regimes can be specified: **L** for low yields from zero to -2.29 mmol $g_{CDW}^{-1}\ h^{-1}$ ($0 \le Y_{P,X} < 0.75$), **T** for transition area between -2.29 and -14 mmol $g_{CDW}^{-1}\ h^{-1}$ ($0.75 \le Y_{P,X} < 1.33$) and **H** for high yields starting at -14 mmol $g_{CDW}^{-1}\ h^{-1}$.

The classification into three regimes is also graphically implied in Fig. 2. The regime classification represents the number of smallest encoding units characterizing the shift between three gradient zones which the bacteria do transverse. Lifelines are characterized by a sequence of regime changes thereby integrating all extracellular stimuli exposed on the cell. Three gradient areas lead to six regime transition events which are schematically shown in Fig. 2 (B) and are additionally described in the following list.

- **HTH**: Event from high to transition and back to high product per biomass yield areas.

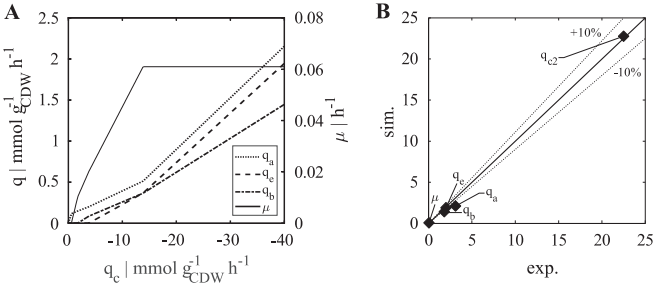

Fig. 1. Optimization results for kinetic correlation (A) and comparison with experimental data (B). In (A) the maximization for product formation results are graphically shown for several possible CO uptake rates q_c. The production rates for acetate q_a, ethanol q_e and 2,3-butanediol q_b are shown as well as the growth rate μ on the left side. The simulation outcome was compared with experimental data in (B). The experimental rates in mmol $g_{CDW}^{-1}\ h^{-1}$ were provided by M. Hermann (ongoing studies, IBVT) who performed synthesis gas fermentations with a gas composition of 55/30/5/10% for $CO/H_2/CO_2/Ar$.

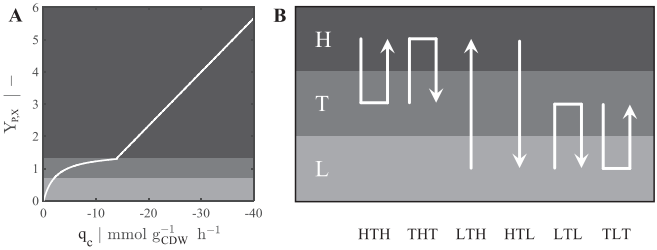

Fig. 2. Regime classification as function of productivity. In (A) the product biomass yield $Y_{P,X}$ is given in c-mol per c-mol as a function of CO uptake rate (see also Eq. (8)). From q_c of zero to −14 mmol g_{CDW}^{-1} h^{-1} the $Y_{P,X}$ function shows Monod-tyke trends with a half-maximum value of −2.29 mmol g_{CDW}^{-1} h^{-1} which is also the threshold for entering the transition regime. The upper limit of transition is indicated by −14 mmol g_{CDW}^{-1} h^{-1} when the $Y_{P,X}$ starts to ascend linearly. All six regime transition strategies are illustrated in (B).

- **THT**: Reverse movement starting from the transition area with retention in the high yield area and back to transition.
- **LTH**: Crossing all regimes from low to high and with dwelling in the transition area.
- **HTL**: Reverse event from low to high product biomass yields.
- **LTL**: Analogous to HTH but from low to higher and back to low yield areas with residence time in the transition domain.
- **TLT**: Same regimes but with a stay in the lower domain with little product biomass yields and start in the transition class.

The residence time is referred to as τ and accounts for the 'sandwich' regime always. The frequency of each regime transition event was counted and the duration recorded.

2.4.2. Evaluation of short- and long-term responses

For qualifying the stress impact of the cells biological criteria are necessary. To distinguish between short- and long-term responses, two sensitive thresholds are needed. The occurrence of critical CO concentrations flags the start of a short-term stress stimulus. The length of the exposure of this stimulus flags the putative triggering of long-term transcriptional responses. The longer a bacterium lingers in an area with the critical concentration the more severe the internal changes and therefore energy costs for the cell will be. Usually, short- and long-term responses can be examined with scale-down approaches such as plug-flow experiments (Löffler et al., 2016).

In the case of *C. ljungdahlii*, no comparable experimental studies are available. Accordingly, related threshold values were estimated taking the well-investigated *Escherichia coli* as reference. Taymaz-Nikerel et al. (2010) and Michalowski et al. (2017) estimated the maintenance demands and the maximum glucose uptake of *E. coli* as m_s = 0.057 g_{gluc} g_{CDW}^{-1} and q_{max} = 1.8 g_{gluc} g_{CDW}^{-1} h^{-1}, respectively. Consequently, 3.2% of the maximum uptake are needed for maintenance demands under optimum growth conditions. In the case of *C. ljungdahlii*, the optimum CO uptake rate can be derived from the Andrew inhibition kinetic as $q_{c,max}^{real} = q_c\left(\sqrt{K_M K_I}\right)$ = 24.87 g_c g_{CDW}^{-1} h^{-1} (0.1 mmol L^{-1}). Assuming that maintenance needs of *E. coli* and *C. ljungdahlii* are somewhat comparable the 3.2% fraction corresponds to $c_{L,CO}^{crit}$ = 0.003 mmol L^{-1}. This concentration is expected to be a good indicator for a biological regime shift as it marks the likely initiation of regulatory programs to adapt metabolic activities to the limiting CO supply.

Translating the metabolic stress stimulus into a transcriptional and translational response takes time. In the case of *E. coli*, early transcriptional responses were found after 30–40 s whereas the bulk of transcriptional activation occurred after 70 s (Löffler et al., 2016). Accordingly, minimum critical residence times in stress-inducing zones were chosen as τ^{crit} = 10 s, τ^{crit} = 40 s and τ^{crit} = 70 s. Because related measurements are missing for *C. ljungdahlii* and because similar findings were found for other microbes (not yet published), the same criteria were set for *C. ljungdahlii* in this study.

Further information on the evaluation of the short- and long-term response can be found in Appendix F: Detailed short- and long-term responses evaluation.

3. Results and discussion

3.1. Flow field and pseudo-stationary gas gradient

To reach a pseudo-stationary gas gradient in an industrial-scale bubble column reactor two simulation set-ups have been chosen. The flow field was developed by solving the Euler-Euler multiphase approach with one entering bubble class of 4 mm and all phase interactions described in Table 1. As steady-state indicator the average gas hold-up ε_G was tracked for 1000 s until it stayed constant at 0.34. Then, the population balance model (bubble classes with breakage, coalescence and expansion) was additionally enabled considering CO mass transfer with respect to the bacterial needs. After 1500 s the final CO gradient was reached (ε_G = 0.21). Fig. 3 shows the mean gas hold-up history in (A) as well as the changes in bubble size distribution (BSD) for the second simulation approach from 1000 s (start, dark grey) to 1500 s (end, red) in (B).

BSDs are indicated as a function of number density n_G in Fig. 3 (B). They reveal that both bubble breakage and coalescence occur, although the bubbles the tendency of coalescence is dominating. Since the initial bubble size is 4 mm (bin 7) this class is represented the most followed by bubble classes with larger diameters (first picture in Fig. 3(B), distribution colored in red). The composition of the final BSD is similar to observations with water–air experiments of Lehr et al. (2002). However, the bubble column of this study is six times larger than the set-up of Lehr et al. (2002) creating longer bubble residence times and thus higher probability for coalescence finally leading to larger bubbles classes up to 3.2 cm (bin 16). Consequently, a lower average gas hold-up was calculated after 1500 s compared to 1000 when coalescence was not yet considered.

The flow field, gas hold-up, and concentration profiles of the CFD simulation are graphically displayed in Fig. 4(A) to (C) after 1500 s simulation time. Whereas graphic (B) and (C) show similar gradient profiles with maximum values at the bottom and reducing values towards the top, the flow field in (A) is different. By trend, high velocities are observed in the upper reactor region close

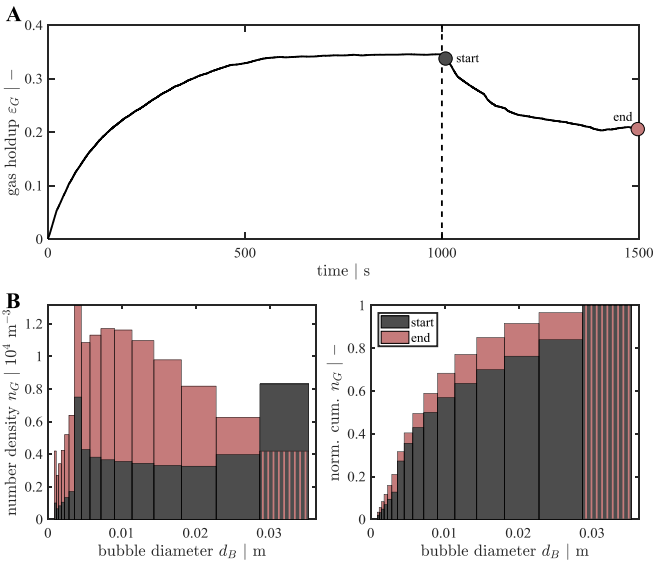

Fig. 3. Simulation development to reach pseudo-stationary gas gradient. In (A) the average gas hold-up in the bubble column reactor is plotted versus time. During the first 1000 s the flow field was developed with one bubble size and no mass transfer from gas to liquid. From 1000 to 1500 s breakage and coalescence and effects of hydrostatic pressure are enabled by including the population balanced model. The average bubble size distribution for start (dark grey) and end point (red) are shown in (B). The number density over diameter bin is given as normal and cumulative distribution. The initial bubble size is always 4 mm (bin 7). (For interpretation of the references to colour in this figure legend, the reader is referred to the web version of this article.)

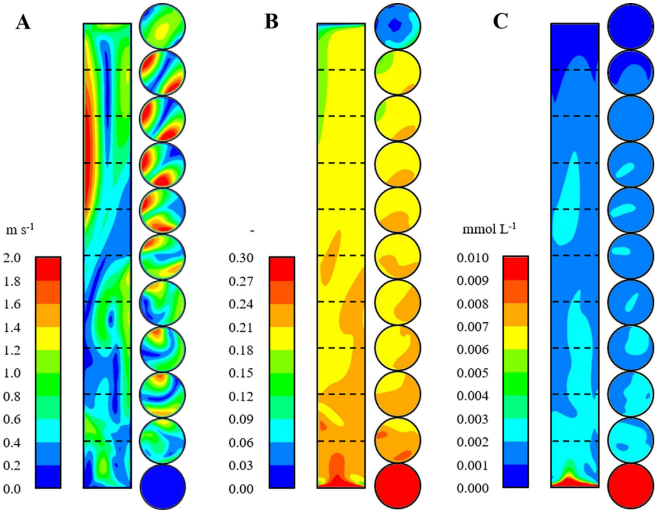

Fig. 4. Flow field (A), gas hold-up (B) and CO concentration profile (C) of the CFD simulation. Colour scale and the unit are given on the left side. Shown are side profiles and eleven section planes indicated by the dashed lines as well as reactor top and bottom. In (A) the velocity magnitude is depicted. (For interpretation of the references to colour in this figure legend, the reader is referred to the web version of this article.)

to the wall and low to moderate flow patterns are dominating in the low part of the bubble column. The spatially distributed flow pattern reflects the impact of changing bubble size distribution very well. To be precise, the more proximate to the outer top regions the larger the average bubble size and the faster the bubble rising velocity is. Accordingly, faster bubble rise creates broader bubble size distributions (data not shown).

As mentioned in the materials and methods section, the flow field has a cyclic behaviour. The distributions of Fig. 4 are 'snapshots' that re-occur frequently whereas the total hydrodynamic scenario is in steady-state with respect to the gas hold-up (see Fig. 3). To investigate the impact of the gradients on the cells, the condition of Fig. 4 has been 'frozen' serving as a background for further studies. Accordingly, the CO gas gradient was used to investigate the bacterial lifelines with respect to productivity, circulation time and long- and short-term responses. As such, the observations should be interpreted as a trend for qualifying the bacterial lifelines and for discussing putative impacts on cellular performance.

3.2. Bacterial lifelines and frequency of regime transition events

To assess statistically the bacterial movements through the gradients in the bubble column, regime shifts (introduced in the Material and Method section) were evaluated. The analysis focusses on the flow pattern qualifying the beginning, residence time and end of the bacterial flows (see Fig. 2(B)). The stay in the transient interim regime is particularly of interest since information about possible performance changes of the microbe can be deduced. The threshold criteria defined in the Material and Method section basically mirror the assumption that the longer a bacterium stays in one regime the more likely it adapts to its surroundings. As a consequence, energetically demanding adaptations of the regulatory programs are initiated that may deteriorate the production capacity of the cells (Löffler et al., 2016).

Fig. 5(A) shows the regime-specific zones inside the bubble column. The regime classification **H** encoding high product biomass yields is depicted in dark grey and is located in the lowest column zone (zoomed detail). In contrast to **H**, the transition regime **T** (in lighter grey) spreads along the majority of the column height whereas the low product biomass yield regime **L** is located predominately at the top of the reactor. Moreover, the 30 s lasting courses of the two lifelines, L1 and L2, are depicted in Fig. 5(B) to (D) together with their translation in product biomass yield profiles (C) and regime classifications (D). While the first lifeline L1 passes through all three regimes the second lingers in the transition regime for the time span of 30 s. For L1 two movement patterns can be recognized, the LTH and the THT regime transition events with dwell times of τ_{LTH} = 18.3 s and τ_{THT} = 2.1 s, respectively. However, L2 always stays in the T zone.

Further lifeline processing comprises counting of transition events and grouping with respect to the residence time in the transient regime (Fig. 6). Related values indicating maximum and average time of stays were calculated and listed in Table 2.

Movement patterns from the transition area to low product biomass yields and back (TLT) are the most common transitions with an overall probability of 46.0%. However, the second most likely regime transition LTL happens almost as often with 44.6% (see also Table 2). All other events have probabilities lower than 4%. As for the average and maximum residence times, very different results can be stated. While the mean dwell times $\bar{\tau}$ ranges from 3.4 s up to 32.8 s the maximum time spans can reach over 100 s for the LTH and HTL pattern. Movements starting in the transition regime and circling back to it (THT and TLT) show the lowest τ_{max} with 15.3 s for THT and 28.4 s for TLT. Movement patterns passing all regimes (LTH and HTL) reveal not only the longest but also a minimum residence time of about 10 s.

Whereas the total event frequency reflects the volumes encompassed by the related regimes the duration of a stay and how often a transition event occurs depends strongly on the gradient profile

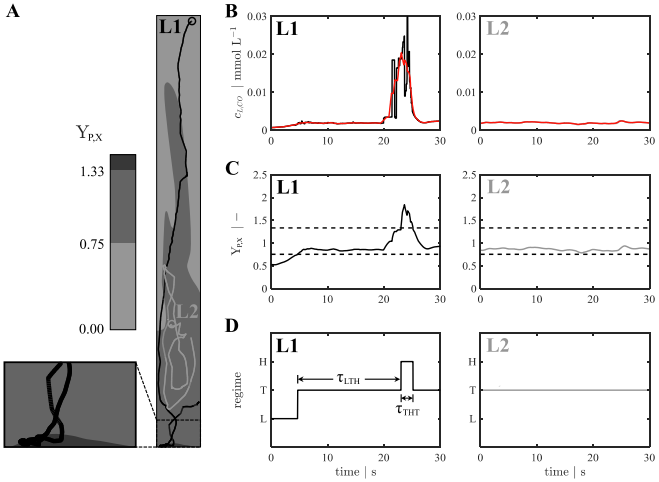

Fig. 5. Processing of bacterial lifelines. Exemplary two 30 s lasting bacterial lifelines L1 (black) and L2 (grey) are shown in spatial resolution in (A). The related CO concentration profiles are given in (B) also indicating the results of the moving-average filter (red line) (see also Kuschel et al., 2017). Concentrations are translated in uptake rates q_c finally yielding the total product-biomass yield $Y_{P,X}$ presented in (C). The black dashed lines indicate the regime transition boundaries which are used to translate the lifelines into regime switch diagrams with transient stays τ of each regime switching event (D). The regimes are divided into high (H), transition (T) and low (L) product biomass yields. For lifeline L1 two strategies are shown (LTH and THT) with different durations of stay τ. (For interpretation of the references to colour in this figure legend, the reader is referred to the web version of this article.)

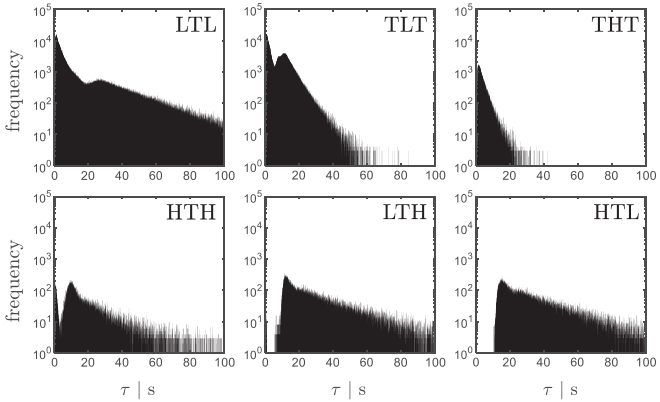

Fig. 6. Regime transition strategies over retention time. The frequency of all six regime transition events are given (log-scale) and plotted against their duration of stay τ in the second (transient) regime. For each histogram 600 bins have been chosen.

Table 2
Total frequency, average and maximum retention time. For each regime transition event the total frequency, mean $\bar{\tau}$ and τ_{max} is listed. For τ_{max} a confidence level of 99% was chosen.

Regime transition event	Total frequency in %	$\bar{\tau}$ in s	τ_{max} in s
LTL	44.6	12.1	86.6
TLT	46.0	7.2	28.4
THT	3.6	3.4	15.3
HTH	1.2	17.4	80.4
LTH	2.4	29.6	107.5
HTL	2.2	32.8	109.8

and on the flow field. Comparing the most likely events LTL and TLT differences in $\bar{\tau}$ and τ_{max} can be detected revealing relatively low values of $\bar{\tau}$ and τ_{max} for TLT. This can be explained by comparing Fig. 4(A) with Fig. 5(A), i.e. the flow field with the gradients divided in regimes. The finding that TLT $\bar{\tau}$ and τ_{max} values are lower than LTL counterparts is in agreement with the higher velocities at the top of the reactor, in particular, close to the wall. They coincide with the low product biomass yield regime anticipating a high turnover of cells passing this zone. Accordingly, the TLT events reveal shorter time spans compared to the LTL although total event frequencies are similar.

The low event frequency of LTH and HTL regime transitions can be explained with the far distance between the high and the low zones (see Fig. 5(A)). The bulk of the T compartment has to be passed either to reach the H area at the bottom or to enter the L zone travelling from the bottom. Regarding the flow pattern, such travels require 10 s at least. Hence, transitions are dominated by moderate regime shifts exposing cells from one adjacent regime to the other – and back. 'Extreme' shifts are relatively rare summing up to about 5% of all events (LTH + HTL). This finding is in agreement with similar observations of Haringa et al. (2017) who investigated stirred tanks equipped with Rushton turbines under production-like conditions.

Additionally, the small volume of the H zone is worth noticing. The compartment represents less than 1% of the total bubble column, only. In other words, physical properties of CO solubility are such poor that only a 'tiny' fraction of the bubble column is operating with maximum CO transfer. The majority of the bioreactor works with moderate or even limiting CO supply. Accordingly, putative CO inhibition is only an issue for a small compartment of the bubble column located at the bottom.

Besides the statistical evaluation of regime transitions, also the average circulation time of a bacterium can be estimated by weighting the average residence time of each regime transition event with its overall probability. Accordingly, the average circulation time in the bubble column is estimated as 10.5 s. The value reflects fairly good the estimation of 14.7 s which is derived from the mixing time (see Appendix C: Circulation time). Interesting enough, this is a remarkably low value for industrial type settings of this size. Often, stirred tank bioreactors reveal average circulation times of about 20 s (Haringa et al., 2017; Kuschel et al., 2017). Noteworthy, such circulation times are found for power inputs of 4185 W/m^3 which is higher than 613 W/m^3 invested in bubble columns. This trend is independent weather simulated or observed power input is used. As a fundamental characteristic, bubble column reactors show good mixing properties due to long axial flow patterns. While stirred tank reactors with Rushton blades predominately reveal radial velocities with typical Eddy formations along the stirrer and hard transitions zones between the vortices. These vortex rolls can cause longer dwelling and therefore equally longer average circulation times.

3.3. Investigation of short- and long-term responses

The statistical evaluation of the Lagrange trajectories offers insight about the possible short- and long-term responses bacterial cells may show after proper induction. For this reason, two critical values have been chosen with respect to the concentration threshold and duration. Taking findings of *E. coli* as a reference, the short-term metabolic responses of *C. ljungdahlii* is expected to be triggered as soon as a critical CO value, namely the equivalence of starting maintenance demands, will be reached. In other words, when the dissolved CO concentration falls below 0.003 mmol L^{-1} the short-term response is assumed to be switched 'on'. Because its translation in transcriptional and translational reprogramming requires time, different residence times of continuing stimulus were investigated: τ^{crit} = 10 s, τ^{crit} = 40 s and τ^{crit} = 70 s.

Fig. 7(A) to (B) depicts the results of the three stress exposure periods and Fig. 8 shows the distribution of cell fractions which

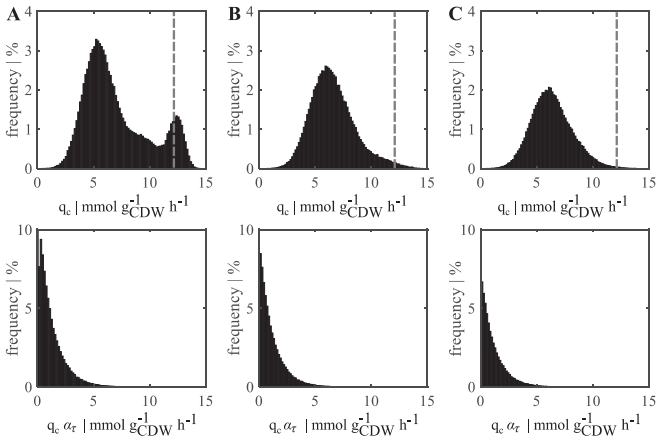

Fig. 7. Expected bacterial responses while experiencing limitation for different exposure periods. As described in Appendix F three critical periods τ^{crit} = 10 s in (A), τ^{crit} = 40 s in (B) and τ^{crit} = 70 s in (C) have been chosen to show the distribution of uptake rates (first row) and the weighted distribution by the actual duration τ_i indicated by the case-specific weighting factor $\alpha_{\tau i}$ (second row). Histograms are normalized to the highest total percentage of the average occurrence (τ^{crit} = 10 s) and divided into 100 bins. The average uptake rate q_c = 12.26 mmol g_{CDW}^{-1} h^{-1} is indicated as a grey dotted line.

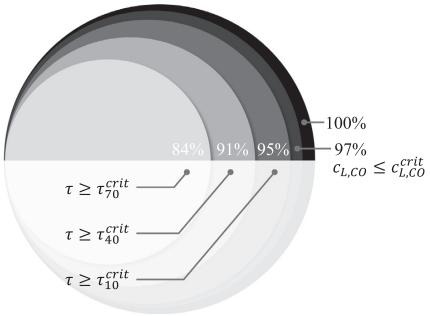

Fig. 8. Distribution of cells exposed to CO stimuli with respect to different resting periods. Black indicates all cell of which (in dark grey) 97% experienced the critical value $c_{L,CO}^{crit}$ = 0.003 mmol L^{-1}. The other grey colours indicate the cell fractions thereof which stayed in the stress zones with the exposure times as indicated.

are exposed to the CO stress stimulus for different residence times. The statistics of τ^{crit} = 10 s include τ^{crit} = 40 s and τ^{crit} = 70 s which is indicated in Fig. 7 and more clearly illustrated in Fig. 8.

According to Fig. 7, the cellular population in the bubble column is not homogenous but heterogeneous instead. Short residence times of 10 s show a bimodal distribution (Fig. 7(A)). Because carbon uptake rates directly correlate with product formation a bimodal distribution of production zones can be expected in this area, too. Additionally, the normalization by residence time indicates very short retention in high concentration areas which concludes with the finding for the THT event (Table 2 with $\bar{\tau}_{THT}$ = 3.4 s). However, longer exposure periods are somewhat homogenous, revealing unimodal distribution (Fig. 7(B) and (C)). All three critical time periods statistics deviate strongly from the average uptake rate q_c = 12.26 mmol g_{CDW}^{-1} h^{-1} (Fig. 7 grey dotted line) which indicates that substrate limitation and time-dependant bacterial adaption will have a major negative effect on the overall production of this fermentation process.

From the biological perspective, the most striking observation is that about 97% of all bacteria experienced severe CO limitation at least once ($c_{L,CO} \leq c_{L,CO}^{crit}$). As indicated in Fig. 8, 95% are likely to show immediate metabolic changes (exposure time 10 s) and even 84% stay in the CO limitation zone longer than 70 s. Taking the *E. coli* case as a reference, 70 s exposure time marks the beginning of transcriptional changes (Löffler et al., 2016). Cells are expected to react on external CO limitation by inducing starvation programs which coincide with severe up- and down-regulation of related genes. In *E. coli*, such transcriptional adaptations could be quantified with respect to additional ATP demands revealing add-on maintenance needs of 15% – 50% depending on the stimulus. By analogy, similar add-on maintenance demands should be expected for *C. ljungdahlii* as well. Reductions of the product biomass yields and the growth rate are fairly probable. Nevertheless, it needs to be stressed that related experimental scale-up studies with *C. ljungdahlii* are simply missing. These are essential to proof the simulation results of the current work.

4. Conclusions

Lagrangian trajectories for *Clostridium ljungdahlii* have been successfully calculated enabling the lifeline analysis in an anaerobic, synthesis gas operated bubble column. Through the eyes of *C. ljungdahlii* the impacts of a pseudo-stationary carbon monoxide gas gradient were recorded with respect to short- and long-term CO stimuli.

Hydrodynamic analysis reveals a well-mixed bubble column showing average circulation times of about 10 s. The value is comparable to conventional stirred tank bioreactors but achieved with less power input. Defining CO-induced thresholds for triggering the short- and long-term response of the cells enabled the bubble column division into the H, T and L zones and – most important – the identification of related transition events. Although most of the

transitions may be qualified as 'moderate', because they only consider shifts between adjacent regimes, they indicate transitions under already CO limiting conditions. In other words, most of the bioreactor is suffering CO supply which outlines the need to improve CO mass transfer and/or to engineer strains that cope with the conditions with the least add-on ATP demand. Given that calculated gradients will be much more pronounced with higher biomass concentrations and more active cells, the need to perform such engineering studies is apparent for further process intensification.

The lifeline analysis depends on the proper prediction of physical and biological impacts. The first requires accurate models for simulating e.g. local energy dissipation rates, mass transfer and flow fields. In particular, multiphase conditions are still very challenging requiring ongoing improvements for accurately predicting local energy dissipation and for providing good estimations of bubble size distributions, breakage and coalescence. Fundamental research is necessary to derive related models also considering particularities of biotechnical application (e.g. media compositions). Intrinsically, said studies provide 'snap-shots' on fermentation performance. Thorough experimental and simulation studies are necessary for statistically evaluating their reliability further.

From the biological perspective, the study depends on the real stress response of *C. ljungdahlii* which – unfortunately – has not been investigated experimentally so far. Related results will surely improve our understanding of large-scale processes using the tool of lifeline analysis as a very promising design and optimization approach.

Acknowledgments

At this point, we want to thank Maike Kuschel, Andreas Ulmer and Julia Zieringer for their inspiring discussion and support during the simulation process. This work was supported by the Federal Ministry of Education and Research (BMBF; FKZ031A468B).

Author Contributions

Prof. Dr.-Ing. Ralf Takors and Dr. Alexei Lapin advised the study while Maria Hermann provided the experimental uptake and production rates. Simulation, evaluation, and writing of the manuscript was conducted by Flora Siebler.

Declaration of Competing Interest

The authors have declared no conflicts of interest.

Appendix A. Mesh

The computational fluid dynamics mesh of the 125 m^3 bubble column reactor was also generated with the commercial program ANSYS Fluent 18.0. Therefore, the reactor was divided into three parts: the inner rectangular section with uniform grid cells, the outer cylinder cut with inflating grid cells as well as the area in-between both geometries. Mainly rectangular grid cells are generated giving a good minimal orthogonal quality of 0.66 and maximum aspect ratio of 4.1. All in all, about 125000 numerical cells are used for the simulation (approx. 1000 per 1 m^3, see also Fig. 9).

Simulations with a higher spatial resolution (250000 and 1000000 numerical cells) and the same set-up repeatedly revealed severe numerical instabilities. Solving Euler-Euler multiphase combined with population balance model turned out to be not only computationally intensive but also very sensitive with respect to the multiphase interactions per cell. Poor approximations of the flow dynamics in a single cell turned out to be easily propagated (and amplified) to other cells finally causing cessation of the whole simulation. Nevertheless, our set-up ensured that global parameters such as gas hold-up are within the expected range of heterogeneous churn-turbulent bubbly flows (Krishna and Sie, 2000). Besides, satisfying flow fields and gas gradients were achieved giving a first glimpse on their effect on bacterial movements and lifelines.

Appendix B. Statistical relevance

As a quality criterion of statistical relevance, the ergodicity can be used. The Lagrange trajectories are ergodic when the time average is the same as the average over the probability space. Therefore, the reactor was spatially discretised into ten uniform columns (Fig. 10(A) z_0-z_9) and the particles can be superimposed at each time step (t_0-t_{end}). The expected value is compared to the result and should lie in the confidence level of 98%.

As shown in Fig. 10(B) the superimposed result lies within the confidence level. Additionally, the average carbon monoxide concentration of the Lagrange trajectories is $c_{L,CO}$ = 0.0020 mmol L^{-1} which is approximately the same as of the liquid phase with $c_{L,CO}$ = 0.0018 mmol L^{-1}.

Appendix C. Circulation time

The mixing time of the reactor set-up was approximated in a dynamic flow field. Therefore, mass transfer and CO uptake were disabled and the dissolved CO concentration mixing tracked at three representative positions (P(x/y/z) in meter) in the reactor:

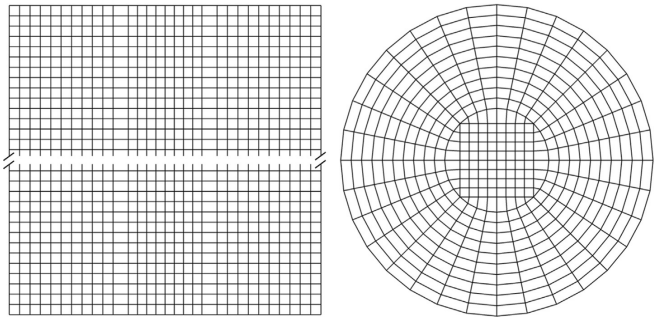

Fig. 9. Computational fluid dynamic grid. Top and bottom section of the grid in side few and top few.

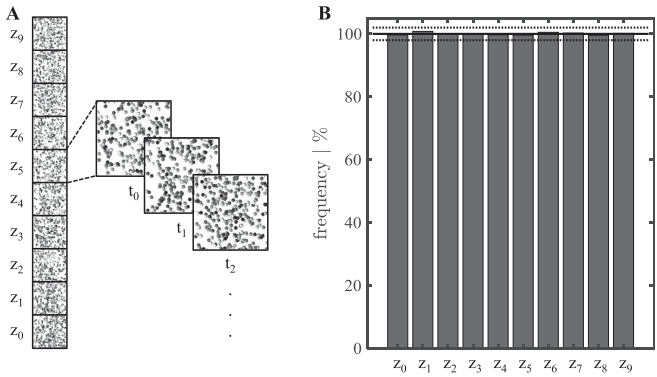

Fig. 10. Statistical relevance of Lagrange trajectories. In (A) 3000 representative enlarged bacteria are depicted to illustrate the spatial (z_0-z_9) and temporal (t_0-t_{end}) residence of the bacteria. For each spatial segment z the probability with respect to the expected value (black line) is shown in (B) as the frequency in percentage. Dotted black lines indicate the ±2% deviation limit.

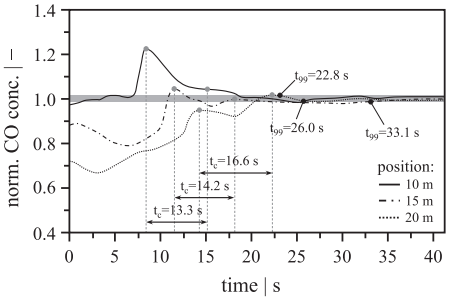

Fig. 11. Determination of the mixing time. To determine the mixing time the CO mass transfer and uptake was disabled. At three positions (P_1(0/0/10), P_2(0/0/15) and P_3(0/0/20)) the dissolved CO concentration was tracked until it reached 99% of the overall concentration. Pictured is the normalized CO concentration over time. On average the mixing time is 27.3 ± 4.3 s and the circulation time 14.7 ± 1.4 s.

P1(0/0/10), P2(0/0/15) and P3(0/0/20). As quality criterion, 99% of the average CO concentration had to be reached.

As shown in Fig. 11 the 99% mixing time t_{99} was obtained at different moments giving an average mixing time of 27.3 ± 4.3 s which is in the range of experimental values of Pandit and Joshi (1983) between 5 s up to 40 s depending on media properties. The circulation time t_c was estimated by the time interval between the CO concentration peaks with 14.7 ± 1.4 s. The circulation velocity is approximately two times the reactor height divided by the circulation time with $v_{L,circ}$ of 3.4 m s^{-1}. also within the range of Pandit and Joshi (1983).

Appendix D. Experimental values

For the experimental data, a 3 L lab scale steal reactor (Bioengineering) equipped with a six-blade Rushton impeller and four baffles was used. A L-tube sparger and a synthesis gas mixture ($CO/H_2/CO_2$/Ar with 55/30/5/10 vol-%) and 1 bar pressure were continuously applied with a gassing rate of 13.2 L h^{-1} (0.15 vvm). The stirrer speed was set to 500 rpm and the fermentation temperature controlled at 37 °C as the pH at 5.9. The Tanner mod. 1754 PETC medium (Tanner et al., 1993) with 15 g L^{-1} MES buffer and 0.5 g L^{-1} yeast extract was used and an initial liquid volume of 1.5 L. The preculture of the *Clostridium ljungdahlii* wildtype strain (DSM 13528) was grown in anaerobic bottles with a gas composition of $CO/H_2/CO_2$ of 50/45/5 vol-%. During the exponential phase, samples were taken for cell dry weight (CDW) and product measurements. The products acetate, ethanol, 2,3-butanediol and lactate were quantified by high-performance liquid chromatography (HPLC). The exhaust gas composition was directly analysed by mass spectrometry (MS). In the exponential phase the growth, uptake and production rates were conducted.

Appendix E. Volumetric mass transfer rate before and after PBM

The volumetric mass transfer without population balance model (PBM) and a constant bubble size of 4 mm is very high with 1190 h^{-1} (first 1000 s). The average interfacial area concentration a is about 980 m^{-1} which decreases drastically when enabling PBM to include bubble breakup, coalescence and bubble expansion due to hydrostatic pressure. After 1500 s the average k_La is only about 40 h^{-1} (a = 60 m^{-1}).

The spatial volumetric mass transfer distributions are shown in Fig. 12. The average mass transfer rates are $k_L(t = 1000\ s) = 3.36\ e^{-4}$ m s^{-1} and $k_L(t = 1500\ s) = 1.73\ e^{-4}$ m s^{-1}.

Appendix F. Detailed short- and long-term responses evaluation

The concentration profiles $c_{L,CO}(t)$ of the bacterial lifelines were processed according to the Nassi-Shneiderman diagram in Fig. 13 for each critical time periods τ^{crit} = 10 s, τ^{crit} = 40 s and τ^{crit} = 70 s. If both thresholds, $c^{crit}_{L,CO}$ and τ^{crit}, are true the average concentration respectively uptake rate (according to Eq. (3)) of the real time period is calculated. Mean concentration and retention time are saved in two arrays $c^{trec}_{L,CO}$ and Δt^{trec}.

For each critical time period, the resulting arrays were clustered into histograms with 100 bins and normalized to the highest total percentage of the average occurrence (τ^{crit} = 10 s). To take the actual duration of each average concentration respectively uptake

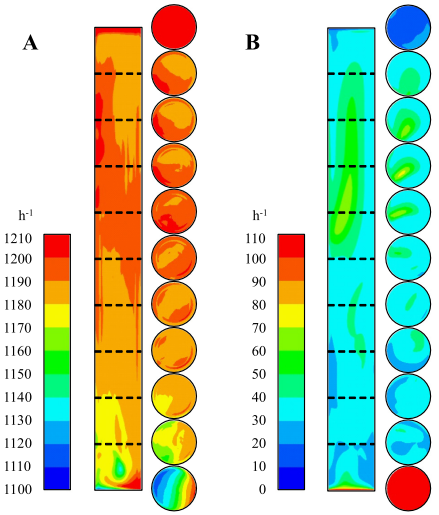

Fig. 12. Volumetric mass transfer rate k_La after 1000 s (A) and 1500 s (B). For 1000 s the first modelling setup described in chapter 2.2 with only one bubble size of 4 mm was used (A). The population balance model with 16 bubble classes was enabled for the second set-up (B), allowing bubble breakup, coalescence and bubble expansion (see chapter 2.2.1).

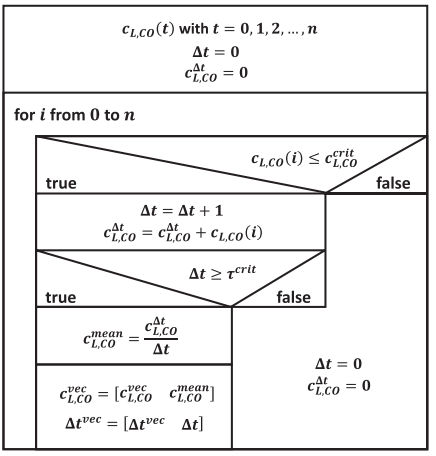

Fig. 13. Nassi-Shneiderman diagram of short- and long-term response evaluation. For three critical periods τ^{crit} = 10 s, τ^{crit} = 40 s and τ^{crit} = 70 s the evaluation of the concentration profiles $c_{L,CO}(t)$ was performed. As a result, the averaged concentrations $c^{mean}_{L,CO}$ and corresponding time periods Δt are summarized in two arrays $c^{vec}_{L,CO}$ and Δt^{vec}.

rate into account, also histograms with weighted distribution (weighting factor $\alpha_{\tau i} = \Delta t_i^{vec} / \sum \Delta t^{vec}$) are visualized (see Fig. 7).

The direct translation histograms of the concentration profiles respectively uptake rates can be found in Fig. 14. Instantiations

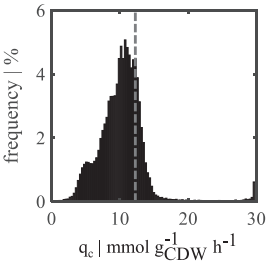

Fig. 14. Instantaneous adaption of bacteria to the gradient. The distribution is normalized to all tracked time points n respectively the length of all trajectories together. Indicated as grey dotted line the average q_c with 12.26 mmol g^{-1}_{CDW} h^{-1} is depicted.

adaption corresponds directly with the spatial gradient and does not take temporal effects into account which makes the comparison with Fig. 7 difficult. Nevertheless, the average uptake rate q_c = 12.26 mmol g^{-1}_{CDW} h^{-1} is a strong indicator to show the difference between average values and more likely time-dependent adaption of the bacteria.

References

Abubacker, H.N., Veiga, M.C., Kennes, C., 2011. Biological conversion of carbon monoxide: rich syngas or waste gases to bioethanol. Biofuels, Bioproducts Biorefining. 5 (1), 93–114.

Akita, K., Yoshida, F., 1973. Gas holdup and volumetric mass transfer coefficient in bubble columns. Effects of liquid properties. Ind. Eng. Chem. Process Des. Dev. 12 (1), 76–80.

Antal, S.P., Lahey, R.T., Flaherty, J.E., 1991. Analysis of phase distribution in fully developed laminar bubbly two-phase flow. Int. J. Multiph. Flow 17 (5), 635–652.

Burns, A.D., Frank, T., Hamill, I., Shi, J.-M.M., 2004. The Favre Averaged drag model for turbulent dispersion in Eulerian multi-phase flows. In: Fifth International Conference on Multiphase Flow, ICMF-2004, No. 392, pp. 1–17.

Chen, J., Gomez, J.A., Höffner, K., Barton, P.I., Henson, M.A., 2015. Metabolic modeling of synthesis gas fermentation in bubble column reactors. Biotechnol. Biofuels 8 (1), 1–12.

Clift, R., Grace, J.R., Weber, M.E., 1978. Bubbles, Drops, and Particles. Academic press.

Daniell, J., Köpke, M., Simpson, S.D., 2012. Commercial biomass syngas fermentation. Energies 5 (12), 5372–5417.

Deckwer, W.D., Louisi, Y., Zaidi, A., Ralek, M., 1980. Hydrodynamic properties of the fischer-tropsch slurry process. Ind. Eng. Chem. Process Des. Dev. 19 (4), 699–708.

Enfors, S.-O., Jahic, M., Rozkov, A., Xu, B., Hecker, M., Jürgen, B., Krüger, E., Schweder, T., Hamer, G., O'Beirne, D., Noisommit-Rizzi, N., Reuss, M., Boone, L., Hewitt, C., McFarlane, C., Nienow, A., Kovacs, T., Trägårdh, C., Fuchs, L., Revstedt, J., Friberg, P.C., Hjertager, B., Blomsten, G., Skogman, H., Hjort, S., Hoeks, F., Lin, H.-Y., Neubauer, P., van der Lans, R., Luyben, K., Vrabel, P., Manelius, Å., 2001. Physiological responses to mixing in large scale bioreactors. J. Biotechnol. 85, 175–185.

Gomez, J.A., Höffner, K., Barton, P.I., 2014. DFBAlab: a fast and reliable MATLAB code for dynamic flux balance analysis. BioMed. Central Bioinformat. 15 (1), 1–10.

Grace, J.R., 1973. Shapes and velocities of bubbles rising in infinite liquids. Trans. Inst. Chem. Eng. 51, 116–120.

Haringa, C., Deshmukh, A.T., Mudde, R.F., Noorman, H.J., 2017. Euler-Lagrange analysis towards representative down-scaling of a 22 m^3 aerobic *S. cerevisiae* fermentation. Chem. Eng. Sci. 170, 653–669.

Haringa, C., Mudde, R.F., 2018. Inter-compartment interaction in multi-impeller mixing part II : Experiments, Sliding mesh and Large Eddy Simulations. Chem. Eng. Res. Des. 136, 886–899.

Haringa, C., Noorman, H.J., Mudde, R.F., 2016a. Lagrangian modeling of hydrodynamic–kinetic interactions in (bio)chemical reactors: Practical implementation and setup guidelines. Chem. Eng. Sci., 1–10

Haringa, C., Tang, W., Deshmukh, A.T., Xia, J., Reuss, M., Heijnen, J.J., Mudde, R.F., Noorman, H.J., 2016b. Euler-Lagrange computational fluid dynamics for (bio) reactor scale-down: an analysis of organism life-lines. Eng. Life Sci., 1–12

Heins, A.-L., Lencastre Fernandes, R., Gernaey, K.V., Lantz, A.E., 2015. Experimental and in silico investigation of population heterogeneity in continuous *Sachharomyces cerevisiae* scale-down fermentation in a two-compartment setup. J. Chem. Technol. Biotechnol. 90 (2), 324–340.

Henson, M.A., 2003. Dynamic modeling of microbial cell populations. Curr. Opin. Biotechnol. 14 (5), 460–467.

Higbie, R., 1935. The rate of absorption of a pure gas into a still liquid during short periods of exposure. Trans. Am. Inst. Chem. Eng. 35, 365–389.
Kantarci, N., Borak, F., Ulgen, K.O., 2005. Bubble column reactors. Process Biochem. 40 (7), 2263–2283.
Köpke, M., Held, C., Hujer, S., Liesegang, H., Wiezer, A., Wollherr, A., Ehrenreich, A., Liebl, W., Gottschalk, G., Dürre, P., 2010. *Clostridium ljungdahlii* represents a microbial production platform based on syngas. Proc. Natl. Acad. Sci. 107 (29), 13097–113092.
Krishna, R., Sie, S.T., 2000. Design and scale-up of the bubble column slurry reactor for Fischer- Tropsch synthesis. Fuel Process. Technol. 64, 73–105.
Kuschel, M., Siebler, F., Takors, R., 2017. Lagrangian trajectories to predict the formation of population heterogeneity in large-scale bioreactors. Bioengineering 4 (2), 1–13.
Lapin, A., Müller, D., Reuss, M., 2004. Dynamic behavior of microbial populations in stirred bioreactors simulated with Euler–Lagrange methods: traveling along the lifelines of single cells. Ind. Eng. Chem. Res. 43 (16), 4647–4656.
Lapin, A., Schmid, J., Reuss, M., 2006. Modeling the dynamics of *E. coli* populations in the three-dimensional turbulent field of a stirred-tank bioreactor-A structured-segregated approach. Chem. Eng. Sci. 61, 4783–4797.
Larsson, G., Törnkvist, M., Ståhl Wernersson, E., Trägårdh, C., Noorman, H.J., Enfors, S.O., 1996. Substrate gradients in bioreactors: Origin and consequences. Bioprocess. Eng. 14, 281–289.
Lehr, F., Millies, M., Mewes, D., 2002. Bubble size distributions and flow fields in bubble columns. Global Home Chem. Eng. 42 (11), 1225–1233.
Löffler, M., Simen, J.D., Jäger, G., Schäferhoff, K., Freund, A., Takors, R., 2016. Engineering *E. coli* for large-scale production – Strategies considering ATP expenses and transcriptional responses. Metab. Eng. 38, 73–85.
Luo, H., 1993. Coalescence, Breakup and Liquid Circulation in Bubble Column Reactors. University of Trondheim.
Luo, H., Svendsen, H.F., 1996. Theoretical model for drop and bubble breakup in turbulent dispersions. The Global Home Chem. Eng. 42 (5), 1225–1233.
Mantzaris, N.V., Liou, J., Daoutidis, P., Srienc, F., 1999. Numerical solution of a mass structured cell population balance model in an environment of changing substrate concentration. J. Bacteriol. 71, 157–174.
Michalowski, A., Siemann-Herzberg, M., Takors, R., 2017. Escherichia coli HGT: Engineered for high glucose throughput even under slowly growing or resting conditions. Metabolic Eng. 40, 93–103.
Mohammadi, M., Mohamed, A.R., Najafpour, G.D., Younesi, H., Uzir, M.H., 2014. Kinetic studies on fermentative production of biofuel from synthesis gas using *Clostridium ljungdahlii*. Sci. World J. 1, 1–8.
Morchain, J., Gabelle, J.-C., Cockx, A., 2014. A coupled population balance model and CFD approach for the simulation of mixing issues in lab-scale and industrial bioreactors. Am. Ins. Chem. Eng. 60 (1), 27–40.
Nagarajan, H., Sahin, M., Nogales, J., Latif, H., Lovley, D.R., Ebrahim, A., Zengler, K., 2013. Characterizing acetogenic metabolism using a genome-scale metabolic reconstruction of *Clostridium ljungdahlii*. Microb. Cell Fact. 12 (118), 1–13.
Nauha, E.K., Kálal, Z., Ali, J.M., Alopaeus, V., 2018. Compartmental modeling of large stirred tank bioreactors with high gas volume fractions. Chem. Eng. J. 334, 2319–2334.
Noorman, H.J., Morud, K., Hjertager, B.H., Trägårdh, C., Larsson, G., Enfors, S.O., 1993. CFD modeling and verification of flow and conversion in a 1 m^3 bioreactor. BHR Group Conf. Ser. Publ. 5, 241–258.
Pandit, A.B., Joshi, J.B., 1983. Mixing in mechanically agitated gas-liquid contactors, bubble columns and modified bubble columns. Chem. Eng. Sci. 38 (8), 1189–1215.
Philp, J., 2018. The bioeconomy, the challenge of the century for policy makers. New Biotechnol. 25 (40), 11–19.
Pigou, M., Morchain, J., 2015. Investigating the interactions between physical and biological heterogeneities in bioreactors using compartment, population balance and metabolic models. Chem. Eng. Sci. 126, 267–282.
Sato, Y., Sekoguchi, K., 1975. Liquid velocity distribution in two-phase bubble flow. Int. J. Multiph. Flow 2 (1), 97–195.
Schmalzriedt, S., Jenne, M., Mauch, K., Reuss, M., 2003, Integration of physiology and fluid dynamics, Advances in Biochemical Engineering/Biotechnology. Edited by Springer.
Takors, R., 2012. Scale-up of microbial processes: impacts, tools and open questions. J. Biotechnol. 160 (1–2), 3–9.
Takors, R., Kopf, M., Mampel, J., Blümke, W., Blombach, B., Eikmanns, B., Bengelsdorf, F.R., Weuster-Botz, D., Dürre, P., 2018. Using gas mixtures of CO, CO_2 and H_2 as microbial substrates: the do's and don'ts of successful technology transfer from laboratory to production scale. Microb. Biotechnol. 11 (4), 606–625.
Tanner, R.S., Miller, L.M., Yang, D., 1993. *Clostridium ljungdahlii* sp. nov., an acetogenic species in clostridial rRNA homology group I. Int. J. Syst. Evol. Microbiol. 43 (2), 232–236.
Taymaz-Nikerel, H., Borujeni, A.E., Verheijen, P.J.T., Heijnen, J.J., van Gulik, W.M., 2010. Genome-derived minimal metabolic models for *Escherichia coli* MG1655 with estimated in vivo respiratory ATP stoichiometry. Biotechnol. Bioeng. 107 (2), 369–381.
Tomiyama, A., Tamai, H., Zun, I., Hosokawa, S., 2002. Transverse migration of single bubbles in simple shear flows. Chem. Eng. Sci. 57 (11), 1849–1858.
Vrábel, P., van der Lans, R.G.J.M., van der Schot, F.N., Luyben, K.C.A.M., Xu, B., Enfors, S.-O., 2001. CMA : integration of fluid dynamics and microbial kinetics in modelling of large-scale fermentations. Chem. Eng. J. 84, 463–474.

A.3 Manuscript III

Synergistically applying 1-D modelling and CFD for designing industrial scale bubble column syngas bioreactors

Flora SIEBLER, Alexey LAPIN and Ralf TAKORS

Received: 12 August 2019 | Revised: 8 January 2020 | Accepted: 31 January 2020

DOI: 10.1002/elsc.201900132

Engineering in Life Sciences

RESEARCH ARTICLE

Synergistically applying 1-D modeling and CFD for designing industrial scale bubble column syngas bioreactors

Flora Siebler[1] | **Alexey Lapin**[2] | **Ralf Takors**[1]

[1]Institute of Biochemical Engineering, University of Stuttgart, Stuttgart, Germany

[2]Stuttgart Research Centre Systems Biology, University of Stuttgart, Stuttgart, Germany

Correspondence
Professor Ralf Takors, Institute of Biochemical Engineering, University of Stuttgart, Allmandring 31, 70569 Stuttgart, Germany.
Email: takors@uni-stuttgart.de

Funding information
Bundesministerium für Bildung und Forschung, Grant/Award Number: FKZ031A468B

The reduction of greenhouse gas emissions and future perspectives of circular economy ask for new solutions to produce commodities and fine chemicals. Large-scale bubble columns operated by gaseous substrates such as CO, CO_2, and H_2 to feed acetogens for product formations could be promising approaches. Valid in silico predictions of large-scale performance are needed to dimension bioreactors properly taking into account biological constraints, too. This contribution deals with the trade-off between sophisticated spatiotemporally resolved large-scale simulations using computationally intensive Euler–Euler and Euler–Lagrange approaches and coarse-grained 1-D models enabling fast performance evaluations. It is shown that proper consideration of gas hold-up is key to predict biological performance. Intrinsic bias of 1-D models can be compensated by reconsideration of Sauter diameters derived from uniquely performed Euler–Lagrange computational fluid dynamics.

KEYWORDS
1-D model approach, bubble column reactor, computational fluid dynamics, pseudo-stationary gas gradient, two-phase Euler–Euler simulation

1 | INTRODUCTION

The Paris Climate Agreement that entered into force in November 2016 created the framework for national contributions to limit the global temperature rise well below 2°C. As such, the reduction of greenhouse gas emissions became part of responsible chemical industry leadership, now aiming to establish a circular economy [1], that is, preventing any carbon losses and ensuring economic and ecological sustainability [2, 3].

Accordingly, using CO_2, H_2, and CO gas mixtures either from gasification of municipal waste, biogenic sources or as off-gas (e.g., from steel industry) is an attractive source of reduced carbon (CO) and H_2. The so-called syngas fermentations with acetogens such as *Clostridiae* sp. are highly promising to access not only natural products (ethanol, acetate, or 2,3-butanediol) [4, 5] but also recombinant compounds such as acetone and butanol [6–8]. Those commodities require for simple, continuously operating large-scale bioreactors that could be designed as bubble columns.

Dimensioning needs thorough in silico parameter analysis to ensure proper, large-scale production. However, large-scale bubble columns are very challenging to simulate, actually comprising three phases (liquid, bubbles, and cells), turbulent flows, mass transfer of poorly soluble gases (CO, H_2), microbial reaction kinetics, and—last but not least—proper bubble population models for predicting mass transfer areas. With the advent of gaseous substrates for large-scale single cell protein production in the 1970 s, the attraction of bubble columns peaked but somewhat leveled out during the last

Abbreviation: CFD, computational fluid dynamics.

decades. Intensive studies in 6–10 m pilot scales [10, 13] unraveled correlations between gas velocities and $k_L a$ and even succeeded to develop 1-D models for predicting gas transfers properly [11]. The applicability of the well-known k-ε model for bubble columns was questioned [12, 14] outlining the need to consider turbulent flow regimes properly. Nevertheless, 1-D modeling of bubble columns should be possible, in particular when iterative optimization cycles are taken into account [9, 13].

Ideally, large-scale simulations should consider spatiotemporal heterogeneities and their impact on cellular performance [9–12]. But related simulations not only require thorough mechanistic models but also sufficient computational power [13]. Accordingly, simplifications are often made either by assuming ideal mixing, 1-D gas gradients [14] or dissembling the large bioreactor into numerous volumes [15–19].

Recent highly valuable examples are given by Chen et al. [20, 21] who evaluated the performance of large-scale *Clostridiae* fermentations with the help of a genome-scale metabolic model applying spatiotemporal bioreactor simulations based on homogenously mixed volumes. The authors applied flux balance analysis to estimate flux distributions for each 1-D discretization. However, despite successful application, growth rates were overestimated by trend and physical criteria such as gas hold-up were not integrated, yet. The latter may have affected the large-scale prediction accuracy, too.

Without doubt, such 1-D models require less computational efforts than sophisticated Euler–Lagrange computational fluid dynamics (CFD). They offer relatively easy-to-implement use but may hide intrinsic drawbacks hampering prediction quality. Furthermore, their predictions might be biased because model granularity is intrinsically coarse. Nevertheless, they are the method of choice in conceptual design to search in operational parameter spaces. This contribution exactly deals with the trade-off between properly simulating large-scale bubble column performance and screening operational parameter spaces with reasonable computational effort. Special emphasis will be put on the impact of gas hold-up on the expected biological performance, that is, product-per-biomass yield. This relation is considered of particular importance as it links a key operational parameter with the most important biological readout.

PRACTICAL APPLICATION

Transferring biochemical processes from the laboratory to industrial scales is very challenging. Physical properties may change drastically and may cause nonwanted performance losses. Accordingly, tools are needed to predict large-scale conditions leading to an optimum design with minimized performance losses.

This study presents a computational tool for conceptual reactor design of an industrial-scale bubble column bioreactor. Time-consuming and computationally challenging design parameter studies were performed with a simplified 1-D model. Noteworthy, key settings including gas hold-up were derived from spatially resolved, computational fluid dynamics (CFD). The interaction of both approaches represents the optimum trade-off between computationally intensive CFD and the essential probing of a broad design parameter space performed via 1-D modeling.

2 | MATERIALS AND METHODS

2.1 | Geometry, reactor set-up, and biological system

Both simulation approaches were conducted for equal reactor geometry using the same biological system, that is, *Clostridium ljungdahlii* DSM 13528 that grows on carbon monoxide as C-source. The choice of CO simplifies the comparison with the previous publication [11] and represents the preferred carbon and electron source for alcohol production. A cylindrical reactor with 25 m liquid height and diameter $D_R = 2.52$ m was chosen resulting in a H_L/D_R-ratio of about 10. Consequently, the setup imposed high hydrostatic pressure gradients. For 1-D modeling, the bubble column simulations considered continuous countercurrent mode with liquid recycling and medium feed at the top of the reactor. At the bottom, synthesis gas was continuously provided via the total cross-sectional area A_R. The media density ρ_L was assumed to be similar to the properties of water with $\rho_L = 1{,}000$ kg m^{-3}. Isothermal process conditions were assumed with an operating temperature of 310.15 K. Heat generation was neglected. Nevertheless, in large-scale bioreactors temperature control might be necessary. No additional pressure was applied beside the ambient pressure of 1 atm and the hydrostatic pressure due to the column height.

State variables such as gas concentrations and gas hold-up were partially differentiated following the scheme presented by Chen et al. [14].

2.1.1 | 1-D approach

This approach is similar to the publications of Chen et al. [14, 20, 21]. The new mass balance equations are described in this section. Growth and production formation are calculated as described in Siebler et al. [11]. Spatial and temporal discretization was kept the same as in Chen et al. [14, 21] and is described in more detail in the Supporting Information. According to the reactor set-up outlined in the previous section, four partial differential equations and four ordinary

differential equations need to be set. Dissolved and gaseous synthesis gas components, the gas hold-ups, and the bubble number density are local, time dependent variables, and serve as input values for calculating dynamics of growth and product formation.

The mass balance for the liquid phase of one discretization volume is derived including convective and diffusive transport, phase-to-phase mass transfer, and consumption terms. The volume of each section is written as: $\Delta V_L = \Delta z A_L$, where Δz is the section height and A_L is the liquid surface area between the sections. The cross-sectional area of the reactor A_R is the sum of A_L and the gaseous interface A_G. The gaseous and liquid volume fractions are indicated by ε_G and ε_L (see Figure S2). It follows

$$\begin{aligned}\frac{\Delta z\, \mathrm{d}c_L A_L}{\mathrm{d}t} = & \underbrace{A_L c_L v_{L,\mathrm{slip}}\Big|_{z+\Delta z} - A_L c_L v_{L,\mathrm{slip}}\Big|_{z}}_{\text{transport}} \\ & + \underbrace{A_{\mathrm{bubbles}} k_L \left(c_L^* - c_L\right)}_{\text{mass transfer}} - \underbrace{\Delta z A_L q_c c_X}_{\text{consumption}} \\ & + \underbrace{D_L A_L \frac{\mathrm{d}c_L}{\mathrm{d}z}\Big|_{z+\Delta z} - D_L A_L \frac{\mathrm{d}c_L}{\mathrm{d}z}\Big|_{z}}_{\text{diffusion}} \end{aligned} \quad (1)$$

with A_{bubbles} as the mass transfer area between the liquid and gaseous phase that leads to $a = A_{\mathrm{bubbles}}/(\Delta z A_L)$ and the well-known $k_L a$ term for modeling the mass transfer term with the equilibrium concentration c_L^* and the soluble gas concentration c_L. The liquid slip velocity $v_{L,slip}$ multiplied by $\varepsilon_L = 1 - \varepsilon_G$ gives the liquid velocity v_L, which can be assumed to be constant. The diffusion term with the liquid phase dispersion coefficient D_L with 4.5 $\mathrm{m^2\ h^{-1}}$ [21] is included as well as the consumption term consists of the uptake kinetic q_c and biomass concentration c_X. By dividing equation (1) by A_R and Δz and using the correlation $1 - \varepsilon_G = A_L / A_R$, the final partial differential equations for the dissolved gases ($m \in [\mathrm{CO}, \mathrm{CO_2}, \mathrm{H_2}]$) can be formulated.

$$\begin{aligned}\frac{\partial c_{L,m}\varepsilon_L}{\partial t} = & -v_{L,\mathrm{slip}} \frac{\partial c_{L,m}\varepsilon_L}{\partial z} + k_{L,m} a \left(c_{L,m}^* - c_{L,m}\right) \\ & - q_m c_X \varepsilon_L + D_L \frac{\partial^2 c_{L,m}\varepsilon_L}{\partial z^2} \end{aligned} \quad (2)$$

Each balance of the gas phase only needs to consider convective mass transport and phase-to-phase mass transfer that leads to

$$\frac{\partial c_{G,m}\varepsilon_G}{\partial t} = v_{G,slip} \frac{\partial c_{G,m}\varepsilon_G}{\partial z} - k_{L,m} a \left(c_{L,m}^* - c_{L,m}\right) \quad (3)$$

Because the gas phase is compressible, the gas hold-ups depend on the local pressure that correlate ε_L and ε_G with the liquid height H_L. The total molar density ρ^* is introduced using the ideal gas law $PV = nRT$ and the hydrostatic pressure $P_H = P_0 + \rho g h$ with $h = H_L - z$

$$\rho^* = \sum_{m=1}^{3} \frac{\rho_m(z)}{M_m} = \frac{P_0 + \left(H_L - z\right) g \rho_L \varepsilon_L}{RT} \quad (4)$$

with the gravitational acceleration g, liquid density ρ_L, universal gas constant R, and the operating temperature T. The index $m = 1, 2, 3$ always represents the synthesis gas composition with CO, $\mathrm{CO_2}$, and $\mathrm{H_2}$. Considering the total molar gas density, the following equation can be derived:

$$\frac{\partial \varepsilon_G \rho^*}{\partial t} = v_{G,\mathrm{slip}} \frac{\partial \varepsilon_G \rho^*}{\partial z} - \sum_{m=1}^{3} k_{L,m} a \left(c_{L,m}^* - c_{L,m}\right) \quad (5)$$

It is further assumed that the number density n_G, that is, the number of bubbles N_B divided by the reactor volume V_R, only depends on convection. No further bubble breakage or coalescence occurs.

$$\begin{aligned}\frac{\partial n_G}{\partial t} &= v_{G,\mathrm{slip}} \frac{\partial n_G}{\partial z} \\ n_G\ (t, z) &= \frac{N_B}{V_R} = \frac{\varepsilon_G}{\frac{4}{3}\pi R_B^3} \end{aligned} \quad (6)$$

Nevertheless, the bubble radius R_B is a function of the gas hold-up and hydrostatic pressure. If the number of bubbles in a section i is multiplied with the bubble volume $V_{B,i}$, the gas hold-up $\varepsilon_{G,i}$ is derived. Therefore, all balance equations are intertwined by the gas hold-up. Noteworthy, this also affects the volumetric surface area a, which is the sum of all bubble surfaces A_B divided by the reactor volume.

$$a = \frac{\sum A_B}{V_R} = \frac{3}{R_B} \varepsilon_G \quad (7)$$

Product formation and growth are formulated as ordinary differential equations (see Equations 8) using the growth rate μ and the dilution rate $D = 0.055\ \mathrm{h^{-1}}$.

$$\begin{aligned}\frac{\mathrm{d}c_X}{\mathrm{d}t} &= \mu c_X - D c_X \\ \frac{\mathrm{d}c_k}{\mathrm{d}t} &= M_k\, q_k c_X - D c_k \end{aligned} \quad (8)$$

Because biomass and product concentrations c_k are in $\mathrm{g\ L^{-1}}$, the molecular weight M_k is needed with $k \in$ [acetate, ethanol, 2, 3−butanediol]. For the sake of simplicity, individual production rates $\mathrm{q_k}$ represent mean values of the section-specific $\mathrm{q_{k,i}}$ that consider local gas uptake kinetics $\mathrm{q_{m,i}}$ (see Supporting Information).

2.2 | Computational fluid dynamics

Recently, the set-up of the simulation framework including results has been published in Siebler et al. [11]. Accordingly, only a draft explanation is given. For details, readers are

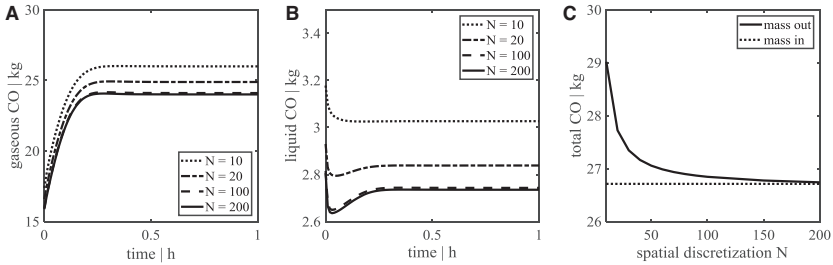

FIGURE 1 Refinement study. In (A) and (B), the gaseous and dissolved (liquid) mass of CO over times is shown. Exemplary, four discretization steps are depicted $N = 10$, 20, 100, and 200. In (C), the relation between total CO leaving and entering the column is illustrated revealing that $N = 100$ closes the mass balance with less than 5% gap

referred to the publication. Euler–Euler two phase simulations were conducted with the CFD tool ANSYS Fluent 18.0. The Reynolds-averaged Navier–Stokes equations combined with the re-normalization group k-ε-model were solved to derive pseudo-stationary gas gradients similar to the 1-D approach. Drag and lift forces, wall lubrication, turbulent dispersion, and interaction as well as breakage and coalescence were enabled. For mass transfer, the same correlation as in Equation (9) was used except for the bubble diameter d_B, which was exchanged by the Sauter mean bubble diameter d_{32}. For the solubility of the gas, the Henry law was also applied. Pressure was considered as static. The initial bubble size was 4 mm. To model CO uptake kinetics, the correlation of Mohammadi et al. [22] was used (see Supporting Information eq. 13). The analyzed fermentation "snap-shot" operation window was defined by chosen the biomass concentration of 10 g L^{-1}.

As indicated for the 1-D approach, the uptake kinetics of CO were translated into production rates according to the approximation described in Siebler et al. [11]. So far, there is no comprehensive model for the prediction of production rates of *C. ljungdahlii*. The simple correlation used does neither include internal redox and energy balances nor maintenance. It is solely based on the element balances of carbon, hydrogen, and oxygen. Nevertheless, the correlation allows to compare both modeling approaches.

3 | RESULTS

3.1 | Basic settings of 1-D

The bubble column was divided in N slices each consisting of a liquid L and a gaseous G fraction with the uprising superficial gas velocity v_S and the downcoming liquid velocity v_L. Homogenous conditions were assumed in each liquid and gaseous phase. For identifying the number N of essential volumes (sections), simulations were performed probing N between 10 and 200 (Figure 1).

Physical state variables were simulated according to Equations (1)–(8). Biochemical reaction rates reflecting microbial metabolic activity were set as described in "Materials and Methods" section and in Siebler et al. [11].

As presented in Figure 1, the mass balance for the chosen discretization does not close but gives reasonable results for $N \geq 100$. No significant improvement of simulation accuracy and convergence could be achieved increasing N from 100 to 200. With respect to computational efforts, $N = 100$ was used for all calculations.

3.2 | Probing the parameter space

For evaluating a proper parameter setting, key impact factors defining the performance of a biotechnological bubble column need to be specified. To characterize the biological output, $Y_{PX}(SS)$ and $C_{fix}(SS)$ were chosen indicating the product per biomass yield and the metabolized amount of carbon under steady-state operating conditions, respectively. The physical operation was qualified by the total mean gas hold-up $\bar{\varepsilon}_G$, the mean bubble diameter $\bar{d}_B$, the mean oxygen transfer coefficient $\overline{k_L a}$, and the bubble number density n_G.

The simulation of the said performance criteria crucially depends on the proper prediction of $k_L a$ and their interaction with the gas hold-up ε_G and the superficial gas velocity v_S. The well-known Higbie correlation [23] was used for estimating k_L as

$$k_L = \frac{2}{\sqrt{\pi}} \left(\frac{v_T D_{CO}}{d_B} \right)^{0.5} \tag{9}$$

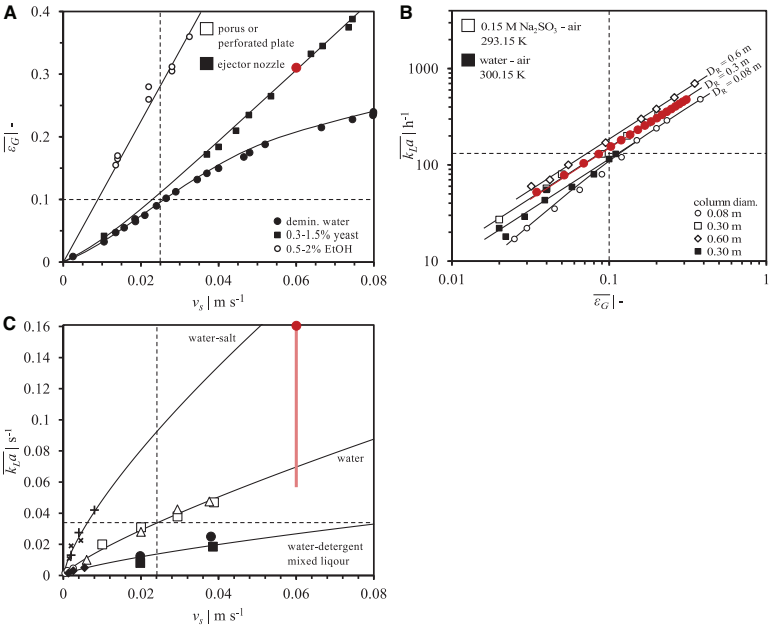

FIGURE 2 Comparing model predictions with experimental observations. In (A), the gas hold-up $\bar{\varepsilon}_G$ as a function of superficial gas velocity v_S for demineralized water, yeast solution, and ethanol solution is shown [27]. The average mass transfer rate $\overline{k_La}$ as a function of $\bar{\varepsilon}_G$ for different column diameters is depicted in (B) [28]. In (C), the $\overline{k_La}$ is shown as a function of superficial gas velocity v_S for water–salt solution, pure water, and water detergent mix [26]

with D_{CO} as the diffusion coefficient of CO in water [24, p. 127] and d_B as the bubble diameter. According to Tomiyama et al. [25], the steady-state uprising bubble velocity v_T can be estimated as

$$v_T = \sqrt{2}\left(\frac{\sigma g\left(\rho_L - \rho_G\right)}{\rho_L^2}\right)^{0.25} \tag{10}$$

for $2 \times 10^{-3} \leq d_B \leq 10 \times 10^{-3}$ m and Eötvös number $Eo = (\rho_L - \rho_G)\, g d_B/\sigma \leq 16$. With the measured surface tension of the cultivation medium $\sigma = 0.0724 \pm 0.0063$ N m (identified via bubble pressure tensiometer), the medium density $\rho_L = 1000$ kg m^{-3} and the air density $\rho_G = 1.2$ kg m^{-3} $v_T = 0.23$ m s^{-1} is calculated, which is pretty similar to the distilled water value $v_T = 0.25$ m s^{-1} [26]. The volume specific gas/liquid mass transfer area a was estimated assuming spherical bubbles:

$$a = \frac{6\varepsilon_G}{d_G} \tag{11}$$

For evaluating bubble diameters $\leq 10 \times 10^{-3}$ m, the following equation was applied:

$$\varepsilon_G = \frac{v_S}{v_T} \tag{12}$$

with $v_T = 0.23$ m s^{-1} [26]. Furthermore, the impact of media components such as organic acids, salts, and alcohols on ε_G and v_S were considered using the experimental findings of Schügerl et al. [27] as reference. By analogy, experimental observations of Heijnen and van't Ried [26] outlining the correlation between k_La and v_S regarding media compositions were used. Figure 2 provides an overview of the experimental measurements.

To challenge the plausibility of experimental findings, the model case of 0.06 vvm (i.e., superficial gas velocity $v_S = 0.025$ m s^{-1} in a 0.6 m bubble column) can be studied in Figure 2. For demineralized water, $\varepsilon_G = 0.1$ is indicated (Figure 2A, dashed line), which leads to k_La of about 130 h^{-1} (Figure 2C, dashed line). This is in agreement with the findings of Akita and Yoshida [28]. Accordingly, Figure 2 shows

the framework for further simulations. To be precise, the ethanol plot in Figure 2A is chosen as *C. ljungdahlii* also produce alcohols such as ethanol and 2,3-butanediol. Although the settings of v_T, D_{CO}, ρ_L, ρ_G, and σ could be fairly assumed as constant, ε_G, d_B, k_L, and k_La are intertwined according to Equations (9)–(12). Each simulation allowed the independent setting of two parameters, while the remaining two were calculated. The simulation scenarios A–E were performed using the following setting as reference (dashed black line): $y_{CO} = 0.55$, 0.06 vvm, $\bar{\varepsilon}_G = 0.1$ ($\varepsilon_{G,0} = 0.06$), and $\overline{k_La} = 130\ h^{-1}$ ($k_La = 90\ h^{-1}$ with $d_{B,0} = 5 \times 10^{-3}$ m and $k_L = 3.4 \times 10^{-3}\ m\ s^{-1}$).

1. Variation in CO gas fraction with $0 \leq y_{CO} \leq 0.9$.
2. Different gassing rates with $0.004 \leq v_S \leq 0.063$ m s^{-1} ($15 \leq \dot{V}_G \leq 225\ m^3\ s^{-1}$, 0.01–0.15 vvm).
3. Variations of k_La (ε_G = const.) with initial settings of 40–180 h^{-1} resulting in mean steady state values of $\overline{k_La}$ ranging from 60 to 250 h^{-1}.
4. Variation of initial gas hold-up $0.02 \leq \varepsilon_{G,0} \leq 0.19$ with fixed k_La resulting in $0.03 \leq \bar{\varepsilon}_G \leq 0.31$ (and variable d_B, see Figure S3 for explanation).
5. Same variation as in *D* but considering variable k_La yielding equal $\bar{\varepsilon}_G$ as in *D* and constant d_B (see Figure S3 for explanation).
6. Final parameter study with new reference set-up according to findings in *A* to *E*: $y_{CO} = 0.55$, 0.15 vvm and $\bar{\varepsilon}_G = 0.31$ ($\varepsilon_{G,0} = 0.19$). Initial k_La settings ranged from 100 to 425 h^{-1} finally reaching mean steady state $\overline{k_La}$ between 140 and 580 h^{-1}.

Figure 4 illustrates the observed sensitivities of the simulation scenarios A–E focusing on the readouts $Y_{PX}(SS)$, $C_{fix}(SS)$, $\bar{\varepsilon}_G$, $\bar{d}_B$, $\overline{k_La}$, and n_G. Values are normalized with respect to the maximum (1) and the minimum (−1) with the baseline (0) indicating the reference. Figure 3 provides an overview of the underlying data that were used for the sensitivity analysis in Figure 4.

The key observations are as follows:

(i) The physical parameters $\bar{\varepsilon}_G$, $\bar{d}_B$, $\overline{k_La}$, and $n_G$are neither dependent on the CO fraction y_{CO} nor on the gassing rate vvm (A,B). Rising CO fractions cause increasing CO fixation $C_{fix}(SS)$, whereas reduction of y_{CO} leads to poor $C_{fix}(SS)$ and production biomass yields $Y_{PX}(SS)$. Interestingly, lowering gassing rates do not cause as severe reduction of $Y_{PX}(SS)$.

(ii) Increasing k_La keeping $\bar{\varepsilon}_G$ constant leads to increasing bubble diameters and bubble numbers as indicated in *C*. As expected, $C_{fix}(SS)$ and $Y_{PX}(SS)$ improve with rising k_La and show lowered values for minimum settings.

(iii) Varying $\bar{\varepsilon}_G$ keeping k_La constant is responded by strong variations of bubble sizes and somewhat minor changes of bubble numbers. Impacts on the biological performance criteria are less pronounced.

(iv) Varying $\bar{\varepsilon}_G$ and liberating k_La caused the strongest amplitudes of the biological and the physical criteria except for the mean bubble diameter.

3.3 | Spatial and temporal results of 1-D approach

Simulation results of the 1-D approach applying the new reference setup are depicted in Figure 5. The time courses of biomass, acetate, ethanol, 2,3-butanediol, outlet gas (CO and CO_2), and mean dissolved CO and CO_2 clearly indicate steady-state process conditions after approximately 800 h. Notably, CO is completely consumed, whereas CO_2 is produced. The products acetate, ethanol, and 2,3-butanediol are constantly formed mirroring the experimental observations of *C. ljungdahlli* formulated in the stoichiometric model. During the first 2 h, the gas accumulates in the medium, since initial estimations of dissolved gas concentrations had not yet considered CO consumption and CO_2 formation with growing biomass.

The spatial analysis (B) reveals changing gas compositions over the column height. Dissolved CO levels are the highest at the bottom of the column, the only zone where growth inhibition (dissolved CO > 0.1 mmol L^{-1}) occurred according to Mohammadi et al. [22]. At about 11 m height, the carbon uptake rate severely dropped due to limiting CO levels ($c_{L,CO} \leq 0.014$ mmol L^{-1}). The model-based threshold value of $q_c = -14$ mmol $g_{CDW}^{-1}\ h^{-1}$ was fallen below. Consequently, by-product and biomass formation slow down. Notably, all by-product and biomass rates were spatially distributed that outlines their strict dependence on gas hold-up and mass transfer. Nevertheless, integral rates corresponded to the steady-state scenario of the entire bubble column.

3.4 | Comparison of 1-D with CFD results

Following the key motivation of this study to compare coarse grained 1-D modeling (F) with CFD, Table 1 provides an overview of the main results. As clearly depicted, almost all criteria reveal severe differences between 1-D (F) and CFD. By trend, the gas transfer simulated via 1-D (F) is much higher than via CFD. This is reflected by larger values of gas hold-up, mean bubble surface, k_L, and smaller mean bubble diameter. As a consequence, the mean k_La of 1-D (F) outnumbers the CFD values by factor 14 approximately. Noteworthy, mean dissolved CO values are predicted to be higher via 1-D (F) than via CFD. The 1-D model with set-up *F* overestimates the biological efficiency and predicts 40% more product biomass yield than CFD.

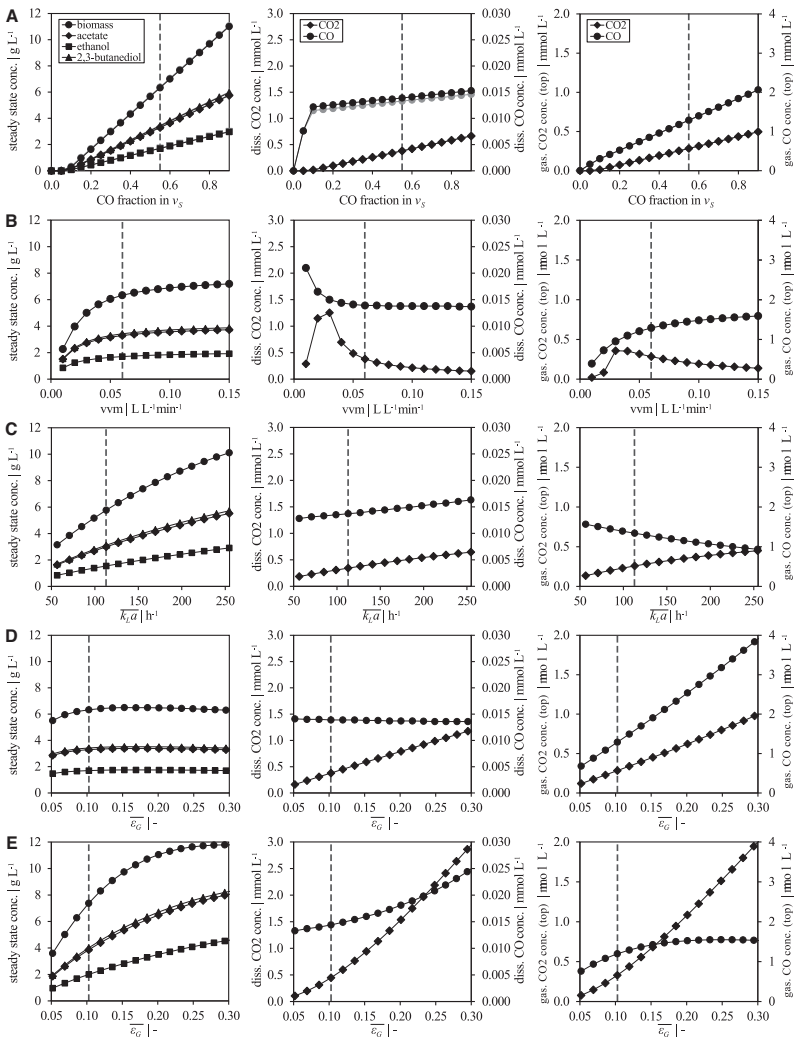

FIGURE 3 Steady-state results of parameter study. Variation of (A) gas composition, (B) gassing rate, (C) initial k_La value, (D) initial gas hold-up $\varepsilon_{G,0}$ with constant k_La value, and (E) initial gas hold-up $\varepsilon_{G,0}$ with variable k_La value. The reference set-up is indicated with a black dashed line. Gray points in (A) are simulation results without consideration of diffusion

In CA (F), the bubble diameter is way off too small in particular in the down part of the column. For this reason, a second run of the 1-D model (G) was conducted replacing the value by the Sauter mean diameter derived from CFD simulations. Results are indicated in Table 1 as 1-D (G) and in Figure 6 as red dashed line. This adaptation of the 1-D approach was further adjusted by approximating the initial gas hold-up and mass transfer rate according to the findings in the CFD approach.

Figure 6 illustrates the differences of 1-D (F), 1-D (G), 1-D*, and CFD simulation as a function of the column height. The trend of divergence depicted in Table 1 is clearly visible

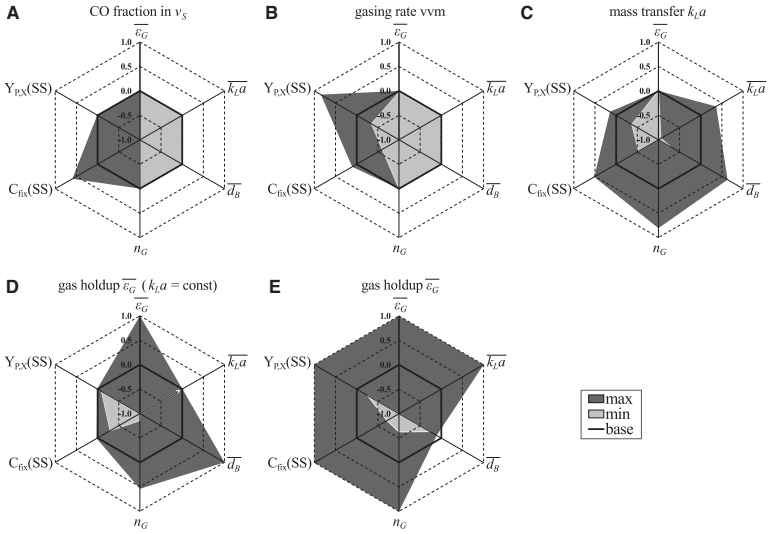

FIGURE 4 Parameter sensitivity analysis for conceptual design. The following scenarios are studied: (A) variation of gas composition (excluding wash-out results), (B) gassing rate, (C) initial k_La value, (D) initial gas hold-up $\varepsilon_{G,0}$ with constant k_La, and (E) initial gas hold-up $\varepsilon_{G,0}$ with variable k_La. Variables with a bar indicate the mean steady-state value. Additionally, the steady-state production biomass yields $Y_{P,X}$(SS), total steady-state carbon fixation C_{fix}(SS) and bubble number density n_G are depicted. All values are normalized to the maximum (1) as well as minimum (−1) value to allow comparability. The black solid line indicates the first parameter set thereby defining the baseline (0) of each radar graph. Areas of light gray (as well as small arrow in (D)) contour the set of minimum values, and dark gray areas encode maximum values

in the height-specific predictions using 1-D and CFD. Only within a small zone close to the bottom of the column 1-D and CFD, calculated gas hold-ups are equal. For all other cases, the above-mentioned criteria differ severely following the same trend as indicated in Table 1 (1-D (F) and CFD). Furthermore, Figure 6 also indicates the heterogeneity of the said values at each column height. In particular, CFD predicted bubble size distributions are very heterogeneous at each height, which also induces variations of gas hold-up. Additionally, using the gas hold-up and mass transfer value of CFD simulations improved the prediction quality of the 1-D model by 32% and 70% for bubble surface and volumetric mass transfer coefficient, respectively (see Table 1, 1-D (G) and 1-D*). The finding is in agreement with the observations of Bauer and Eigenberger [29] who suggested an iterative optimization strategy to optimize prediction quality of a so-called "zone" model. Notably, the statement holds equally true when additional biological readouts are considered: Acceptable 1-D model predictions can be achieved when Sauter diameter, gas hold-up, and mass transfer are derived from CFD simulations.

Figure 7 complements the comparison of the initial simulation results of 1-D (F) and (G) with CFD. The difference in percentage of the most diverging parameters, namely dissolved CO concentration, gas hold-up, and bubble diameter, is illustrated. By trend, CO levels are heavily overestimated almost everywhere using 1-D (F). Gas hold-ups of 1-D (F) and CFD are similar in the lower part of the column but are overestimated in the upper part. Figure 7 also provides detailed insights in the heterogeneities at each column height. Coloring indicates that severe discrepancies may even occur on the same height. The bottom and the upper part are particularly prone to heterogeneous conditions with respect to gas hold-up and bubble sizes.

4 | DISCUSSION

Intrinsically, 1-D modeling is a coarse-grained approach lumping local heterogeneities, thereby reducing the modeling complexity to a minimum. On contrast, CFD aims to unravel spatial particularities exploiting the local resolution. The latter is restricted by the maximum mesh size as well as the general model approach (e.g., multiphase) and therefore the resulting computational effort. For instance, resolving mixing and mass transfer of a 200-L stirred tank reactor with 500 k mesh yields a mean resolution of 0.5 mL and

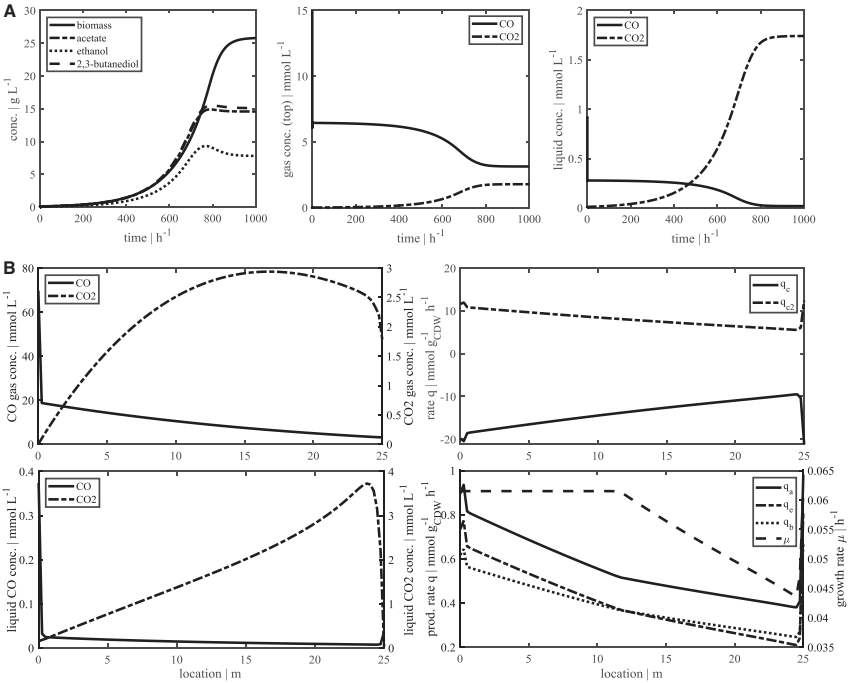

FIGURE 5 Temporal and spatial results for final parameter set-up. In (A), the average concentrations are pictured over time until the process reaches a steady state. (B) Spatially resolved steady-state results of the liquid and gaseous concentrations are shown on the left side. The right side illustrates the related consumption and production rates (acetate q_a, ethanol q_e, and 2,3-butanediol q_b and the growth rate μ)

TABLE 1 Average results of both simulation approaches in comparison

Average	Variable	1-D (F)	CFD	1-D (G)	1-D*	Units
CO concentration	$\bar{c}_{L,CO}$	0.018	0.002	0.016	0.0015	mmol L^{-1}
Gas hold-up	$\bar{\varepsilon}_G$	0.31	0.34/0.21[a]	0.31	0.21	–
Diameter	$\bar{d}_B$	4.4	20.9[b]	20.9	20.9	Mm
Bubble surface	$\bar{a}$	408.3	61.8	86.9	59.1	m^{-1}
Mass transfer rate	$\bar{k}_L$	3.93×10^{-4}	1.75×10^{-4}	3.93×10^{-4}	1.75×10^{-4}	m s^{-1}
Mass transfer	$\overline{k_L a}$	577	39	123	37	h^{-1}
Product-biomass yield	$\bar{Y}_{P,X}$	1.5	0.9	1.3	1.4	–

[a] Second value with breakage, coalescence, bubble expansion, and mass transfer.

[b] Sauter mean for CFD.

Both approaches, 1-D (1-D(F), (G) and *) and computational fluid dynamics (CFD) simulation used the same initial conditions with superficial gas velocity of 0.0625 m s-1 and initial bubble diameter of 4 mm. 1-D (G) used the Sauter mean diameter of the CFD simulation as mean bubble diameter. In the final simulation 1-D*, besides the Sauter diameter, the gas hold-up and mass transfer rate were adjusted accordingly. The product-biomass yield was calculated spatially with the correlation described in Siebler et al. [11].

requires about 2–3 days computing using state-of-the-art personal computers (here: calculation on 16 cores with double precision). However, demanding the same resolution for a 125 m^3 bioreactor calls for high-performance computing with supercomputers. As a consequence, evaluating tests probing different design sets for large-scale application need be performed in a less computationally challenging framework. Still, the same set of essential design parameters should be evaluated but computational speed allows for the identification of a preliminary design optimum that should

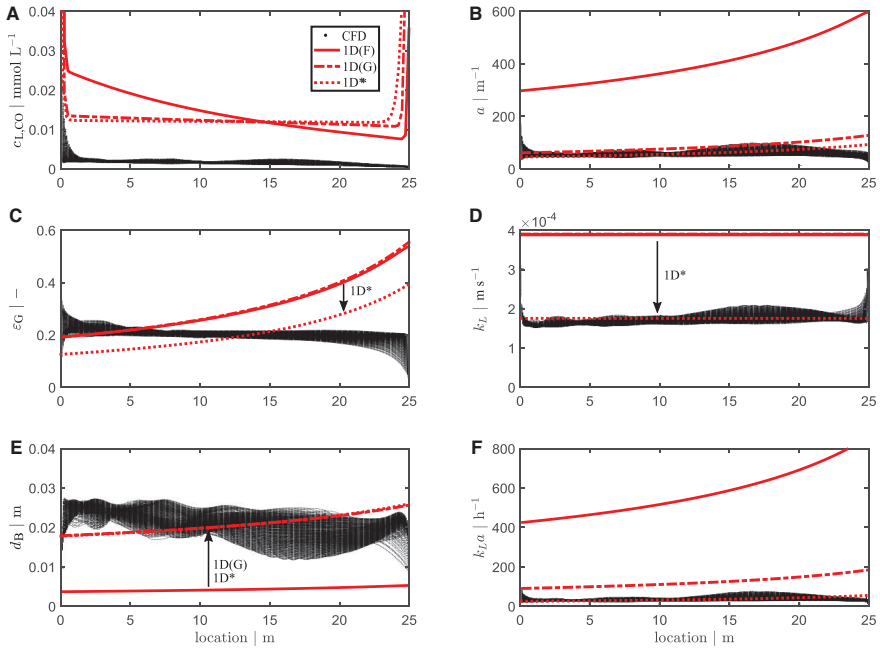

FIGURE 6 Profiles over reactor height in comparison. Each graph depicts profiles of CFD (dots) and 1-D (red lines) simulation. In case of CFD, each dot represents values of individual numerical cells, thereby visualizing the varying conditions at each column height. (A)–(F) Dissolved CO concentration $c_{L,CO}$, bubble area a, gas hold-up ε_G, mass transfer rate k_L, bubble diameter d_B, and volumetric mass transfer k_La are compared

be further investigated by CFD approaches. It is exactly this scenario that is exemplified in this study.

4.1 | Parameter space analysis

As indicated in Figs. 3 and 4, increasing CO fraction finally improves the biomass and the (by-)product formation indicated by the readouts C_{fix} and Y_{PX}. This observation reflects predominately low CO levels in the column which do not (yet) cause growth inhibition. Accordingly, any measure to improve CO levels is responded by rising C_{fix} and Y_{PX}. Noteworthy, the physical parameters $\bar{\varepsilon}_G$, $\bar{d}_B$, $\overline{k_La}$, and n_G are not affected by CO fractions, which allows their independent fine-tuning.

In agreement, variations of the gassing rate vvm support the necessity to install proper CO supply. Additionally, the important minimum threshold value of about 0.06 vvm is outlined (see Figure 4). Below, the biological readouts C_{fix} and Y_{PX} increase with strong positive correlation on vvm raise, whereas higher vvm settings improve biological performance only marginally. Accordingly, any gassing rate limitation beyond 0.06 vvm can be ruled out that renders this value an important design parameter. Noteworthy, low vvm settings may even cause maximum dissolved CO_2 levels, which reflect the counteracting mechanisms of gassing input, hold-up, and stripping.

The improvement of k_La values (variation C) is always beneficial for the biological readouts. Again, the finding mirrors the fact that most CO levels are far below inhibiting thresholds, which highlights the necessity to improve CO mass transfer.

One possibility to improve mass transfer is to increase gas hold-up. Equations (9)–(13) show that the set of related physical parameters is intertwined, linking changes of gas hold-up ε_G to changes of a, k_L, d_B, and k_La. For the sake of simplicity, large-scale simulations may exclude putative impacts of gas hold-up ε_G [14, 21]. However, this study aims to light related impacts by investigating two possible simulation regimes (see Figure S3): variation D keeps k_La constant; variation E allows flexible k_La (setting k_L and d_B constant with characteristic values, see Section 3.2).

The increase of ε_G (variation D) results in minor changes of the biological readouts (see Figure 4D). This reflects the fact that gas hold-up rise is responded by k_L reduction, which in turn reduces CO availability. However, the regime

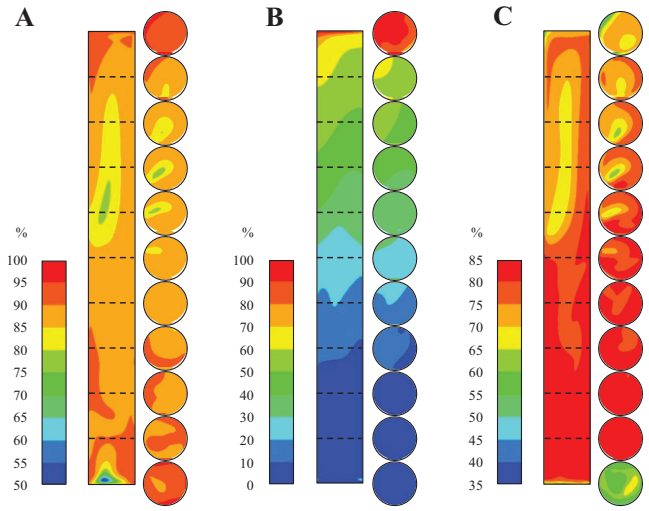

FIGURE 7 Differences between 1-D and CFD simulation over reactor height. Concentration $c_{L,CO}$ (A), gas hold-up ε_G (B), and mean diameter d_B (C) deviation profiles are demonstrated in percentage over the reactor height. Additionally, horizontal section planes (dashed lines, top and bottom) are graphically shown on the right side for each deviation profile. In (A), $100\% - c^{CFD}_{L,CO}(z)/c^{1D}_{L,CO}(z) \cdot 100\%$ is shown, which translates high similarity into low values. By analogy, graphic (B) is set. In (C), the criterion $100\% - d^{1D}_B(z)/d^{CFD}_B(z) \cdot 100\%$ was applied to avoid negative values. Still, high percentages encode large deviations

of variable k_La allows to transfer ε_G raise proportionally to rising a, which improves k_La and leads to alleviated process performance (see Figure 3E). Both cases illustrate that gas hold-up impacts have to be considered properly to get valid design values for further analysis.

Based on this evaluation, the setting of the reference process as the new optimal setting F was chosen as follows: The CO fraction was not adjusted since converter gas of metallurgical production processes rather not exceeds this value [30]. However, a moderate gassing rate of 0.15 vvm was chosen that responds to the gas hold up of $\varepsilon_G = 0.31$ ($\varepsilon_{G,0} = 0.19$). According to Bailey and Ollis [31, p. 611], this is the critical threshold value of starting heterogeneous bubbly flow in air–water systems. Finally, moderate to high mean steady-state k_La values range (140–580 h^{-1}) was rerun. The setting yielded the final simulation results in Figure 5.

4.2 | 1-D versus CFD

Figures 6 and 7 depict the discrepancy between 1-D and CFD modeling. Not only spatial differences are shown (Figure 7) but also discrepancies in fundamental trends (Figure 6). The first may have been expected as they reflect the missing granularity of 1-D modeling. However, the second clearly pinpoint to the lacking mechanistic details of modeling bubble size distributions with the 1-D (F) approach. Apparently, simply considering gas fractions and bubble numbers leads to severe overestimation of a values, which in turn reflect too small bubble diameters d_B. As a consequence, 1-D (F) overestimates k_La, which creates too high CO levels and increases biological performance. Consequently, 1-D modeling should already consider proper approaches to simulate bubble sizes. Simply estimating bubble numbers creates biased simulation results. This trend was already indicated in the gas hold-up analysis and is clearly visible in Figure 6. Noteworthy, the consideration of the Sauter diameter of the CFD simulation improved the prediction quality of 1-D (G) with respect to physical and biological readouts. Additionally, using the gas hold-up and mass transfer value of CFD simulations enhanced simulation quality even further. Predictions of 1-D (G), 1-D*, and CFD converged but average rates and constants of mass transfer are still too high in 1-D (G). Nevertheless, the biological readouts approximated to approximately 40% deviation of the CFD value.

5 | CONCLUSIONS

Without doubt, CFD simulations inherently offer the most accurate prediction of physical and biological readouts, spatially resolved, in large-scale bioreactor fermentations. However, they also require detailed mechanistic understanding

and—equally challenging—proper computational power for dealing with industrial scale multiphase, mass transfer, mixing, and reaction problems. Conceptual design approaches need to search through parameter spaces of putative operational windows. Although CFD simulations would be ideal to fulfill the task, limited computational power constraints calculations on the use of 1-D models. Users must be aware that physical readouts are most likely overestimating bioreactor performance because impacts of bubbles are reflected poorly. Nevertheless, the use of properly estimated Sauter mean diameters from CFD helps to improve model predictions, in particular for highly relevant biological readouts such as product-biomass yields.

NOMENCLATURE

a	[m^{-1}]	Interfacial area concentration
A	[m^2]	Cross-sectional area
c_k	[g L^{-1}]	Product concentration
c_m	[mmol L^{-1}]	Gas concentration
C_{fix}(SS)	[-]	Total steady state carbon fixation
D	[h^{-1}]	Dilution rate
d_{32}	[m]	Sauter mean bubble diameter
d_B	[m]	Bubble diameter
D_{CO}	[m^2 s^{-1}]	Diffusion coefficient
D_L	[m^2 s^{-1}]	Liquid phase dispersion coefficient
D_R	[m]	Reactor diameter
$\mathbf{g}$	[m s^{-2}]	Gravitational acceleration
H_L	[m]	Liquid height
H_m^{cp}	[mol L^{-1} atm^{-1}]	Henry coefficient
k_L	[m s^{-1}]	Mass transfer coefficient
M	[g mol]	Molecular weight
n	[-]	Numerical volumes
N	[-]	Number of sections
N_B	[-]	Number of bubbles
n_G	[m^{-3}]	Number density
n_m	[mol]	Number of moles of gas
P	[atm]	Pressure
q_k	[mmol g_{CDW}^{-1} h^{-1}]	Production rates
$\dot{Q}_L$	[m^3 h^{-1}]	Media flow
q_m	[mmol g_{CDW}^{-1} h^{-1}]	Gas consumption rates
$\dot{Q}_R$	[m^3 h^{-1}]	Back flow
R	[$kg \cdot m^2 \cdot s^{-2} \cdot K^{-1} \cdot mol^{-1}$]	Universal gas constant
R_B	[m]	Bubble radius
t	[s]	Time
T	[K]	Temperature
v	[m s^{-1}]	Velocity
V	[m^3]	Volume
y_m	[-]	Gas fraction
Y_{PX}(SS)	[-]	Steady-state production biomass yields
z	[m]	Direction and unit of length
Δz	[m]	Section height
Greek symbols		
α	[-]	Combined back and media flow
ϵ	[-]	Volume fraction
μ	[h^{-1}]	Growth rate
ρ	[kg m^{-3}]	Density
ρ^*	[mol m^{-3}]	Total molar density
σ	[N m]	Surface tension
Indices		
*		Equilibrium concentration
0		Initial value
A		Acetate
B		2,3-Butanediol
B		Bubble
C		Indices for CO uptake rate
E		Ethanol
G		Gaseous
i		Section counter for 1-D approach
k		Product $k \in [\text{acetate, ethanol, } 2,3-\text{butanediol}]$
L		Liquid
m		Gas composition $m \in [CO, CO_2, H_2]$
R		Reactor
s		Indices superficial gas velocity
bubbles		Mass transfer area between the liquid and gaseous phase
slip		Slip velocity
T		Indices for terminal velocity
X		Biomass

ACKNOWLEDGMENTS

The authors would to thank the research group of Chen et al. [14, 20, 21] for their previous work on this subject. This work was supported by the Federal Ministry of Education and Research (BMBF; FKZ031A468B).

AUTHOR CONTRIBUTIONS

R.T. and A.L. proposed this study. Simulation and evaluation were conducted by Flora Siebler. The manuscript was written by F.S. and R.T.

CONFLICT OF INTEREST

The authors have declared no conflict of interest.

REFERENCES

1. Liguori, R., Faraco, V., Biological processes for advancing lignocellulosic waste biorefinery by advocating circular economy. *Bioresour. Technol.* 2016, *215*, 13–20.
2. Straathof, A.J.J., Wahl, S.A., Benjamin, K.R., Takors, R., et al., Grand research challenges for sustainable industrial biotechnology. *Trends Biotechnol*. 2019, *37*, 1042–1050.
3. Philp, J., The bioeconomy, the challenge of the century for policy makers. *N. Biotechnol.* 2018, *25*, 11–19.
4. Diender, M., Stams, A.J.M., Sousa, D.Z., Pathways and bioenergetics of anaerobic carbon monoxide fermentation. *Front. Microbiol.* 2015, *6*, 1–18.
5. Latif, H., Zeidan, A.A., Nielsen, A.T., Zengler, K., Trash to treasure: production of biofuels and commodity chemicals via syngas fermenting microorganisms. *Curr. Opin. Biotchnol.* 2014, *27*, 79–87.
6. Takors, R., Kopf, M., Mampel, J., Blümke, W., et al., Using gas mixtures of CO, CO_2 and H_2 as microbial substrates: the do's and don'ts of successful technology transfer from laboratory to production scale. *Microb. Biotechnol.* 2018, *11*, 606–625.
7. Bengelsdorf, F.R., Dürre, P., Gas fermentation for commodity chemicals and fuels. *Microb. Biotechnol.* 2017, *10*, 1167–1170.
8. Dürre, P., Butanol formation from gaseous substrates. *FEMS Microbiol. Lett.* 2016, *363*, fnw040.
9. Haringa, C., Tang, W., Deshmukh, A.T., Xia, J., et al., Euler-Lagrange computational fluid dynamics for (bio)reactor scale-down: an analysis of organism life-lines. *Eng. Life Sci.* 2016, 16, 652–663.
10. Kuschel, M., Siebler, F., Takors, R., Lagrangian trajectories to predict the formation of population heterogeneity in large-scale bioreactors. *Bioengineering* 2017, *4*, 1–13.
11. Siebler, F., Lapin, A., Hermann, M., Takors, R., The impact of CO gradients on *C. ljungdahlii* in a 125 m^3 bubble column: mass transfer, circulation time and lifeline analysis. *Chem. Eng. Sci.* 2019, 207, 410–423.
12. Haringa, C., Tang, W., Wang, G., Deshmukh, A.T., et al., Computational fluid dynamics simulation of an industrial *P. chrysogenum* fermentation with a coupled 9-pool metabolic model: towards rational scale-down and design optimization. *Chem. Eng. Sci.* 2018, *175*, 12–24.
13. Zieringer, J., Takors, R., In silico prediction of large-scale microbial production performance: constraints for getting proper data-driven models. *Comput. Struct. Biotechnol. J.* 2018, *16*, 246–256.
14. Chen, J., Gomez, J.A., Höffner, K., Phalak, P., et al., Spatiotemporal modeling of microbial metabolism. *BMC Syst. Biol.* 2016, *10*, 1–13.
15. Lapin, A., Lübbert, A., Numerical simulation of the dynamics of two-phase gas—liquid flows in bubble columns. *Chem. Eng. Sci.* 1994, *49*, 3661–3674.
16. Vrábel, P., van der Lans, R.G.J.M., van der Schot, F.N., Luyben, K.C.A.M., et al., CMA: integration of fluid dynamics and microbial kinetics in modelling of large-scale fermentations. *Chem. Eng. J.* 2001, *84*, 463–474.
17. Heins, A.-L., Lencastre Fernandes, R., Gernaey, K. V., Lantz, A.E., Experimental and in silico investigation of population heterogeneity in continuous *Sachharomyces cerevisiae* scale-down fermentation in a two-compartment setup. *J. Chem. Technol. Biotechnol.* 2015, *90*, 324–340.
18. Pigou, M., Morchain, J., Investigating the interactions between physical and biological heterogeneities in bioreactors using compartment, population balance and metabolic models. *Chem. Eng. Sci.* 2015, *126*, 267–282.
19. Delafosse, A., Collignon, M.-L., Calvo, S., Delvigne, F., et al., CFD-based compartment model for description of mixing in bioreactors. *Chem. Eng. Sci.* 2014, *106*, 76–85.
20. Chen, J., Gomez, J.A., Höffner, K., Barton, P.I., et al., Metabolic modeling of synthesis gas fermentation in bubble column reactors. *Biotechnol. Biofuels* 2015, *8*, 1–12.
21. Chen, J., Daniell, J., Griffin, D., Li, X., et al., Experimental testing of a spatiotemporal metabolic model for carbon monoxide fermentation with *Clostridium autoethanogenum*. *Biochem. Eng. J.* 2018, *129*, 64–73.
22. Mohammadi, M., Mohamed, A.R., Najafpour, G.D., Younesi, H., et al., Kinetic studies on fermentative production of biofuel from synthesis gas using *Clostridium ljungdahlii*. *Sci. World J.* 2014, *2014*, 1–8.
23. Higbie, R., The rate of absorption of a pure gas into a still liquid during short periods of exposure. *Trans. Am. Inst. Chem. Eng.* 1935, *35*, 365–389.
24. Cussler, E.L., *Diffusion: Mass Transfer in Fluid Systems*, 3rd ed., Cambridge University Press, Cambridge, UK 2009.
25. Tomiyama, A., Kataoka, I., Zun, I., Sakaguchi, T., Drag coefficients of single bubbles under normal and micro gravity conditions. *Japan Soc. Mech. Eng.* 1998, *41*, 472–479.
26. Heijnen, J.J., van't Riet, K., Mass transfer, mixing and heat transfer phenomena in low viscosity bubble column reactors. *Chem. Eng. J.* 1984, *28*, 21–42.
27. Schügerl, K., Lücke, J., Oels, U., Bubble column bioreactors: tower bioreactors without mechanical agitation. *Adv. Biochem. Eng.* 1977, 1–84.
28. Akita, K., Yoshida, F., Gas holdup and volumetric mass transfer coefficient in bubble columns. Effects of liquid properties. *Ind. Eng. Chem. Process Des. Dev.* 1973, *12*, 76–80.
29. Bauer, M., Eigenberger, G., A concept for multi-scale modeling of bubble columns and loop reactors. *Chem. Eng. Sci.* 1999, *54*, 5109–5117.
30. Clarke Energy ®. Furnace Gas for Power Production: Gases from Metallurgical Production Processes. Clarke Energy, Algeria 2018.
31. Bailey, J.E., Ollis, D.F., *Biochemical engineering fundamentals*, 2nd ed. Chemical Engineering Education, Mc Graw-Hill Inc., USA 1986.

SUPPORTING INFORMATION

Additional supporting information may be found online in the Supporting Information section at the end of the article.

How to cite this article: Siebler F, Lapin A, Takors R. Synergistically applying 1-D modeling and CFD for designing industrial scale bubble column syngas bioreactors. *Eng Life Sci*. 2020;1–13. https://doi.org/10.1002/elsc.201900132